University of Southampton

Variability of water masses and circulation in the subtropical North Atlantic

Robert Marsh

Doctor of Philosophy

School of Ocean and Earth Sciences

December 1999

UNIVERSITY OF SOUTHAMPTON

ABSTRACT
FACULTY OF SCIENCE
SCHOOL OF EARTH SCIENCES

Doctor of Philosophy
VARIABILITY OF WATER MASSES AND CIRCULATION IN THE SUBTROPICAL NORTH ATLANTIC
by Robert Marsh

Observations of interannual variability in 18° Water (Talley and Raymer 1982) and Gulf Stream transport (Worthington 1977) motivate an ocean model sensitivity study. The North Atlantic circulation is simulated with a three-dimensional isopycnic-coordinate GCM. Idealized anomalous buoyancy-forcing fields (associated with outbreaks of cold, dry continental air over the Gulf Stream/Sargasso Sea region) are constructed. In a series of sensitivity experiments, wintertime buoyancy loss over the Gulf Stream and Sargasso Sea is thus increased to varying degrees, with anomalous ocean-to-atmosphere buoyancy fluxes of up to double climatological values.

Under excess buoyancy loss, winter mixed layer depths increase, and a greater volume of model 18° Water is formed. End-of-winter mixed layer density also increases, leading to the formation of a denser variety of 18° Water. The anomalous 18° Water recirculates around the Sargasso Sea as a signal of low potential vorticity, which spreads out and weakens on a decadal timescale. Strengthened horizontal pressure gradients in the vicinity of the anomalous 18° Water drive intensified baroclinic transports at the "immediate" end of winter (in March), after which a full-depth barotropic intensification of the Gulf Stream develops. Strongest intensification occurs in May, when the Gulf Stream barotropic transport is increased locally by up to 10 Sv.

The anomalous transports which account for barotropic intensification are confined to deep and abyssal layers of the model. Where the associated anomalous bottom currents traverse isobaths, "extra" bottom pressure torque (BPT) is invoked. An anomalous BPT term in the barotropic vorticity balance may therefore account for the intensification. Computed from the model fields of density and sea surface height, such a term does appear to produce the extra negative vorticity associated with anticyclogenic intensification. It is concluded that wintertime excess buoyancy loss drives a springtime barotropic response of the subtropical gyre, through BPT, due to "JEBAR" (the Joint Effect of Baroclinicity And Relief).

The Gulf Stream intensification decreases after May as lateral eddy mixing weakens anomalous cross-stream pressure gradients. This eddy mixing is parameterized in the model by a layer thickness diffusion velocity, u_d, nominally chosen to be 1.0 cm s^{-1}. Further experiments establish the sensitivity of intensification strength to the choice of u_d. With u_d = 0.1 cm s^{-1} (weak thickness diffusion), the intensification is increased by ~50%, while, for u_d = 10 cm s^{-1} (strong thickness diffusion), the intensification is roughly halved. These further sensitivity experiments also reveal the varying degrees to which the model subtropical gyre can be dominated by diffusive eddy mixing (Rhines and Young 1982a, 1982b) or adiabatic (non-diffusive) ventilation of the thermocline (Luyten, Pedlosky and Stommel 1983).

Recent (1980-97) interannual variability in the formation and recirculation of 18° Water, and other water masses, is deduced from observed surface heat and freshwater fluxes. Interannual variations in the strength of 18° Water renewal (thus deduced) and a wintertime index of the North Atlantic Oscillation (NAO) are found to be strongly anti-correlated (with a correlation coefficient of -0.70, statistically significant at a 99% confidence level). A further sensitivity experiment establishes that anomalous wind forcing, characteristic of a minimum phase in the NAO, does not intensify the Gulf Stream in the manner of excess cooling. It is concluded that 18° Water is more strongly renewed, with accompanying Gulf Stream intensification, under NAO-minimum *buoyancy* forcing.

LIST OF CONTENTS

LIST OF FIGURES AND TABLES

Acknowledgments

First and foremost, I must thank Neil Wells for suggesting in early 1992 that I test the Worthington hypothesis with the Atlantic Isopycnic Model (AIM), and then agreeing to be my supervisor for an unspecified duration of part time study.

Implicit in Neil's original idea was the surprisingly realistic 18° Water variability which appeared as a bonus in my AIM experiments (and subsequently became a central theme). Neil read a great deal of preliminary text, and I much appreciated his honest comments on early versions of chapters! I am also grateful to Harry Bryden for reading the penultimate version of this thesis. Aside from constructive suggestions, his encouragement, as the finishing post retreated and my optimism flagged, was a great boost to my morale.

In that this study depended so much on AIM, I am indebted to my colleagues Adrian New and Yanli Jia, who "built" the original AIM between autumn 1990 and summer 1991. I must further recognize the pioneering work of Rainer Bleck, Linda Smith, Eric Chassignet, Claes Rooth and Dingming Hu, colleagues at the University of Miami who, having developed the isopycnal model code during the 1980s, then helped us enormously as we set up AIM. From 1992 onwards, George Nurser helped me in the development of many AIM diagnostics. With George's assistance, I have gained an understanding of AIM (and hence the real world!) that would otherwise have remained elusive.

I thank my old colleague Phil Jones, of the Climatic Research Unit (UEA, Norwich), for providing the historical sea surface temperature and pressure data which helped me to develop idealized forcing fields. Collaboration with Bob Dickson, spanning autumn 1994 to spring 1996, brought to my full awareness the truly extensive impact of the North Atlantic Oscillation, and motivated the wind forcing sensitivity experiment. Simon Josey allowed me privileged access to "pre-release" monthly global fields of surface heat and freshwater flux spanning 1980-97 - data which yielded very interesting results.

Finally, I must acknowledge my mum and dad, who instilled in me a boundless fascination for the natural world, and unfailingly reminded me for the last couple of years that I had not yet finished this work. Also, so many friends remained good company throughout the last few years: Simon, Ben, Boris, Dave, Paul to name just the regulars. Last of all, Lisa so lovingly understood, tolerated, shared and assisted the difficult completion of this work, for which I will always be grateful.

CHAPTER 1. INTRODUCTION

1.1 The context of the present study

Over the last decade (1990-97) the World Ocean Circulation Experiment (WOCE) has been undertaken. More a global survey than an experiment in the traditional sense, WOCE has seen the unprecedented collection of a near-synoptic three-dimensional oceanographic dataset, allied with continuing development of numerical models of ocean circulation. Over the first decade of the new millenium an international program to study Climate Variability and Predictability (CLIVAR), the central component of the World Climate Research Programme, will maintain large-scale, long-term monitoring of the global ocean.

Decadal variations in the climate of Europe and North America are probably driven by changing air-sea interaction over the North Atlantic, of which the subtropical gyre is a major component. The following extract from the Science and Implementation Plan for the proposed Atlantic Climate Variability Experiment (Visbeck *et al.* 1998) summarizes the role of the subtropical gyre and two outstanding research issues:

> *In the north eastern part of the subtropical gyres much of the upper ocean thermocline ventilation takes place. Variability of the sea surface properties in those subduction zones can enter into the upper ocean. Now shielded from the direct air-sea interaction they can propagate with the mean flow throughout the subtropical gyre until they get re-exposed to the surface in the entrainment zone close to the western boundary current region.*
>
> *- Can subducted water mass anomalies survive many years subsurface and finally modify the sea surface condition in the entrainment region in the western part of the gyre?*
>
> *- How important are changes in the circulation relative to changes in the surface fluxes to generate and maintain subducted temperature anomalies?*

In the present study, an ocean-only numerical model of the North Atlantic is used to simulate variability in the water masses and circulation of the subtropical gyre. The model used here is the Atlantic Isopycnic Model (AIM), which was developed as part of the UK contribution to WOCE.

This study was originally motivated by observational evidence for intensification of the Gulf Stream after the severe winter of 1977 (Worthington 1977) and strong formation during the cold 1960s of "18° Water" (Talley and Raymer 1982), a warm water mass which forms convectively in the western subtropical gyre of the North Atlantic (Worthington 1959). The primary focus, therefore, is on interannual variability in the surface buoyancy forcing of this region (primarily through wintertime cooling) and the impact of this variability on 18° Water and the Gulf Stream. Model sensitivity experiments examine the renewal of 18° Water and Gulf Stream transport under excess wintertime cooling and evaporation. Further experiments reveal the varying degrees to which the model subtropical gyre can be dominated by diffusive eddy mixing (Rhines and Young 1982a, 1982b) or adiabatic (non-diffusive) ventilation of the thermocline (Luyten, Pedlosky and Stommel 1983), establishing the significance of parameterized eddy mixing in the present study.

The anomalous buoyancy forcing considered here may, to an extent, be associated with a minimum phase of the North Atlantic Oscillation (NAO). North Atlantic fields of recent (1980-97) surface heat and freshwater flux are used to infer interannual-to-decadal changes in the meridional circulation of water masses, in particular to identify NAO-related variability of 18° Water recirculation. A final sensitivity experiment examines the relative impact of NAO-minimum wind forcing on the subtropical gyre.

1.2 Thesis outline

This thesis is organized into the following seven chapters. The background to the area of study is reviewed in chapter 2. Chapter 3 outlines the methodology, introducing the numerical model, experimental strategy, diagnostic methods and historical datasets (used to aid experimental design and to diagnose variability in water mass renewal rates). Chapter 4 presents the results of the model experiments which address the impacts of anomalous buoyancy forcing (specifically 18° Water variability and Gulf Stream intensification). Chapter 5 presents the results of experiments repeated with more/less model layer thickness diffusion (lateral eddy mixing) and a more detailed diagnosis of the Gulf Stream intensification. In chapter 6, a novel diagnostic, the surface-forced meridional streamfunction, is introduced and obtained for the North Atlantic over 1980-97, revealing variability in water mass recirculation which is related to the NAO. Chapter 7 presents the experiment in which the model is forced with idealized NAO-minimum wind fields. Chapter 8 is a summary and discussion of what may, at first sight, appear to be a disparate set of findings, concluding with outlines for further work and final remarks.

CHAPTER 2. LITERATURE REVIEW

This chapter is organized into five sub-sections. The observed hydrography and circulation, relevant to the study, are reviewed (§2.1). The development of theoretical ideas, which sought to explain the circulation and three dimensional structure of the subtropical gyre, is outlined (§2.2). The evidence for seasonal variations in western boundary current transport is reviewed (§2.3), followed by a consideration of interannual variability (of forcing, hydrography and circulation) in the study region (§2.4). Finally, the literature review is summarized and primary objectives of the present study are outlined (§2.5).

2.1 An overall picture

2.1.1 The general circulation of the North Atlantic

For clarity, the three-dimensional general (i.e., large-scale) circulation of the ocean is generally decomposed into horizontal "gyres" (terminology introduced by Walter Munk, describing circulation on some two-dimensional surface, or vertically-averaged) and zonally-averaged meridional overturning "cells".

The horizontal circulation of the extratropical North Atlantic is characterized by two counter-rotating gyres: an anticyclonic subtropical gyre and a cyclonic subpolar gyre, separated by an inter-gyre zone in mid-latiudes.

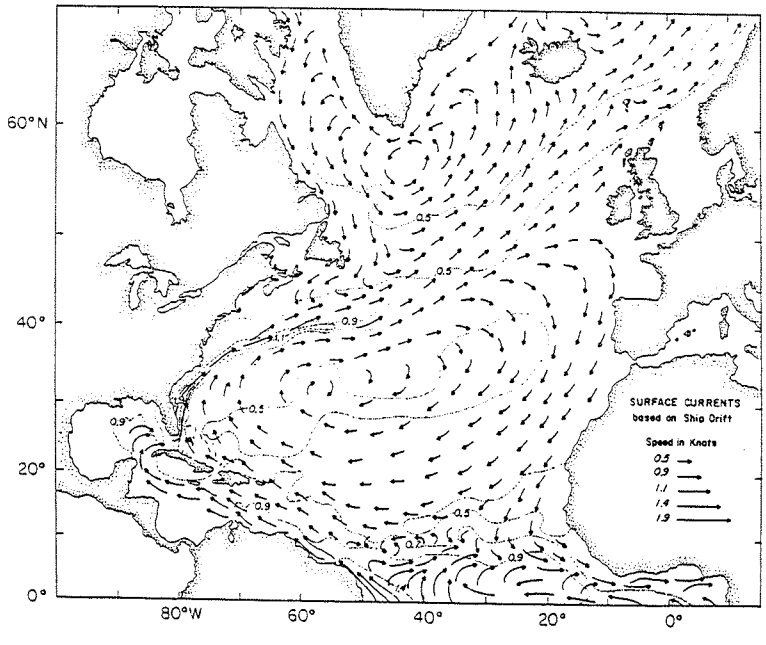

Figure 2.1: North Atlantic surface currents, estimated from ship drift (U.S. Naval Oceanographic Office 1965).

The surface circulation associated with these features is apparent in **Fig. 2.1** (Schmitz 1996, from the U.S. Naval Oceanographic Office Publ. 700, 1965), which shows average currents for the North Atlantic, based on summer ship drift data. Currents in **Fig. 2.1** are typically 0.5 knots ($\cong$25 cm s^{-1}), although stronger currents are evident along the western boundary of the subtropical gyre, reaching 2 knots ($\cong$1 m s^{-1}), off the east coast of Florida.

The meridional overturning of the North Atlantic is dominated by a thermohaline-forced cell which incorporates the northward flow of warm water in the surface and upper layers, strong sinking and associated "warm-to-cold" conversion at mid to high latitudes (McCartney and Talley 1984), and the southward flow of cold water in intermediate and deep layers. The first direct evidence for a deep southward flow - the Deep Western Boundary Current (DWBC) - was obtained by Swallow and Worthington (1957). Since then, many further observations have lead to the development of overturning schemes such as that shown in **Fig. 2.2** (a personal communication from McCartney and Curry to Schmitz 1996).

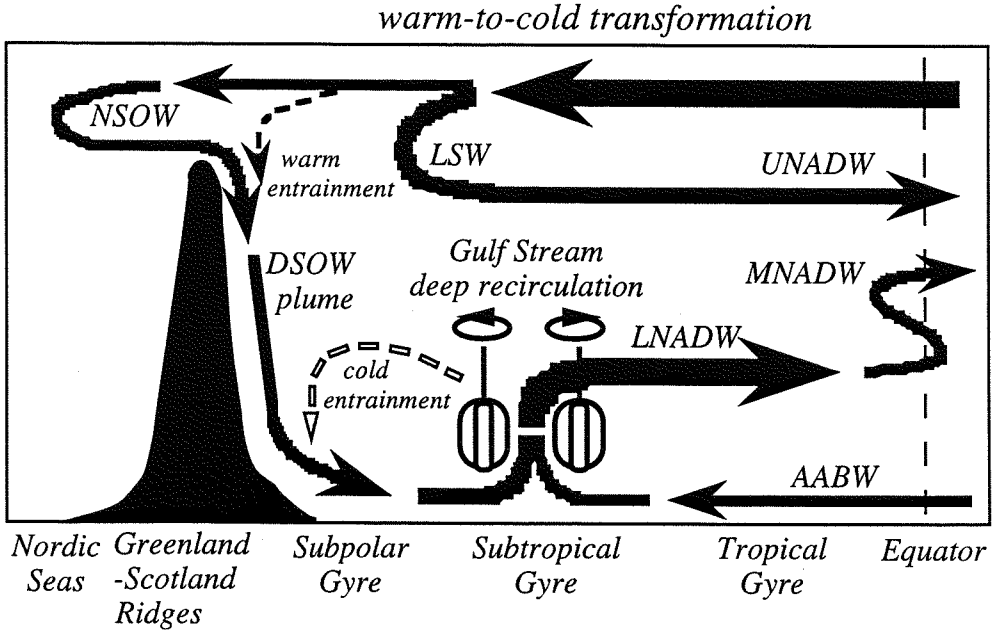

Figure 2.2: Meridional circulation scheme for the North Atlantic (adapted from McCartney and Curry, in Schmitz 1996).

Associated with the lower branches of overturning shown in **Fig. 2.2** are various water masses, dominated by southward flows of Upper, Middle and Lower North Atlantic Deep Water (UNADW, MNADW and LNADW). UNADW is a product of

the near-isopycnal mixing of cold, fresh Labrador Sea Water (LSW) and warm, salty Mediterranean Water (Talley and McCartney 1982). MNADW originates as Denmark Straits Overflow Water (DSOW), supplied by a reservoir of Nordic Sea Overflow Water (NSOW), which escapes to the subpolar gyre through a series of deep gaps in the ridge system connecting Greenland to Scotland. DSOW flows as a turbulent plume along and down the continental slope from Denmark Strait to Cape Farewell (at the southern tip of Greenland), strongly modified by entrainment en route to the abyss (Dickson and Brown 1994). Where the DWBC crosses the Gulf Stream, strong recirculation and entrainment further modify MNADW (Pickart and Smethie 1992). LNADW is the product of slower diffusive mixing with Antarctic Bottom Water (AABW) in the abyssal Eastern Basin (McCartney *et al.* 1991).

The three-dimensional general circulation thus incorporates horizontal gyres and meridional overturning cells in a rather complicated manner. The present study, however, focuses on the subtropical gyre.

2.1.2 The Gulf Stream

Strong currents in the Straits of Florida were first noted by European mariners as long ago as 1513 (Stommel 1950). Water flows out of the Gulf of Mexico as the Florida Current, then turns sharply northward to the southeast of Florida. In the vicinity of Blake Plateau (which lies to the northwest of the Bahamas), the Florida Current is joined (and enhanced) by the Antilles Current, forming the Gulf Stream. The Gulf Stream thereafter follows the coastline of Florida, Georgia and the Carolinas, exhibiting maximum surface currents of around 200 cm s^{-1} at 100-200 km offshore. At Cape Hatteras, the Gulf Stream "separates" from the coastline, develops into a nearly zonal jet, and begins to meander. The amplitude of meandering amplifies downstream, until the standard deviation of the Stream axis (normal about a mean axis) reaches around 100 km east of ~60°W (Cornillon 1986). At around 50°W the Gulf Stream weakens and branches into four principal currents: north and south recirculations (which return to intensify upstream transports), the Azores Current (essentially feeding the wind-driven return flow across the subtropical gyre), and the North Atlantic Current.

Much has been written about the Gulf Stream, but the seminal work of Stommel (1958a, 1965) stands out as the first comprehensive description of the physics and dynamics of the Stream. **Fig. 2.3** shows the main features of the Gulf Stream System, illustrating how recirculation gyres enhance transport downstream of Cape Hatteras. The southern recirculation gyre is the dominant mode of recirculation, more than doubling Gulf Stream transport.

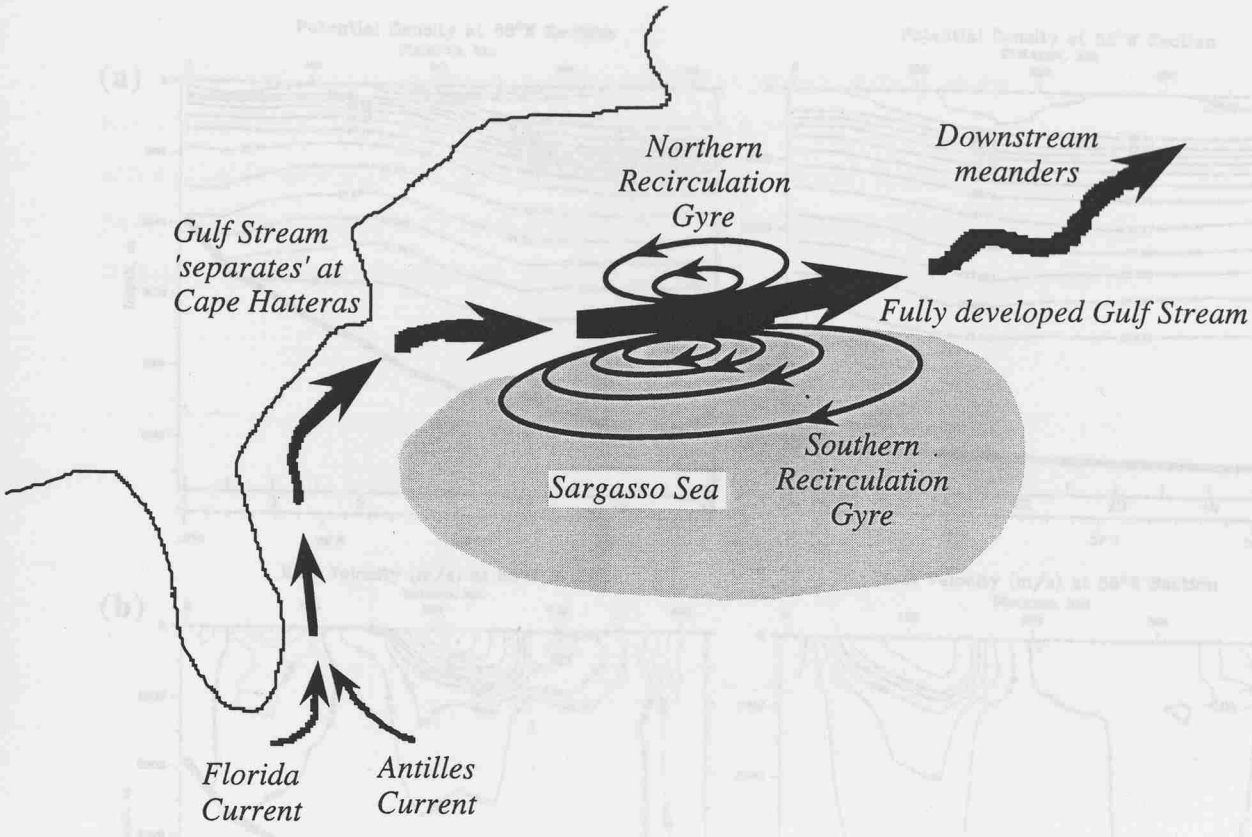

Figure 2.3: Schematic showing main features of the Gulf Stream System (mean circulation).

Between the Florida Straits and the region downstream of Cape Hatteras, the Gulf Stream widens from ~100 km to ~200 km, while strongest surface currents decrease from ~200 cm s^{-1} to ~100 cm s^{-1}. Gulf Stream transport varies widely in the along-stream sense. The Florida Current reliably measures ~30 Sv. After merging with the Antilles Current, and due to a degree of recirculation en route along the coastline, Gulf Stream transport at Cape Hatteras has increased to about 60 Sv. Downstream from Cape Hatteras the Gulf Stream "develops" considerably, and transport increases to a maximum of ~150 Sv in the longitude range 45-55°W (Schmitz 1996).

The Gulf Stream is also characterized by a quite distinctive cross-sectional structure, notably a strong lateral density gradient associated with offshore deepening of the thermocline. The two full-depth sections across the Gulf Stream (of potential density and total current) shown in **Fig. 2.4** are composited from various figures of Hall and Fofonoff (1993), who recently surveyed the Gulf Stream at 68°W and 55°W, in a near-synoptic attempt to observe downstream development, evidenced by total transport estimates, across 68°W and 55°W respectively, of 125 Sv and 139 Sv.

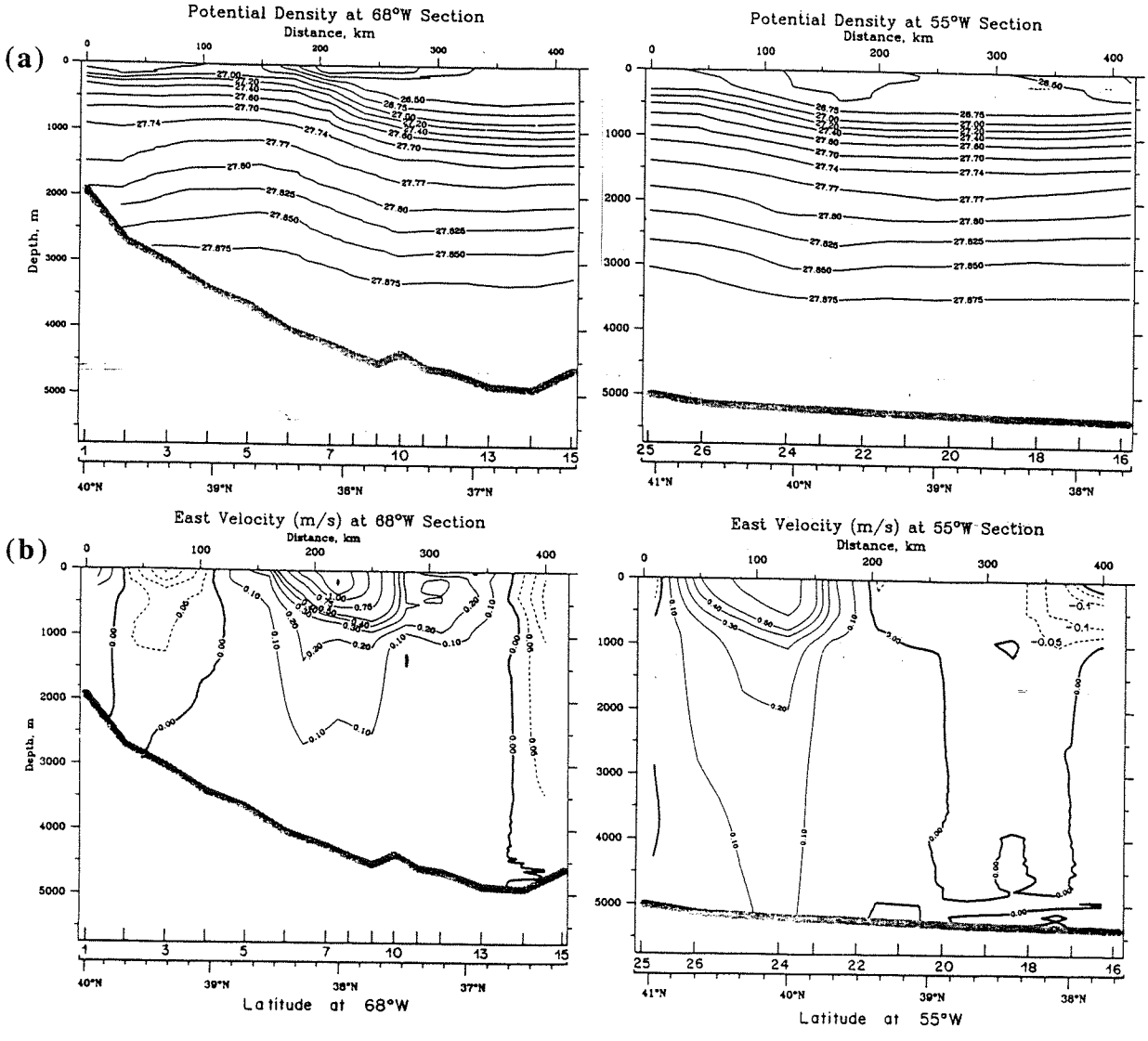

Figure 2.4: North-south hydrographic sections across the Gulf Stream at 68°W and 55°W, showing (a) potential density, and (b) total velocity (Hall and Fofonoff 1993)

Total transport can be decomposed into depth-dependent *baroclinic* and depth-independent *barotropic* components. The total currents in **Fig. 2.4b** are thus obtained by adding the local barotropic velocity to baroclinic velocity profiles. Baroclinic currents are computed from the geostrophic relation (pressure gradients due to lateral density differences are balanced by the Coriolis force due to the Earth's rotation), applied to adjacent density profiles (**Fig. 2.4a**), conventionally assuming a reference level of no motion (at the ocean bottom in this case). Barotropic currents are obtained as differences between absolute (total) currents (measured by co-located current meters and a shipboard acoustic Doppler current profiler) and the baroclinic currents.

The downstream increase in total transport is almost entirely in the barotropic component. **Fig. 2.5** (reproduced from Schmitz 1996) summarizes some reliable estimates of Gulf Stream transport downstream from Cape Hatteras. Note the near-constant baroclinic component of transport (~50 Sv) while barotropic transport roughly doubles (from 50 to 100 Sv) between Cape Hatteras and ~60°W.

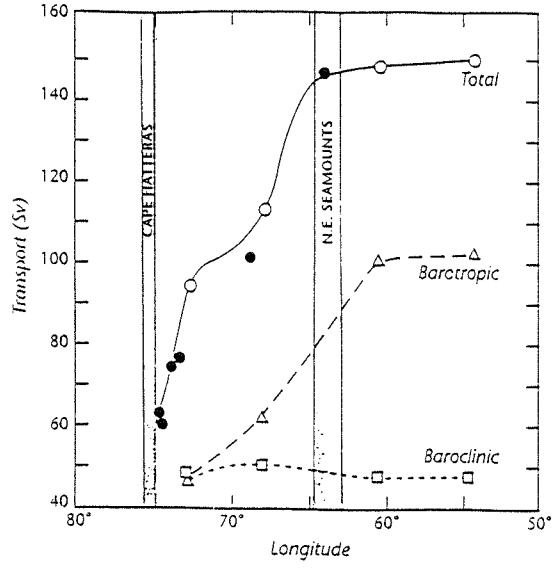

Figure 2.5: Barotropic and baroclinic along-stream increases in Gulf Stream transport (Schmitz 1996).

2.1.3 18° Water

Upon completing a volumetric temperature-salinity (*T-S*) census of North Pacific hydrographic data, Masuzawa (1969) found that, within the region of Kuroshio recirculation, a relatively large volume of water fell into a particular *T-S* class, implying a bivariate "mode". Masuzawa (1969) termed this water type "Subtropical Mode Water" (STMW). STMWs are, in fact, found throughout the World Ocean (McCartney 1982). Particular to the Sargasso Sea, a region south and east of the Gulf Stream (see **Fig. 2.3**), is the STMW known as "18° Water" (Worthington 1959).

As long ago as 1873, a section of temperature soundings between New York, Bermuda and St Thomas (in the Virgin Islands) revealed an isothermal layer in the upper 500 m which extended a remarkable distance southward (Thomson 1877). By the 1930s bathythermograms could reveal the development of deep

mixed layers in the northern Sargasso Sea during winter, attaining maximum depths of ~400 m in early March and representing an obvious source region for the southward-spreading isothermal layer (Iselin 1936).

(a)

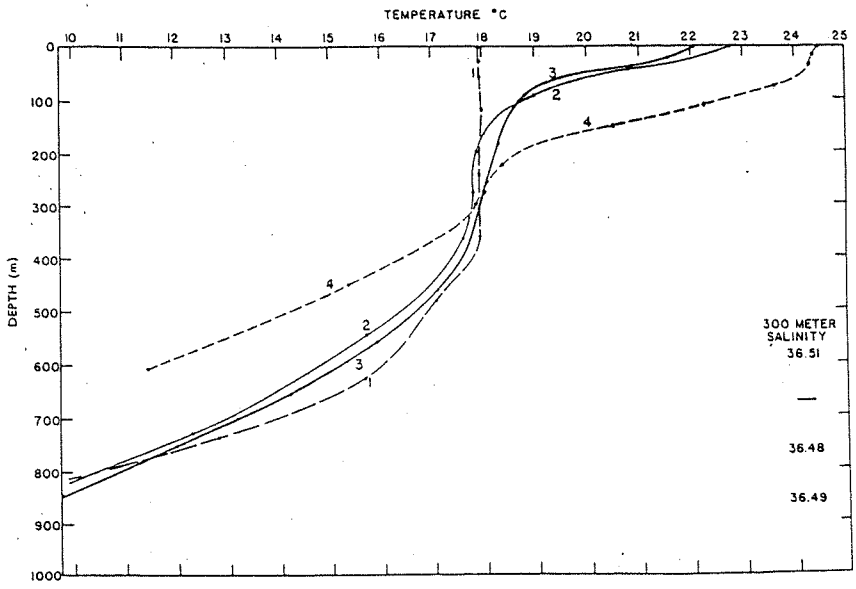

Fig. 1. Temperature-depth curves in the Sargasso Sea.
1 *Atlantis* 1153, 28 Feb. 1932 34° 02′ N 54° 05′ W
2 *Challenger* 53, 26 May, 1873 36° 30′ N 63° 40′ W
3 *Atlantis* 5306, 11 June, 1955 34° 53′ N 70° 16′ W
4 *Atlantis* 1483, 4 March, 1933 21° 46′ N 62° 48′ W.

(b)

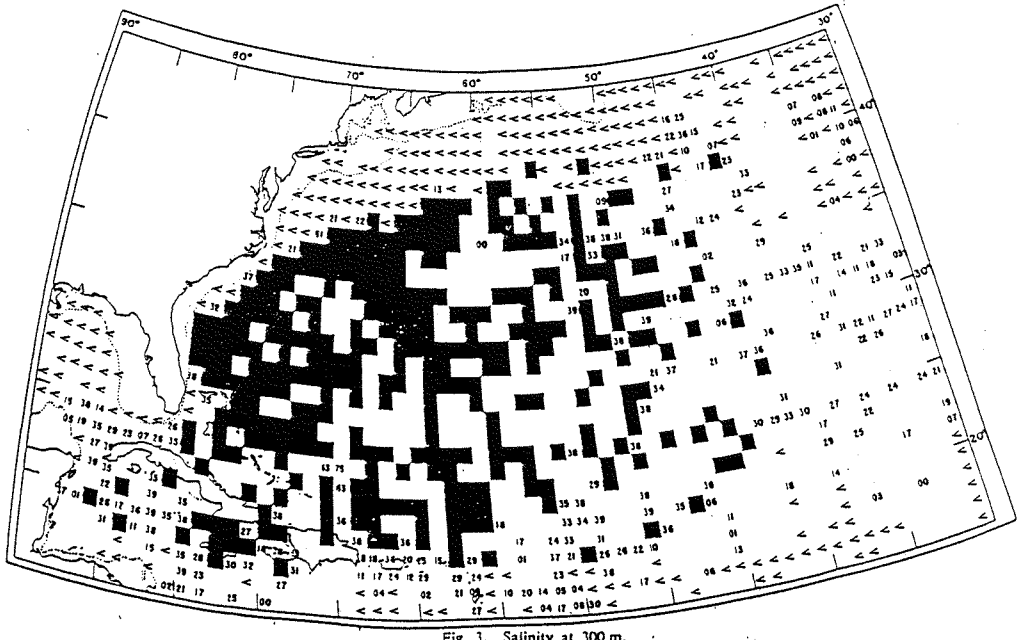

Fig. 3. Salinity at 300 m.
Black squares – 36·40‰ to 36·60‰ only
Numbered squares – 36·00‰ to 36·39‰ and 36·61‰ to 36·99‰
< for values below 36·00‰.

Figure 2.6: Worthington's (1959) 18° Water: (a) bathythermogram profiles, (b) salinity-traced across the Sargasso Sea.

With the early mapping of temperature and salinity in the upper North Atlantic, it became clear that this isothermal layer was also isohaline (Böhnecke 1936). Worthington (1959) noted that, during spring/summer, a seasonal thermocline develops in the upper 100 m of the Sargasso Sea, but that the isothermal/isohaline layer persists, evidenced by a pronounced inflexion in T and S at around 300 m (**Fig. 2.6a**, reproduced from Worthington 1959). Worthington therefore defined "core" T-S properties of 18° Water (at this inflexion point) as 17.9°±0.3°C and 36.5±0.1 practical salinity units (psu) and identified traces of such water (with salinity in the range 34.4-34.6 psu across the Sargasso Sea at a depth of 300 m (**Fig. 2.6b**, also from Worthington 1959). Worthington (1959) concludes that 18° Water is formed by a "convergence" of water properties towards modal values at the end of nearly every winter, and subsequently flows southward along the density surface defined by $\sigma_\theta \approx 26.4$.

Worthington (1959) furthermore considers the layer of 18° Water to form a crude wedge, 2000 km long (from east to west), 250 m thick at a northern "wall", and tapering linearly to zero thickness at a distance of 1500 km to the south. The volume of such a wedge is 375 000 km^3, allowing Worthington to reason that if a conservative 20% of 18° Water was renewed each winter, there would be an implied convective turnover of 75 Sv, roughly equivalent to the baroclinic Gulf Stream transport. This consideration forms the basis for Worthington's (1972) theory of anticyclogenesis - a dominant forcing mechanism, accounting for Gulf Stream transports well in excess of theoretical (wind-driven) predictions (see §2.3.1 below).

Schroeder *et al.* (1959) found that, over the 85 year period up to 1958, the inflexion point in temperature soundings just off Bermuda deviated from 18.0°C by no more than a few tenths of a degree, suggesting that 18° Water is remarkably stable. Subsequent monitoring of 18° Water at Bermuda has, however, revealed significant thermal variability from the 1950s onwards (see §2.4.2 below).

2.2 Ocean circulation theory: The steady state

Our understanding of the steady state three-dimensional ocean circulation has evolved rapidly in the post-war period, thanks to intense observation programs, early theoretical insights, and, more recently, computational advances. In the following sub-sections, the concept of potential vorticity is outlined, and

theories for the large-scale circulation of the subtropical gyre, thermocline structure and the thermohaline overturning are introduced.

2.2.1 Potential vorticity

Vorticity is the measure of rotation in a fluid (a vector field, defined as the curl of velocity, $\nabla \times \mathbf{v}$). The "absolute" vorticity of a fluid must account for motion of both fluid and a chosen frame of reference. In our rotating frame of reference (on Earth), the absolute vorticity of fluid is sum of "relative" vorticity (due to rotation of the fluid in the frame of reference) and "planetary" vorticity (due to the rotation of the Earth):

$$\zeta_a = \zeta + f \tag{2.1}$$

where $\zeta = \nabla \times \mathbf{v}$ is relative vorticity, and $f = 2\Omega \sin\Theta$ is planetary vorticity (Ω is the angular rate of rotation of Earth, and Θ is latitude). In a rotating frame of reference, Newton's Second Law of Motion (specifying unaccelerated motion of a body under balanced forcing) requires that the angular momentum (or absolute vorticity) of a body is conserved. In applying this conservation law to a compressible fluid, vortex stretching must be taken into account. For a fluid layer of uniform density and variable thickness, h, the conservation of angular momentum is therefore expressed as:

$$\frac{d}{dt}\left(\frac{\zeta + f}{h}\right) = 0 \tag{2.2}$$

and the conserved quantity $(\zeta + f)/h$ is the "potential" vorticity (PV).

PV is central to modern ideas about the three-dimensional ocean circulation, although first introduced in geophysical fluid dynamics through study of the atmospheric general circulation. In early pioneering work, Rossby (1939) explained the development of perturbations about the strongly zonal circulation of the upper atmosphere in terms of the relative and planetary vorticity of individual air parcels, thus introducing the theory of Rossby waves. That work was soon followed by the introduction of the terminology "potential vorticity" in the open literature (Rossby 1940, Starr and Neiburger 1940). In concurrent and independent work, Ertel (1942) generalized formulation of the hydrodynamical vorticity equations, which formally established several important conservation principles (in particular, that entropy must be conserved for adiabatic motion of an ideal gas).

Analysing meteorological data over North America on consecutive days, Starr and Neiburger (1940) first attempted to use PV as a tracer of air masses, a method which quickly came to underpin operational weather forecasting. Hoskins *et al.* (1985) review the use of isentropic PV in dynamical meteorology.

PV first appeared in studies of ocean circulation during the 1950s. Stommel (1955) presented a simple argument for PV conservation in the Gulf Stream, by comparing current estimates obtained from geostrophy and integrated PV respectively. Using data obtained by Worthington (1954) in a north-south hydrographic section across the Gulf Stream at about 68°W, and noting, towards the region of high velocity, a marked decrease of isothermal layer thickness at temperatures above 16°C, Stommel used the conservation of PV,

$$\frac{f+\partial v/\partial x}{h}=\frac{f}{h_o} \tag{2.3}$$

to derive $v(x)$, the zonal component of current velocity as a function of meridional distance x (with x increasing southwards), for a layer of thickness h bound by the isotherms 17°C and 19°C (with thickness h_o at the south end of the section). Integrating (2.3) with respect to x,

$$v(x)=\int_x^{\infty} f(x)\left(\frac{h(x)}{h_o}-1\right)dx \tag{2.4}$$

The resulting velocity profiles (from both geostrophy and integrated vorticity) are reproduced in **Fig. 2.7**. Finding these two independent estimates to be in very good agreement, Stommel concluded that PV is well conserved in the Gulf Stream, and remarked that PV conservation importantly determines the width and velocity of the Stream. However, PV is only conserved in the Lagrangian sense, and is by no means constant across the Gulf Stream (although mesoscale eddies do act to largely homogenize upper ocean PV in the recirculation region - see below).

In recent years PV has proved to be a powerful tool in studies of ocean circulation. McDowell *et al.* (1982) present maps of PV between adjacent density surfaces in the North Atlantic, revealing how the wind-driven circulation distorts the PV field, allowing flow across latitude lines (changing planetary vorticity) while still approximately conserving PV. McDowell *et al.* (1982) also distinguish between regions where PV is conserved or homogenized. Holland *et al.* (1984) demonstrate a close correspondance between contours of geostrophic flow and PV

in a numerical model of the wind-driven circulation in a rectangular ocean basin, but recognize the importance of injected low PV waters (e.g. STMW). The use of PV as a dynamical tracer of STMWs is demonstrated by McCartney (1982).

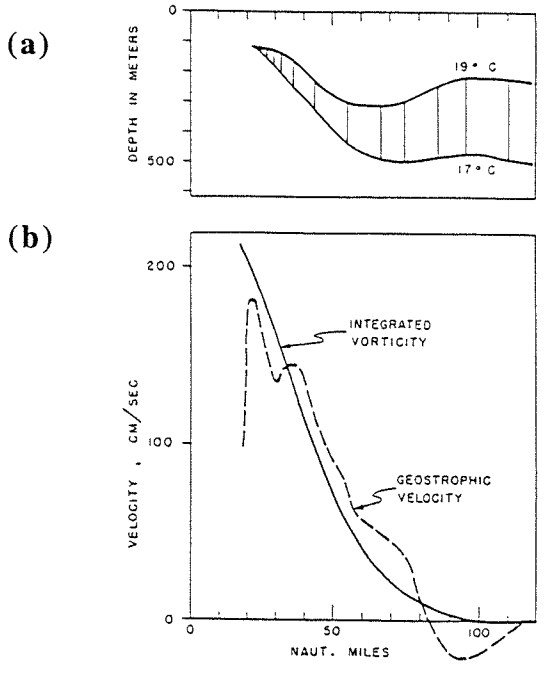

Figure 2.7: Stommel's (1955) Gulf Stream diagnoses of (a) cross-stream thickness of the 18° Water layer, and (b) velocity profiles, obtained from a potential vorticity balance, and from geostrophy.

2.2.2 The large-scale circulation of the subtropical gyre

How is the subtropical gyre forced? This simple question has, in large part, propelled forwards our understanding of the oceanic general circulation. The pioneering theories of Sverdrup (1947), Stommel (1948), Munk (1950) and Fofonoff (1954) sought to obtain analytical solutions of the equations of motion (simplified in different ways) which approximated gross features of the observed circulation. The linear theories of Sverdrup, Stommel and Munk (based on linear equations for the horizontal streamfunction) first sought solutions for the steady state circulation, omitting time-dependent and non-linear terms from the equations of motion, while Fofonoff and others (Charney 1955, Morgan 1956) began the challenging task of including non-linear terms, leading to inertial theories for the Gulf Stream.

Sverdrup (1947) recognized that, over the majority of the ocean gyres (excepting the western boundaries), there is a balance between the Coriolis, pressure gradient, and frictional (wind) forces:

$$-fv = -\frac{1}{\rho}\frac{\partial p}{\partial x} + \frac{1}{\rho}\frac{\partial \tau_x^s}{\partial z} \tag{2.5a}$$

$$fu = -\frac{1}{\rho}\frac{\partial p}{\partial y} + \frac{1}{\rho}\frac{\partial \tau_y^s}{\partial z} \tag{2.5b}$$

where (u,v) are depth-averaged zonal and meridional components of velocity, f is the Coriolis parameter, p is pressure, ρ is the density of seawater, and $\boldsymbol{\tau}^s = (\tau_x^s, \tau_y^s)$ is the (depth-dependent) horizontal stress due to surface wind forcing. For a flat-bottomed ocean of constant depth H, cross-differentiation of (2.5a,b) with respect to y and x yields the Sverdrup balance, which expresses poleward transport at a given latitude as:

$$vH = \frac{1}{\rho\beta}\left(\frac{\partial \tau_y^s}{\partial x} - \frac{\partial \tau_x^s}{\partial y}\right) \tag{2.6}$$

where β is the latitudinal variation of f, $\beta = \partial f / \partial y$.

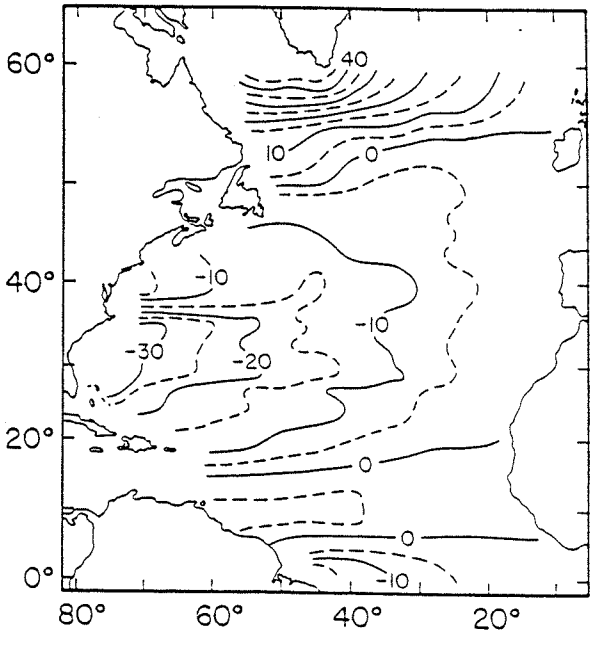

Figure 2.8: Sverdrup mass transport over the North Atlantic (Leetmaa and Bunker 1978)

With observed wind stress data Eqn. (2.6) can be used to construct a map of Sverdrup transport. **Fig. 2.8** shows the annual mean Sverdrup mass transport thus obtained by Leetmaa and Bunker (1978), using wind stress averaged into gridboxes of 2° latitude x 5° longitude, and integrating westward from a value of zero mass transport at the eastern boundary.

In the subtropics, strong southward wind-driven transport at the western boundary (reaching a peak at 31°N of 32 x 10^{12} g s^{-1}, equivalent to 31.2 Sv) must be balanced, as is the case, by a northward-flowing western boundary current. The east to west integration, which implies such a current, is intuitive but arbitrary. Mathematically valid but intuitively wrong, west to east integration yields an unrealistic *eastward* intensification. Stommel (1948) offered the first plausible explanation for the observed *westward* intensification, by solving the depth-integrated vorticity equation for a flat-bottomed ocean,

$$vH\beta = -\frac{1}{\rho}\frac{\partial \tau_x^s}{\partial y} - \left\{\frac{1}{\rho}\frac{\partial \tau_y^b}{\partial x} - \frac{1}{\rho}\frac{\partial \tau_x^b}{\partial y}\right\} \qquad (2.7)$$

simplifying solution by the neglect of zonal variations in wind stress, but crucially now including bottom frictional stress, (τ_x^b, τ_y^b), free to vary linearly with u and v. Rewritten in terms of the horizontal streamfunction, Stommel solved Eqn. (2.7) to obtain the classical picture of westward intensification shown in **Fig. 2.9** (Stommel 1948).

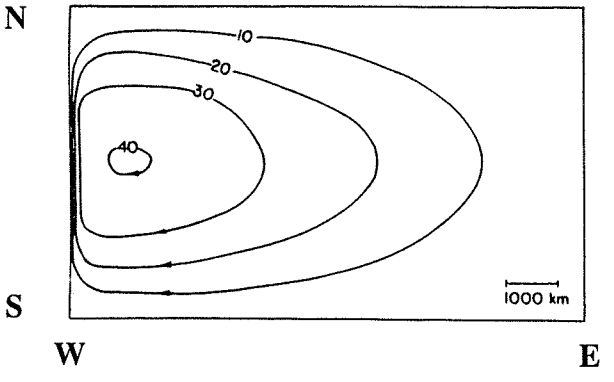

Figure 2.9: Streamlines in a rectangular basin for which Coriolis force varies as a linear function of latitude (Stommel 1948)

A major defect of Stommel's (1948) theory was the use of unrealistic linear bottom friction. Munk (1950) introduced more realistic lateral friction, parameterized by a coefficient of horizontal eddy viscosity (K_H), and solved the equations of motion thus approximated:

$$-\rho f v = -\frac{\partial p}{\partial x} + K_H\left(\frac{\partial^2}{\partial x^2} + \frac{\partial^2}{\partial y^2}\right)u + \tau_x^s \tag{2.8a}$$

$$\rho f u = -\frac{\partial p}{\partial y} + K_H\left(\frac{\partial^2}{\partial x^2} + \frac{\partial^2}{\partial y^2}\right)v + \tau_y^s \tag{2.8b}$$

Although a streamfunction qualitatively similar to that of Stommel is obtained, Munk's theory also predicted a countercurrent lying offshore and adjacent to the western boundary current. Furthermore, using realistic patterns of wind stress, Munk computed depth-integrated western boundary current mass transports in the Atlantic and Pacific which matched well with observed values. At a given latitude, total western boundary current transport (obtained with Munk's theory) depends on the width of the ocean basin, the value of β, and the wind stress curl, while K_H determines only the width of the current.

Although successful in predicting the east-west asymmetry in circulation patterns, the linear, viscous models of Stommel and Munk both required (for realistic solutions) large frictional terms to input vorticity at the western boundary, and observed western boundary current transports far exceed predictions based on these frictional theories. However, by retaining the non-linear terms, Fofonoff (1954) obtained free, steady solutions for the circulation in a frictionless ocean, for which the vorticity equation expressed only conservation of absolute vorticity following the motion:

$$\frac{D}{Dt}(\zeta + f) = 0 \tag{2.9}$$

Fofonoff's resulting circulation pattern was characterized by a northward intensification, supported and maintained by an inertial recirculation of the zonal flow, shown here in **Fig. 2.10** (Fofonoff 1954).

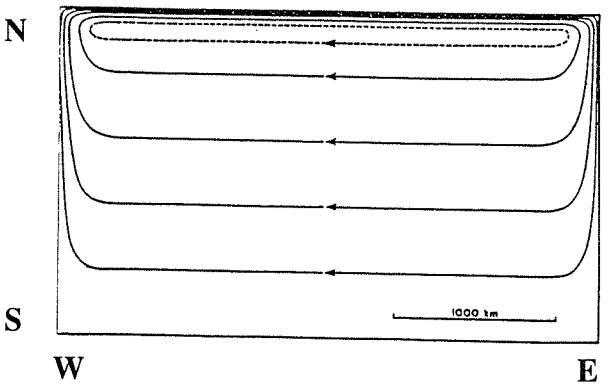

Figure 2.10: Streamlines in a frictionless, homogeneous ocean (Fofonoff 1954)

Taken together, linear and non-linear theories explained many features of the steady state Gulf Stream in terms of both viscous and inertial dynamics. In the early 1960s, the feasibility of numerical integration provided an opportunity to investigate further the subtle interplay between frictional and non-linear (inertial) terms in the equations of motion. In a pioneering study, Bryan (1963) obtained numerical solutions of the circulation (defined by the depth-integrated streamfunction ψ) in a rectangular-basin homogeneous ocean - analytically unattainable in practical terms - and was able to investigate the transition of solution between viscous (steady) and inertial (unsteady) flow regimes. The transition is seen by varying a Reynolds number (the ratio of non-linear terms to frictional terms in the equations of motion) for the western boundary current, *RE*, and solving an appropriately scaled vorticity equation in which the non-linear terms $\frac{\partial}{\partial y}\psi\left(\frac{\partial}{\partial x}\nabla^2\psi\right)-\frac{\partial}{\partial x}\psi\left(\frac{\partial}{\partial y}\nabla^2\psi\right)$ are retained. **Fig. 2.11** (Bryan 1963) shows the time-averaged streamfunction patterns obtained for four values of *RE* (increasing from the left to right panels).

As *RE* is increased, the frictional terms weaken (relative to the non-linear terms) and there is a corresponding tendency for a north-south asymmetry to develop. In physical terms, the symmetry-asymmetry can be explained in terms of vorticity conservation. Anticyclonic vorticity is acquired by the northward flowing boundary current (as f increases with latitude - the β-effect). In the low *RE* regime (left hand panel), strong friction is an effective sink of this vorticity, these gains/losses of vorticity are almost entirely confined to the western boundary, and

Stommel's east-west symmetry is closely reproduced. As *RE* is increased, friction is weaker and fluid travels further before a given western boundary vorticity input is dissipated. The northern boundary is encountered before excess vorticity is fully diffused, and a northward intensification is maintained.

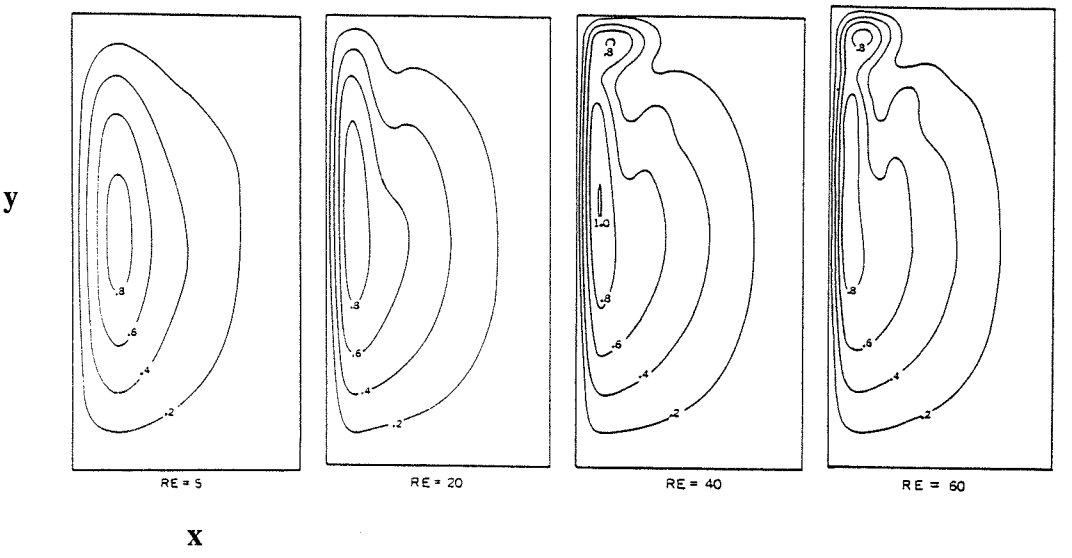

Figure 2.11: Time-averaged streamfunction patterns obtained for four different values of effective Reynolds number (Bryan 1963)

The preceding theories and models of the large-scale circulation assumed a flat-bottomed, homogeneous (one-layer, constant density) ocean. As an alternative to Fofonoff's theory for an inertial recirculation-enhanced WBC transport, Holland (1973) showed that baroclinic structure and variable bottom topography can combine to enhance transport, through a "bottom pressure torque" (BPT) term in the full barotropic vorticity balance, which can be written in one of three forms (Hughes and Killworth 1995) as:

$$\frac{\partial}{\partial t}\nabla^2\psi = \mathbf{k}.\nabla\times\left(f\nabla\psi + \boldsymbol{\tau}^s + H\nabla p_b + \nabla E + \mathbf{F} + \mathbf{N} - \boldsymbol{\tau}^b\right) \qquad (2.10)$$

The left hand term in Eqn. (2.10) is the tendency for relative vorticity to change, and the expanded right hand terms, from left to right, represent sources and sinks of vorticity through the β-effect, the wind stress curl, BPT (p_b is the bottom

pressure), baroclinicity (where potential energy $E = g\int_{-H}^{0} z\rho dz$), lateral friction (**F**), non-linear advection (**N**), and bottom friction ($\boldsymbol{\tau}^b$). In Eqn. (2.10), $\nabla \times (\nabla E) = 0$, and baroclinicity is shown to play no *direct* role in the budget of depth-integrated vorticity. Furthermore, the BPT term, $\mathbf{k}.\nabla \times \left(H\nabla p_b\right)$, can be more conveniently written as $-J\left[p_b, H\right]$, where J is the Jacobian operator and $J[P,Q] = (\partial P/\partial x).(\partial Q/\partial y) - (\partial P/\partial y).(\partial Q/\partial x)$. Assuming a steady state, and neglecting non-linear and friction terms, vertically integrating Eqn. (2.10) yields the topographic Sverdrup balance:

$$vH = \frac{1}{\rho\beta}\left\{\left(\frac{\partial \tau_y^s}{\partial x} - \frac{\partial \tau_x^s}{\partial y}\right) - J\left[p_b, H\right]\right\} \tag{2.11}$$

From the hydrostatic relation, $p_b = p_s + g\int_{-H}^{0} \rho dz$, where p_s is the surface pressure and the depth-integral represents baroclinicity. The BPT term may therefore be split as

$$J\left[p_b, H\right] = J\left[p_s, H\right] + J\left[g\int_{-H}^{0} \rho dz, H\right] \tag{2.12}$$

to separate the effects of sea surface topography and baroclinicity.

Holland (1973) demonstrated that baroclinicity largely compensates surface pressure effects, and obtained the BPT as a residual term [by Eqn. (2.12)]. In the case of an idealized subtropical gyre, Holland (1973) further showed that, in a steady state, BPT generates vorticity in the same sense as the wind stress curl, enhancing WBC transport in a numerical model which incorporates baroclinicity (variable surface temperature and salinity are prescribed, heat and salt equations predict interior fields) and variable topography (an idealized continental slope along the western boundary). **Fig. 2.12**, reproduced from Holland (1973), shows graphically how the effect of baroclinicity and topography is to drive a strong barotropic circulation which is absent in model experiments lacking either refinement. This subtle interplay of topography and baroclinic structure, earlier recognized by Sarkisyan and Ivanov (1971), has been dubbed the Joint Effect of Baroclinicity and Relief, "JEBAR" (see also Huthnance 1984).

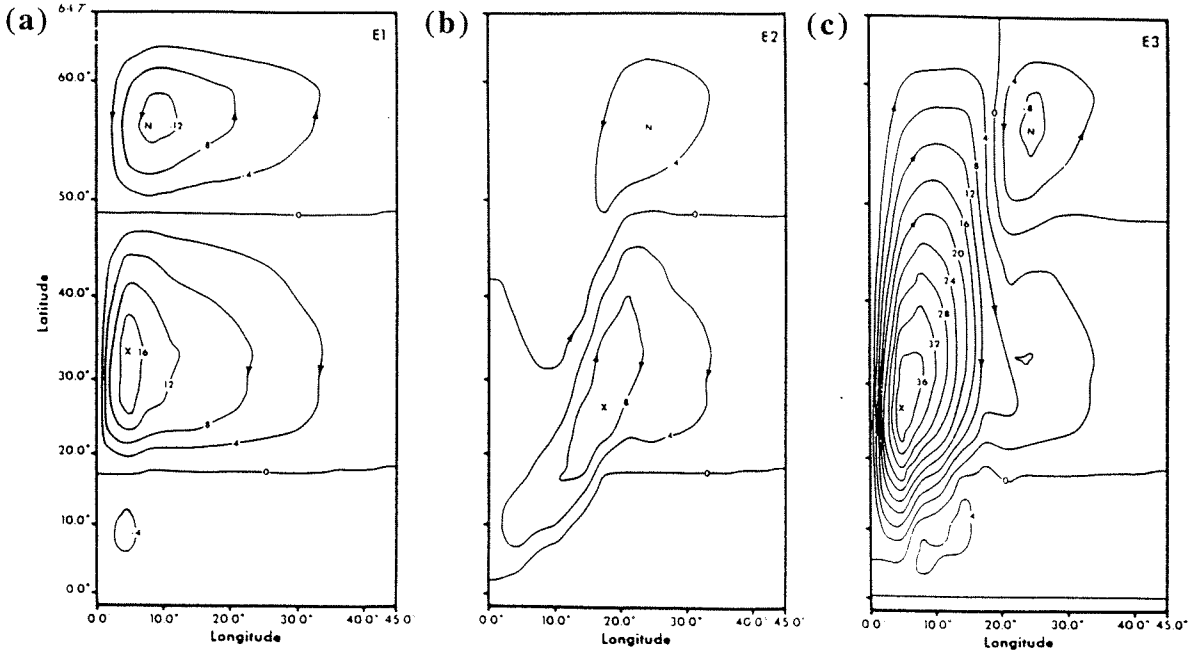

Figure 2.12: Mass transport streamfunction (10^6 tonnes s^{-1}) for three different numerical experiments: (a) baroclinic ocean, constant depth; (b) homogeneous ocean, variable depth; (c) baroclinic ocean, variable depth (from Holland 1973).

As well as frictional, non-linear and topographic effects, the wind-driven circulation is also subject to buoyancy forcing. In particular, the role of cooling on the Gulf Stream has been the subject of several recent studies. Cushman-Roisin (1987) demonstrates how surface cooling acts to restore the PV balance of parcels which accumulate downstream of the western boundary jet, permitting them to subsequently rejoin the southward interior flow as a buoyancy-driven recirculation. Using a coarse resolution general circulation model (GCM), Spall (1992) shows how surface cooling forces a counter-clockwise spiral of the velocity vector with depth, in opposition to wind-driven "β-spirals". Derived from continuity and geostrophic equations,

$$\beta v = f(\partial w/\partial z) \tag{2.13}$$

represents a vorticity conservation equation for geostrophic flow. Eqn. (2.13) predicts clockwise rotation in the subtropical gyre due to the vertical profile of w characteristic of the wind forcing in that region (but only for $\beta \neq 0$, hence the terminology). Alternatively, the thermal wind equations (relating vertical shears of

horizontal velocity to lateral density gradients) can be combined with a steady density equation (assuming no mixing, but accounting for local heating/cooling, Q) to yield an expression which relates rotation with depth of the horizontal velocity vector ($V\cos\theta$, $V\sin\theta$) to Q, the vertical velocity (w) and the vertical density gradient ($\partial\rho/\partial z$):

$$\frac{\partial\theta}{\partial z} = \frac{g}{\rho_o f V^2}\left\{ w\frac{\partial\rho}{\partial z} - Q \right\} \tag{2.14}$$

Spall (1992) shows that the trajectories of parcels near the western boundary current of the GCM are strongly influenced by counter-clockwise cooling spirals, which thus influence the scale and structure of the recirculation.

2.2.3 The thermocline problem

By the late 1950s, and with a plausible hierarchy of theories explaining the large-scale horizontal circulation, attention turned to the thermocline problem: namely an explanation of the vertical structure of ocean circulation. At the heart of the thermocline problem is the need to reconcile dynamic and thermodynamic forcing of the ocean. The inter-dependence of the temperature (density) field and the velocity field (through the thermal wind balance) renders the thermocline problem non-linear, and therefore mathematically intractable. To avoid complexities associated with the three-dimensional nature of the underlying physics, early workers sought similarity solutions of the non-linear partial differential equations which naturally arise in models of a continuously stratified thermocline. Two opposite limits on thermocline control were advocated: diffusive (Robinson and Stommel 1959) and advective (Welander 1959).

However, to make further progress, it has been necessary to relate the vertical structure of the thermocline to the horizontal structure of the ocean circulation. In this regard, the three-dimensional circulation of the subtropical gyre has recently been explained by two competing theories. Luyten, Pedlosky and Stommel (1983) - henceforth denoted as LPS - present a non-diffusive thermocline theory, seeking analytical solutions for the wind-driven circulation. LPS obtain thickness and velocity fields for isopycnic layers "followed" downstream and downward from a prescribed surface "outcrop line". LPS thus predict streamlines which define three distinct circulation regimes: a recirculating gyre - the unventilated "pool region" - to the west, a quiescent "shadow zone" to the south and east, and, sandwiched between these two regions, the "ventilated

thermocline". The shadow zone cannot be reached by any of the streamlines emanating from the outcrop line. To conserve PV acquired at the outcrop line, these streamlines turn westwards. The shadow zone, isolated from this predicted circulation, remains motionless. In contrast to the ventilated thermocline is the essentially diffusive theory of Rhines and Young (1982a, 1982b) - henceforth denoted as RY - which emphasizes the recirculation (the pool region defined by LPS) as a submerged gyre, controlled by weak lateral diffusion due to the mixing effects of eddies, and consequently homogenized in PV.

The models of LPS and RY have been combined to reveal the impact of ventilation on the pool region and vice versa (Pedlosky and Young 1983), while Pedlosky (1983) estimates the relative importance of ventilation and mixing of potential vorticity. The wind-driven ventilated thermocline theory of LPS has now been extended to include an uppermost mixed layer (Pedlosky, Smith and Luyten 1984) and buoyancy forcing (Pedlosky 1986; Luyten and Stommel 1986). Pedlosky (1990) reviews these recent advances in light of present observational evidence. The layered model of LPS (and refinements thereof) was subsequently complemented by continuously stratified models (Huang 1986, Nurser and Marshall 1991, Marshall and Nurser 1992, Marshall and Marshall 1995).

Associated with thermocline ventilation is the process of subduction. In the North Atlantic, warm stratified water flows north in the Gulf Stream and loses heat to the atmosphere during winter. In the resulting end-of-winter mixed layers, atmospheric influences penetrate to depths of many hundreds of metres. Once cooled, water then returns southwards into the subtropical gyre and so begins to regain heat from the atmosphere. A warm stratified surface layer forms, shielding an underlying "fossil" mixed layer from further atmospheric influence. Further downstream, the recently mixed water may reach the so-called "permanent" thermocline (isolated from seasonal influences), and get caught up in the gyre scale circulation, spiralling downwards under the influence of Ekman pumping. Such a scenario outlines large-scale subduction associated with seasonal buoyancy forcing and the wind-driven circulation, for which annual rates of up to 200 m $year^{-1}$ across the subtropical gyre have been estimated from climatological data (Marshall *et al.* 1993). Subduction is also associated with the mesoscale eddy field, subduction "events" occuring on weekly timescales as parcels of water subduct at baroclinically unstable ocean fronts. Spall (1995) used an isopycnal primitive equation model to demonstrate such a mechanism, obtaining a net annual subduction rate (through frontal instability) of 20 m $year^{-1}$.

2.2.4 The surface-forced thermohaline circulation

Superimposed on the largely horizontal wind-driven circulation is the vertical-meridional thermohaline circulation (THC). To explain the THC, Stommel (1958b), and Stommel and Arons (1960a,b) developed a model which incorporated a deep westward-intensified southward flow along the western boundary of the North and South Atlantic. This current is maintained by strong convective sinking during winter in the Nordic Seas, with uniform upwelling in the interior driving slow northward flow towards the source of deep convection.

In a separate approach, Walin (1982) related the thermal circulation of the ocean directly to the surface heat flux (see schematic in **Fig. 2.13**, adapted from Walin's paper), via the simple relation:

$$cG(T,t) = -\frac{\partial}{\partial T} Q(T,t) \qquad (2.15)$$

where, poleward of a latitude Θ, $G(T,t)$ is the volume flux of water across isotherm T at time t, $Q(T,t)$ is the total heat flux integrated over the area poleward of the surface outcrop of T, and c is the heat capacity per unit volume for sea water. Walin (1982) thus found that climatological surface fluxes over the North Atlantic (Andersson *et al.* 1982) implied a surface poleward drift, to balance typical values for $G(T,t)$, of order 10 Sv.

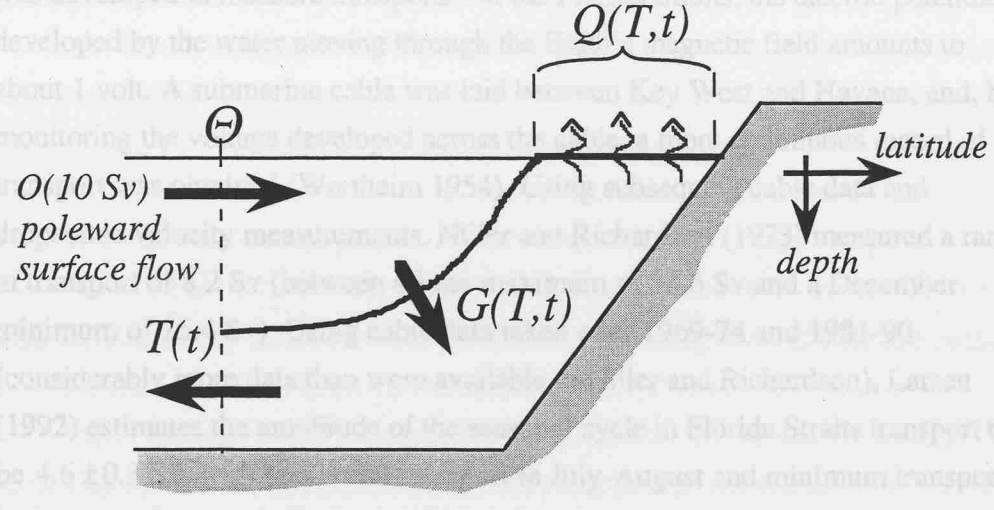

Figure 2.13: Schematic showing the relationship between meridional thermal circulation and the surface heat flux.

2.3 Seasonal variability in the subtropical North Atlantic

Appropriately parameterized and scaled, the linear, viscous, theories of wind-driven circulation successfully account for much of the observed Gulf Stream transport. However, transport estimates seem to exceed theoretical wind-driven predictions. How is the excess transport forced? Theoretical consideration of inertial and/or buoyancy-driven recirculation offers a plausible explanation. Further insight is afforded by observations of seasonal variability in transport across sections in the Florida Straits and downstream from Cape Hatteras. The following three sub-sections review the evidence for seasonal variability in Florida Straits transport (mostly wind-driven) and the developed Gulf Stream (wind and buoyancy-driven), and outline the synoptic meteorological phenomena known as "cold outbreaks" (during which the Gulf Stream is intensely cooled).

2.3.1 The seasonal cycle and variability of Florida Straits transport: wind-forced?

The seasonal variation of Florida Straits transport exhibits a particularly well observed and heavily studied seasonal cycle. During the 1930s and 1940s, tide gauges, sited on both sides of the Florida Straits, were used to establish the cross-stream slope of the sea surface, and hence the total geostrophic transport of the Florida Current. Stommel (1953) used such data to show a seasonal cycle in this transport, with maximum transport in July. In the early 1950s a new technique was developed to measure transports - in the Florida Straits, the electric potential developed by the water moving through the Earth's magnetic field amounts to about 1 volt. A submarine cable was laid between Key West and Havana, and, by monitoring the voltage developed across the cable, a more continuous record of transport was obtained (Wertheim 1954). Using subsequent cable data and dropsonde velocity measurements, Niiler and Richardson (1973) measured a range in transport of 8.2 Sv (between a June maximum of 33.6 Sv and a December minimum of 25.4 Sv). Using cable data taken over 1969-74 and 1981-90 (considerably more data than were available to Niiler and Richardson), Larsen (1992) estimates the amplitude of the seasonal cycle in Florida Straits transport to be 4.6 ± 0.3 Sv, with maximum transport in July-August and minimum transport in October-November. Both sets of observations are obtained from a section between the coast of Florida and the Bahamas (at ~79°W).

In his review of the North Atlantic circulation, Schmitz (1996) remarks on the temporal stability (both seasonal and interannual) of the Florida Current at

around 30 Sv. Less certain is the source of, and hence forcing mechanism for, this transport. In his thermohaline circulation scheme, Stommel (1958b) required 20 Sv cross-equatorial southward abyssal flow, with a corresponding northward transport in the upper ocean, all of which was conjectured to be part of the North Brazil, Caribbean and Florida Currents. Worthington (1976) controversially postulated a North Atlantic origin (via the Antilles island arc) for more or less the entire Florida Current. Most recently, Schmitz and Richardson (1991) present evidence (based on traces of Antarctic Intermediate Water) that ~45% of the Florida Current is of South Atlantic origin, in general agreement with Stommel (1958b). The small seasonal cycle of Florida Current transport is perhaps consistent with a remote source. In accordance with the evidence to date, Schmitz (1996) apportions Florida Current transport in equal measure between the two quite separate sources: intermediate water originating from the South Atlantic and basin-scale recirculation of the North Atlantic subtropical gyre (including "old" 18° Water).

Despite displaying only weak seasonality, the uniquely well-sampled Florida Straits transport has motivated several studies of forcing mechanisms. Using barotropic and baroclinic models of the subtropical Atlantic, Anderson and Corry (1985) investigate the relationship between seasonal variation of transport through the Florida Straits and model representations of topography, geography and winds. A July maximum of transport is predicted, and this is shown to be intimately related to the combined effects of topographic gradients and seasonality in wind stress.

For the case of a flat-bottomed ocean, Fanning *et al.* (1994) predict large amplitudes (20-30 Sv) of the seasonal cycle in Florida Straits transport, with February-March maxima and October-November minima. Using realistic bottom topography the seasonal cycle is completely changed - the amplitude is reduced to 3-6 Sv, with a July maximum, and minima in October-November and February. They argue that the difference in seasonal cycles (between the cases of flat-bottomed and realistic topography) is due to "blocking" (principally by Caribbean sills) of the barotropic response to variations in wind stress curl, the hypothesis originally tested by Anderson and Corry (1985). Böning *et al.* (1991) use output from the Kiel version of the high-resolution WOCE-CME model (World Ocean Circulation Experiment, Community Modelling Effort; Bryan and Holland 1989), forced by Hellerman and Rosenstein (1983) and Isemer and Hasse (1987) wind stress data. These two different wind stress climatologies force widely differing seasonal ranges in transport of 3.4 Sv and 6.3 Sv respectively, but in both cases successfully reproduce the observed phase.

The seasonal cycle actually depends critically on how the transport section is defined (i.e., between the coast and some arbitrary point offshore). Fanning *et al.* (1994) find that, as the offshore boundary of their "Florida Straits" is moved offshore from 78.5°W (chosen for the main purpose of their study) to 75.5°W, the amplitude strengthens, the summer maximum collapses and the fall minimum deepens. The seasonal cycle thus begins to resemble that predicted by the flat-bottomed Sverdrup relation.

Other modelling studies (Barnier 1988, Herrmann and Krauss 1989, Gerdes and Wübber 1991) show that seasonal cycles in barotropic transport are a response, essentially in the form of barotropic and baroclinic Rossby waves, to seasonality, principally in wind forcing. This wave-like response is strongly influenced by topography. Herrmann and Krauss (1989) use a quasi-geostrophic mode model to demonstrate that annual-period baroclinic Rossby waves which emanate off the eastern boundary are subsequently strongly influenced by the Mid-Atlantic Ridge.

A primarily wind-forced seasonal cycle in Florida Straits transport has been well established by long-term measurements and model studies. More irregular fluctuations in Florida Current transport have also been shown to be wind-forced. Stommel (1958a) plotted year-long records of submarine-cable measurements and five-day mean zonal pressure differences between 30°N and 20°N, to show that periodic increases in Florida Current transport of 8 Sv are preceded, about 30 days earlier, by breakdowns of the Bermuda-Azores high. Stommel (1958a) explains this relationship as due to a weakening of the trades (during the breakdowns of high pressure) and a cessation of the basin-wide northward Ekman drift, so that the surface flow into the Caribbean increases, and augments the Florida Current. Using a typical value for the wind stress curl at 25°N, Stommel estimated that 8.3 Sv of Ekman drift is diverted into the Caribbean, and that this extra water reaches the Florida Straits around 15 days after abrupt cessation of the trades - i.e., the amplitude and phase (with respect to changes in the Bermuda-Azores High) of observed fluctuations in Florida Current transport are consistent with changes in large-scale wind forcing.

2.3.2 Seasonal variation and intensification of the Gulf Stream: wind forcing versus cooling

Owing to sampling problems, temporal variability in Gulf Stream transport is less reliably established. The earliest evidence for a seasonal variation in Gulf Stream transport was presented by Iselin (1940). On the basis of thirteen

hydrographic sections occupied in the period 1937-40, Iselin claimed an annual variation in baroclinic transport of 15 Sv, with a winter-spring maximum and fall minimum. Stommel (1958a), while remaining sceptical of the scant evidence for seasonal variability in Gulf Stream transport, found a good correspondence between the monthly-mean sea level height observed by tide gauge at Bermuda (a proxy for barotropic Gulf Stream transport) and an estimate of the same quantity, based only on the monthly-mean wind stress curl at 32.5°N. Stommel (1958a), as Iselin (1940), concluded that there *is* a seasonal cycle of Gulf Stream transport, with maximum transport in winter and minimum transport in fall. Thus, by 1960, available evidence suggested a predominantly wind-forced seasonal cycle in Gulf Stream transport.

By the 1970s, further transport estimates indicated that Gulf Stream transport does indeed vary over a wide range. Worthington (1977) considered 32 reliable estimates of Gulf Stream geostrophic transport relative to 2000 m (computed from hydrographic data collected over 1932-68 in a triangular region bounded by Bermuda, Nova Scotia and Cape Hatteras). Worthington (1977) plots these transports against time of year (the solid dots in **Fig. 2.14**).

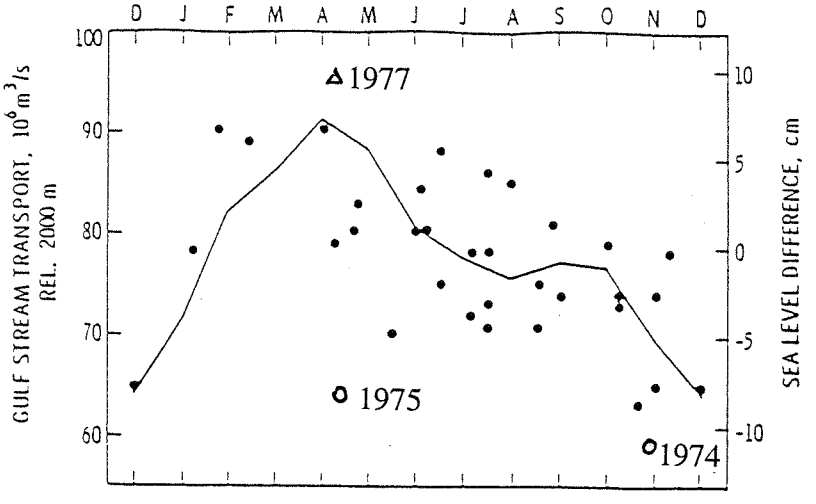

Figure 2.14: Scatterplot of Gulf Stream transport estimates against time of year (dots, Worthington 1977) and the seasonal cycle of cross-stream sea level difference estimated by altimeter (solid line, Fu *et al.* 1987).

These data collectively suggest a seasonal cycle in at least the baroclinic component of transport, characterized by a maximum in late winter (~85 Sv) and a

minimum in late autumn (~70 Sv). Although it is generally thought that seasonal cycles in transport simply reflect the Sverdrup response to seasonality in wind forcing, Worthington (1972) hypothesized that much of the seasonal variability in Gulf Stream transport is driven by anticyclogenesis. Deep winter mixing is thus followed by late winter intensification of the Gulf Stream. The anticyclogenesis involves a shallow overturning of 18° Water - a poleward drift of warm surface waters which cool and sink just south of the Gulf Stream, returning equatorward at a depth of around 400 m (see **Fig. 2.15**, adapted from Worthington 1972).

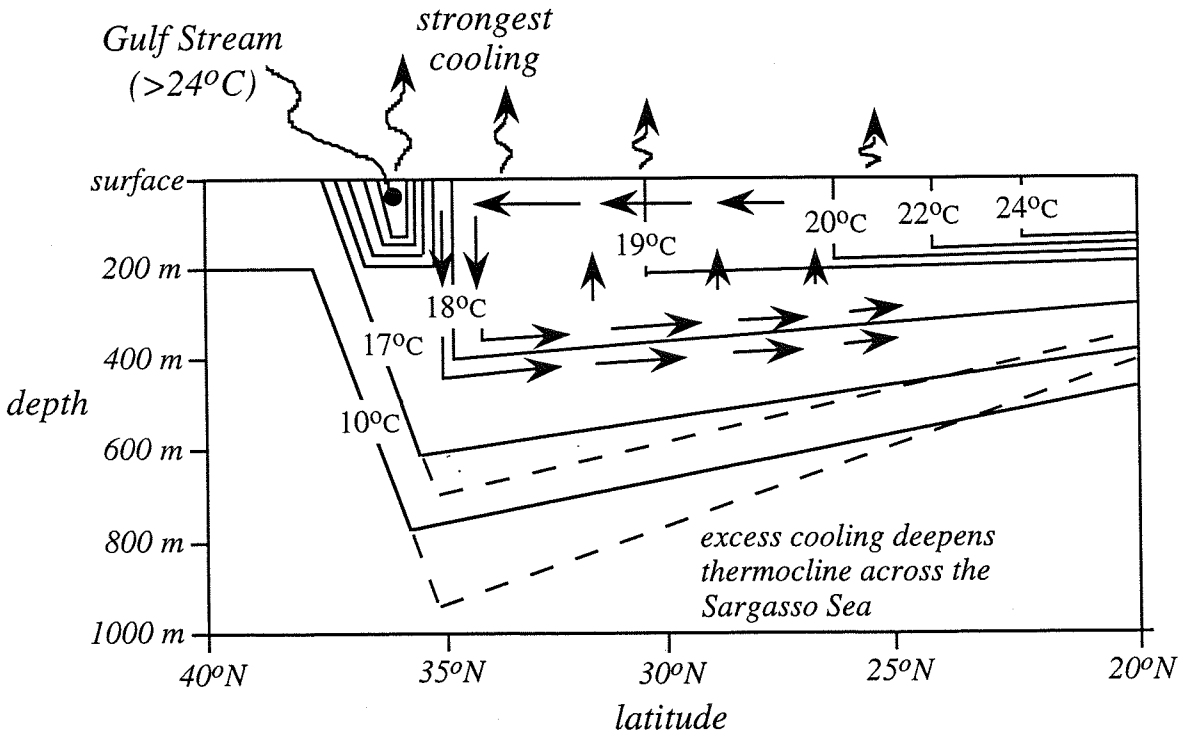

Figure 2.15: Schematic of the meridional 18° Water cell driven by surface cooling over the Sargasso Sea (adapted from Worthington 1972).

By the end of winter (and most notably after a severe winter), the 18° Water layer has thickened and lower isotherms have deepened (e.g., the 17°C and 10°C isotherms in **Fig. 2.15**). A larger volume of water feels the strong horizontal shear (at around 37°N in **Fig. 2.15**), strengthening the Gulf Stream. Although not indicated in **Fig. 2.15**, it is also believed that the Gulf Stream front migrates southwards under excess cooling (Marshall and Nurser 1988), contracting the recirculation gyre and further strengthening Gulf Stream transport.

Since the mid-1970s, satellite-borne altimeters have been used to measure sea surface height with an accuracy of ±O(1 cm), sufficient to remotely sense seasonal variability in the large-scale barotropic circulation. Using 3.5 years of sea surface height data in the western North Atlantic obtained from the GEOS 3 mission (April 1975 to November 1978), Fu *et al.* (1987) estimate a seasonal range of 15 cm in the cross-stream sea level difference (in the region 33-38°W, 70-75°W), with a maximum in April and a minimum in December. A plot of this remotely-sensed seasonal cycle (the solid line in **Fig. 2.14**) appears to match the in situ observations presented by Worthington (1977).

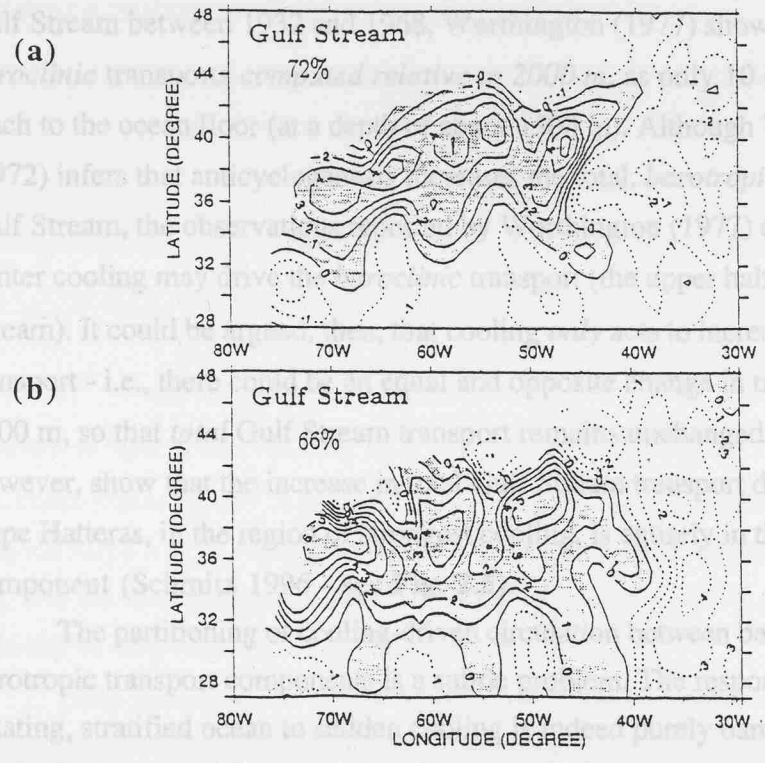

Figure 2.16: Amplitude of the first EOF modes of annual variability in sea level height over the Gulf Stream region (indicating % of total variance explained), obtained from (a) Topex/Poseiden and (b) Geosat altimeters (Wang and Koblinsky 1996).

Wang and Koblinsky (1996) use altimeter data from the more recent Geosat and Topex/Poseiden missions to study annual variability of the subtropical recirculation. The amplitude of the first EOF (Empirical Orthogonal Function) mode represents seasonal variation in sea level height. A map of this amplitude

(reproduced here in **Fig. 2.16**) reveals that seasonality is confined to the recirculation region. However, in contradiction to the seasonal cycle found by Worthington (1977) and Fu *et al.* (1987), seasonal recirculations observed by Wang and Koblinsky (1996) are characterized by a maximum in late fall and a minimum in late spring. Herein lies a dilemma. Wang and Koblinsky (1996), recognizing this, argue that while the annual-mean recirculation *is* driven by wintertime buoyancy forcing, a different mechanism must force the seasonal cycle.

In originally proposing the anticyclogenesis hypothesis, Worthington (1972) cited "total" Gulf Stream transport estimates relative to 4000 m, computed from full-depth data by Fuglister (1963). However, from 32 sections across the Gulf Stream between 1932 and 1968, Worthington (1977) showed geostrophic *baroclinic* transports *computed relative to 2000 m*, as only 10 of the sections reach to the ocean floor (at a depth of about 4500 m). Although Worthington (1972) infers that anticyclogenesis increases the total, *barotropic*, transport of the Gulf Stream, the observations reported by Worthington (1977) only show that winter cooling may drive the *baroclinic* transport (the upper half of the Gulf Stream). It could be argued, then, that cooling *only* acts to increase baroclinic transport - i.e., there could be an equal and opposite change in transport below 2000 m, so that *total* Gulf Stream transport remains unchanged. Observations do, however, show that the increase in total Gulf Stream transport downstream of Cape Hatteras, in the region of strongest cooling, is entirely in the *barotropic* component (Schmitz 1996 - see **Fig. 2.5**).

The partitioning of cooling-driven circulation between baroclinic and barotropic transport components is a subtle problem. The response of a non-rotating, stratified ocean to sudden cooling is indeed purely baroclinic - i.e., vertically integrated flow vanishes. However, if the system is rotating, geostrophic velocities can balance the density differences and the vertically integrated transports need not vanish locally. Stommel and Veronis (1980) examined the barotropic response to cooling with idealized two and three-layer frontal models, by studying geostrophic adjustment to suddenly-imposed cross-frontal density differences. With model parameters (initial layer thicknesses and imposed cooling-related density difference) chosen to correspond to those for the region where 18° Water is formed, a barotropic transport of 6 Sv was obtained. The barotropic response appears as a relative (lateral) displacement of the upper and lower layer transports which arise during adjustment to the density difference, supporting a conclusion that cooling-enhanced upper layer transport may approximately double the wind-

driven Gulf Stream. However, a partly-compensating, oppositely-directed, deep transport is predicted to lie further offshore, leading Stommel and Veronis (1980) to infer a cautionary note regarding the estimation of Gulf Stream transport: if deep flow is not taken into account (i.e., if the wrong reference level is used in geostrophic calculations), the Gulf Stream transport could be over-estimated by as much as a factor of three. In conclusion, they remark that their models are too idealized for direct quantitative estimates, as transient processes during adjustment to cooling may be significant, and the background existence of a large current such as the Gulf Stream would undoubtably affect the response to cooling.

In the general case of a stratified (multi-layered) ocean, linear normal mode theory (Gill 1982) can be used to estimate a barotropic current driven by cooling. Defining a cooling rate Q as the sum of n normal modes,

$$Q = \sum_{i=1,n} \tilde{Q}_i(\hat{w}_0 N^2) \qquad (2.16)$$

the effects of cooling can be incorporated into a horizontal momentum equation,

$$h_t + h_0 \nabla.\mathbf{u} = Q \qquad (2.17)$$

where h is layer thickness, and h_0 is a constant scaling factor. Taking length and thickness scales typical of the Gulf Stream cooling scenario (1000 km and 100 m respectively), a high value of buoyancy frequency typical of the upper ocean (10^{-1} s^{-1}), and the rather large free surface vertical velocity of 10^{-5} m s^{-1}, a barotropic velocity of only O(0.01 mm s^{-1}) is obtained.

There have been several attempts to substantiate the Worthington (1972) hypothesis. Csanady (1982) likened cross-frontal thermohaline circulation in the upper layers of the Gulf Stream (driving an oceanic jet stream) to atmospheric Hadley cells (driving an atmospheric jet stream). In an analytical model, based on the potential vorticity tendency equation, this thermohaline circulation is treated as a perturbation flow field, and advection of heat and momentum into the Gulf Stream frontal region is determined. Solution of the problem yields thermocline depth in the cross-frontal sense, which is a distortion of the initial state due to excess heat loss (the front moves south and the thermocline deepens).

Marshall and Nurser (1988) proposed that anticyclogenesis is a resonant response of non-linear "free" modes of recirculation - a baroclinic extension of Fofonoff's (1954) barotropic recirculation (see **Fig. 2.10**) - and use a three-layer quasi-geostrophic model to show the dynamical consequences of anticyclogenesis.

In particular, the recirculation is confined to a "bowl" which is associated with 18° Water in the upper 500 m, and with a lower interface lying at a depth governed by PV conservation. The northwards descending base of such a bowl is suggested in observations (see **Fig. 2.17**), and - based on PV conservation - is predicted by Marshall and Nurser (1988) - see the thick line in **Fig. 2.17**. Predicted hyperbolic descent of the lower interface suggests that the bowl strikes the ocean floor around 300 km south of the separated Gulf Stream. The implication is that there is a *barotropic* component to the buoyancy-forced recirculation within 300 km of the Gulf Stream, evidenced by abyssal layer currents in the three-layer model of Marshall and Nurser (1988). The circulation subsequently equilibrates when accumulated potential energy is released through mesoscale instability and the lateral transfer of PV.

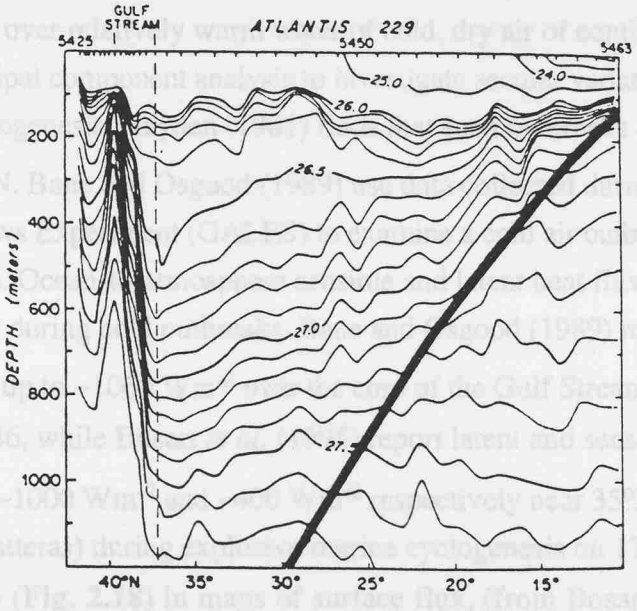

Figure 2.17: Isopycnals in a north-south section across the Gulf Stream-Sargasso Sea at 50°W, with the depth of a recirculation bowl predicted from PV constraints (from Marshall and Nurser 1988).

In a study similar to Stommel and Veronis (1980), Huang (1990) proposes a two-layer (isopycnic) model of the recirculation, and supposes that the model is suddenly subjected to strong surface cooling. By forcing upper layer water to sink

and become lower layer water, momentum is "mixed" vertically, and the initially steady eastward jet is unbalanced. After subsequent geostrophic adjustment, high and low pressure centres are established north and south of the front, with the main effect of driving a stronger eastward barotropic flow. Huang (1990) thus obtains a ~60% increase in transport of the jet, due to recirculation gyres associated with the new pressure centres.

2.3.3 "Cold Outbreaks" over the Gulf Stream

In wintertime, extratropical cyclones develop along the eastern US seaboard and track northeastward into the mid-Atlantic Bight. Intense marine (atmospheric) cyclogenesis is a well-documented phenomenon. In an overview of the subject, Sanders and Gyakum (1980) present a climatology of so-called "bombs" (defined as extratropical cyclones which develop "explosively", exhibiting central pressure falls of more than 1 mb h^{-1} for at least 24 hours). Associated with such storms are "outbreaks" over relatively warm water of cold, dry air of continental origin. Using principal component analysis to investigate secular variation in Atlantic coastal cyclogenesis, Hayden (1981) finds that such outbreaks are centred at around 35°N. Bane and Osgood (1989) use data collected during the Genesis of Atlantic Lows Experiment (GALES) to examine a cold air outbreak over January 25-30, 1986. Ocean-to-atmosphere sensible and latent heat fluxes can reach very large values during cold outbreaks. Bane and Osgood (1989) report a combined heat loss of up to ~1060 Wm^{-2} over the core of the Gulf Stream during 27-28 January 1986, while Bosart *et al.* (1995) report latent and sensible heat flux maxima of ~1000 Wm^{-2} and ~400 Wm^{-2} respectively near 35°N and 75°W (just off Cape Hatteras) during explosive marine cyclogenesis on 17 February 1974, shown here (**Fig. 2.18**) in maps of surface flux, (from Bosart *et al.* 1995). Considering the entire Northern Hemisphere (including both Gulf Stream and Kuroshio regions), Sanders and Gyakum (1980) find that approximately two bombs per three days occur in January, a frequency which halves by March. In the North Atlantic, the most frequent local occurrence of such events (up to five per season) is centred just north of, and along, the mean axis of the Gulf Stream, as illustrated in **Fig. 2.19** (from Sanders and Gyakum 1980).

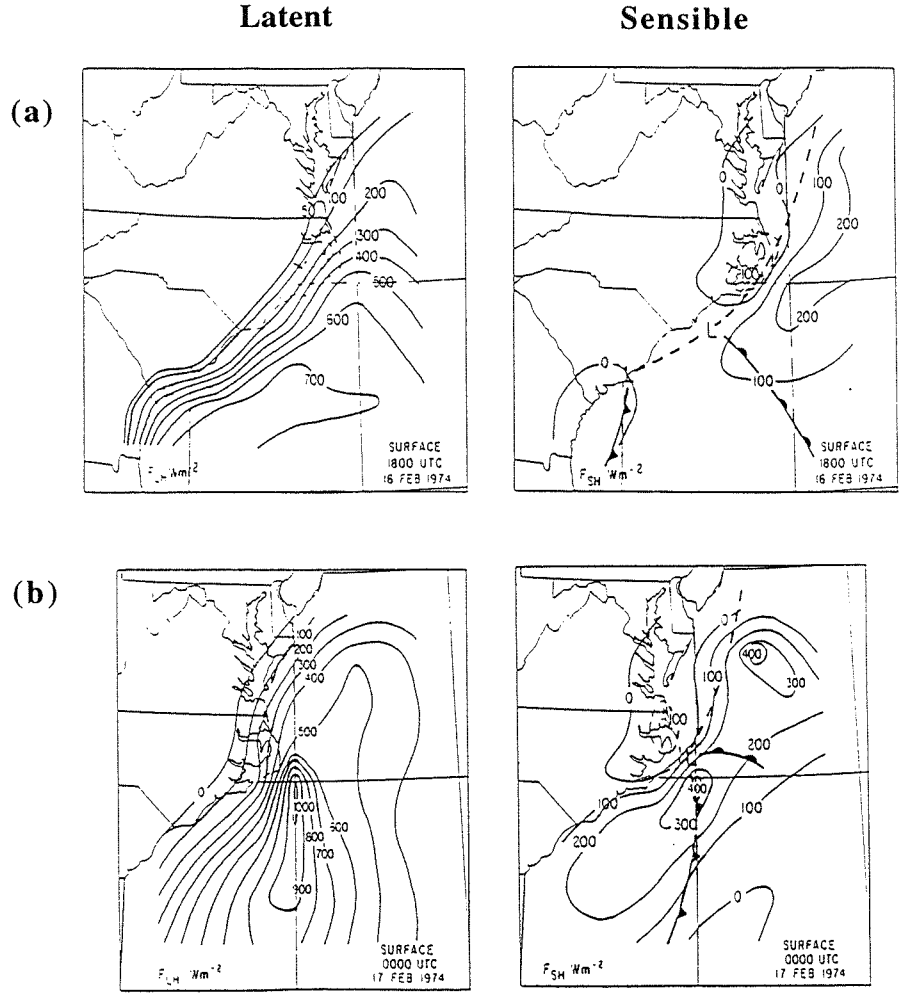

Figure 2.18: Maps of latent and sensible heat flux (Wm^{-2}) during a 1974 cold outbreak, on (a) 1800 on 16 Febraury, (b) 0000 on 17 February (Bosart *et al.* 1995).

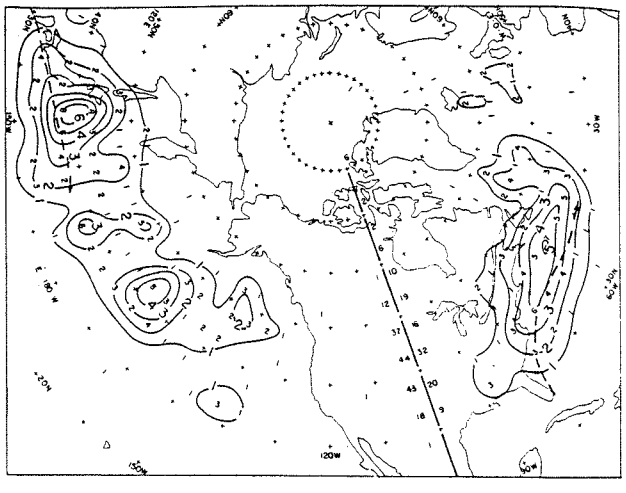

Figure 2.19: Annual frequency of "bombs" in the Northern Hemisphere, obtained from the winters of 1976/77 - 1978/79 (Sanders and Gyakum 1980).

2.4 Interannual variability in the subtropical North Atlantic

The present study addresses interannual variability of water masses and circulation in the subtropical North Atlantic. With respect to air-sea interaction in the Gulf Stream region, §2.4.1 describes the influence of the North Atlantic Oscillation (NAO). Evidence for interannual variability of 18° Water and the Gulf Stream is outlined in §2.4.2, raising the possibility of a cause-and-effect relationship between strong 18° Water renewal and Gulf Stream intensification, during and after severe winters.

2.4.1 Severe winter conditions in the Gulf Stream region and influences of the North Atlantic Oscillation (NAO)

Although an individual cold outbreak lasts typically for only a few days, the integral effect of outbreaks which are more frequent, long-lived, or severe, than normal, will result in a relatively cold winter in the Gulf Stream-Sargasso Sea region. The most severe winter of recent years was that of 1976/77, discussed at length by Diaz and Quayle (1978). Worthington (1977) shows surface atmospheric pressure averaged from mid-January to mid-February of 1977, to illustrate westward expansion of the Icelandic Low towards Newfoundland. Associated with this pressure pattern was a sea level flow of continental polar air across the northwestern Sargasso Sea. The implication is that cold winters over the Gulf Stream-Sargasso Sea are characterized by such synoptic pressure patterns, and that excess wintertime cooling of the Gulf Stream is associated with quasi-stationary anomalies in the atmospheric general circulation.

The atmospheric pressure pattern of winter 1976/77 was characteristic of a mode of climate variability in the wintertime North Atlantic. Dickson and Namias (1976) showed that winters of extreme cold over the southeastern United States are characterized by enhanced atmospheric baroclinicity at the Atlantic seaboard, with the result that the zone of peak winter storm frequency is shifted far to the southwest of normal. Such variability is now understood in a broader context (Dickson *et al.* 1996) to be part of the North Atlantic Oscillation (NAO), the dominant mode of atmospheric variability in the North Atlantic sector.

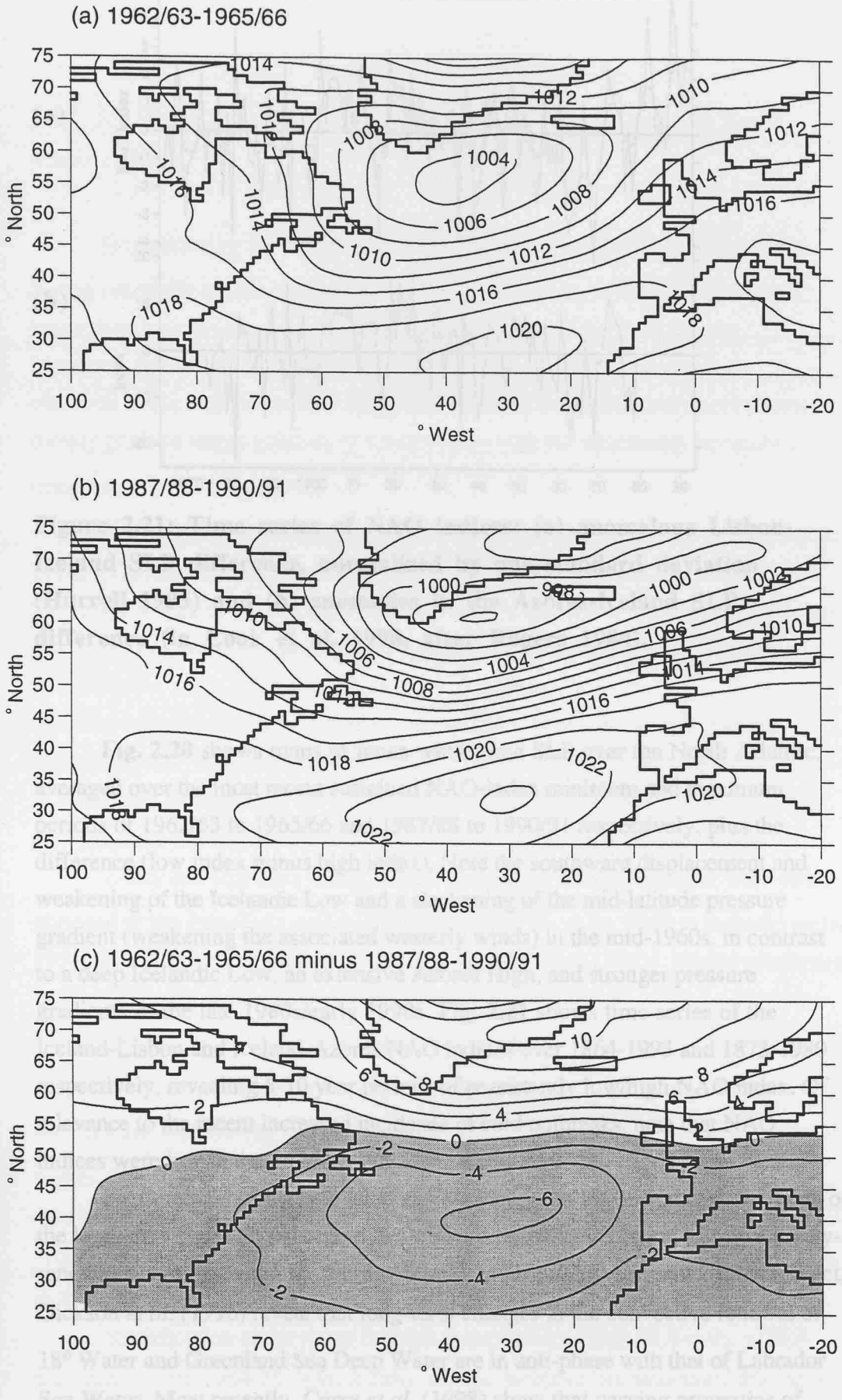

Figure 2.20: Wintertime SLP (mb) over the North Atlantic during (a) NAO low phase, (b) NAO high phase, (c) difference (SLP data from CRU - see §3.4.3).

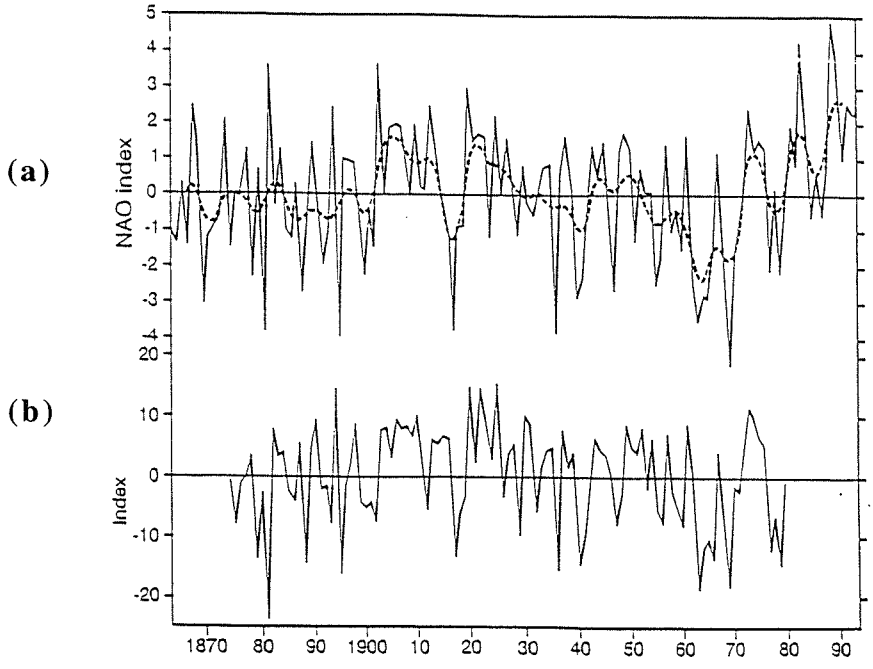

Figure 2.21: Time series of NAO indices: (a) anomalous Lisbon-Iceland SLP difference, normalized by one standard deviation (Hurrell 1995) and (b) anomalies in the Azores-Iceland SLP difference (in Cook et al. 1998, after Rogers 1984).

Fig. 2.20 shows maps of mean wintertime SLP over the North Atlantic, averaged over the most recent sustained NAO-index minimum and maximum periods of 1962/63 to 1965/66 and 1987/88 to 1990/91 respectively, plus the difference (low index minus high index). Note the southward displacement and weakening of the Icelandic Low and a slackening of the mid-latitude pressure gradient (weakening the associated westerly winds) in the mid-1960s, in contrast to a deep Icelandic Low, an extensive Azores High, and stronger pressure gradients in the late 1980s/early 1990s. **Fig. 2.21** shows time series of the Iceland-Lisbon and Iceland-Azores NAO indices over 1864-1993 and 1873-1980 respectively, revealing 5-10 year periods of persistently low/high NAO index. Of relevance to the recent increased incidence of cold outbreaks, note that NAO indices were low in the mid/late 1960s and the late 1970s.

NAO-related changes in wind and buoyancy forcing appear to drive much of the long-term variability observed in the properties and circulation of convectively-renewed water masses in the North Atlantic. In an extensive review of this subject, Dickson *et al.* (1996) reveal that long-term changes in the convective renewal of 18° Water and Greenland Sea Deep Water are in anti-phase with that of Labrador Sea Water. Most recently, Curry *et al.* (1998) show that varying properties of Labrador Sea Water, tracked to mid-depths in the subtropics about 6 years later, are clearly lag-correlated with the NAO-index of Hurrell (1995).

2.4.2 18° Water variability and the response of the Gulf Stream to severe winter cooling

In considering 18° Water variability, Worthington (1959) speculated that, during unusually severe winters, SST may fall as low as 17°C (an arbitrary 1°C lower than typical values) in the cooling region south of the Gulf Stream. However, up until the late 1950s, such low values of SST had never been observed in the region, and Worthington concluded that anomlously cold winters merely produce larger volumes of a water mass with the remarkably invariant temperature of 17.9 ± 0.3°C.

During the 1970s anomalous 18° Water began to be observed (Worthington 1972, 1977; McCartney *et al.* 1980). However, only a reliable, representative, long and continuous time series of the upper water column at a fixed location in the Sargasso Sea could substantiate these reports. The existence of such a time series is a testament to the foresight and persistence of Henry Stommel. In 1953 Stommel tried and failed to start a long-term "oceanographic observatory" off Bermuda (Stommel 1954). However, regular hydrographic stations off Bermuda did begin in June 1954, occupied by the Bermuda Biological Station vessel *Panulirus*, the data prepared and recorded at Woods Hole (Schroeder and Stommel 1969).

Talley and Raymer (1982) present analyses of the hydrographic time series obtained at the *Panulirus* station (32°10'N, 64°30'W, at the 3000 m isobath) up to 1978. **Fig. 2.22** is composited from Talley and Raymer (1982). Modal properties in **Fig. 2.22a** are defined at the depth where PV is minimum in the near-surface STMW layer. It is evident from **Fig. 2.22a** that the "classic" *T-S* properties of 18° Water thus defined are in fact significantly variable. In particular, modal temperature is lower (by nearly 1°C, from 18.0°C to 17.1°C) and modal density is higher (by about 0.2 mg cm^{-3}, from 26.4 to 26.6 mg cm^{-3}) over 1964-75, compared to the periods 1954-64 and 1975-78. More recently, Klein and Hogg (1996) present evidence for a warmer (18.0-18.2°C) variety of 18° Water forming in the late 1980s.

Stratification of the water column in the density range $26.4 < \sigma_\theta < 26.6$ also varies over 1954-78 (**Fig. 2.22b**). A time series of the associated PV, as a function of density, reveals fresh "injections" of low PV in late winter of most

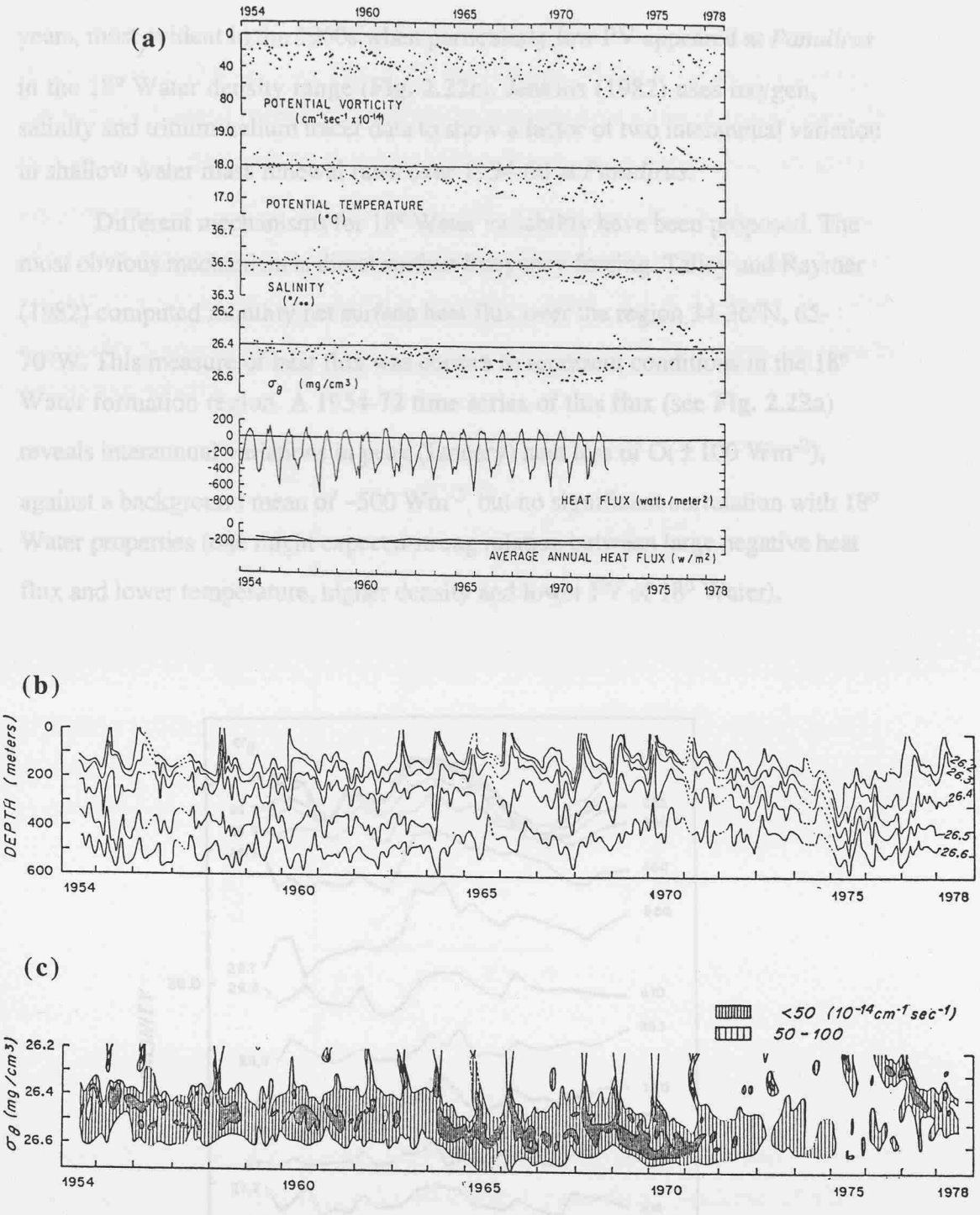

Figure 2.22: Time series at *Panulirus* over 1954-78: (a) modal (18° Water) properties (and net heat flux over a region of the Sargasso Sea - see text), (b) stratification, and (c) potential vorticity (Talley and Raymer 1982).

years, most evident in the 1960s when particularly low PV appeared at *Panulirus* in the 18° Water density range (**Fig. 2.22c**). Jenkins (1982) uses oxygen, salinity and tritium-helium tracer data to show a factor of two interannual variation in shallow water mass renewal rates over 1954-80 at *Panulirus*.

Different mechanisms for 18° Water variability have been proposed. The most obvious mechanism is direct surface buoyancy forcing. Talley and Raymer (1982) computed monthly net surface heat flux over the region 34-36°N, 65-70°W. This measure of heat flux was chosen to represent conditions in the 18° Water formation region. A 1954-72 time series of this flux (see **Fig. 2.22a**) reveals interannual variations in peak (January) heat loss of O($\pm$100 Wm^{-2}), against a background mean of ~500 Wm^{-2}, but no significant correlation with 18° Water properties (one might expect a strong relation between large negative heat flux and lower temperature, higher density and lower PV of 18° Water).

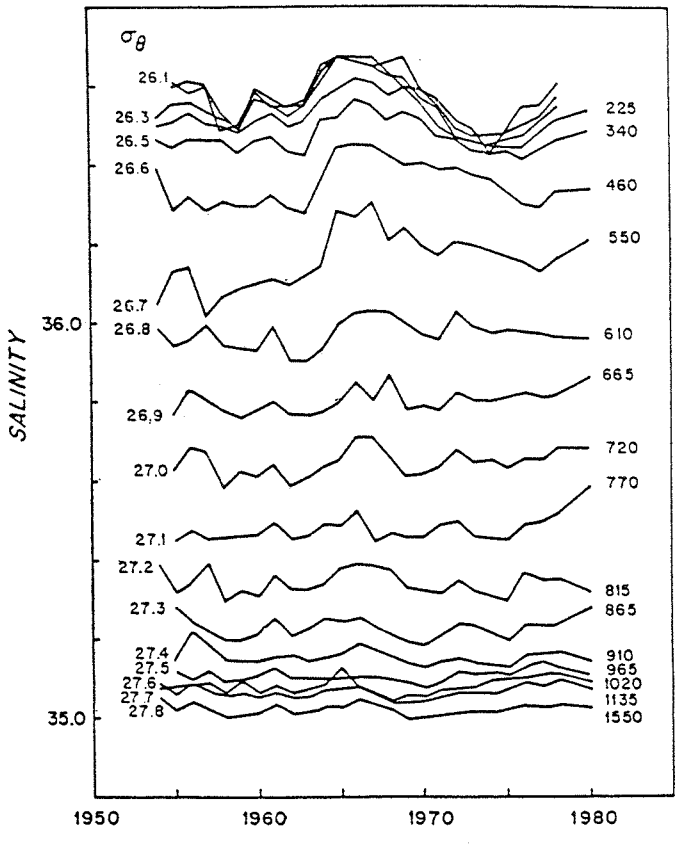

Figure 2.23: Time series over 1954-80 of annual-mean Isopycnal Salinity on potential density in the range 26.1-27.8 (Jenkins 1982)

The vertical and temporal coherence of Isopycnal Salinity (IS) observed at Bermuda over 1954-80 (see **Fig. 2.23**) led Jenkins (1982) to propose a storage mechanism. Lagged correlation coefficients between time series of annual-mean IS (for σ_θ = 26.1, 26.3 and 26.5) and local heat flux (area-averaged over 30-40°N, 60-70°W) reach maxima of ~0.4 at lags of 2-3 years (see **Fig. 2.24**). Lag times of >1 year suggest some "memory" of surface forcing over previous years. Denser and saltier water in the upper gyre (as appeared around 1965 at Bermuda) may thus favourably precondition the upper layer, thus increasing 18° Water renewal rates in successive winters.

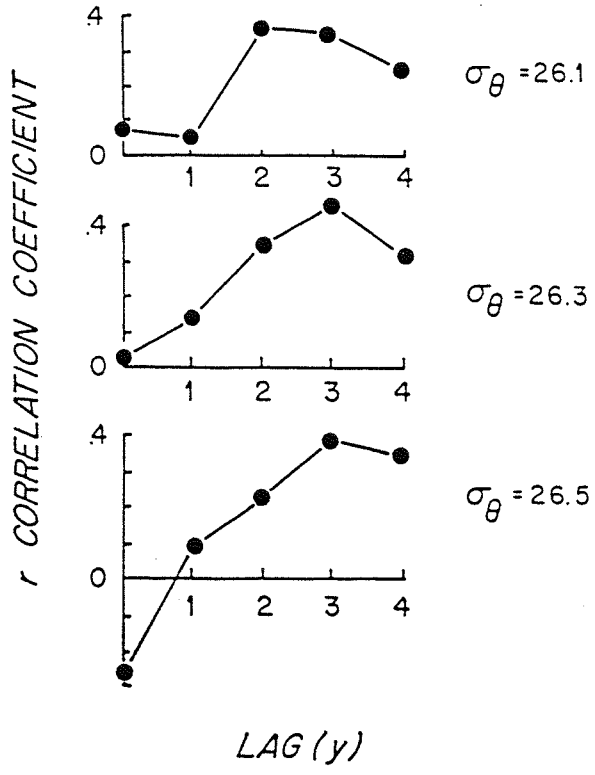

Figure 2.24: Lagged linear correlation coefficients between 1954-72 time series of annual-mean IS and local heat flux (Jenkins 1982)

Recent modelling studies have addressed the issue of mode water variability. Liu and Pedlosky (1994) investigate the thermocline response to annual and decadal variation of SST in a two-layer thermocline model which is coupled to a passive upper mixed layer. Two types of buoyancy-forced solutions are obtained, depending on the speed of advance, during winter, of the line where the subducting layer outcrops into the mixed layer. The implication is that thermocline properties are biased towards those of the late winter mixed layer, and that seasonal

variability does not impact on the thermocline (in contrast to the strong impact of decadal variability in winter conditions). Hazeleger and Drijfhout (1998, 1999) use a more realistic isopycnal-coordinate model of an idealized-geometry North Atlantic subtropical gyre to investigate the variability of mode water formation under a variety of forcing scenarios: excess cooling of varying description, NAO-minimum wind forcing, a combination of both, and stochastic forcing. Hazeleger and Drijfhout (1998) find that, while realistic amplitudes and timescales of mode water variability are generated under excess cooling, anomalous wind forcing generates westward-propagating thickness anomalies but does not impact on mode water formation.

If 18° Water formation rates are principally dependent on wintertime cooling (by no means proven to be the case) and if the recirculation does intensify through anticyclogenesis (also somewhat contentious), Gulf Stream transport may notably strengthen under exceptionally severe winter cooling. To some extent, theoretical studies support this possibility. Stommel and Veronis (1980), Marshall and Nurser (1988) and Huang (1990) sought the equilibrium, adjusted response of the Gulf Stream to cooling. The pioneering studies of Nof (1983) and Adamec and Elsberry (1985a,b) addressed the *transient* response of the Gulf Stream to sudden cooling. Nof (1983) used a two-layer model of the separated Gulf Stream (a zonal jet, coincident with the front between the layers) which encounters a specified zonal surface density (pressure) gradient. This pressure gradient drives a depth-dependent cross-stream flow which is akin to an atmospheric thermal wind: at the surface, the cross-stream flow is southward, while at depth weaker flows are directed northward. As a consequence the zonal front steepens with distance eastwards (downstream), and the surface jet is displaced southwards, by O(100 km) over a zonal distance (cooling zone) of O(1000 km) - see **Fig. 2.25a**. The jet intensifies as the north-south frontal zone narrows, but total transport of the jet remains constant.

Adamec and Elsberry (1985a) used a cross-sectional (two-dimensional) model of the Gulf Stream to investigate the dynamical response to a cross-stream cooling event (by imposing a meridional cooling gradient on the model, with the ocean-to-atmosphere heat flux ranging from zero on the north, cold, side of the front to a maximum of ~970 Wm^{-2} on the south, warm side). The transient response thus obtained is sensitive to the competition between vertical mixing of heat and momentum. In the case of heat-mixing only, convection weakens the cross-stream temperature (pressure) gradient. In the model momentum equation, the Coriolis term slightly dominates the pressure gradient term, and the flow becomes super-geostrophic. This imbalance leads to a near-surface southward

cross-stream flow, directed against the meridional pressure gradient. Thus, while the meridional cooling gradient acts to destroy the front (preferentially cooling the warm side of the front), the dynamical response is thermally-indirect (warm water sinks, cold water rises), and, although the jet does weaken somewhat, the front is maintained over a period of 72 hours (see **Fig. 2.25b**). When vertical mixing of momentum is included in the model, a very different response to cooling is obtained. Momentum is generally exchanged vertically on the same timescales as the mean flow - much faster than diffusive timescales of heat exchange, except where shear instability or convection leads to near-simultaneous heat and momentum mixing in a weakly stratified environment (Thorpe 1973). The strong surface flow is therefore weakened through the vertical momentum mixing. Furthermore, the Coriolis term is now dominated by the (less altered) pressure gradient term, and the flow becomes sub-geostrophic. The resultant cross-frontal surface flow is now in the same sense as the pressure gradient, and a thermally-direct circulation is set up, which acts to destroy the front and weaken the associated zonal flow to a greater extent (see again **Fig. 2.25b**).

Adamec and Elsberry (1985b) extended the work of Nof (1983) and Adamec and Elsberry (1985a) to three dimensions, including the effects of both along-stream and cross-stream cooling gradients on a numerical model of the separated Gulf Stream (a zonal jet as before). If vertical mixing of momentum is not included in the model, the predominantly zonal cooling gradient drives a slight southward displacement of the jet, due to cross-stream drifts of O(0.1 cm s^{-1}), qualitatively confirming the main result of Nof (1983). As in Adamec and Elsberry (1985a), however, the inclusion of momentum mixing leads to a quite different response. Where vertical shear is large (in the vicinity of a strong meridional cooling gradient), the effect of momentum mixing is to set up a northward cross-stream drift of O(2.5 cm s^{-1}), and correspondingly larger *northward* displacements of the jet (see **Fig. 2.25c**). Where shear is small the effects of heat mixing are dominant, and smaller southward displacements are obtained (see again **Fig. 2.25c**).

To investigate the effect of cooling on the separated Gulf Stream, Nurser and Williams (1990) used an idealized model in which an upper dynamically-active layer overlies a deep abyssal layer, and the path of the separated western boundary current is characterized by an outcrop of the lower layer (Parsons 1969). A realistic level of cooling, imposed along the outcrop line which represents the separated current, leads to a strengthening of the separated current from 39 Sv (adiabatic case) to 53 Sv, and southeastward displacement of the separation point by 320 km.

(a) Nof (1983)

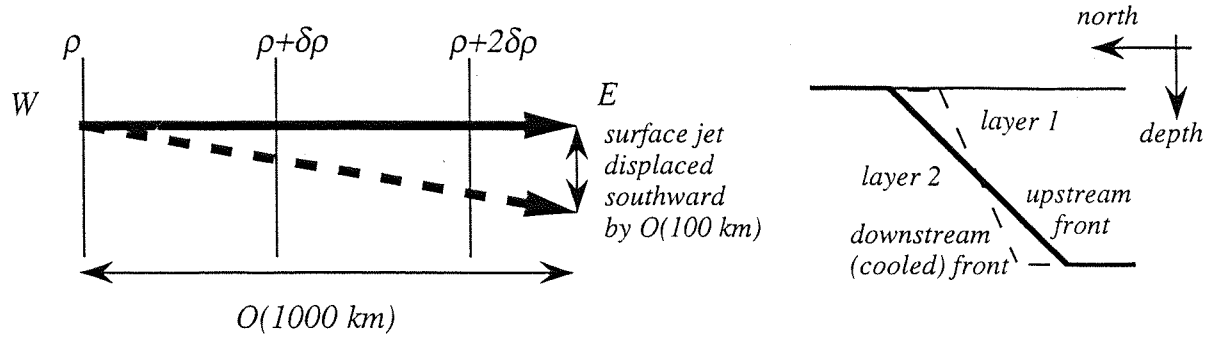

(b) Adamec and Elsberry (1985a)

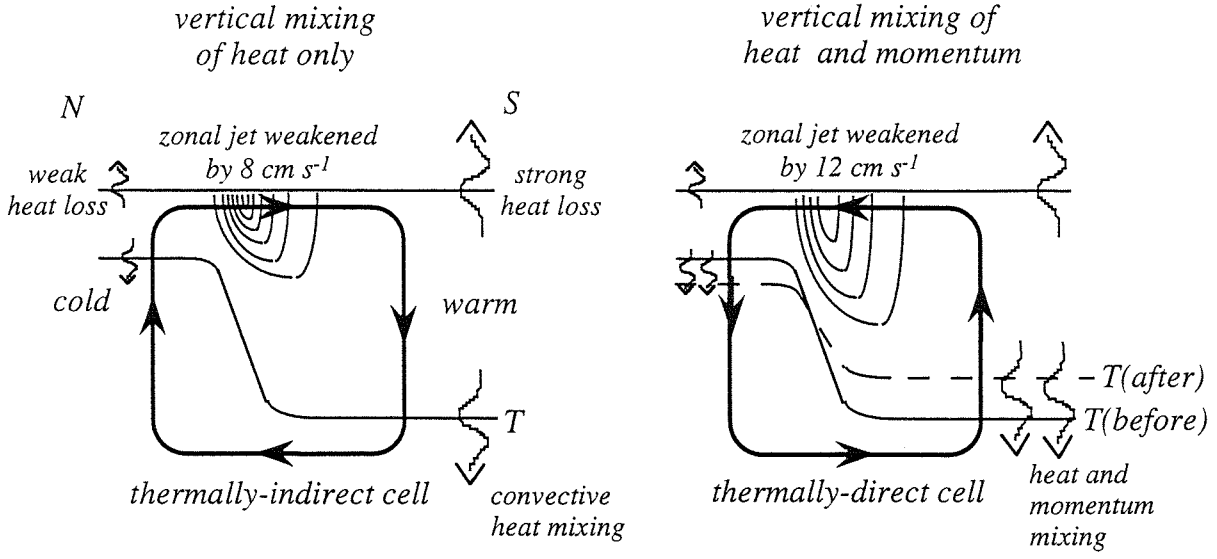

(c) Adamec and Elsberry (1985b)

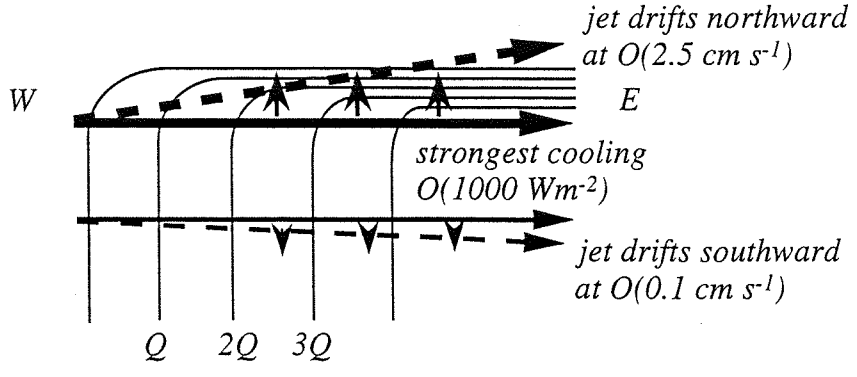

Figure 2.25: Schematics summarizing previous idealized studies of the Gulf Stream response to cooling: (a) Nof (1983), (b) Adamec and Elsberry (1985a), and (c) Adamec and Elsberry (1985b)

More recent studies have addressed the *local* response to cold outbreaks of the Gulf Stream off the southeastern United States. In an air-sea interaction study, Chao (1992) coupled a dry atmospheric model with a primitive equation ocean model, to investigate how atmospheric cold fronts interact with the Gulf Stream and adjacent waters during cold-air outbreaks. The coupled model reveals a process responsible for *weakening* Gulf Stream transport on a weekly timescale: a postfrontal downdraft over the coastal ocean intensifies a low-level southward wind. Chao (1992) concludes that conventional ocean models, treating ocean cooling as a forcing independent of the wind stress, may fail to capture the full short-term effects of cold-air outbreaks.

Xue *et al.* (1995) investigated the response of the Gulf Stream (off the southeast coast of the United States) to the cold outbreak during 25-30 January 1986 (Bane and Osgood 1989). A time-dependent, cross-sectional model (based on the Princeton Ocean Model, Blumberg and Mellor 1987) of the Gulf Stream, extending from 50 to 550 km offshore, is forced for 5 days with heat and wind forcing based on observations. An idealized cold outbreak is characterized by the passage of excess cooling (with maximum heat loss of 1500 Wm^{-2} centred over the Gulf Stream) associated with the southern portion of an offshore-moving low pressure system. Strong westerly winds coincide with peak cooling.

In three sensitivity experiments, Xue *et al.* (1995) force the model with cooling alone, winds alone and the combination of both. The primary effect of cooling over the model Gulf Stream is to reduce SST by about 1.5°C and to deepen the mixed layer by typically 50 m. Vertical mixing of downstream momentum dominates the mixing of heat (as in Adamec and Elsberry 1985a). Furthermore, vertical mixing is largely balanced by acceleration in the alongshore momentum balance. As a consequence, currents above/below a depth of 25 m decrease/increase by O(5 cm s^{-1}) when heat loss is strongest. However, against background Gulf Stream currents of up to 200 cm s^{-1}, this amounts to a very weak response to cooling. The response to wind forcing is somewhat stronger. The along-stream component of wind-driven Ekman flow (generally southward in response to the strong westerlies) weakens currents by up to 15 cm s^{-1} in the upper 25 m. The Gulf Stream is also Ekman-advected 10-20 km offshore, strengthening offshore currents by up to 20 cm s^{-1} at 25 m, and by up to 3 cm s^{-1} at 200 m. The strongest dynamical response is a predominantly wind-forced transient cell, maintained by cross-stream flows (up to 30 cm s^{-1}) and strong vertical motion (up to 0.1 cm s^{-1}). At 10 km horizontal resolution and with 51 vertical levels (including vertical resolution of ~10 m in the mixed layer), the study of Xue *et al.* (1995)

thus captures the detailed dynamical response of the "pre-separation", coastal Gulf Stream under cold outbreak forcing.

On larger scales, cold outbreaks must also influence the separated Gulf Stream intensification. In driving the deeper mixing which enhances 18° Water formation, excessive cooling due to successive cold outbreaks during an unusually severe winter may act to intensify the end-of-winter Gulf Stream, as proposed by Worthington (1977). Of particular note is the high Gulf Stream transport estimate of 95 Sv after the severe winter of 1976-77, in contrast to the low value of 62 Sv after the mild winter of 1974-75 (see **Fig. 2.14**).

Gulf Stream transport also varies significantly on inter-decadal time-scales. A series of recent studies (Greatbatch *et al.* 1991; Greatbatch and Xu 1993; Ezer *et al.* 1995) indicate that the Gulf Stream was up to 30 Sv weaker during 1970-74 compared to 1955-59. Greatbatch *et al.* (1991) use a diagnostic model (Mellor *et al.* 1982) to compute transport from historical fields of wind stess (Da Silva 1991) and three-dimensional density (Levitus 1989a,b,c; 1990). Greatbatch and Xu (1993) use a vertical section model to further investigate the vertical structure of 1955-59 to 1970-74 transport changes, highlighting the significance (of the vertical structure) for heat transport through selected sections. Paradoxically, Ezer *et al.* (1995) find that weaker Gulf Stream transport in the 1970s was accompanied by stronger mid-latitude heat transport. Ezer *et al.* (1995) confirm the central results of Greatbatch *et al.* (1991) and Greatbatch and Xu (1993) with diagnostic and short-term prognostic calculations, using a free-surface, three-dimensional model of the North Atlantic (Ezer and Mellor 1994). Changes in both wind forcing and the thermohaline circulation are found to play an important role, and there is further suggestion of dynamic coupling between the thermohaline and wind-driven circulation.

2.5 Summary of literature review and objectives of present study

The North Atlantic subtropical gyre is essentially a wind-driven (Sverdrup 1947), westward-intensified (Stommel 1948) anticyclonic gyre. The intensified western boundary current (WBC) - the Gulf Stream - may be enhanced through the interaction of baroclinicity and topography (Holland 1973) and augmented by recirculations, both inertial (Fofonoff 1954) and thermally-driven (Cushman-Roisin 1987, Spall 1992).

The seasonal cycle in Gulf Stream transport is quite different at two principal along-path locations: at the Florida Straits and downstream from Cape

Hatteras. Large variability in developed Gulf Stream transport (Worthington 1977) contrasts with remarkably constant transport through the Florida Straits (Larsen 1992). Stommel (1958) showed that fluctuations in Florida Straits transport are directly wind-forced. The stronger variability downstream of Cape Hatteras is more likely due to variable thermohaline forcing (Worthington 1977). The latter region is characterized by annual-net surface buoyancy loss, associated with large air-sea temperature differences which reach extreme values during wintertime outbreaks of cold, dry air over the Gulf Stream (Bane and Osgood 1989).

A by-product of strong wintertime buoyancy loss over the Gulf Stream is 18° Water, found in the upper 500 m throughout the Sargasso Sea (Worthington 1959). Climatologically, 18° Water is renewed at an annual rate of about 5 Sv (Speer and Tziperman 1992). However, a hydrographic time series at Bermuda reveals considerable interannual variability in the potential vorticity of 18° Water (Talley and Raymer 1982), suggesting a variable rate of renewal. Worthington (1972) argued that Gulf Stream transport is intimately related to 18° Water via anticyclogenesis, a hypothesis supported by idealized model studies (e.g., Marshall and Nurser 1988).

The cause of 18° Water variability is unclear. The most obvious mechanism is local surface buoyancy forcing, but Talley and Raymer (1982) could not obtain a significant correlation between time series of 18° Water properties at Bermuda, and area-integrated heat flux data. Jenkins (1982) did obtain 2-3 year lagged correlation coefficients, between heat flux and isopycnal salinity, of up to ~0.4, suggesting some oceanic memory of surface forcing over previous years (a storage mechanism).

In that the Gulf Stream might be significantly modified by cold outbreaks, several studies have addressed dynamical responses to cooling. In particular, Xue *et al.* (1995) modelled the local effect of outbreaks, upstream of Cape Hatteras, while Worthington (1977) speculated that the intensified Gulf Stream (downstream of Cape Hatteras) of spring 1977 was forced by the preceding severe winter. Other studies of the Gulf Stream response to sudden cooling (Veronis and Stommel 1980; Nof 1983; Adamec and Elsberry 1985a,b; Huang 1990) have been based on simplified models of the dynamics. The earlier work of Holland (1973) suggests that a barotropic response may arise through the interaction of a cooling-implied change in baroclinic structure and bottom topography.

On the basis of observations and theoretical considerations reviewed here, it would seem that 18° Water formation and Gulf Stream intensification are intimately related. By the same token, 18° Water *variability* must be accompanied

by changes in end-of-winter Gulf Stream transport. East of Cape Hatteras, the along-stream increase in Gulf Stream transport (and perhaps also intensification due to excess cooling) is predominantly barotropic. In contrast, 18° Water formation (and variability thereof) is part of a shallow, predominantly meridional, overturning of the Sargasso Sea. This represents a baroclinic circulation (for which vertically-integrated transport is zero). The relationship between barotropic and baroclinic responses to cooling may involve the interplay of baroclinicity and topography.

In the present study, a realistic model of the North Atlantic is used primarily to examine the response of the Gulf Stream to excess cooling, and to address the principal questions:

- How realistically does the model reproduce annual mean circulation, seasonal transport cycles and 18° Water formation?

- Can a series of severe winters force model 18° Water variability of the type observed at Bermuda in the 1960s?

- Does excess wintertime cooling of the model Gulf Stream lead to end-of-winter intensification such as that in spring 1977?

- Is the Gulf Stream intensification significantly barotropic, and if so, how is this related to enhanced 18° Water formation?

CHAPTER 3. METHODOLOGY

Central to this study is the use of a General Circulation Model (GCM) - described in §3.1 below - in a set of control and sensitivity experiments (§3.2), applying idealized anomalous surface buoyancy and wind forcing to a North Atlantic GCM. The comparison of control and sensitivity GCM experiments has become a standard procedure, particularly in the study of transient and equilibrium responses to climate change (IPCC 1990). The routine diagnostic methods used in this study are outlined in §3.3 (more novel diagnostics are introduced in later chapters). Historical datasets of surface temperature, sea level pressure and air-sea heat and freshwater fluxes (described in §3.4) are used to guide experiment design, and in separate diagnoses of water mass variability.

The use of a GCM in the present study is motivated by similar studies with more idealized models (see §2.3.2 and §2.4.2). The present experiments (Marsh and New 1996) and more recent work of Hazeleger and Drijfhout (1998, 1999) represent the first GCM studies of mode water variability. Early results with the present model (New *et al.* 1995) showed that the model is particularly successful in explicitly representing the process of thermocline ventilation and mode water formation. New and Bleck (1995) show significant decadal evolution of mode waters in the model subtropical gyre, even under climatological surface forcing, due to variations in the relaxation fluxes of heat and freshwater (outlined in §3.1.4 below). This suggests that mode water variability can be readily forced by imposing excess surface buoyancy loss. Furthermore, the suitability of the model for studying this variability can be explored by varying appropriate parameters, in particular the thickness diffusion velocity (see §3.1.2).

The buoyancy flux sensitivity experiments are related back to observations by novel diagnosis of a new air-sea heat and freshwater flux climatology (Josey *et al.* 1999). While the modelling study is motivated by variability of 18° Water observed at Bermuda over 1954-78, the new climatology is used to more broadly assess recent (1980-97) variability. To complement the buoyancy flux sensitivity experiments, NAO-minimum wind forcing is applied to the model in a separate experiment. The main emphasis of the study, however, is on the role of anomalous buoyancy forcing.

3.1 The Model

3.1.1 Model code

The model used in this study is based on the generic "Miami Isopycnic-Coordinate Ocean Model" (MICOM, which is a primitive equation GCM, and is described by Bleck *et al.* 1989; Bleck and Smith 1990; Smith *et al.* 1990; Bleck *et al.* 1992). MICOM exploits potential density referenced to the surface [$\sigma_\theta = (\rho/\rho_o - 1) \times 10^3$; where ρ is the in-situ density and ρ_o = 1000 kg m^{-3}] as a non-dimensional vertical coordinate, modelling the ocean as a stack of isopycnic layers. In essence, MICOM numerically solves layer-integrated horizontal momentum, continuity and hydrostatic equations on the "C grid" of Arakawa and Lamb (1977), velocity and mass field variables being staggered horizontally such that u (v) grid points are located halfway between mass grid points in the x (y) direction. A "split-explicit" scheme (Gadd 1978) separately integrates the fast barotropic mode and slower baroclinic mode.

A major advantage of employing a potential density coordinate is that advective-diffusive processes, which are believed to be oriented preferentially along isopycnals in the real world, are explicitly included in MICOM. A recent tracer release experiment in the eastern subtropical North Atlantic (Ledwell *et al.* 1993) confirmed, by direct observation of mixing on an annual timescale, that diapycnal diffusivity is generally very weak compared to isopycnal diffusivity [although recent observations have revealed much stronger mixing near topography in the abyssal ocean (e.g., Polzin *et al.* 1995)]. The inference is that fluid must penetrate the thermocline mostly by mixing along, rather than across, density surfaces.

Numerical difficulties associated with the "vanishing" layers of MICOM (whereby isopycnals outcrop into boundaries, especially at the mixed layer base) have been overcome. To demonstrate this success, Sun *et al.* (1993) showed that MICOM can closely reproduce analytical solutions of wind and buoyancy-forced flow in a two and three-layer ocean. Chassignet and Bleck (1993) further show that layer outcropping is integral to realistic separation of western boundary currents in an idealized Atlantic model based on MICOM.

The Atlantic model used in the present study is based on version 2.4 of MICOM (Bleck *et al.* 1992), an upgrade of MICOM version 1.3 [on which the original Atlantic Isopycnic Model was based (New *et al.* 1995)]. Version 2.4 features salinity-only advection and diffusion in isopycnic layers (layer temperature

being determined from an inversion of the equation of state) and an optional parameterization of diapycnal mixing between interior layers.

3.1.2 Model physics and parameterizations

The following physical processes can be represented by MICOM:

(1) mechanical forcing of a "slab" mixed layer by the surface wind stress,
(2) wind stirring and buoyancy forcing of a Kraus-Turner-type mixed layer (Kraus and Turner 1967), including a parameterization of the effects of sea ice,
(3) entrainment/detrainment at the base of a deepening/shoaling mixed layer,
(4) vertical mixing of momentum between the mixed layer and underlying layer(s) on entrainment/detrainment,
(5) convective mixing of the mixed layer and underlying layers when instabilities arise due to baroclinic shear,
(6) lateral (diapycnal) mixing (by eddies) in the mixed layer (with horizontal eddy diffusivity, $\kappa_H \approx 1000\ m^2s^{-1}$),
(7) isopycnal mixing (by eddies) of temperature and salinity in interior layers, with κ_H as in (6),
(8) cabbeling due to isopycnal mixing of temperature and salinity,
(9) stratification-dependent diapycnal mixing across layer interfaces (diapycnal diffusiviy, $\kappa_V = c/N$, where $c = 10^{-3}\ cm^2s^{-2}$, and N is buoyancy frequency, yielding $\kappa_V \approx 10^{-4}\ cm^2s^{-1}$ in the deep ocean),
(10) lateral mixing of thickness (PV) by eddies, with κ_H as in (6),
(11) viscous dissipation of momentum at coasts and the seafloor.

In the version of MICOM used here, cabbeling (8) is "disabled" (through salinity-only mixing in layers - temperature is computed as a function of layer density and salinity from an inverted equation of state), while interior diapycnal mixing (9) was not available in the version used for the first set of experiments (1992-95), but was included at a later stage (1996-98). For the purposes of the present study, the inclusion/exclusion of cabbeling and interior diapycnal mixing is of only minor significance. A much more important process (in applying anomalous surface buoyancy forcing) is (3), the near-surface diapycnal mixing due to entrainment at the base of the model mixed layer (see Bleck *et al.* 1989), driven by the combined effects of surface buoyancy forcing and turbulent kinetic energy input by the wind. In simulating a response of the near-surface circulation to cooling, momentum exchange between the mixed layer and interior layers (4) may

play an important role (as in Huang 1990), although there is no exchange of momentum through diapycnal mixing across interior layer interfaces.

The seasonal cycle of buoyancy forcing dominates the effect of wind stirring in the region of interest (the Gulf Stream and Sargasso Sea). **Fig. 3.1** shows how surface buoyancy loss during the autumn and winter leads to mixed layer deepening through entrainment of underlying layers. Subsequent surface buoyancy gain after the end of winter leads to restratification of the upper water column and mode water formation (akin to 18° Water renewal). The newly formed mode water layer in spring (when h_2 reaches maximum thickness) may "disappear" by the following autumn, as a consequence of advection and mixing.

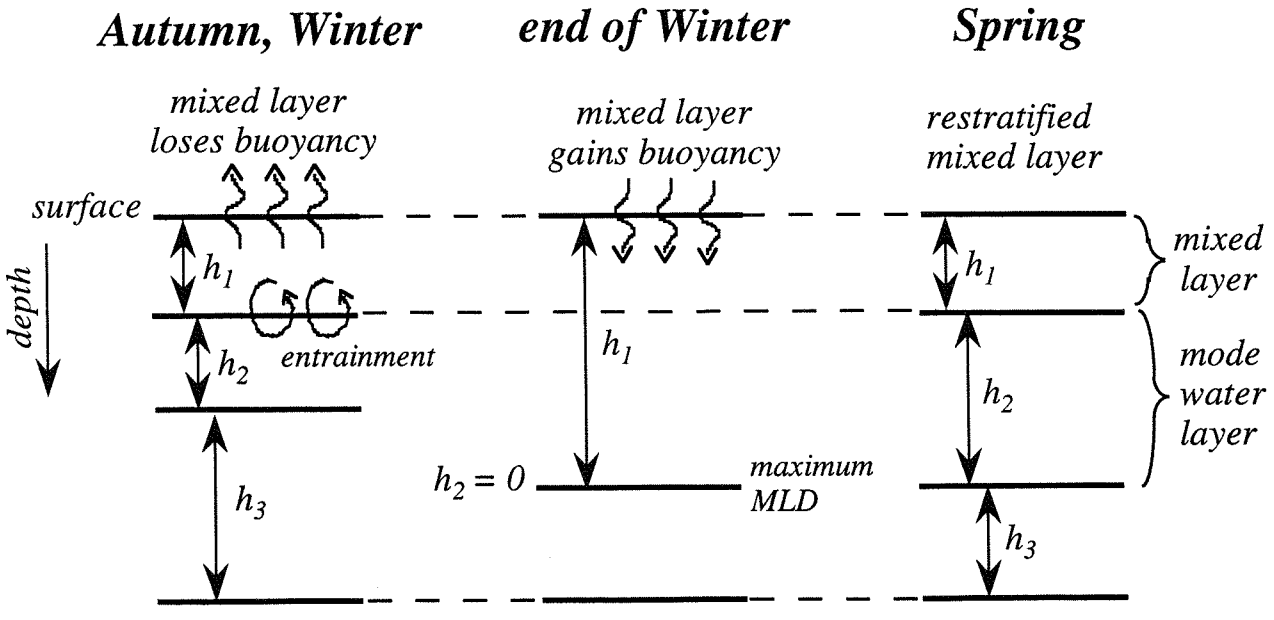

Figure 3.1: A schematic of MICOM near-surface stratification during autumn-spring evolution.

Another important physical mechanism (in determining the model response to anomalous forcing) is the lateral diffusion of layer thickness (10), which acts to smooth layer thickness fields, thus modifying horizontal pressure gradients and circulation. Tracers and density are advected by the mean flow and also by an eddy-induced horizontal "bolus velocity" (Gent and McWilliams 1990, McDougall and McIntosh 1996),

$$\mathbf{u}^* = \overline{\mathbf{u}'h'}/\overline{h} \qquad (3.1)$$

where h is isopycnal layer thickness, and dashes and overbars represent "eddy" and "mean" quantities respectively. An equivalent bolus velocity is parameterized in the model by lateral diffusion of layer interface depth, and hence of layer thickness. **Fig. 3.2a** illustrates a simple case of thickness diffusion in a two-layer flat-bottomed version of MICOM.

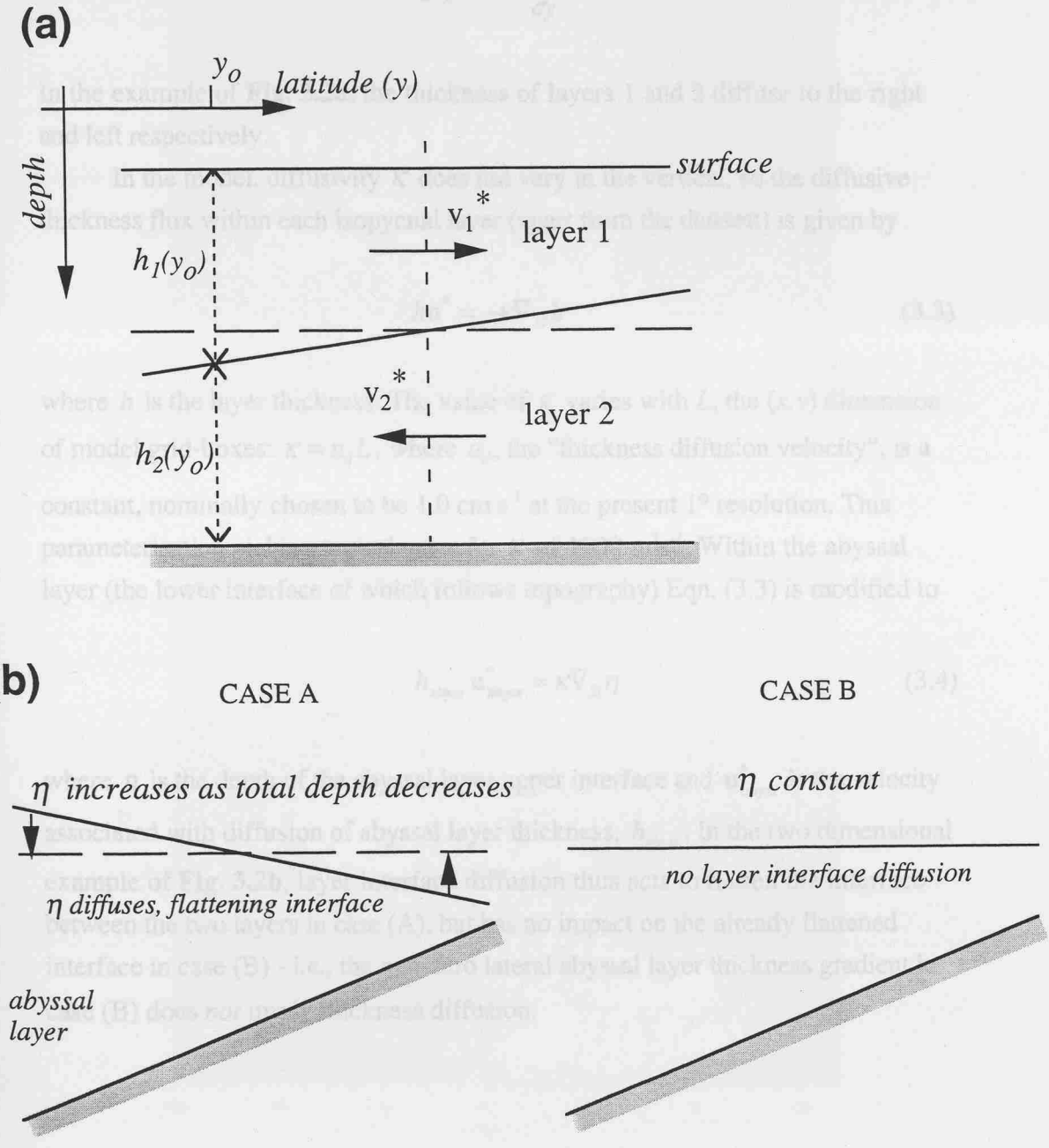

Figure 3.2: Schematic of layer thickness diffusion in a two-layered, version of MICOM: (a) flat-bottomed, (b) over sloping topography.

Equal and opposite bolus velocities, v_1^* and v_2^*, arise as a consequence of lateral gradients in the layer thicknesses, h_1 and h_2, in proportion to the strength of thickness diffusion. These bolus velocities are parameterized by a diffusivity κ:

$$h_1 v_1^* = -\kappa \frac{\partial h_1}{\partial y} \tag{3.2a}$$

$$h_2 v_2^* = -\kappa \frac{\partial h_2}{\partial y} \tag{3.2b}$$

In the example of **Fig. 3.2a**, the thickness of layers 1 and 2 diffuse to the right and left respectively.

In the model, diffusivity κ does not vary in the vertical, so the diffusive thickness flux within each isopycnal layer (apart from the densest) is given by

$$h\mathbf{u}^* = -\kappa \nabla_H h \tag{3.3}$$

where h is the layer thickness. The value of κ varies with L, the (x,y) dimension of model grid-boxes: $\kappa = u_d L$, where u_d, the "thickness diffusion velocity", is a constant, nominally chosen to be 1.0 cm s^{-1} at the present 1° resolution. This parameterization yields a typical value for κ of 1000 $m^2 s^{-1}$. Within the abyssal layer (the lower interface of which follows topography) Eqn. (3.3) is modified to

$$h_{abyss}\, \mathbf{u}^*_{abyss} = \kappa \nabla_H \eta \tag{3.4}$$

where η is the depth of the abyssal layer upper interface and $\mathbf{u}^*_{abyss}$ is the velocity associated with diffusion of abyssal layer thickness, h_{abyss}. In the two dimensional example of **Fig. 3.2b**, layer interface diffusion thus acts to flatten the interface between the two layers in case (A), but has no impact on the already flattened interface in case (B) - i.e., the non-zero lateral abyssal layer thickness gradient in case (B) does *not* imply thickness diffusion.

3.1.3 Model configuration

In 1991 MICOM was implemented at the James Rennell Centre (Southampton, UK) as the Atlantic Isopycnic Model (AIM - see New *et al.* 1995), essentially the same model used here. In order to include the Greenland-Iceland-

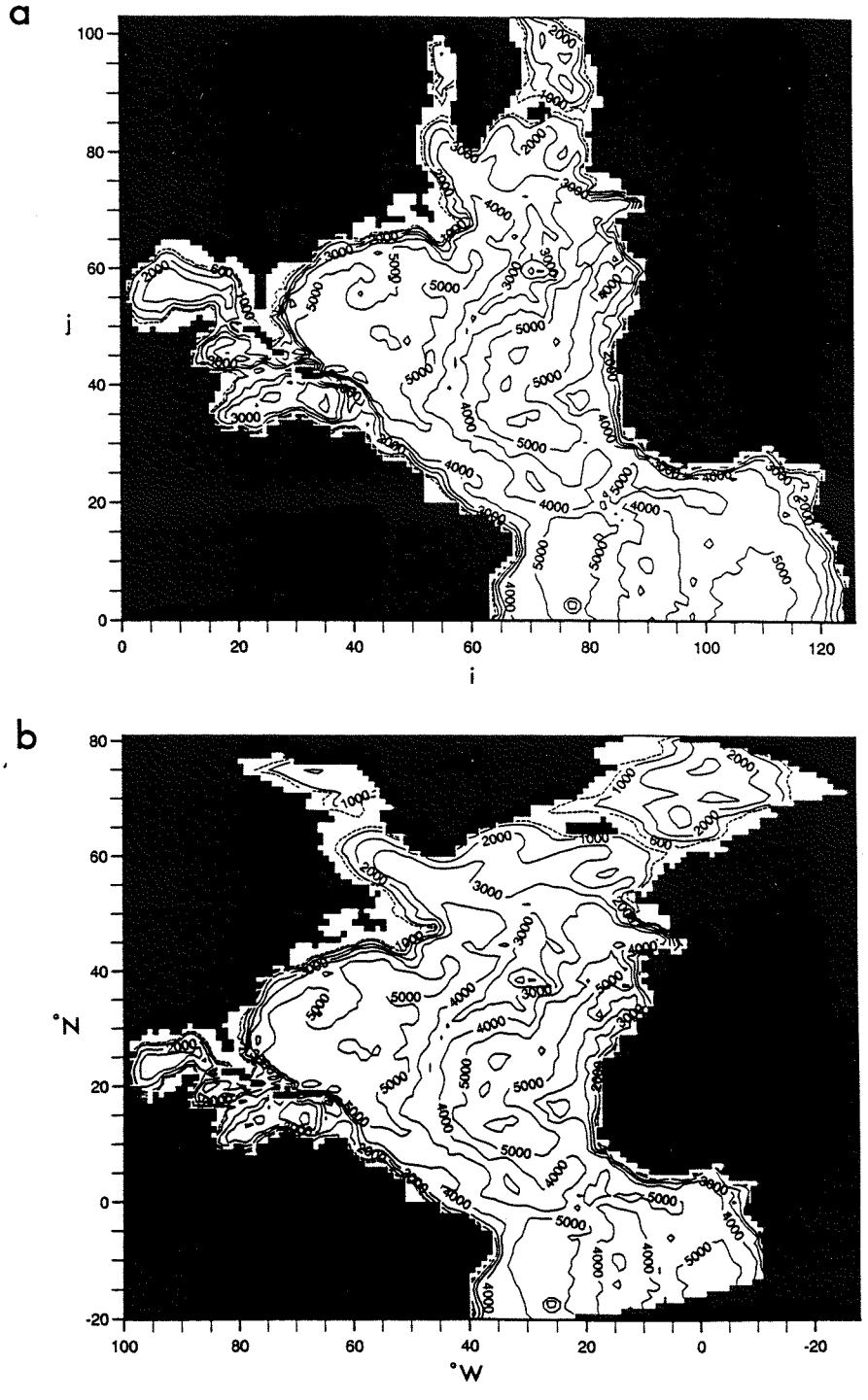

Figure 3.3: The model bathymetry (a) on the rotated grid, (b) "backrotated" to an equatorial Mercator projection.

Norwegian Sea, AIM extends to around 80°N. At such high latitudes, the zonal gridbox dimension on a grid of constant longitude-latitude resolution (based on an equatorial Mercator projection) is around 20% of that at the Equator.

This strong poleward distortion of gridbox size severely constrains Δt_{max}, the maximum permissible model timestep. Under the forward-backward time-differencing scheme of MICOM (Bleck *et al.* 1992), the Courant-Friedrichs-Lewy stability criterion stipulates $\Delta t_{max} = \Delta x_{min}/c_{max}$, where Δx_{min} is the minimum discretized length scale and c_{max} is the speed of the fastest waves in the system. In the ocean, gravity waves travel fastest, with a depth-dependent phase speed, $c_{max} = \sqrt{gH}$, where H is depth. In water of depth 4000 m, such gravity waves travel at around 200 m s^{-1}. On a 1° x 1° equatorial Mercator projection the zonal gridbox dimension at 80°N is ~15 km. On such a grid the maximum permissible timestep is therefore ~75 s, which is prohibitively short.

To alleviate this problem, the model grid is based on a rotated Mercator projection, ranging approximately from 15°S to 82°N, with a horizontal resolution of around 1°. **Fig. 3.3** (from New *et al.* 1995) shows how the rotated grid is related to the original Mercator projection. **Fig. 3.3a** shows the model bathymetry (derived from the Scripps 1° depth database) on the rotated grid, while **Fig. 3.3b** is a "backrotation" [all subsequent plots of model fields are shown on the rotated grid, with a 10° x 10° latitude-longitude grid overlaid]. The model grid has been rotated through 90° anticlockwise, about the point 40°W on the Equator. The "equator" and north/south "poles" of the rotated grid thus lie along the "true" 40°W meridian and at 130°W/50°E respectively. The rotated grid has a much more limited "north-south" (pseudo east-west) range and hence considerably less overall distortion of gridbox dimension, allowing a reasonably long barotropic timestep of 180 seconds to be used.

Vertically, the model comprises 20 layers. Beneath the Kraus-Turner-type mixed layer (index 1) nineteen isopycnic layers (index 2 to 20) represent the ocean interior, with σ_θ increasing from 25.65 (layer 2) to 27.75 (layer 16) in intervals of 0.15, thereafter increasing from 25.75 to 28.15 (layer 20) in intervals of 0.10 - see **Table 3.1**. In presenting the results, emphasis is on changes to STMW layers 7-10 (with σ_θ of 26.40, 26.55, 26.70 and 26.85 respectively).

The Levitus (1982) dataset is used to obtain a hydrographic initial state comprising three-dimensional descriptions of layer thickness, temperature and salinity for September (discussed in New *et al.* 1995). Layer interfaces correspond

with the depths of surfaces which have densities halfway between the densities of the layers above and below the particular interface. **Fig. 3.4** shows basin-mean profiles of thickness and potential density, obtained by averaging initial model thickness fields and the Levitus data respectively. The two profiles, though directly related, appear rather different. The deepest levels (4000 to 6000 m) in the Levitus dataset are represented by relatively small areas of the basin. The mean thickness profile of AIM reaches only to 3600 m (the basin-mean depth), but more clearly represents thin, dense abyssal layers. The initial mixed layer density of AIM is set to 25.50 everywhere, while lighter near-surface water is apparent in the Levitus dataset.

Table 3.1 Model layer indices, densities and water masses

Layer index	Layer density (σ_θ)	Water mass
1	arbitrary	mixed layer/surface
2	25.65	
3	25.80	
4	25.95	
5	26.10	
6	26.25	
7	26.40	light 18° Water
8	26.55	dense 18° Water
9	26.70	Central Atlantic STMW
10	26.85	Eastern Atlantic STMW
11	27.00	Northeast Atlantic STMW
12	27.15	Subpolar Mode Water (SPMW)
13	27.30	SPMW
14	27.45	SPMW
15	27.60	light Labrador Sea Water
16	27.75	dense Labrador Sea Water
17	27.85	North Atlantic Deep Water
18	27.95	Denmark Straits Overflow Water
19	28.05	Greenland Sea Deep Water
20	28.15	

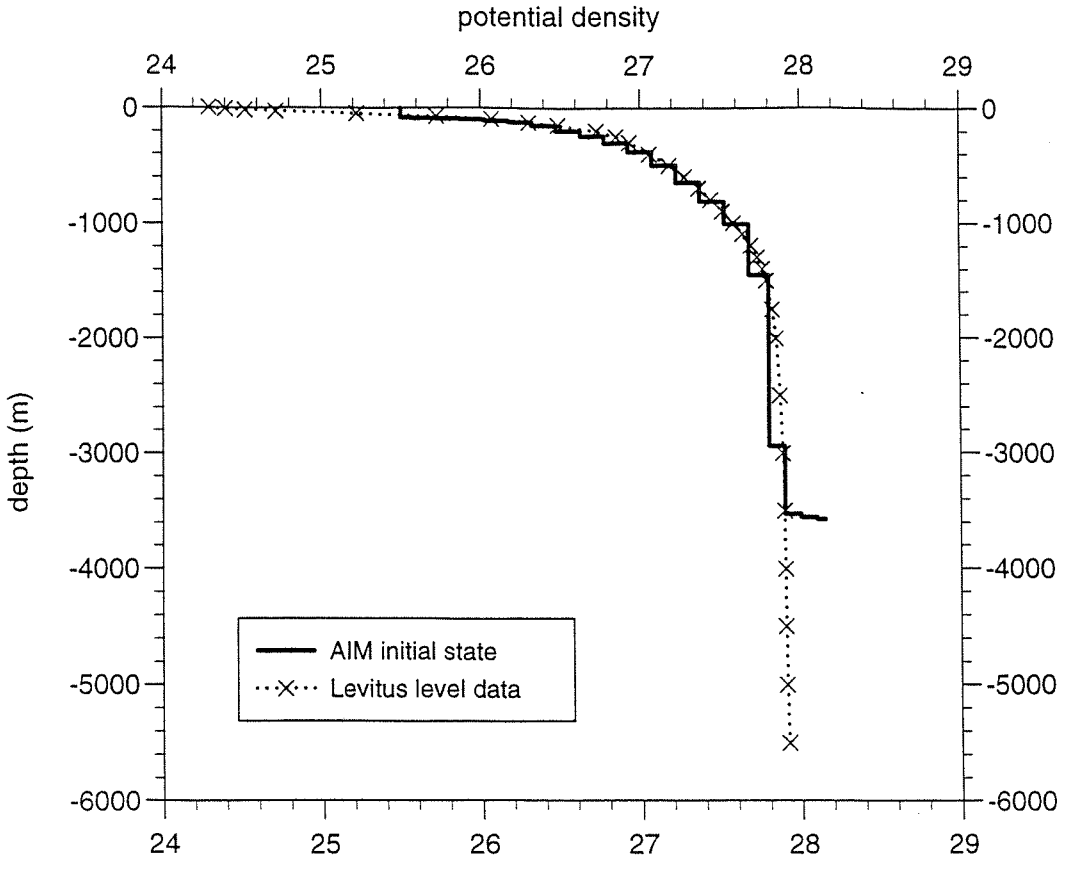

Figure 3.4: Basin-mean profiles: initial model layer thickness and Levitus (1982) potential density.

3.1.4 Climatological forcing

The model is forced with monthly mean climatological fluxes [Hellerman and Rosenstein (1983) wind stress, Esbensen and Kushnir (1981) heat fluxes and evaporation rate, Jaeger (1976) precipitation rate], but to maintain realism in surface distributions of heat and salt it is also necessary to relax the sea surface temperature and salinity to monthly mean climatological values (Levitus 1982). The method used here is similar to that of Haney (1971), although a fixed relaxation coefficient, λ, is used. The surface heat and freshwater fluxes applied to the model, Q and E-P, are formulated as

$$Q = Q_{obs} + \lambda\left(T_{obs} - T\right) \tag{3.5a}$$

$$E - P = (E - P)_{obs} + \frac{\lambda}{C_p \rho}\left(\frac{S_{obs}}{S} - 1\right) \tag{3.5b}$$

where, in the model, Q is the net heat flux (the sum of radiative, latent and sensible fluxes of heat, taken to be positive *into* the ocean), E-P is the net freshwater flux (evaporation minus precipitation), and T and S are mixed layer (surface) temperature and salinity; Q_{obs}, $(E-P)_{obs}$, S_{obs} and T_{obs} are corresponding climatological values; and λ is constant at 35 Wm^{-2} K^{-1}, a value consistent with climatological estimates (Barnier *et al.* 1995).

3.2 Experimental design

3.2.1 The experiments

The spun-up response of the model ocean to climatological forcing is established in expt. CLIM1, which then serves as a control experiment. All subsequent sensitivity experiments begin after 20 years of spin-up. Excess Gulf Stream buoyancy loss over five consecutive years (typical of the NAO-minimum 1960s) is applied in expt. COOL1. The sensitivity of the model to a different degree and distribution of anomalous cooling and evaporation is investigated in expts. COOL2 and COOL3.

The effects of eddies on thermocline PV anomalies is parameterized by the layer thickness diffusion velocity. The dependence on this parameter of the model response to intense cooling and evaporation (as COOL3) is addressed with experiment pairs LOMIX and LOMIXCOOL, HIMIX and HIMIXCOOL (all started from a 20-year spinup of revised control expt. CLIM2).

The role of anomalous wind forcing is addressed with expt. NAOWIND, in which idealized NAO-minimum wind forcing is applied for five years (after the 20-year spinup of CLIM1). All model experiments are summarized in **Table 3.2.**

3.2.2 Logistical considerations

During 1992-95 (expts. CLIM1, COOL1, COOL2, COOL3 and NAOWIND) the model was implemented and integrated on the (then) Cray-YMP supercomputer of the Rutherford Appleton Laboratory. Thereafter (experiments from 1997 onwards), further Cray time was unavailable, but local Silicon Graphics (SGI) workstations by then offered a viable alternative. Although slower, the SGI workstation was sufficiently fast to complete the necessary experiments. While machine precision differs (between the Cray-YMP and SGI), identically configured

and forced experiments produced visually indistiguishable model fields after 20 years of spin-up - e.g., SST was identical to two decimal places everywhere on the model grid. Given the machine FLOPS (FLoating-point Operations Per Second), speeds of model integration were respectively:

(a) 8 hours per model year on the Cray-YMP

(b) 60 hours per model year on the SGI workstation

Table 3.2: A summary of the model experiments in this study.

Model Run	Years integrated	Attributes	Year completed
CLIM1	1-30	MICOM version 2 without diapycnal mixing, climatologically-forced	1992
COOL1	21-30	CLIM1 continued, with idealized excess Gulf Stream wintertime buoyancy loss over years 21-25, followed by year-round climatological buoyancy forcing in years 26-30	1993
COOL2	21	as COOL1 year 21, but with excess buoyancy loss spread over a wider area	1994
COOL3	21	as COOL1 year 21, but doubling the excess buoyancy loss	1994
CLIM2	1-30	MICOM version 2 with diapycnal mixing, climatologically-forced	1997
LOMIX	21	CLIM2 continued, but with thickness diffusion decreased by a factor of 10	1998
LOMIXCOOL	21	as LOMIX, with the excess buoyancy loss of COOL3	1998
HIMIX	21	CLIM2 continued, but with thickness diffusion increased by a factor of 10	1998
HIMIXCOOL	21	as HIMIX, with the excess buoyancy loss of COOL3	1998
NAOWIND	21-30	CLIM1 continued, with idealized NAO-minimum monthly wind forcing over years 21-25, followed by climatological wind forcing over years 26-30	1995

Another important requirement was that both the Cray-YMP and the SGI workstation provided sufficient core memory to integrate the model without using the "swap-disc" (which would severely limit model integration time).

A "PAKK-ed" binary format was used to compress the three-dimensional datasets used in model analysis and restart. The sizes of each dataset routinely saved (for analysis every month, and for restarting at the end of each year respectively) were as follows:

(a) 2.7 and 7.5 Mbytes on the Cray-YMP,

(b) 21.8 and 60.4 Mbytes on the SGI workstation.

Excluding the spin-up phases, all monthly datasets used in analysis amounted to a total of 7.8 Gbytes, which was further compressed, to typically 20% original file size, for storage on a RAID (Redundant Array of Independent Discs) facility. The model runs outlined above took 416 hours on the Cray-YMP and 2040 hours on the SGI workstation - a grand total six months of computer time. The model code and diagnostic progams were written in FORTRAN. All plots of model data are generated with FORTRAN programs which call UNIRAS subroutines.

3.3 Routine diagnostic methods

To assess the model response to anomalous forcing, "off-line" diagnostics are routinely computed from the basic monthly fields of model output. "Snapshots" of large-scale horizontal circulation are obtained with fields of barotropic streamfunction and Montgomery potential. A field of annual subduction rate reveals where thermocline layers are ventilated, and can be area-integrated to obtain water mass formation rates. The potential vorticity of mode water layers is computed for comparison with observed values. Meridional recirculation of water masses is revealed by the overturning streamfunction in density space. Details of these diagnostics are as follows.

3.3.1 The barotropic streamfunction

Depth-integrated currents represent the barotropic mode of circulation in MICOM. If the field of barotropic velocity (eastward and northward components u_{baro} and v_{baro} respectively) satisfies a continuity equation,

$$\frac{\partial u_{baro}}{\partial x} + \frac{\partial v_{baro}}{\partial y} = 0 \qquad (3.6)$$

then the flow is non-divergent, and a barotropic streamfunction, ψ_{baro}, can be defined:

$$u_{baro} = -\frac{\partial \psi_{baro}}{\partial y} \tag{3.7a}$$

$$v_{baro} = \frac{\partial \psi_{baro}}{\partial x} \tag{3.7b}$$

Now the relative vorticity of the barotropic circulation, ζ, is defined as:

$$\zeta = \frac{\partial v_{baro}}{\partial x} - \frac{\partial u_{baro}}{\partial y} \tag{3.8}$$

and so, substituting Eqns. (3.7a,b) in Eqn. (3.8) yields a Poisson equation for ψ_{baro}:

$$\frac{\partial^2 \psi_{baro}}{\partial x^2} + \frac{\partial^2 \psi_{baro}}{\partial y^2} = \zeta(x, y) \tag{3.9}$$

As a boundary condition, $\psi_{baro} = 0$ along model "continental" coastlines. The three model islands of Cuba, Hispaniola and Iceland are therefore "submerged" by 1 mm to force ψ_{baro} very close to zero at island gridpoints. Eqn. (3.9) is then solved iteratively for ψ_{baro}, using a successive overrelaxation (SOR) Poisson solver (available as a diagnostic module of MICOM).

3.3.2 The Montgomery potential

Montgomery (1937) defined the horizontal geostrophic flow on a surface of constant specific volume anomaly ($\alpha = \rho^{-1}$) in terms of a streamfunction which has become known as the Montgomery potential, M (equivalent to a Bernoulli function). For the case of a continuously stratified ocean, M is given by:

$$M = gz + \int_{p(0)}^{p(z)} \alpha dp \tag{3.10}$$

where g is gravitational acceleration and $p(z)$ is the pressure at depth z. The Montgomery potential is central to MICOM, appearing as $-\nabla M$ (the horizontal pressure force term) in the layer-integrated horizontal momentum equation (Bleck *et al.* 1992). Model layer streamfunctions are obtained as fields of layer Montgomery potential, M_k:

$$M_k = gz_k + \frac{\frac{1}{2}(p_k - p_{k-1})}{\rho_k} + \sum_{kl=1}^{kl=k-1} \frac{p_{kl} - p_{kl-1}}{\rho_{kl}} \qquad (3.11)$$

which incorporates gz_k, the geopotential of the layer (where the mid-point of the layer is at depth z_k), and the integrated effect of overlying layers (where p_{kl} and ρ_{kl} are the base pressure and density of overlying layer kl).

3.3.3 The annual subduction rate

Marshall *et al.* (1993) define an annual subduction rate, S_{ann}, due to the combined annual-net effects of "lateral induction" (horizontal advection of fluid across a sloping end-of-winter mixed layer base) and Ekman pumping:

$$S_{ann} = -\left(\overline{w_H} + \overline{\mathbf{u}_H.\nabla H}\right) \qquad (3.12)$$

where $\overline{w_H}$ and $\overline{\mathbf{u}_H.\nabla H}$ are annual mean vertical velocities across the level of deepest winter mixing (H) due to purely vertical motion and implied by lateral induction of fluid (moving along isopycnals) respectively. [Subduction is defined as positive downwards, hence the negative sign which preceeds the summation in (3.12)]. Eqn. (3.12) can be used to diagnose subduction rates in the model, using monthly datasets to determine annual means. The lateral induction rate, $\overline{\mathbf{u}.\nabla H}$ is well aproximated using monthly data, $\overline{\mathbf{u}.\nabla H} \approx \frac{1}{12}\sum_{m=1,12} \mathbf{u}.\nabla H$.

Calculation of w_H (defined at the depth H, and therefore not a prognostic variable in the model) can be obtained by vertical interpolation of the vertical velocities implied by integrated horizontal mass fluxes. Alternatively, w_H can be estimated from the linearized vorticity balance, $\beta v = f\,\partial w/\partial z$ [where β is the meridional variation of f], vertically-integrated and discretized as follows:

$$\frac{f}{\beta}\left(w_{Ek}-w_H\right)=h_1 v_1'+\sum_{k=2}^{K-1}h_k v_k+\left[H-\sum_{k=1}^{K-1}h_k\right]v_K \tag{3.13}$$

where h_k and v_k are the thickness and meridional velocity component of layer k, $w_{Ek}=curl_z\left(\boldsymbol{\tau}/f\rho_o\right)$ is Ekman pumping at the ocean surface ($\boldsymbol{\tau}$ is the surface wind stress), and, in the mixed layer, $v_1'=v_1-v_{Ek}$, where v_{Ek} is the meridional velocity component of Ekman drift. This estimate of w_H neglects non-linear effects and friction, both of which play an important role in the western boundary current. However, the subduction zone is away from boundaries (i.e., friction is weak) where circulation is slower (i.e., non-linear effects are weak), so Eqn. (3.13) should provide accurate estimates of w_H.

3.3.4 Water mass formation rates

Qiu and Huang (1995) obtain water mass net conversion (formation) rates for the North Atlantic and North Pacific by area-integrating and density-partitioning ventilation rates [diagnosed using the Levitus (1982) and Hellerman and Rosenstein (1983) climatologies]. A similar method can be applied to the model. For model layer k, an annual change in volume (essentially the layer formation rate in Sv year^{-1}), ΔV_k, is estimated by integrating S_{ann} over the end-of-winter outcrop of that layer:

$$\Delta V_k=\frac{1}{year}\sum_{i,j}\Delta A_{i,j}S_{ann,i,j}\Lambda\left(\sigma_{\theta,k},\sigma^W_{i,j,kout}\right) \tag{3.14}$$

where $\Delta A_{i,j}$ is the surface area of gridbox (i,j), and $\Lambda\left(\sigma_{\theta,k},\sigma^W_{i,j,kout}\right)$ is a sampling function, which takes the value

$$\Lambda\left(\sigma_{\theta,k},\sigma^W_{i,j,kout}\right)=\begin{cases}1 & \text{if } \sigma_{\theta,k-1}\le\sigma^W_{i,j,kout}\le\sigma_{\theta,k}\\ 0 & \text{otherwise}\end{cases}$$

and $\sigma^W_{i,j,kout}$ is the density of the uppermost finite-thickness interior layer (in other words, the density of the outcropping layer, index *kout*) at the end-of-winter, defined in the month when mixed layer depth is maximum (generally March).

3.3.5 Sverdrupian potential vorticity

McCartney (1982) establishes the value of "Sverdrupian" potential vorticity (PV) as a useful diagnostic in mode water studies. PV minima in upper ocean vertical profiles are taken to define mode water "core depths". The Sverdrupian PV of a model layer k is here defined as:

$$q_k = \frac{f}{\rho_o}\frac{\Delta\sigma_\theta}{h_k} \tag{3.15}$$

where f is the Coriolis parameter, ρ_o is the mean density of seawater, $\Delta\sigma_\theta$ is the density interval across a given layer ($\Delta\sigma_\theta = 0.15$ in the thermocline of the model subtropical gyre), and h_k is the thickness of that layer.

3.3.6 The meridional streamfunction in density space

In a GCM study of the North Atlantic heat balance, Bryan and Sarmiento (1984) introduce $\psi(\Theta,\sigma)$, the overturning streamfunction as a function of latitude Θ and arbitrary density σ, in principle providing a direct relation between the circulation and transformation of water masses (further elaborated in §6.1). Following the same approach, the model overturning is computed here as a function of layer density, σ_k:

$$\psi(\Theta,\sigma_k) = \sum_{k}^{20}\sum_{east}^{west}\left\{\Pi(\sigma_k,\sigma_{i,j,1})h_{i,j,1}\left(\bar{v}_{i,j,1}+v^*_{i,j,1}\right)+h_{i,j,k}\left(\bar{v}_{i,j,k}+v^*_{i,j,k}\right)\right\}\Delta x_{i,j} \tag{3.16}$$

where $h_{i,j,k}$ is the thickness, $\bar{v}_{i,j,k}$ and $v^*_{i,j,k}$ are meridional components of mean and "bolus" currents, of layer k at gridpoint (i,j), $\Delta x_{i,j}$ is an east-west length-scale for gridpoint (i,j), and $\Pi(\sigma_k,\sigma_{i,j,1})$ is a mixed layer sampling function (which includes mixed layer transports in the integration if mixed layer density, $\sigma_{i,j,1}$, falls in the range of density represented by layer k). Interpretation of $\psi(\Theta,\sigma)$ in terms of water mass transformation rests on an implicit assumption of water mass steadiness. Water mass *unsteadiness* in a global implementation of MICOM has been evaluated by Nurser and Marsh (1998), and is taken into consideration in the present model (see §6.1.1 and §6.1.2).

3.4 Historical datasets

Historical datasets (summarized in **Table 3.3**) were obtained, archived, and used (with permission of their originators) to both guide the design of idealized surface forcing for sensitivity experiments, and - in the case of the SOC flux data - to further (and separately) diagnose recent variability in transformation and meridional circulation of water masses.

Table 3.3 Historical datasets used in this study

Dataset name and source	Variables used	spatial coverage and resolution	Time span and frequency
land/sea surface temperature climatology (CRU*)	surface temperature (SST over oceans)	global, 5° x 5°	1854-1991 monthly
air-sea flux climatology (SOC**)	net heat flux, evaporation, precipitation	global, 1° x 1°	1980-1997 monthly
land/sea surface pressure climatology (CRU*)	sea level pressure	25-75°N, 10° longitude x 5° latitude	1873-1991 monthly

* CRU = Climatic Research Unit, University of East Anglia, Norwich, UK.

** SOC = Southampton Oceanography Centre, Southampton, UK.

3.4.1 Surface air temperature anomalies

Jones and Briffa (1992) have compiled a monthly time series (for 1854-1991) of global (5°x5° resolution) surface air temperature anomalies (referred to monthly means over 1950-79). Maps of mean wintertime temperature anomalies in the North Atlantic region for selected winters show the spatial characteristics of cold outbreaks - e.g., **Fig. 3.5** shows large negative temperature anomalies in the southeastern United States during the particularly severe winter of 1977.

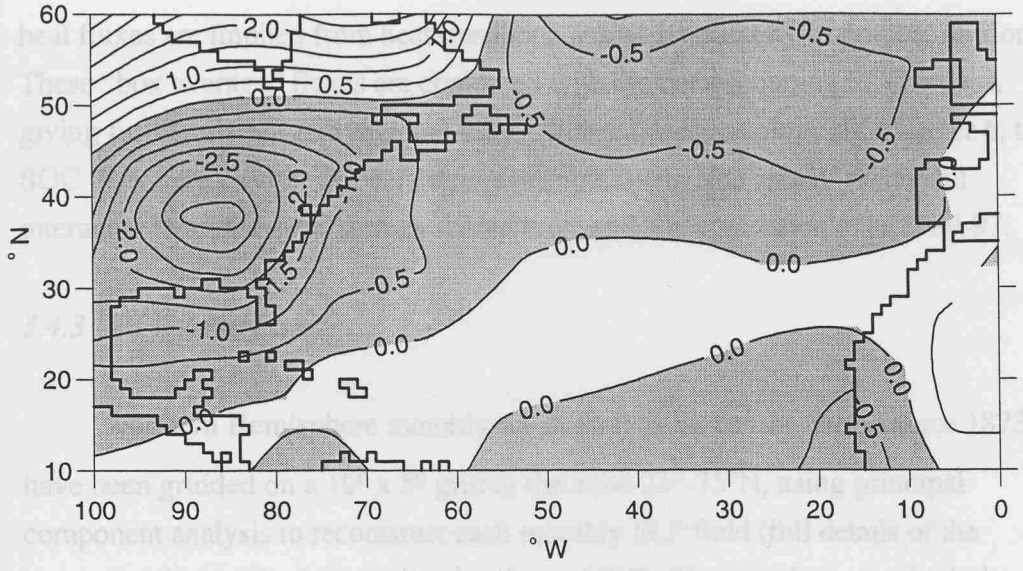

Figure 3.5: January/February 1977 surface temperature anomaly in the North Atlantic sector.

3.4.2 Sea surface heat and freshwater fluxes

A new global air-sea heat flux climatology has been generated at the Southampton Oceanography Centre (SOC) from an enhanced version of the Comprehensive Ocean Atmosphere Dataset 1a (COADS1a, Woodruff *et al.* 1993). COADS1a comprises marine meteorological reports spanning the period 1980-93 (a further four years of COADS data, spanning 1994-97, was subsequently available for the present study). The global distribution of ship reports is spatially inhomogeneous (Woodruff *et al.* 1993), with a relatively large number of observations in the mid-latitude North Atlantic and North Pacific but very few in the Southern Hemisphere.

The SOC climatology features several improvements on past studies, in both generation and analysis of the climatology. For the first time, individual ship meteorological reports have been corrected for biases arising from variations in observing procedure (Kent *et al.* 1993). Furthermore, the results of several supporting studies have been used to justify the choice of visual wind estimate conversion scale (Kent and Taylor 1997), the longwave flux formula (Josey *et al.* 1997) and the "sampling" method employed to average the flux fields (Josey *et al.* 1995).

Josey *et al.* (1999) describe the evaluation of the SOC climatology. The accuracy of the individual monthly flux fields is assessed by comparing SOC fluxes with high quality research buoy measurements at several climatically different locations. To assess integral effects, regionally-averaged mean surface

heat fluxes are implied from heat transports across adjacent hydrographic sections. These "box average" fluxes are compared with the corresponding SOC values, giving further insight into regional biases within the climatology. In Chapter 6, the SOC fluxes are used in a novel calculation, to examine the annual-mean and interannual variability of surface-forced thermohaline circulation over 1980-97.

3.4.3 Sea level pressure

Northern Hemisphere monthly-mean SLP fields for the period since 1873 have been gridded on a 10° x 5° grid in the zone 25°-75°N, using principal component analysis to reconstruct each monthly SLP field (full details of the reconstruction method are outlined in Jones 1987). The raw data, on which these reconstructions are based, are extracted from land weather station records and historical weather charts, archived at the United Kingdom Meteorological Office. Mean wintertime anomalous SLP maps reveal patterns such as that associated with a low NAO index - e.g., **Fig. 3.6** shows a belt of anomalously low pressure across mid-latitudes throughout the winter of 1976-77, when unusually cold continental air reached the southeastern US and the Gulf Stream (**Fig. 3.5**). Wind stress patterns computed from composited anomalous SLP fields are used to guide the design of idealized NAO-minimum wind forcing, which is subsequently applied to the model (see §7.1).

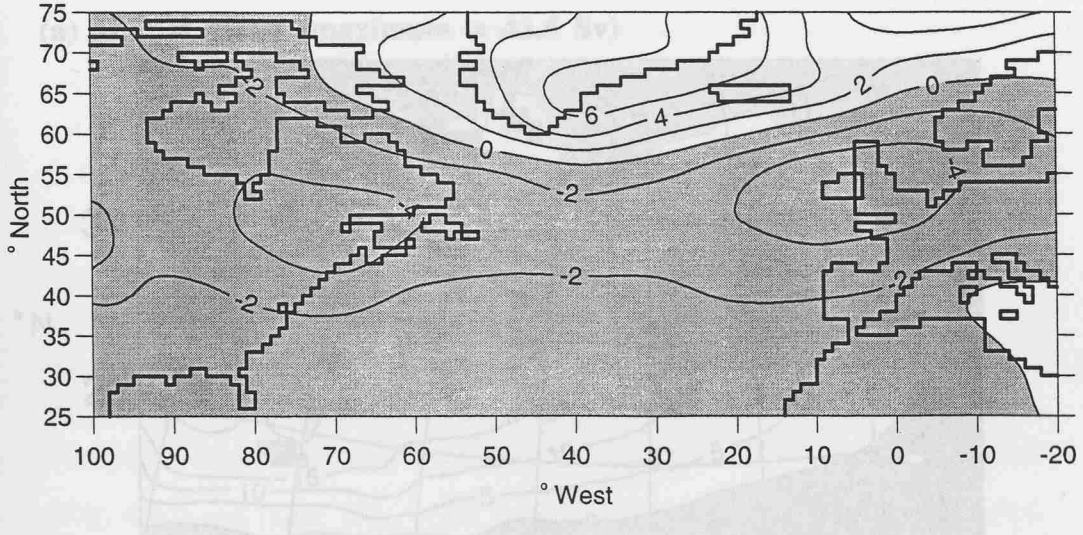

Figure 3.6: December-April 1976/77 SLP anomaly (mb) field in the North Atlantic sector (obtained by subtracting climatological SLP).

CHAPTER 4. CONTROL EXPERIMENT AND BUOYANCY FLUX SENSITIVITY STUDIES: 18° WATER VARIABILITY AND GULF STREAM INTENSIFICATION

This chapter outlines the 30-year control experiment (§4.1) and design of idealized anomalous buoyancy flux fields (§4.2), followed by results of buoyancy flux sensitivity experiments (§4.3), and finally a summary (§4.4) of model 18° Water variability and Gulf Stream intensification in the latter experiments.

4.1 The control experiment (CLIM1)

Spin-up and basin-wide hydrographic equilibration are broadly as described in New *et al.* (1995). In the context of this study, more detailed descriptions are made of: the barotropic circulation of the subtropical gyre; potential vorticity; evolution of the upper ocean in the model Sargasso Sea (near Bermuda); and ventilation of the subtropical gyre.

4.1.1 Subtropical gyre dynamics

Fig. 4.1a shows the annual-mean barotropic streamfunction (ψ_{baro} - see §3.3.1), in the subtropics of the model, for year 20 of CLIM1, while **Fig. 4.1b** shows the annual range in ψ_{baro} (strength of the seasonal cycle at each gridpoint).

(a) annual mean (maximum = 43.5 Sv)

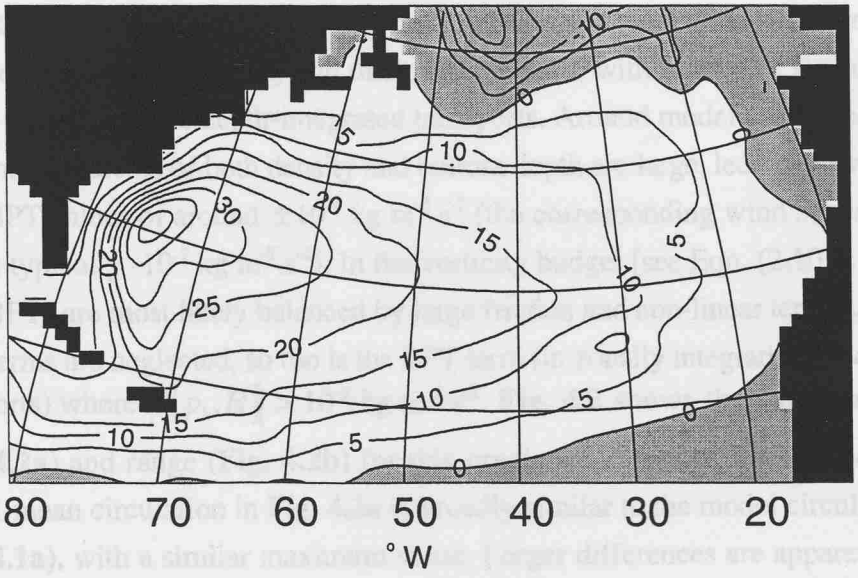

Figure 4.1: Year 20 barotropic streamfunction (Sv, C.I. = 5 Sv): (a) annual-mean, (b) annual range (continued overleaf).

(b) annual range (maximum = 23.7 Sv)

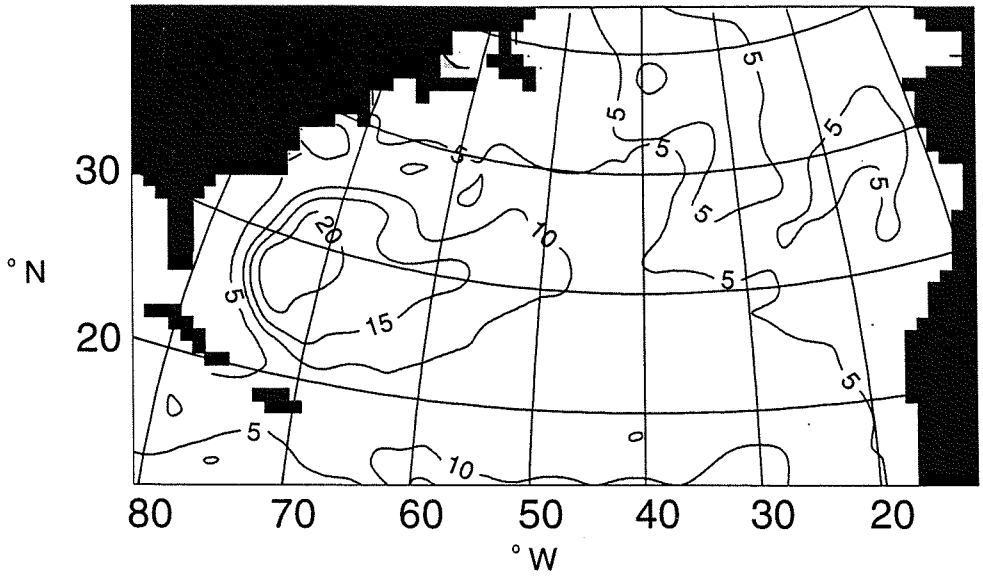

Fig. 4.1 (ctd)

Both annual-mean and range are westward-intensified. The peak range (**Fig. 4.1b**) almost coincides with the position of maximum annual-mean transport (**Fig. 4.1a**).

To determine the extent to which the large-scale circulation is driven by the combined effect of wind stress curl and bottom pressure torque (BPT), the topographic Sverdrup balance is used to predict meridional transports at each model gridpoint. These individual transports are integrated from east to west to obtain transport streamlines. Monthly fields of climatological wind stress, model sea level height, layer density and thickness are used, with Eqns. (2.11) and (2.12), to compute the depth-integrated transports. Around model coastlines, horizontal gradients of both density and bottom depth are large, leading to very large BPT values of around $\pm 10^{-4}$ kg m^{-2} s^{-2} (the corresponding wind stress curl term is typically -10^{-7} kg m^{-2} s^{-2}). In the vorticity budget [see Eqn. (2.10)], these large BPTs are most likely balanced by large friction and non-linear terms. As these terms are neglected, so too is the BPT term (in zonally integrating predicted transports) where $\left|J[p_b,H]\right| > 10^{-6}$ kg m^{-2} s^{-2}. **Fig. 4.2** shows the annual mean (**Fig. 4.2a**) and range (**Fig. 4.2b**) for this predicted transport. The predicted annual-mean circulation in **Fig. 4.2a** is broadly similar to the model circulation (**Fig. 4.1a**), with a similar maximum value. Larger differences are apparent between the respective fields of the range in transport (**Fig. 4.1b** and **Fig. 4.2b**), predicted transports varying more widely than model transports. The

particularly wide range in predicted transports off Florida (exceeding 50 Sv) reflects seasonal migration of maximum wind stress curl.

(a) annual mean (maximum = 41.7 Sv)

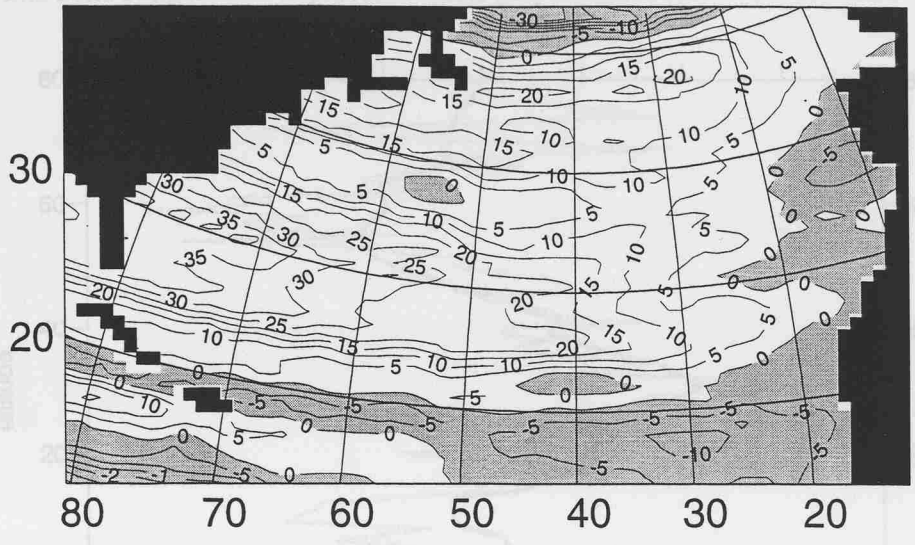

(b) annual range (maximum = 62.1 Sv)

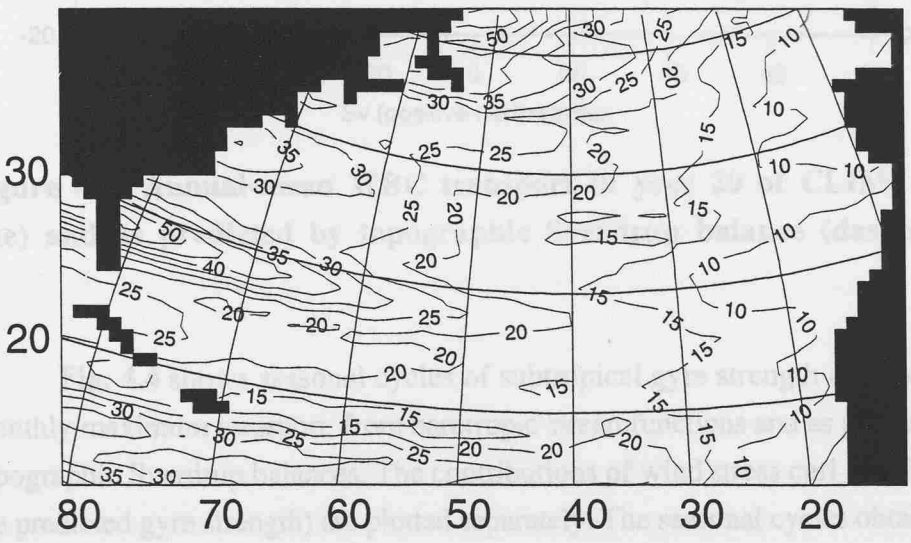

Figure 4.2: As Fig. 4.1, but predicted by the topographic Sverdrup balance.

Fig. 4.3 shows the annual-mean western boundary current (WBC) transport as a function of latitude, defined as the maxima/minima of barotropic

streamfunction at a given latitude, in year 20 of CLIM1 (solid line) and as predicted by the topographic Sverdrup balance (dashed line). The reasonably good correspondance between solid and dashed curves in the zone 25-40°N suggests that *annual-mean* WBC transport in the subtropical gyre is primarily governed by wind forcing and topography. The large discrepancies appearing north and south of this zone suggest that neglected effects play a significant role elsewhere.

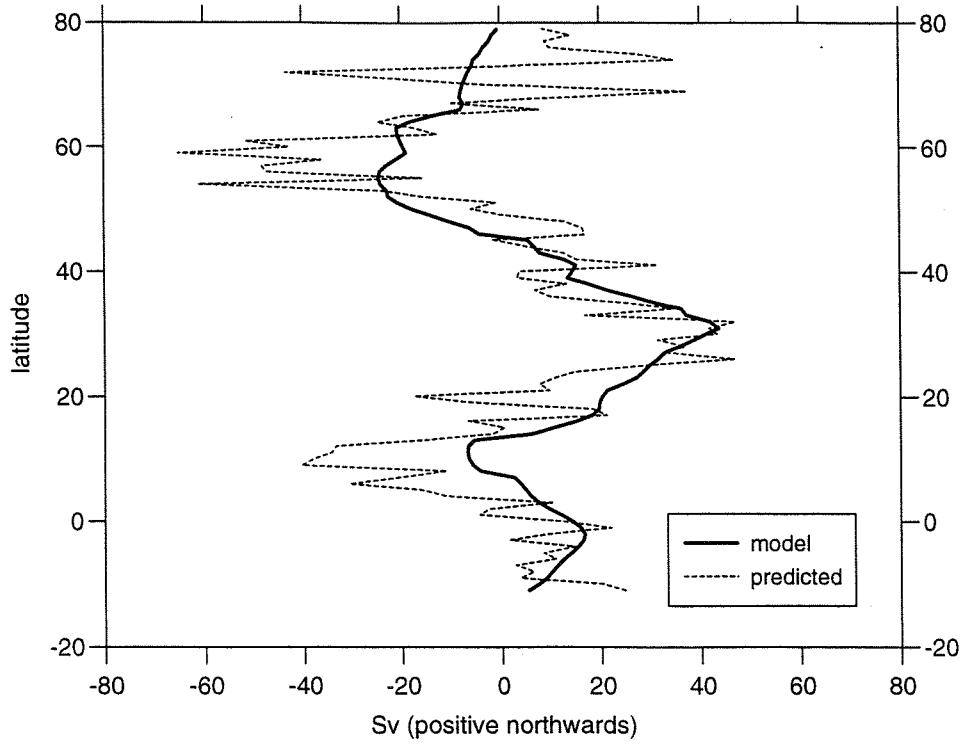

Figure 4.3: Annual-mean WBC transport in year 20 of CLIM1 (solid line) and as predicted by topographic Sverdrup balance (dashed).

Fig. 4.4 shows seasonal cycles of subtropical gyre strength obtained as monthly maximum transport, from barotropic streamfunctions and as predicted by topographic Sverdrup balances. The contributions of wind stress curl and BPT (to the predicted gyre strength) are plotted separately. The seasonal cycles obtained in the model and from the prediction are in phase with each other (reaching maxima in winter, minima in early fall), but of different amplitude (~15 Sv and ~30 Sv respectively). The seasonal cycles due to variations of the wind stress curl and BPT display larger amplitudes (~75 Sv and ~50 Sv respectively). However, the effect of BPT is to oppose the effect of wind forcing, through topographic "blocking" of the barotropic response to seasonal variation in wind stress curl (Anderson and Corry 1985). As a consequence, the predicted "net" seasonal cycle

is of relatively smaller amplitude. Because the maximum predicted gyre strength is located away from the Florida coast (see the maximum annual-mean transport in **Fig. 4.2a**), the seasonal range of this transport is somewhat smaller than the largest values seen in **Fig. 4.2b**.

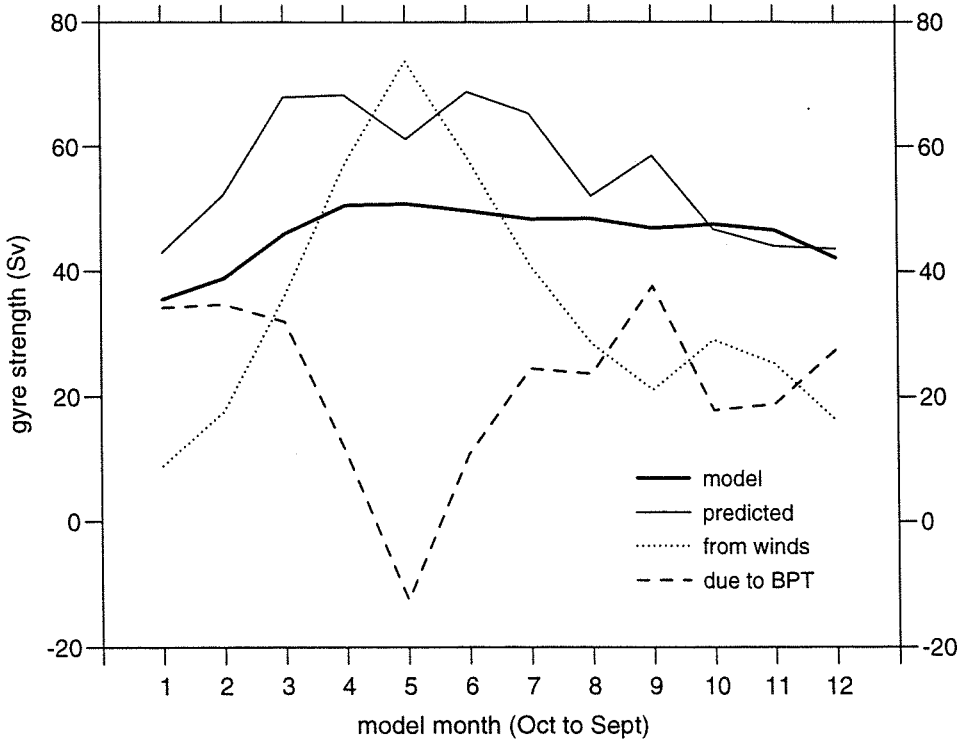

Figure 4.4: Seasonal cycles of maxima in barotropic streamfunction during model year 20 (thick solid line), and as predicted by the topographic Sverdrup balance (thin solid line) through the combined effect of wind forcing (dotted line) and BPT (dashed line).

The annual-mean WBC transport and the seasonal cycle in subtropical gyre strength are reasonably well predicted by the topographic Sverdrup balance, demonstrating that both steady state and seasonally-varying subtropical gyre circulation are *primarily* wind-driven and topographically-modified. The seasonal effect of BPT (incorporating baroclinicity) on subtropical gyre intensity is opposite to that attributed to wind stress curl, forcing maximum transports in spring and minimum transports in winter. The following sensitivity experiments will investigate the extent to which seasonal cycles in Gulf Stream transport are therefore modified by excess winter cooling and corresponding changes in baroclinicity and BPT.

4.1.2 Vorticity considerations

The extent to which PV in the subtropical gyre is approximated by "Sverdrupian" potential vorticity, q_k (see §3.3.5), depends on the dominance of planetary vorticity over relative vorticity. **Fig. 4.5** shows the field of relative vorticity for layer 7 (with σ_θ = 26.40, representative of light 18° Water) in March year 20 of CLIM1. The values in **Fig. 4.5** are generally negative (reflecting the anticyclonic circulation), reaching a minimum value of -2.17 x 10^{-6} s^{-1} near the western boundary. The majority of the gyre is characterized by weak relative vorticity, in the range $0 > \zeta > -0.5 \times 10^{-6}$ s^{-1}. Planetary vorticity, f, is positive (cyclonic) in the Northern Hemisphere, with values in the subtropics varying between ~50 x 10^{-6} at 20°N and 95 x 10^{-6} at 40°N. As a consequence, absolute vorticity, $\zeta + f$, is dominated by the planetary component, f, which increases northwards and is everywhere more than one order of magnitude greater than ζ. Insofar as $f >> \zeta$ everywhere, layer PV is well approximated by q_k.

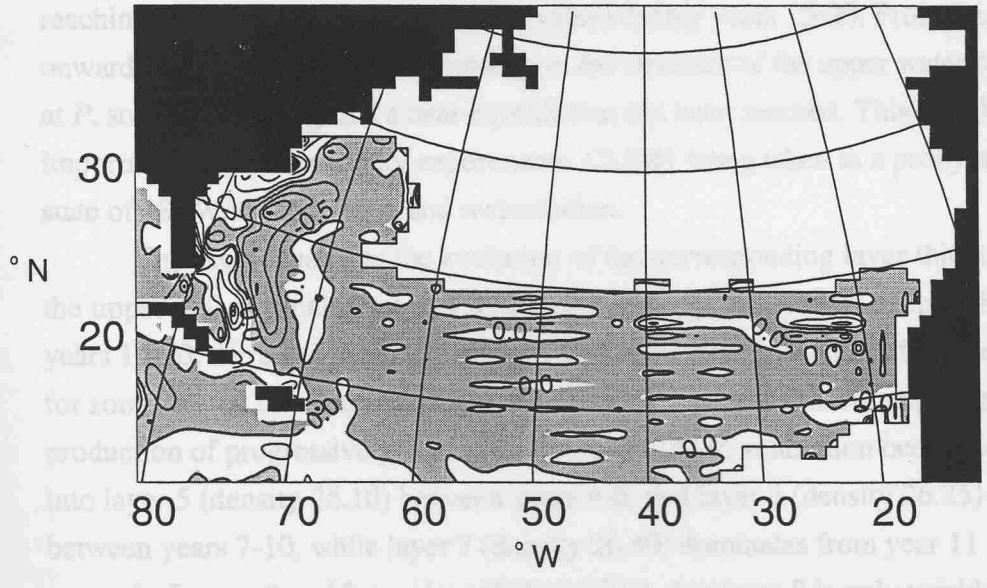

Figure 4.5: March year 20 layer 7 field of relative vorticity. The units are 10^{-6} s^{-1}, with a contour interval of 0.5 x 10^{-6} and a minimum value of -2.17 x 10^{-6} s^{-1}.

4.1.3 Spinup at Bermuda

Fig. 4.6 shows year 0-30 time series at the model *Panulirus* location (the rotated mesh gridbox centred on 32.5°N, 64.6°W), henceforth abbreviated to *P*. **Fig. 4.6a** shows the evolution of q_k, plotted in time-density space for comparison with **Fig. 2.22c**. Overall, the model reproduces a Sverdrupian (layer) PV minimum (50-100 x 10^{-14} cm^{-1} s^{-1}) in roughly the same density range as seen in the *Panulirus* time series (although the relatively coarse density resolution in **Fig. 4.6a** limits realism). Over years 20-30 annual-minimum PV reaches values of < 50 x 10^{-14} cm^{-1} s^{-1} (black shaded) in layer 7 (with properties closest to classical 18° Water - see **Figs. 4.6c,d**), but only in spring (after deep winter mixed layers have restratified). **Fig. 4.6a** reveals considerable evolution of mode water over the 30-year spin-up. During the first two years, the mode water at *P* (denoted by the thermocline layer with lowest PV) is of density 26.40 (corresponding to the 18° Water in the Levitus dataset used for the model initialisation). Over the next two years, the mode water evolves rapidly to lighter densities, thereafter evolving more slowly towards heavier densities, again reaching 26.40 (i.e., the climatological value) during years 15-20. From this time onwards, there is relatively little change in the structure of the upper water column at *P*, so demonstrating that a near-equilibrium has been reached. This is of key importance for the sensitivity experiments, CLIM1 being taken as a proxy steady state of 18° Water formation and recirculation.

Fig. 4.6b illustrates the evolution of the corresponding layer thickness in the upper 600 m (analagous to **Fig. 2.22b**). Initially, isopycnals deepen, but over years 10-20, there is a generally upward migration, and thickening (followed by, for some layers, thinning) of progressively deeper layers. This corresponds to the production of progressively denser mode waters. At *P*, ventilation occurs primarily into layer 5 (density 26.10) between years 4-6, and layer 6 (density 26.25) between years 7-10, while layer 7 (density 26.40) dominates from year 11 onwards. Layers 8 and 9 are also relatively thick, but layer 8 is only weakly ventilated after year 15. Layer 9 lies beyond the deepest *local* winter mixing, but is directly ventilated elsewhere.

The evolution at *P* of layer 7 and 8 potential temperature and salinity is also shown, in **Figs. 4.6c,d**. Layers 7 (σ_θ 26.40) and 8 (σ_θ 26.55) span the density range of observed 18° Water modes. Near-equilibration by year 20 is again clear, with temperatures close to 18°C and salinities close to 36.60 psu. The small seasonal cycle superposed on the layer 7 time series is due to local interaction with the mixed layer. Layer 8 is isolated from any such local interaction, and the

corresponding potential temperature and salinity in that layer therefore remain almost constant.

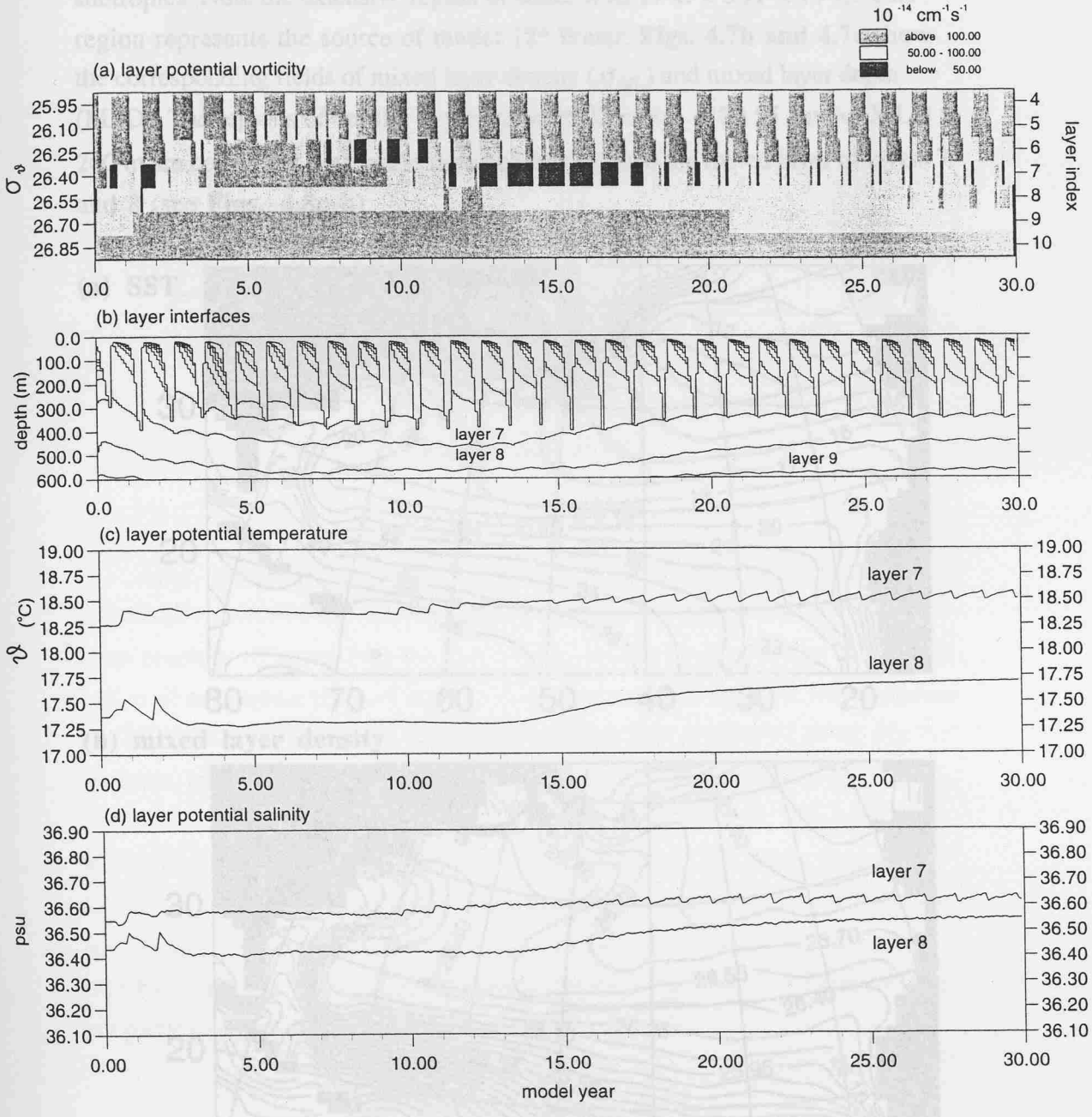

Figure 4.6: Evolution of model 18° Water at Bermuda during 30-year spinup in terms of (a) layer potential vorticity, (b) upper 600 m stratification, and (c) temperature and (d) salinity of layers 7 and 8.

4.1.4 Thermocline ventilation

Figs. 4.7-4.10 illustrate ventilation of the subtropical gyre at the end of winter (taken to be March) in year 20. **Fig. 4.7a** shows March SST in the model subtropics. Note the extensive region of water with 17°C < SST < 19°C. This region represents the source of model 18° Water. **Figs. 4.7b and 4.7c** show the corresponding fields of mixed layer density (σ_{ML}) and mixed layer depth (MLD). The regions of density in the range $26.25 < \sigma_{ML} < 26.55$, and of MLD > 200 m are coincident with wintertime outcropping into the mixed layer of layers 7 and 8 (see **Figs. 4.8a-b**).

(a) SST

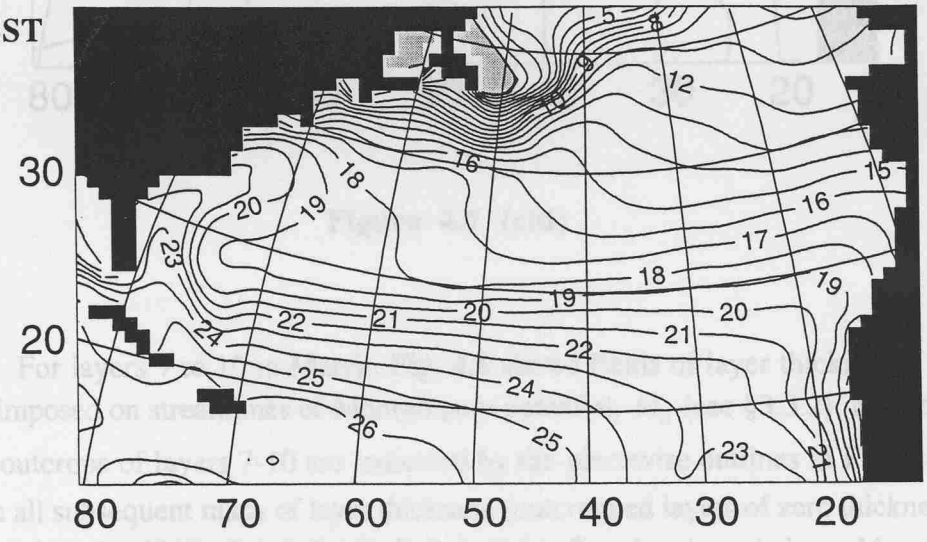

(b) mixed layer density

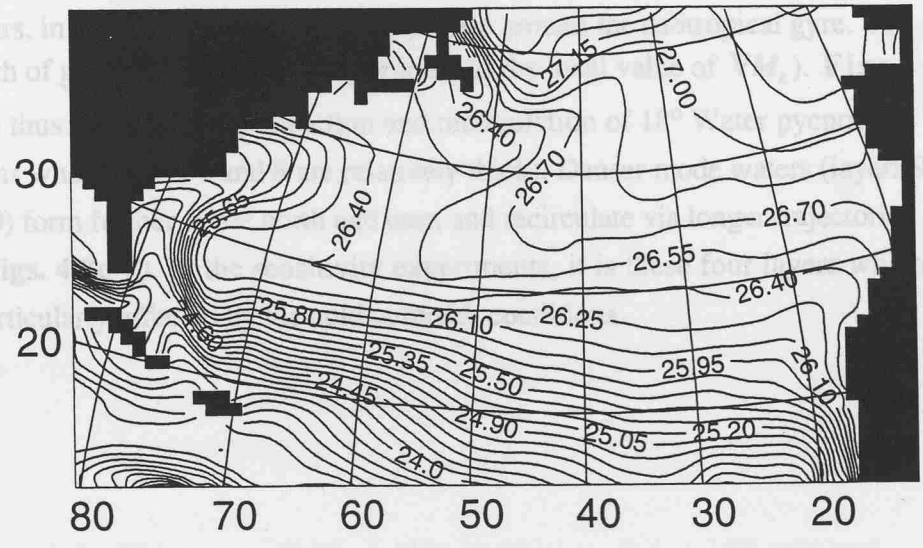

Figure 4.7: CLIM1 March year 20 fields of (a) SST (°C), (b) mixed layer σ_θ (non-dimensionalized, but equivalently kg m^{-3}), (c) mixed layer depth (m) (continued overleaf).

(c) mixed layer depth

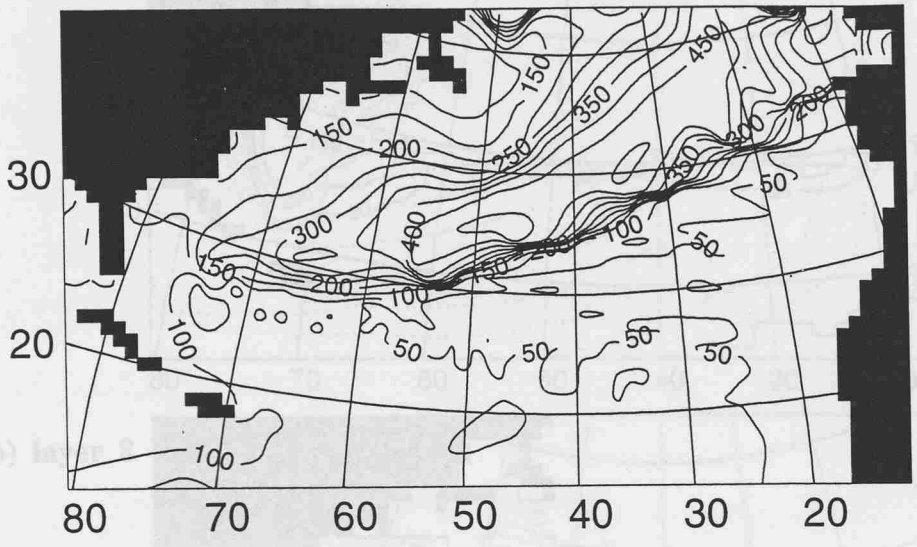

Figure 4.7 (ctd)

For layers 7 to 10 in March, **Fig. 4.8** shows fields of layer thickness superimposed on streamlines of Montgomery potential, M_k (see §3.3.2). Mixed layer outcrops of layers 7-10 are indicated by the piecewise outlines in **Fig. 4.8**, and in all subsequent maps of layer thickness (outcropped layers of zero thickness lie "in" the mixed layer base). Layer k geostrophic flow is oriented along M_k contours, in an anticyclonic (clockwise) sense around the subtropical gyre. The strength of geostrophic flow is proportional to the local value of ∇M_k). **Figs. 4.8a-b** thus illustrate the subduction and recirculation of 18° Water pycnostads (regions where layers 7 and 8 are relatively thick). Denser mode waters (layers 9 and 10) form further to the north and east, and recirculate via longer trajectories (see **Figs. 4.8c-d**). In the sensitivity experiments, it is these four layers which are particularly affected by the cold outbreak conditions.

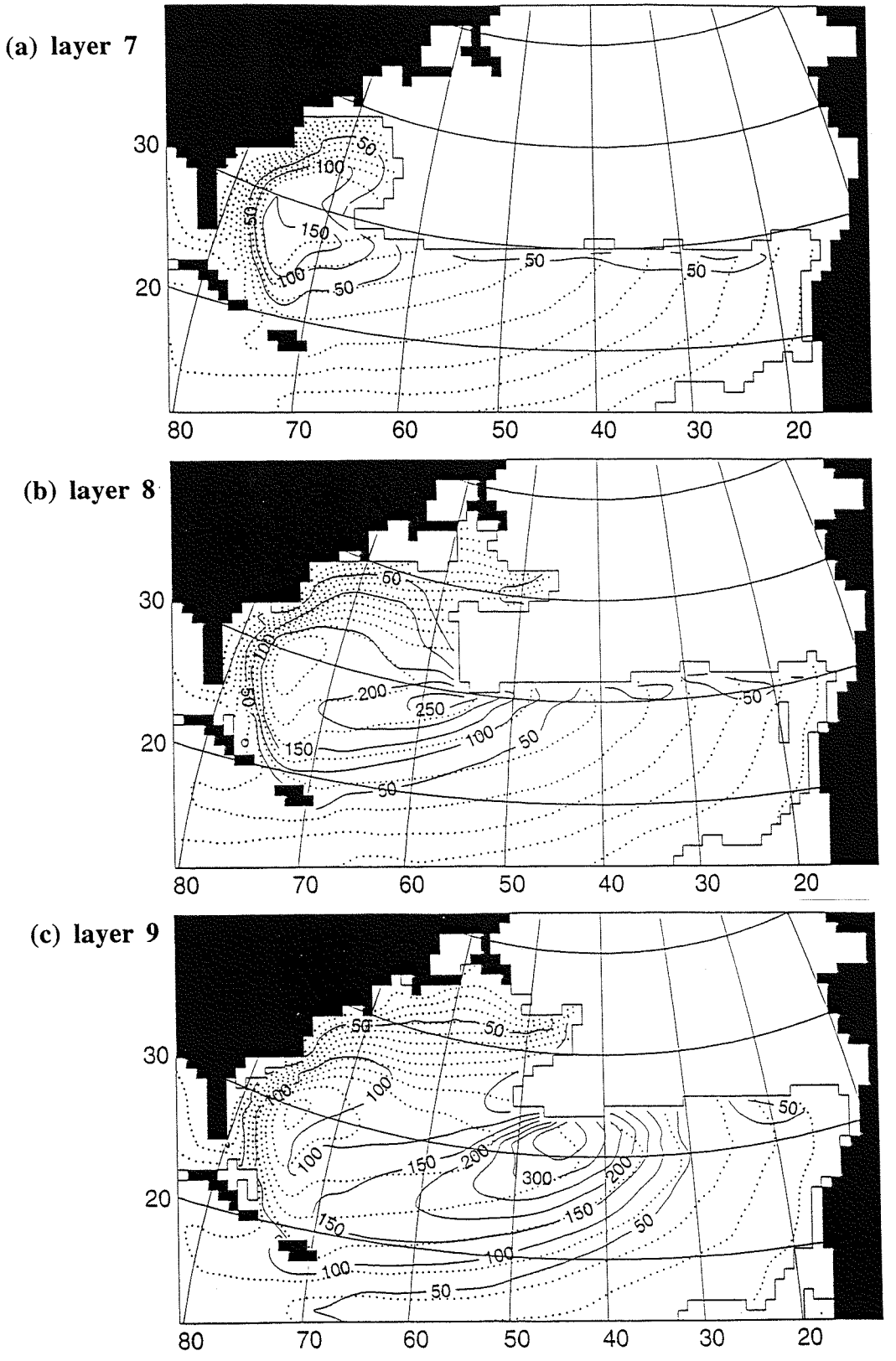

Figure 4.8: Thickness fields (solid contours, C.I. = 50 m) and Montgomery potential (dotted contours, C.I. = 0.5 m^2s^{-2}) for four mode water layers in the subtropical gyre, in March year 20 of the control experiment (continued overleaf).

(d) layer 10

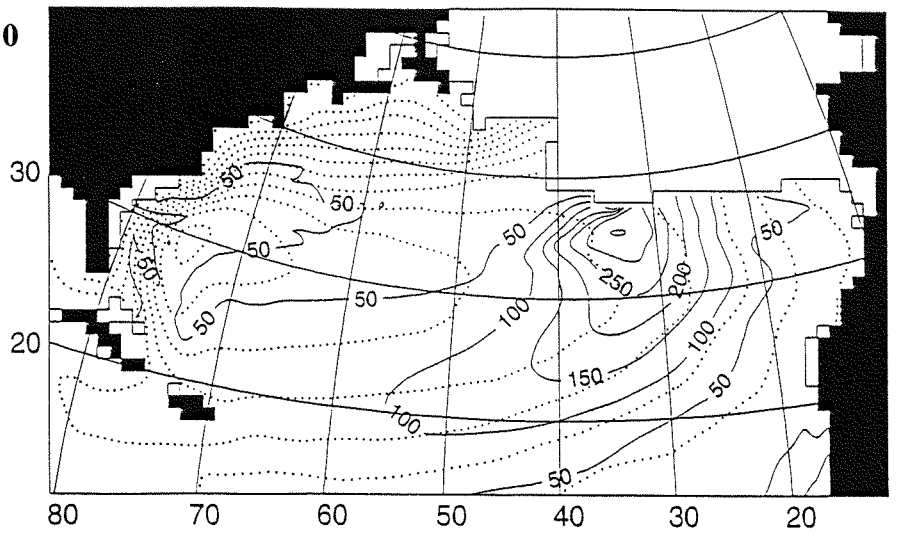

Figure 4.8 (ctd)

Subtropical mode waters (represented mainly by layers 7-10 in the model) are formed by the process of subduction. Eqn. (3.12) is used to diagnose subduction rates in year 20 of the control run, using monthly datasets to determine annual means. Calculation of vertical velocity at the maximum mixed layer depth, w_H is based on a linearization of the vorticity balance using Eqn. (3.13). A more accurate value for w_H was determined from integrated model volume fluxes, sampling every six days over a further year at the end of CLIM1. While this method was too data-intensive to repeat routinely, Eqn. (3.13) appears to estimate w_H (as derived from volume continuity) reasonably well (see **Fig. 4.9**). The biggest discrepancies between **Fig. 4.9a** (w_H from volume balance) and **Fig. 4.9b** (w_H from vorticity balance) are found at the western boundary, where non-linear and frictional effects can dominate the local vorticity balance and large values of w_H arise. Across the majority of the subtropical gyre, in the regions where layers 7-10 are ventilated (see **Fig. 4.8**), w_H is typically in the range -25 to -50 m year^{-1}, and seemingly well approximated by the simple vorticity balance. The correlation between w_H computed by the two methods is 0.19 ± 0.02, using all the data in **Figs. 4.9a,b**. Limiting the selection of data to gridpoints where w_H from volume balance lies in the range $-50 < w_H < 0$ m year^{-1} (sampling 61.9% of gridpoints), the correlation improves to 0.42 ± 0.02. Further restricting the data sampled by requiring that *both* w_H values lie in that negative range (sampling 54.2% of gridpoints), the correlation improves again to 0.61 ± 0.02, confirming that the estimated values are most accurate where w_H is relatively weak and negative (across the interior of the subtropical gyre).

(a) from volume balance

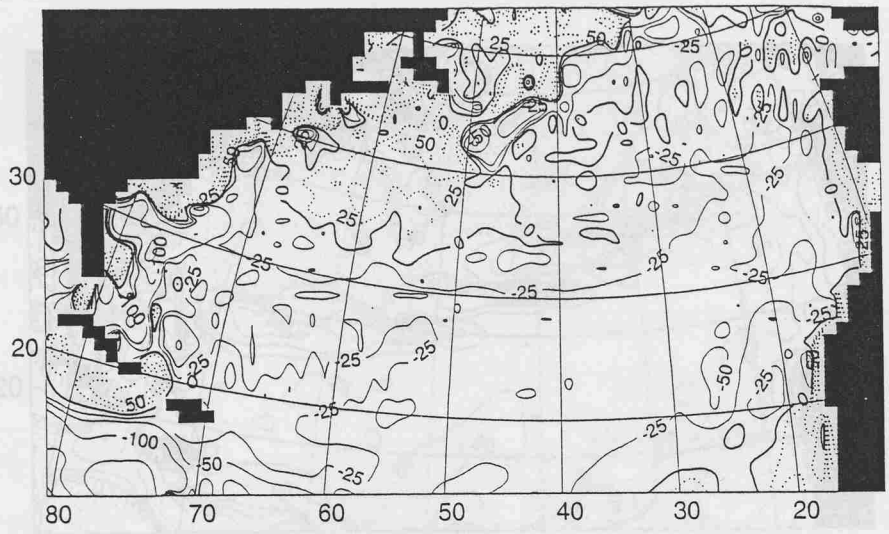

(b) estimated from vorticity balance

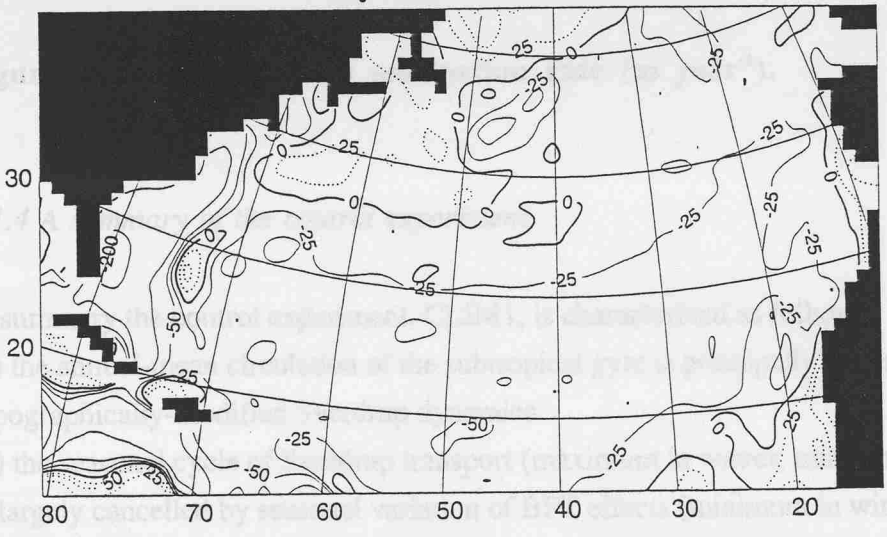

Figure 4.9: Annual-mean w_H (contoured every 25 m year^{-1}, postive upwards), obtained by two different methods, from balances of (a) volume, (b) vorticity.

Fig. 4.10 shows, for year 20 of CLIM1, the field of S_{ann}. A narrow band of $S_{ann} > 50$ m year^{-1} stretches from southwest to northeast across the subtropical gyre. This is the model subduction zone, where surface-formed mode waters leave the mixed layer. To the north of this zone are regions where thermocline water ("old" mode water) is strongly entrained back into the mixed layer (S_{ann} negative). The subduction field is largely accounted for by lateral induction [the term $\overline{\mathbf{u}_H . \nabla H}$ in Eqn. (3.12)], although $\overline{w_H}$ enhances S_{ann} south of the subduction zone.

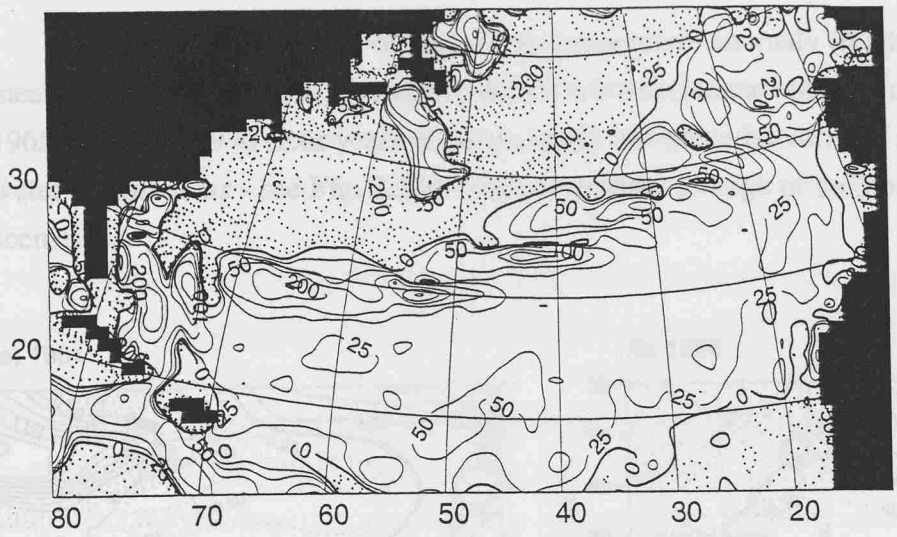

Figure 4.10: Annual-mean subduction rate (m year^{-1}).

4.1.4 A summary of the control experiment

In summary the control experiment, CLIM1, is characterized as follows:
(1) the annual-mean circulation of the subtropical gyre is principally governed by topographically-modified Sverdrup dynamics
(2) the seasonal cycle of Sverdrup transport (maximum in winter, minimum in fall) is largely cancelled by seasonal variation of BPT effects (minimum in winter, maximum in spring and fall)
(3) absolute (hence potential) vorticity is dominated by the *planetary* component (planetary vorticity is typically two orders of magnitude larger than relative vorticity)
(4) stratification at Bermuda is largely equilibrated after 20 years of spin-up, by which time a weak PV minimum (representing model 18° Water) is evident
(5) the subtropical gyre is strongly ventilated (i.e., a fraction of subtropical mode water is annually renewed), with annual subduction rates reaching 100 m year^{-1} in a narrow southwest-to-northeast band.

4.2 Designing the anomalous surface buoyancy forcing

Fig. 4.11 shows fields of surface air temperature anomaly (relative to the mean value over 1950-79), averaged over the winters (January-March) of 1964, 1965, 1969 and 1970 (four years of anomalously low potential vorticity mode water at *Panulirus* - see **Fig. 2.22c** - chosen to show a range of cold outbreak scenarios).

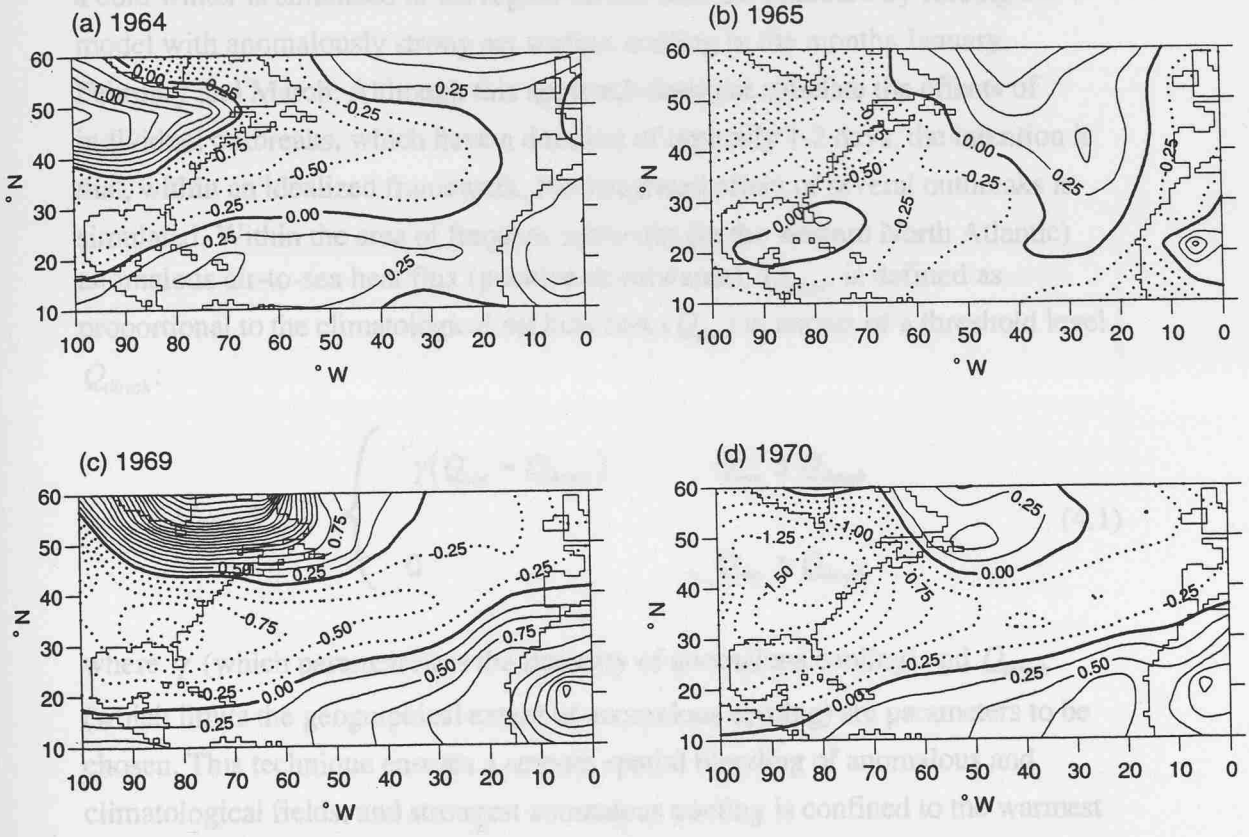

Figure 4.11: Surface temperature anomaly (°C) in four "cold-1960s" winters (from CRU surface temperature data).

In 1964 (**Fig. 4.11a**), although positive temperature anomalies lie over most of North America, negative anomalies are located along the Gulf Stream. In 1965 (**Fig. 4.11b**) negative anomalies lie across continental North America and extend to a local maximum centred at around (40°N, 75°W), but negative anomalies are not oriented along the axis of the Gulf Stream (as is the case in 1964). In 1969 (**Fig. 4.11c**) negative anomalies appear to originate from the southeast US and extend far across the Atlantic. The 1970 anomaly pattern (**Fig. 4.11d**) is perhaps

most consistent with cold outbreaks. Large negative anomalies (< -1.75°C) centred over the US eastern seaboard extend to the west, with anomalies of below -1.0°C covering an extensive area of the Gulf Stream and Sargasso Sea. In both 1969 and 1970, the Atlantic-wide negative anomalies (oriented roughly from Florida to the British Isles) may also imply a southward displacement of the mid-latitude storm track (associated with cold outbreaks), the feature of decadal variability established by Dickson and Namias (1976).

Given this variability in the observed patterns of maritime air temperatures, a cold winter is simulated in the region off the east US seaboard by forcing the model with anomalously strong net surface cooling in the months January, February and March. Although this approach does not simulate the effects of individual outbreaks, which have a duration of typically 1-2 days, the intention is that, within an idealized framework, the integrated effect of several outbreaks is simulated. Within the area of frequent outbreaks (in the western North Atlantic) anomalous air-to-sea heat flux (positive downwards), Q_{anom}, is defined as proportional to the climatological net heat flux (Q_{obs}) in excess of a threshold level, Q_{thresh}:

$$Q_{anom} = \begin{cases} \gamma(Q_{obs} - Q_{thresh}) & , Q_{obs} \le Q_{thresh} \\ 0 & , Q_{obs} > Q_{thresh} \end{cases} \qquad (4.1)$$

where γ (which parameterizes the intensity of anomalous cooling) and Q_{thresh} (which limits the geographical extent of anomalous cooling) are parameters to be chosen. This technique ensures a smooth spatial blending of anomalous and climatological fields, and strongest anomalous cooling is confined to the warmest Gulf Stream waters (see **Fig. 4.12** below). Including the additional relaxation heat flux (see discussion below), the total heat flux is $Q_{obs} + Q_{anom} + \lambda(T_{obs} - T)$.

Consistent with fields of anomalous net heat loss are anomalous fields of "evaporation minus precipitation", $(E - P)$. In the Gulf Stream region, Isemer and Hasse (1987) estimate wintertime Bowen ratios (of sensible to latent heat flux) of up to 0.4. Taking radiative longwave heat flux into consideration, these Bowen ratios suggest that typically two thirds of total heat loss is due to the latent heat lost during evaporation. Furthermore, Bunker (1976) estimates that the *annual* evaporation rate (in units of cm $year^{-1}$) should be multiplied by 1.29 to get an approximate latent heat flux (in units of W m^{-2}) - the amount of latent heat released being directly proportional to the amount of water evaporated. An anomalous

monthly freshwater flux, $(E-P)_{anom}$, in cm month^{-1}, is therefore calculated from Q_{anom} as follows:

$$(E-P)_{anom} = \frac{1}{12}\frac{\left(\frac{2}{3}Q_{anom}\right)}{1.29} \tag{4.2}$$

In three separate sensitivity experiments (COOL1, COOL2 and COOL3) the intensity and extent of Q_{anom} was varied by choosing the values of γ and Q_{thresh} [with an equivalent threshold freshwater flux, $(E-P)_{thresh}$] listed in **Table 4.1**.

Table 4.1. Parameters used to generate idealized fields of excess heat loss and evaporation in the three buoyancy flux sensitivity experiments.

Experiment	γ	Q_{thresh} (Wm^{-2})	$(E-P)_{thresh}$ (cm month^{-1})
COOL1	2	-280	12.06
COOL2	1.45	-240	10.34
COOL3	4	-280	12.06

Anomalous fluxes are added to the heat flux and *E-P* fields for January, February and March (climatological forcing resumes in April). Values for γ and Q_{thresh} in COOL1 were chosen to yield peak cooling anomalies in January, February and March of 210, 190 and 120 Wm^{-2} respectively, roughly corresponding to the amplitude of interannual variability in wintertime net heat loss inferred from the heat flux analysis of Talley and Raymer (1982) (see **Fig. 2.22a**). In COOL2, a lower value of Q_{thresh} implies a more widespread cooling than in COOL1 (γ is adjusted to maintain the same peak cooling), as suggested by the temperature anomaly fields of **Figs. 4.11c,d**. The doubling of γ in COOL3 yields strongest net cooling rates of 800 Wm^{-2}. Cooling of this extreme magnitude has been observed in the Gulf Stream region (e.g., peak cooling rates of ~700 Wm^{-2} are evident in **Fig. 2.22a**).

Averaging over January-March for the winter-mean impact, **Fig. 4.12a** shows the field of Q_{obs} (applied in CLIM1). **Figs. 4.12b-d** show fields of $Q_{obs} + Q_{anom}$ for the sensitivity experiments. Note the position of anomalous buoyancy loss relative to the location of *Panulirus*.

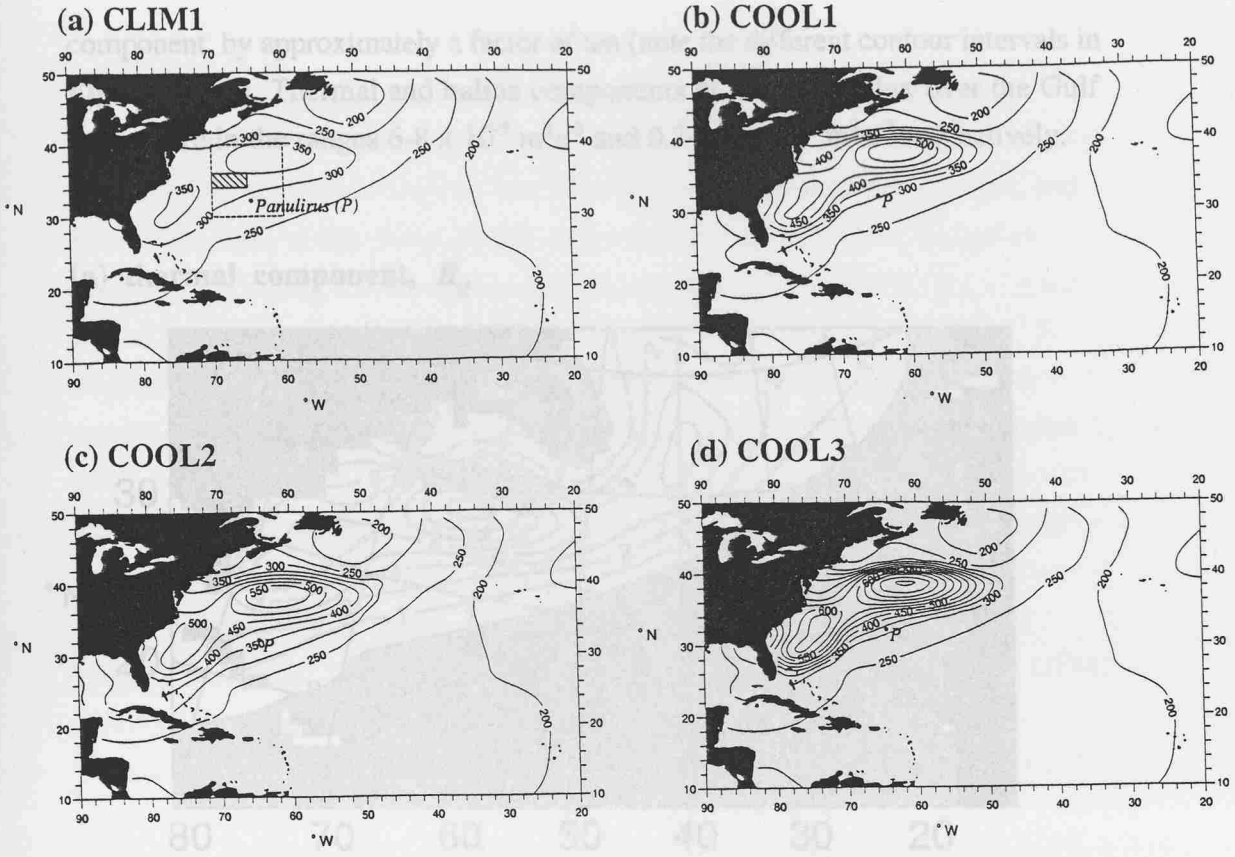

Figure 4.12: Winter (JFM) mean ocean heat loss to the atmopshere (W m^{-2}) in control and sensitivity experiments (Panulirus is indicated as *P*, dashed and shaded boxes in (a) indicate regions taken by Talley and Raymer (1982), and Jenkins (1982), to represent Gulf Stream cooling.

Associated with the heat and freshwater fluxes are buoyancy fluxes B_Q and B_{E-P}, thermal and haline components of the net buoyancy flux, B_{net} (in SI units of $m^2 s^{-3}$):

$$B_{net} = B_Q + B_{E-P} = \frac{g}{C_p \rho_o} \frac{\partial \sigma}{\partial T} Q + g \frac{\partial \sigma}{\partial S} S(E-P) \qquad (4.3)$$

where $\sigma, T, S, C_p, \rho_o$ and g are the specific density, temperature, salinity, specific heat of seawater (4000 J kg^{-1} m^{-3}), mean density of seawater (1025 kg m^{-3}) and gravitational acceleration (9.81 m s^{-2}) respectively. **Fig. 4.13** shows annual-mean fields of B_Q and B_{E-P} over the Gulf Stream subtropical gyre, computed from the climatological heat and freshwater fluxes used to force the model. **Fig. 4.13** shows that climatological net buoyancy fluxes are dominated by the thermal

component, by approximately a factor of ten (note the different contour intervals in **Figs. 4.13a,b**). Thermal and haline components of buoyancy flux over the Gulf Stream are in the ranges 6-8 x 10^{-5} $m^2 s^{-3}$ and 0.7-1.0 x 10^{-5} m^2 s^{-3} respectively.

(a) thermal component, B_Q

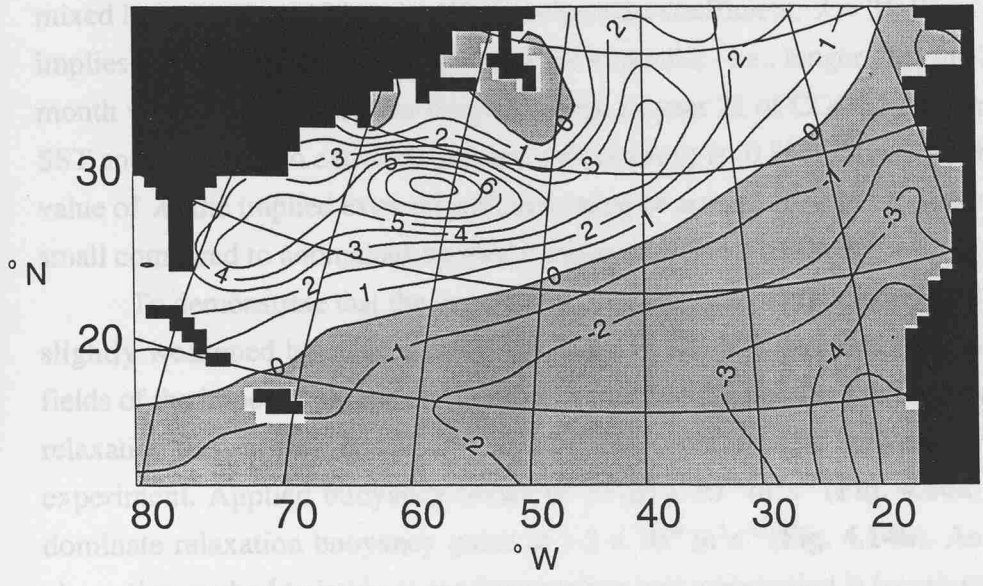

(b) haline component, B_{E-P}

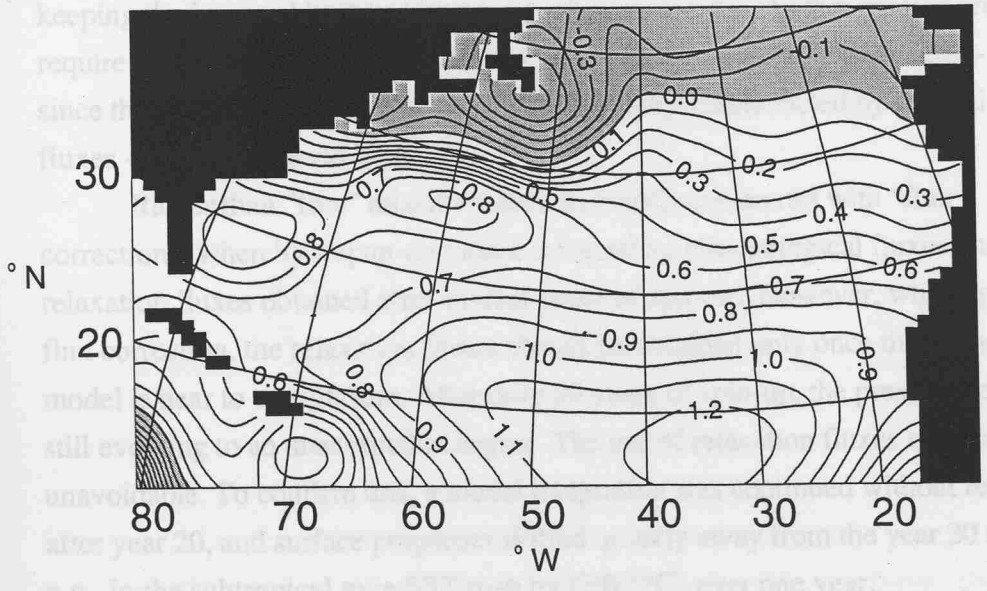

Figure 4.13: Components of climatological annual-mean surface buoyancy flux (10^{-5} $m^2 s^{-3}$, positive where the ocean is losing buoyancy): (a) thermal (C.I. = 1.0), (b) haline (C.I. = 0.1).

The Haney-style relaxation to climatological values of sea surface temperature and salinity (see §3.1.4) will dampen surface temperature and salinity anomalies (due to the anomalous heat and freshwater forcing). The strength, and hence timescale, of this damping will determine the extent to which relaxation warming/freshening will counteract anomalous cooling/evaporation. For a typical mixed layer depth of 100m, the chosen relaxation coefficient, $\lambda = 35$ W m^{-2} K^{-1}, implies an e-folding relaxation timescale of 4 months - i.e., longer than the 3-month winter period of excess buoyancy loss. In year 21 of COOL1, the largest SST anomaly (due to extra cooling and evaporation) is -0.8°C. Given the chosen value of λ, the implied extra relaxation heating of around 10 Wm^{-2} is relatively small compared to anomalous applied cooling of around 100 Wm^{-2}.

To demonstrate that the imposed excess buoyancy loss is indeed only slightly weakened by relaxation fluxes, **Figs. 4.14a-b** show winter mean (JFM) fields of the imposed anomalous buoyancy flux and the resulting *anomalous* relaxation flux, in year 21 of LOMIXCOOL, the most strongly buoyancy-forced experiment. Applied buoyancy *losses* of 10-20 x 10^{-5} $m^2 s^{-3}$ (**Fig. 4.14a**) dominate relaxation buoyancy *gains* at 1-2 x 10^{-5} $m^2 s^{-3}$ (**Fig. 4.14b**). An alternative method to imply anomalous cooling and evaporation is by relaxation of SSTs and surface salinities towards prescribed low and high values respectively, keeping the imposed heat and freshwater fluxes constant. As this method would require a careful prescription of surface temperature and salinity anomalies - and since the applied anomalous fluxes are only slightly counteracted by relaxation fluxes - it is not pursued here.

Rather than "free" relaxation fluxes, models can be run with "flux correction", whereby a spun-up model is forced by climatological fluxes plus fixed relaxation fluxes obtained after several years of spin-up. However, when applying flux correction, the relaxation fluxes should be obtained only once the spun-up model is near to equilibrium. After only 20 years of spin-up, the present model is still evolving to an unacceptable degree. The use of relaxation fluxes is certainly unavoidable. To confirm this, a model integration was continued without relaxation after year 20, and surface properties drifted quickly away from the year 20 state - e.g., in the subtropical gyre SST rose by O(0.5°C) over one year.

(a) applied anomalous flux

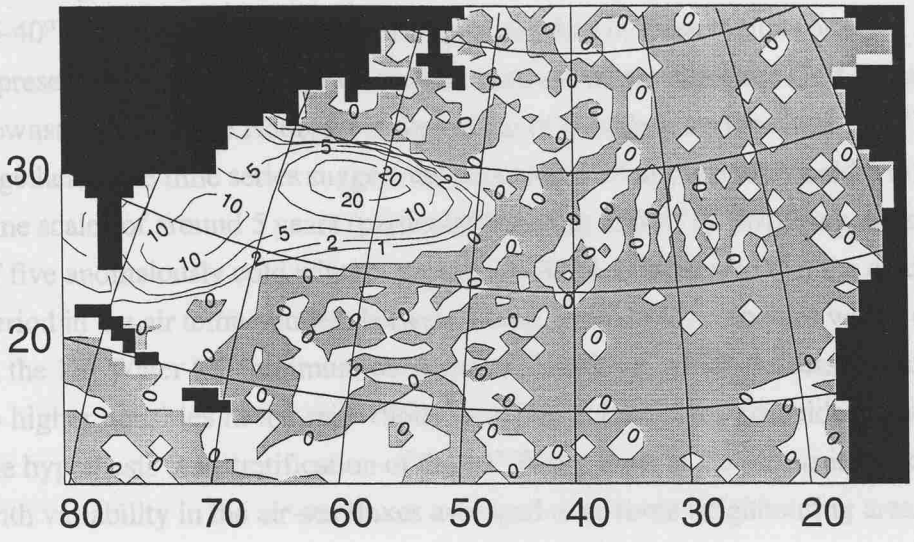

(b) anomalous relaxation flux

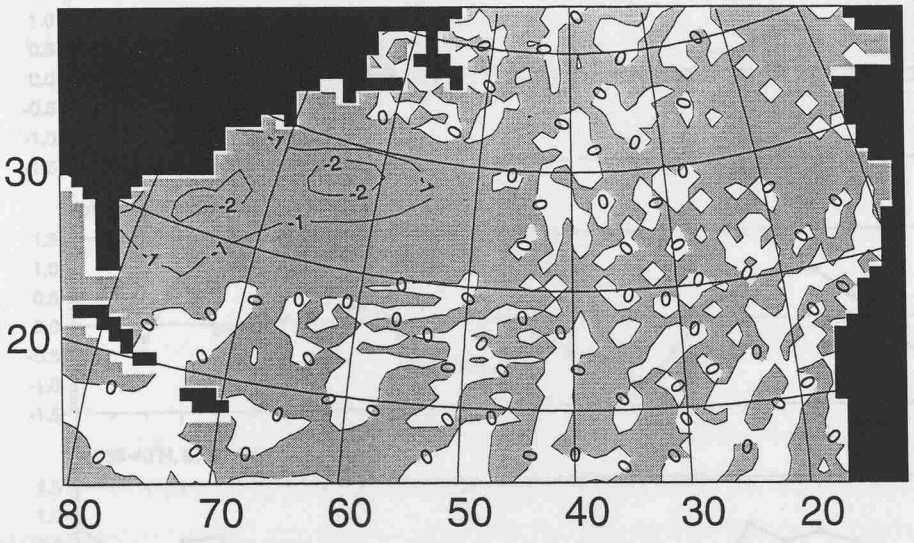

Figure 4.14: The winter-mean (JFM) surface buoyancy flux (contoured at ±1, 2, 5, 10, 20 x 10^{-5} m^2s^{-3}, positive where the ocean is losing buoyancy) in year 21 of LOMIXCOOL: (a) applied anomalous flux, (b) anomalous relaxation flux.

Selecting the period 1954-78 from the dataset of surface air temperature anomalies, **Fig. 4.15a-c** shows mean wintertime anomalies for gridboxes bounding the regions (70-75°W, 30-35°N), (65-70°W, 35-40°N) and (60-65°W, 35-40°N) respectively. Temperature anomaly data in these regions are representative of the relative warmth or coolness of air above the Gulf Stream downstream of Cape Hatteras, in the region of strongest surface heat loss. Taken together, these time series suggest the persistence of anomalously cold winters on time scales of around 5 years (particularly during 1964-71), justifying the sequence of five anomalously cold winters applied in COOL1. Note also that the coldest period in the air temperatures, between about 1964-1971, coincides with a change in the 18° Water PV minimum observed at *Panulirus*, which decreased and shifted to higher densities in the mid-1960s (see **Fig. 2.22c**). This coincidence supports the hypothesis that stratification of the 18° Water layer at *Panulirus* is correlated with variability in the air-sea fluxes averaged over some neighbouring area, and supports part of the rationale for the buoyancy flux sensitivity experiments.

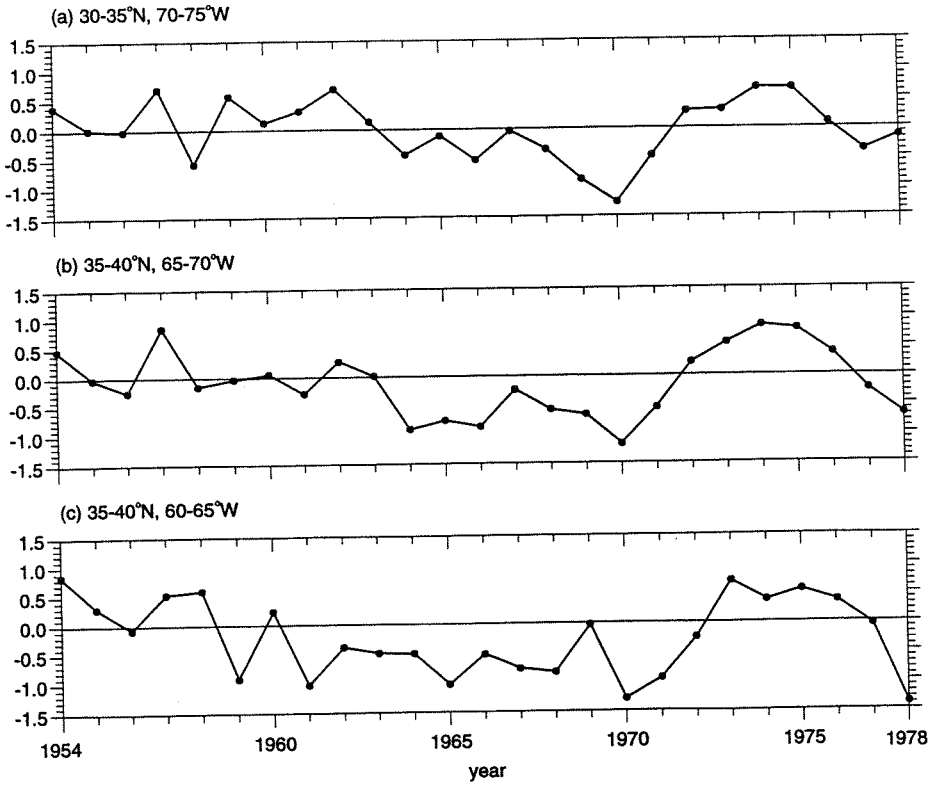

Figure 4.15: Time series of winter air temperature anomaly (°C) over three different sectors of the Sargasso Sea, 1954-78 (from CRU air temperature data).

The sensitivity experiments begin at the end of year 20 of CLIM1 (model years begin and end in mid-September). In COOL1 the model is forced for 5 years with the anomalous winter (January-March) conditions described above, followed by 5 years reverting back to year-round climatological forcing, in order to monitor the fate of anomalous water formed over years 21-25. In COOL2 and COOL3 the model is forced with just one cold winter (year 21), to examine the sensitivity of the model response (established in COOL1) to choices of γ and Q_{thresh}.

4.3 Results of the buoyancy flux sensitivity experiments

The results of the sensitivity experiments are considered in three sub-sections. Sub-section 4.3.1 describes the impact on thermocline ventilation of the anomalous wintertime conditions imposed in COOL1. The results of this experiment correspond closely with 18° Water variability observed at *Panulirus* during the 1960s. Sub-section 4.3.2 addresses mode water formation rates in each of the four experiments (CLIM1, COOL1, COOL2 and COOL3), quantifying the sensitivity of 18° Water renewal to anomalous surface forcing. Sub-section 4.3.3 presents the evidence for end-of-winter Gulf Stream intensification in all three sensitivity experiments, and COOL3 is chosen for closer examination, to establish the spatial structure, and evolution, of intensification.

4.3.1 The decade-long sensitivity experiment

For the decade-long sensitivity experiment, COOL1, **Fig. 4.16** and **Fig. 4.17** show the impact of excess cooling on the end-of-winter mixed layer density and depth, after one and five cold winters respectively (in March of year 21 and year 25). The direct impact of excess cooling is twofold: by the end of winter, mixing reaches greater depths (by up to 182 m) and surface density is increased (by up to 0.30 sigma units), compared to CLIM1. After five cold winters, there is however a band of anomalously *shallow* mixed layer depth south of the main band of deeper mixing. This arises where mixing is impeded in the presence of anomalously dense mode waters (beneath the mixed layer), formed during the previous four winters.

At the end of the first cold winter, a deeper and denser mixed layer is generally coincident with the area of anomalous heat loss. At the end of the fifth cold winter, deeper mixing extends slightly further east of the region of applied extra cooling, and the region of higher surface density extends northeastward.

These changes over years 21-25 (especially those in the surface density field) are the consequence of advection/diffusion and wintertime re-entrainment of layer thickness anomalies in the model (see **Fig. 4.19**).

(a) change in mixed layer density after one cold winter (max 0.30)

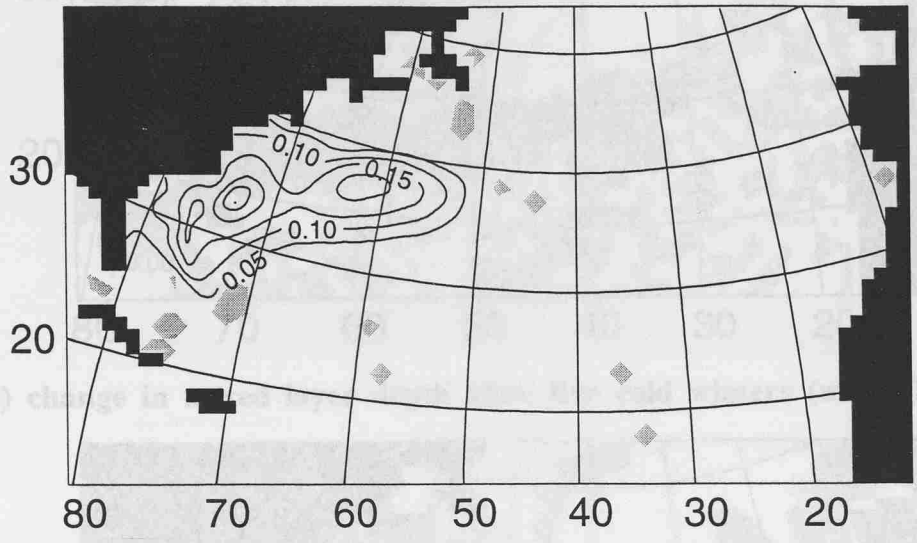

(b) change in mixed layer depth after one cold winter (max 182 m)

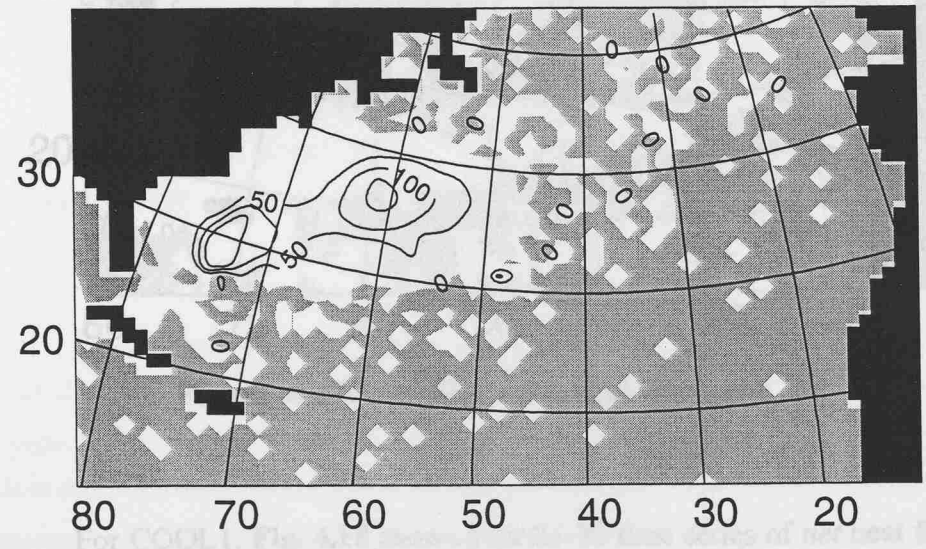

Figure 4.16: March year 21 COOL1 minus CLIM1 fields of (a) mixed layer density (C.I. = 0.05 kg m^{-3}), (b) mixed layer depth (C.I. = 50 m).

(a) change in mixed layer density after five cold winters (max 0.31)

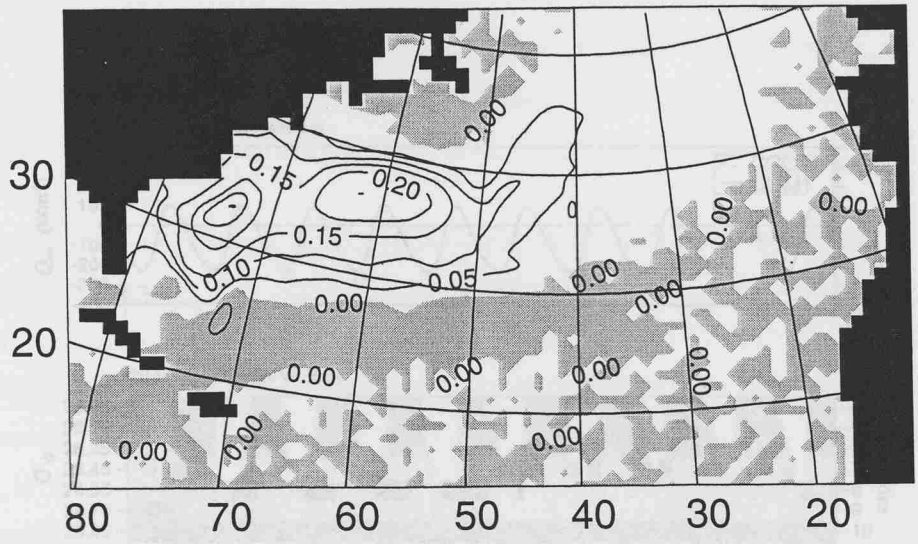

(b) change in mixed layer depth after five cold winters (max 179 m)

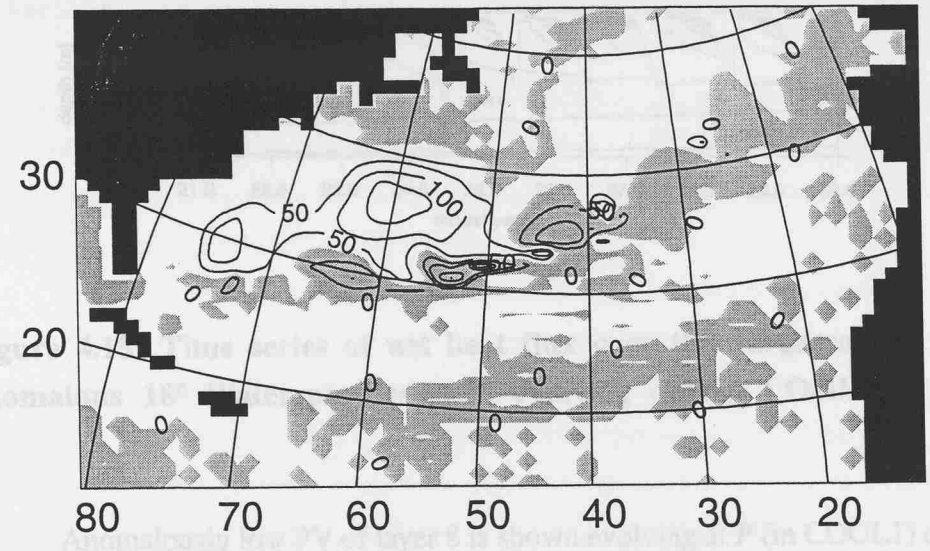

Figure 4.17: As Fig. 4.16, but for year 25.

For COOL1, **Fig. 4.18** shows year 21-30 time series of *net* heat flux averaged over the Sargasso Sea, and of 18° Water profiles at *P* (as **Fig. 4.6a,b**). As a measure of the variability in winter cooling comparable with the analysis of Talley and Raymer (1982), the monthly net (applied plus relaxation) surface heat fluxes for CLIM1 and COOL1 (**Fig. 4.18a**) are averaged over the area 34-36°N, 65-70°W (the shaded box shown in **Fig. 4.12a**). The signature of the simulated cold outbreak (see the dotted line in **Fig. 4.18a**) is unambiguous, and it is a robust feature of winters in years 21-25 of COOL1. This implies that there is

insufficient time for the relaxation fluxes to adjust to the anomalous forcing during January-March.

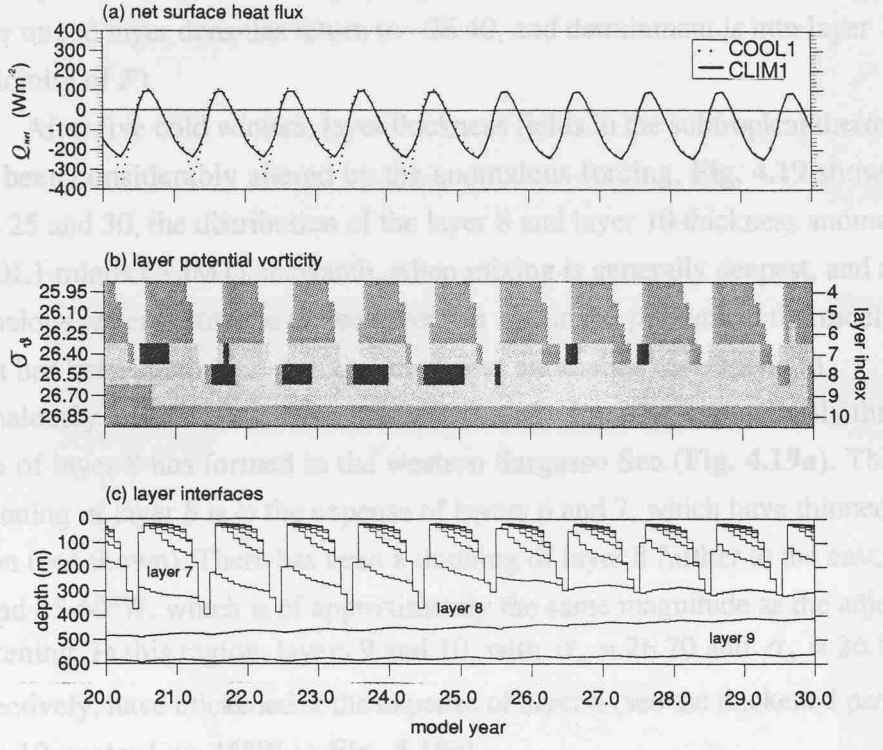

Figure 4.18: Time series of net heat flux over the Sargasso Sea and anomalous 18° Water profiles at *P*, evolving during COOL1.

Anomalously low PV of layer 8 is shown evolving at *P* (in COOL1) over years 21-25 in **Fig. 4.18b**. Layer 7 (σ_θ = 26.40) represents the mode water at *P* in year 21 (the thermocline layer with minimum PV, hence heaviest shading), but this is replaced by layer 8 (σ_θ = 26.55) from year 22 onwards. While layer 7 outcrops at *P* during January-March, layer 8 is not fully entrained into the mixed layer. The thickening of layer 8 at *P* is through strengthened subduction where the layer outcrops further to the east (see **Fig. 4.19a** below). After the winter of year 26, layer 7 again resumes the mode water identity at *P*. Development of the PV minimum at *P* over a simulated cold period is remarkably similar to the evolution of mode water PV observed at *Panulirus* over the period 1964-71 (see **Fig. 2.22c**). **Fig. 4.18c** shows the corresponding layer thicknesses in the upper 600 m of the water column, illustrating the deeper wintertime mixing and the thickening

of layer 8, at the expense of layer 7, over years 21-25. For each of the cold years, the end-of-winter mixed layer density in the vicinity of *P* is close to 26.55, the density of layer 8, so that water detrains preferentially into layer 8, increasing the thickness of this layer at *P*. After the resumption of climatological cooling (in year 26), PV profiles and stratification at *P* gradually revert to those of CLIM1 (end-of-winter mixed layer densities return to ~26.40, and detrainment is into layer 7, in the vicinity of *P*).

After five cold winters, layer thickness fields in the subtropical thermocline have been considerably altered by the anomalous forcing. **Fig. 4.19** shows, for years 25 and 30, the distribution of the layer 8 and layer 10 thickness anomalies (COOL1 minus CLIM1), in March, when mixing is generally deepest, and any anomalous water below the mixed layer lies within the *permanent* thermocline - i.e., it has been subducted. Positive thickness anomalies correspond to anomalously low PV. After five successive cold winters an anomalously thick patch of layer 8 has formed in the western Sargasso Sea (**Fig. 4.19a**). This thickening of layer 8 is at the expense of layers 6 and 7, which have thinned in this region (not shown). There has been a thinning of layer 8 further to the east, at around 45-60°W, which is of approximately the same magnitude as the adjacent thickening. In this region, layers 9 and 10, with σ_θ = 26.70 and σ_θ = 26.85 respectively, have thickened at the expense of layer 8 (see the thickened patch of layer 10 centred on 45°W in **Fig. 4.19c**).

The ventilation pattern of layer 8, with maximum thickness at around (30°N, 60°W) in CLIM1 (**Fig. 4.8b**), has moved appreciably to the west by year 25 of COOL1. This coincides with a westward-shift of mixed layer isopycnals associated with anomalous buoyancy loss over the separated Gulf Stream. Increases of end-of-winter mixed layer density (see **Fig. 4.16a** and **Fig. 4.17a**) imply that corresponding mixed layer isopycnals (see **Fig. 4.7b**) must shift to the west. At a given location, water is subducted at the end of winter into the layer with density closest to the mixed layer density. Hence the pattern of ventilation into given layers will move to the west with the shifting mixed layer isopycnals.

After a further five climatological winters, anomalous layer 8 thickness is largely negative (see **Fig. 4.19b**), after re-entrainment back into the mixed layer of a large part of the positive anomaly. The persistence of *negative* layer 8 thickness anomalies, compared to the rapid attenuation of corresponding positive anomalies, is due to differences in recirculation timescales. The negative anomalies originate further to the east (see **Fig. 4.19a**) and follow longer trajectories around the gyre. **Fig. 4.19c** shows that, after the fifth cold winter, a positive anomaly of layer 10 thickness has been formed to the east of the region where extra cooling is

(a) layer 8 thickness anomaly, March year 25

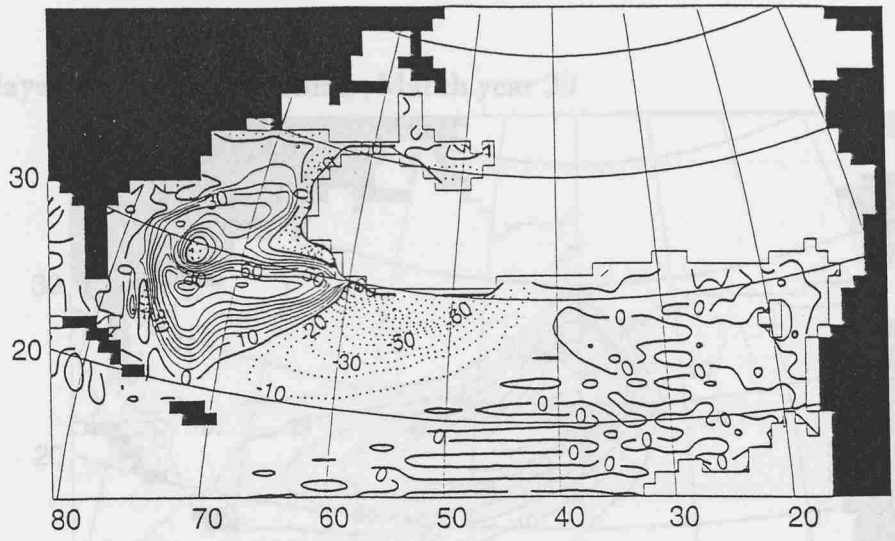

(b) layer 8 thickness anomaly, March year 30

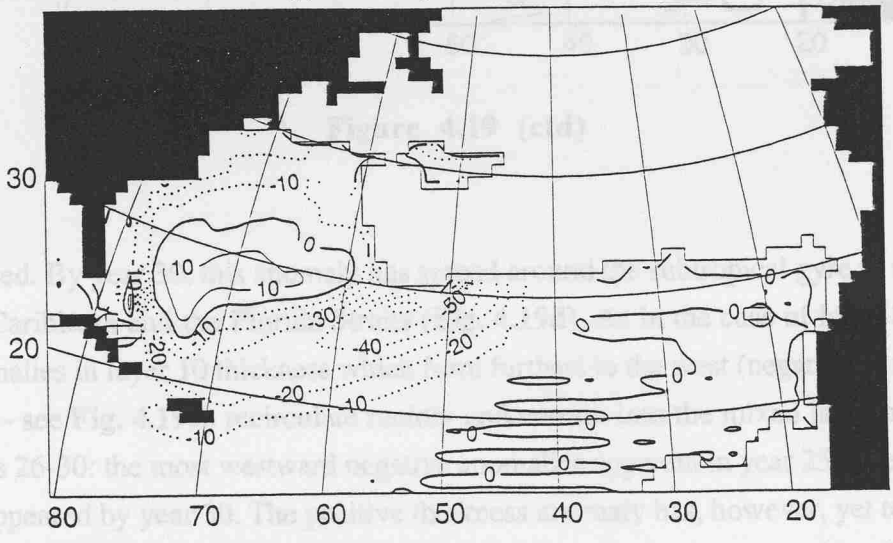

(c) layer 10 thickness anomaly, March year 25

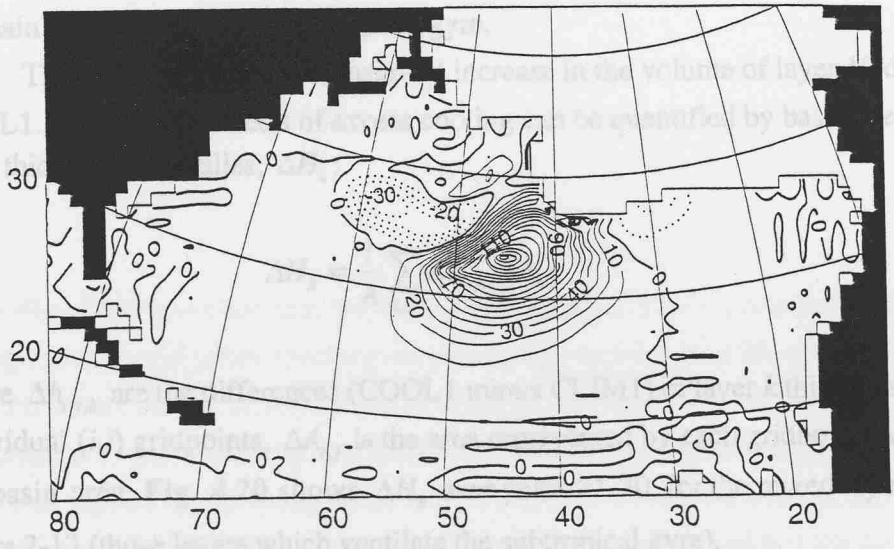

Figure 4.19: Fields of thickness anomaly (C.I. = 10 m) for two mode water layers, after five cold winters, and after five further climatological winters.

(d) layer 10 thickness anomaly, March year 30

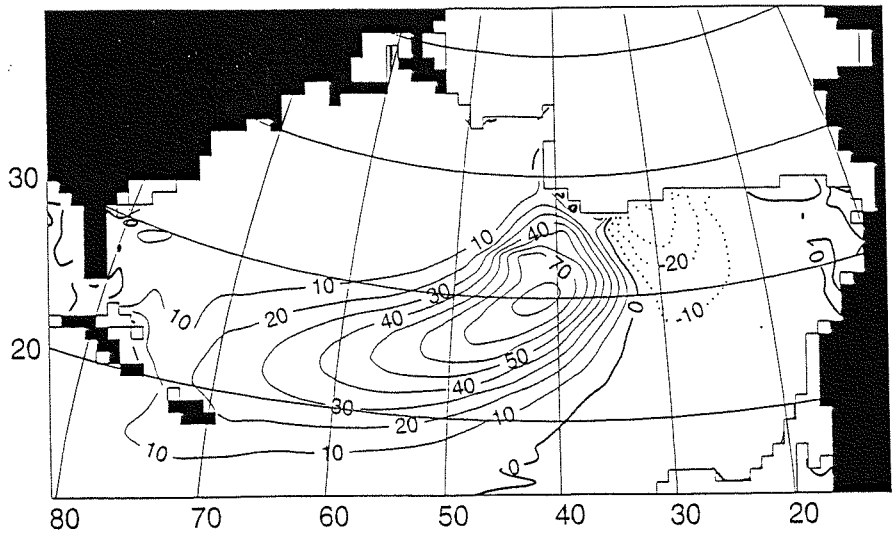

Figure 4.19 (ctd)

applied. By year 30, this anomaly has spread around the subtropical gyre to reach the Caribbean and the Florida Straits (**Fig. 4.19d**). As in the case of layer 8, anomalies in layer 10 thickness which form furthest to the west (negative in this case - see **Fig. 4.19d**) recirculate rapidly and entrain into the mixed layer over years 26-30: the most westward negative anomalies apparent in year 25 have disappeared by year 30. The positive thickness anomaly has, however, yet to reach the Gulf Stream, and may survive for several more years as a signal of low PV in the main thermocline of the subtropical gyre.

There has clearly been a basin-net increase in the volume of layer 10 during COOL1. The integral effects of excess cooling can be quantified by basin-mean layer thickness anomalies, ΔH_k:

$$\Delta H_k = \frac{1}{A}\sum_{i,j} \Delta h_{i,j,k} \Delta A_{i,j} \qquad (4.4)$$

where $\Delta h_{i,j,k}$ are the differences (COOL1 minus CLIM1) in layer k thickness at individual (i,j) gridpoints, $\Delta A_{i,j}$ is the area represented by each gridbox, and A is the basin area. **Fig. 4.20** shows ΔH_k over years 21-30, for the mixed layer and layers 2-13 (those layers which ventilate the subtropical gyre).

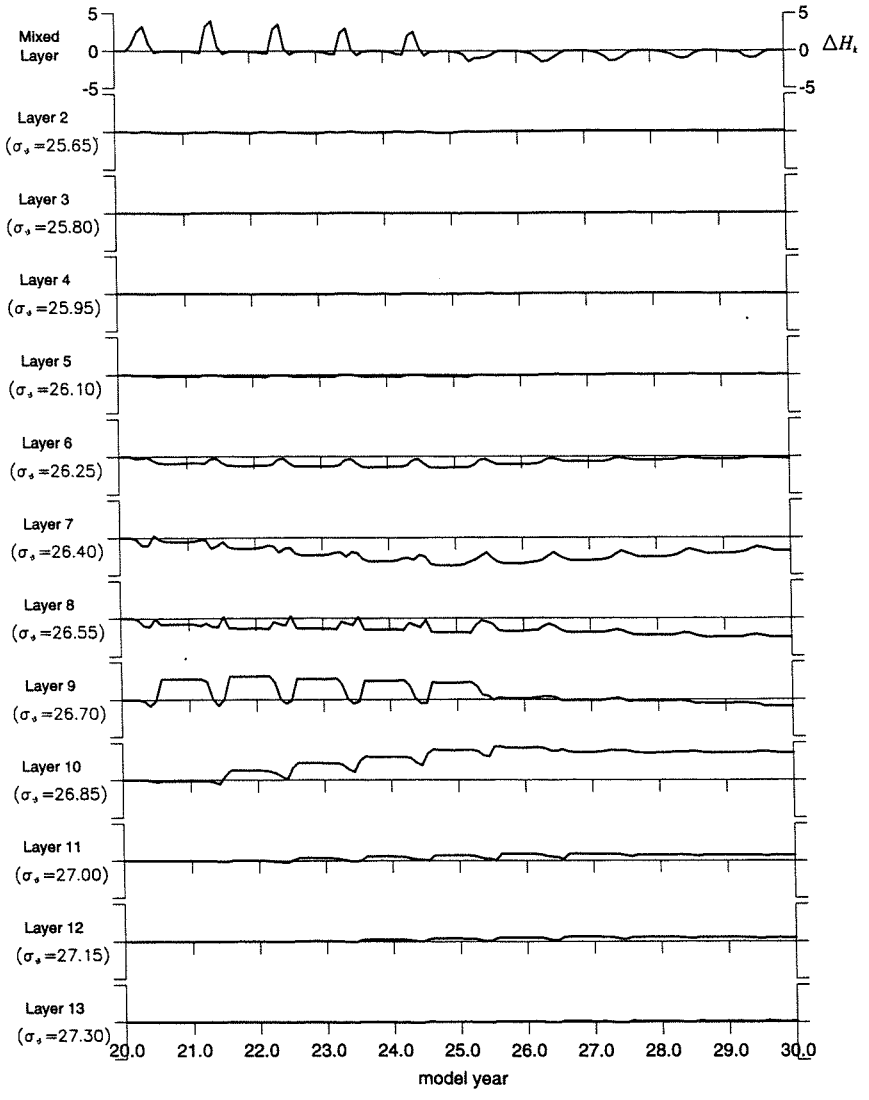

Figure 4.20: Basin-integrated layer thickness anomaly trends during COOL1.

From **Fig. 4.20**, it is clear that the model hydrography evolves relatively rapidly during the five cold years, reaching an anomalous state by year 25, which is thereafter more slowly changing (the strength of anomalous mixed layer-thermocline interaction being indicated by the amplitudes of the seasonal cycles). The more rapidly recirculating mode waters (layers 6-9) show a small tendency for continuing evolution over the next five years. It can be presumed that the whole model would eventually re-equilibrate to the same state as CLIM1, although this process could take several further decades. Over years 21-30 as a whole, however,

the net basin-mean effect is an increase in the volume of layer 10 and a decrease in the volume of layers 7 and 8.

That layer 10 inflates at the expense of layers 7 and 8 can be explained as follows. The rapidly recirculating positive layer 7 and 8 thickness anomalies are entrained into the Gulf Stream mixed layer throughout COOL1, while more persistent negative anomalies slowly recirculate further to the east (see, for example, **Fig. 4.19a,b**), and persist to year 30. These negative thickness anomalies are, in turn, the consequence of enhanced layer 10 ventilation, augmented over years 21-25 by increasing winter mixed layer density in the region 40-50°W, 30-40°N (compare **Fig. 4.16a** and **Fig. 4.17a**). This density increase reflects the entrainment of an anomalously large volume of layers 7 and 8. Recirculating layer 7 and 8 thickness anomalies thus predcondition the enhanced ventilation of layer 10. Note that layer 9 *seasonally* inflates in years 21-25, the majority of anomalous layer 9 volume transferring back into the mixed layer during each cold winter. This is evidenced in **Fig. 4.20** by corresponding wintertime increases and decreases, respectively, in the mean thickness of the mixed layer and layer 9.

4.3.2 The sensitivity of 18° Water formation to anomalous buoyancy forcing

The control and three sensitivity experiments are now compared, using the method outlined in §3.3.4 to diagnose the annual formation of "new" STMW in each experiment. Integrating over the whole basin, there is little annually-averaged net change in layer volume - while new STMW is forming in the Sargasso Sea, "old" STMW, having advected around the subtropical gyre and into the Gulf Stream, is being re-entrained back into the mixed layer (see the large negative values for S_{ann} in the northwest subtropical gyre in **Fig. 4.10**). To concentrate on the STMW formation process, Eqn. (3.14) is used in the latitude range 10-50°N, and only where there is subduction of fluid into the thermocline (i.e., wherever $S_{ann} > 0$). [In tests, such estimates agree favourably with exact calculations of STMW formation, based on exact mass balances in the subtropical gyre, a more data-intensive diagnosis which cannot be repeated routinely].

Fig. 4.21 shows ΔV_k, in the density range $25.80 < \sigma_\theta < 27.30$ (layers 3-13), for year 21 of each experiment. It is clear that each of the sensitivity experiments, with increased buoyancy loss, displays an increased STMW formation rate. Also, the *total* anomalous buoyancy loss is weaker for COOL1 than for COOL2 and COOL3 (which share similar levels of buoyancy loss). This results in a larger enhancement of STMW formation for COOL2 and COOL3, than

for COOL1. Furthermore, while the highest formation rate in CLIM1 is for layer 7, the enhanced cooling in the sensitivity experiments leads, not surprisingly, to highest formation of heavier STMW (layer 8).

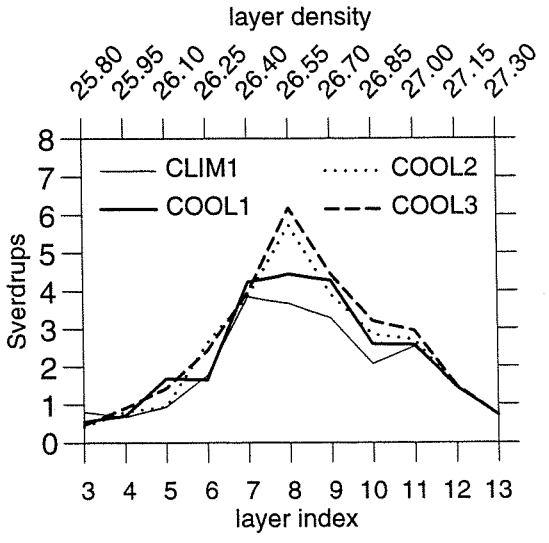

Figure 4.21: Year 21 layer formation rates for control and sensitivity expts.

4.3.3 End-of-winter Gulf Stream intensification

The thickening of 18° Water layers drives an end-of-winter dynamical response which is best exemplified by anomalies in the circulation of layer 8 in the Sargasso Sea. Fig. **4.22a** shows how, in mid-April, this circulation is intensified. Currents in layer 8 increase by up to 7 cm s^{-1} in a narrow (100-200 km) band along the southern flank of the Gulf Stream, and by up to 3 cm s^{-1} in a broader recirculation zone (300-400 km wide). Layer 8, with σ_θ = 26.55, represents the denser variety of 18° Water forming in the model, and is more strongly formed under excess cooling. The anomalous geostrophic currents computed from layer thickness anomalies are shown in **Fig. 4.22b**. The similarity of actual and geostrophic currents (comparing **Figs. 4.22a,b**) demonstrates that the intensified layer 8 currents are in approximate geostrophic balance with steepened pressure gradients. This raises the intriguing possibility of a positive feedback between intensified recirculation (around a thickened layer of mode water) and enhanced subduction rates (through lateral induction). In the case of layer 8, however,

ventilation takes place further to the east, and an intensified recirculation, limited to the model Sargasso Sea, is unlikely to feedback on subduction rates.

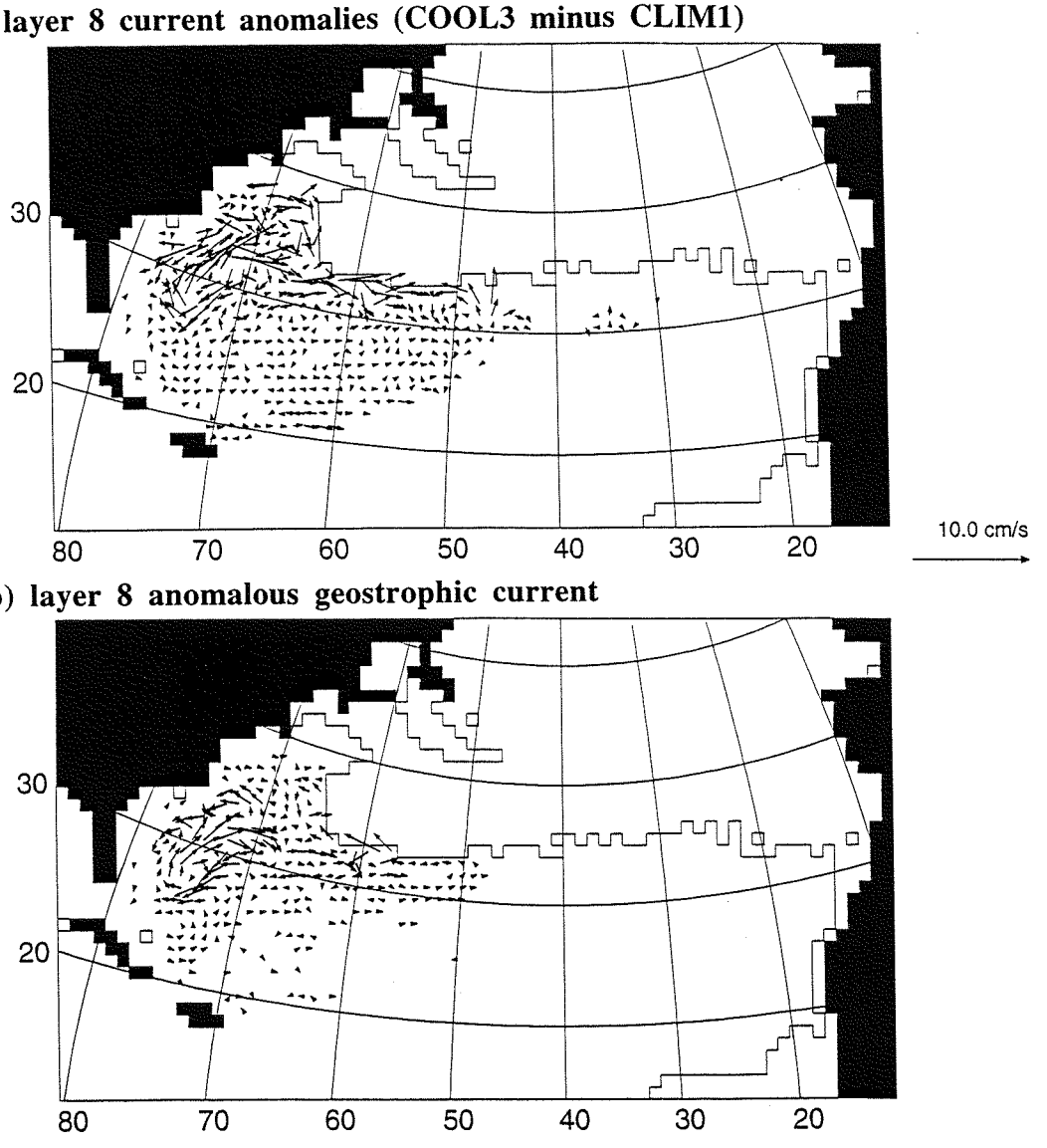

Figure 4.22: Mid-April year 21 layer 8 anomalous currents, (a) actual (COOL3 minus CLIM1) and (b) geostrophic (computed from anomalous horizontal pressure gradients).

As a first check on the variability of model Gulf Stream transport, **Fig. 4.23** shows, for year 21 of each experiment, monthly zonal full-depth volume transport between 32°N and the coast of North America (in the model), across four longitudes: 72°W, 70°W, 68°W and 64°W. These sections capture the predominantly zonal transport downstream of Cape Hatteras, at longitudes which

fall in the Bermuda-Cape Hatteras-Cape Sable triangle used by Worthington (1977) to establish both seasonal and interannual variation of Gulf Stream transport (eastern and western boundaries of the triangle being at Cape Hatteras and Bermuda, ~76°W and ~64.5°W respectively).

Fig. 4.23 reveals seasonal cycles in zonal transport (similar to the seasonal cycle of Gulf Stream transport shown in **Fig. 4.4**), with maximum and minimum transport in January and October respectively. Transports generally decrease eastwards (downstream from 72°W), as some of the zonal flow recirculates to the south (see **Fig. 4.1**). In all three sensitivity experiments, transport is generally enhanced during April-May. The largest increases are in COOL3 at 70°W, with enhancements of up to ~25% (from 27.5 Sv in CLIM1 to 34.1 Sv in COOL3).

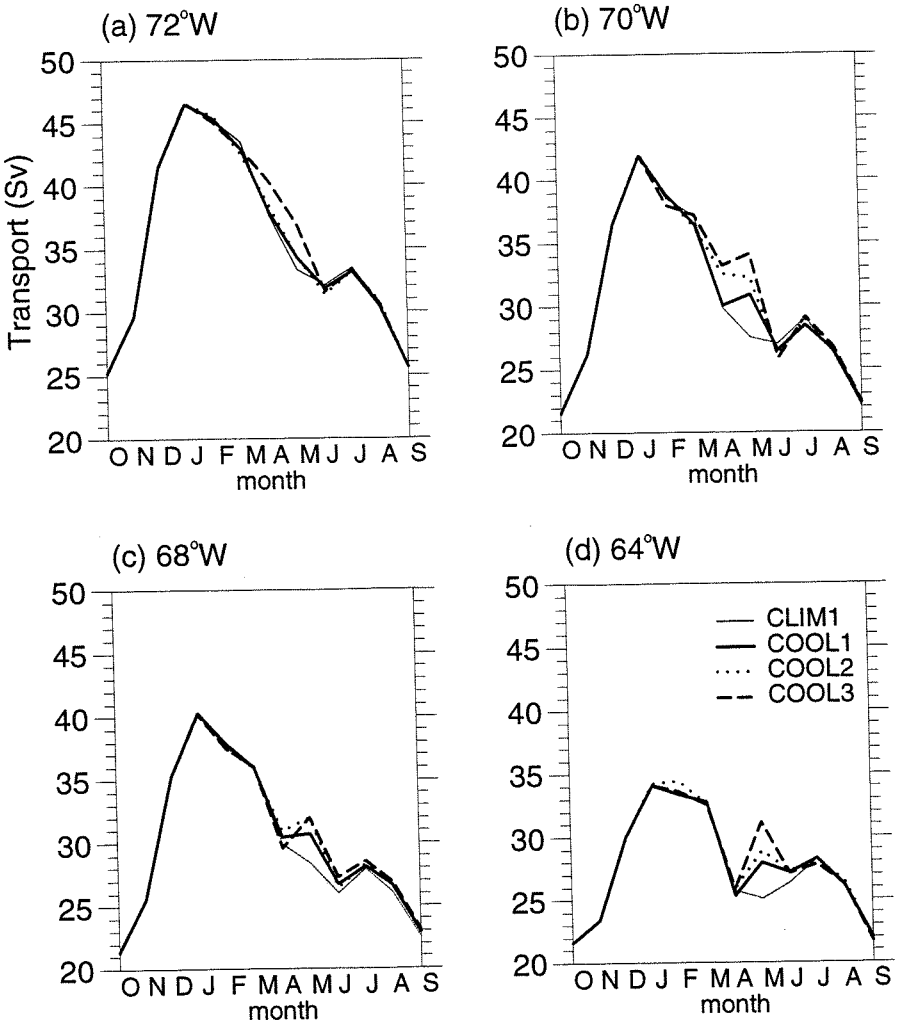

Figure 4.23: Seasonal cycles of zonal Gulf Stream transport in control and sensitivity expts, at four positions downstream of Cape Hatteras.

Consider in more detail the extreme case of COOL3. Three-daily model output is saved and diagnosed for ψ_{baro}, the barotropic streamfunction (outlined in §3.3.1), **Fig. 4.24** shows the evolution, from mid-December to mid-September, of the peak cooling rate and of maximum/minimum positive/negative ψ_{baro} anomalies (ψ'_{baro}). Peak cooling rates of 650 Wm^{-2} occur in early February (**Fig. 4.24a**), while maximum/minimum values of ψ'_{baro} (around +9 Sv and -11 Sv) arise suddenly (although not quite coincidentally) around mid-May (**Fig. 4.24b**).

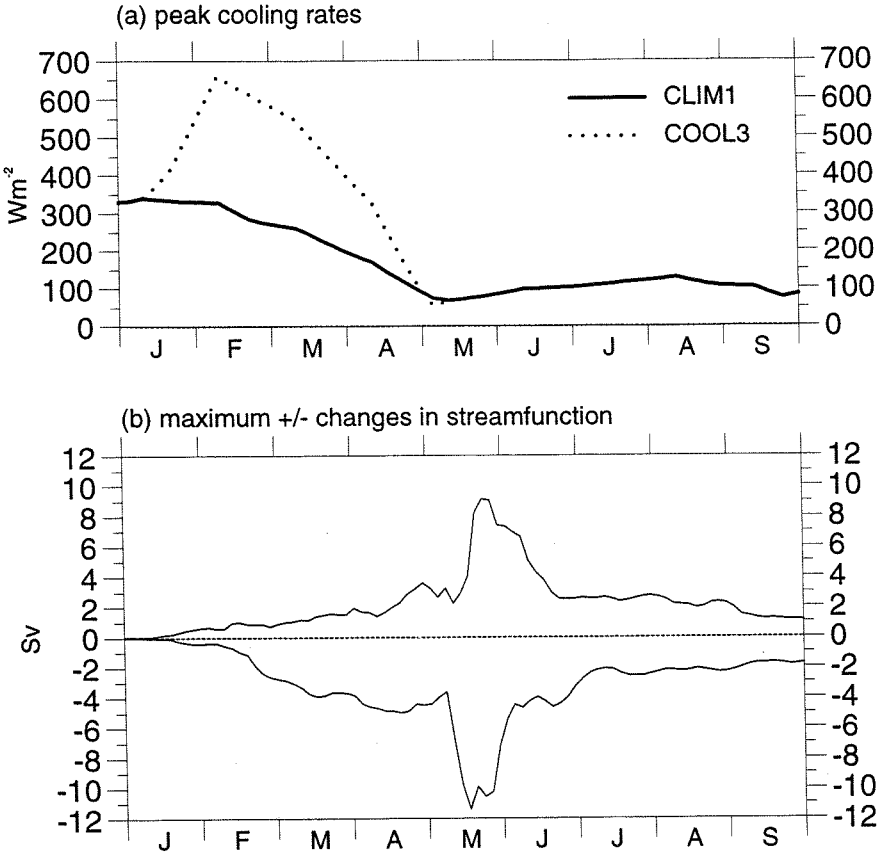

Figure 4.24: Time series of (a) peak cooling rates in CLIM1 and COOL3, and (b) maximum/minimum positive/negative changes of ψ_{baro} in COOL3.

Fig. 4.25 shows maps of ψ_{baro} and ψ'_{baro} around the period of peak intensification, in mid-May. The ψ'_{baro} map (**Fig. 4.25c**) indicates an additional anticyclonic circulation of ~7 Sv in COOL3, centred on (64°W, 33°N). This intensified circulation lies about 500 km to the south and west of maximum imposed excess cooling at (63°W, 38°N) - see **Fig. 4.12d**. At the latter location

(a) CLIM1

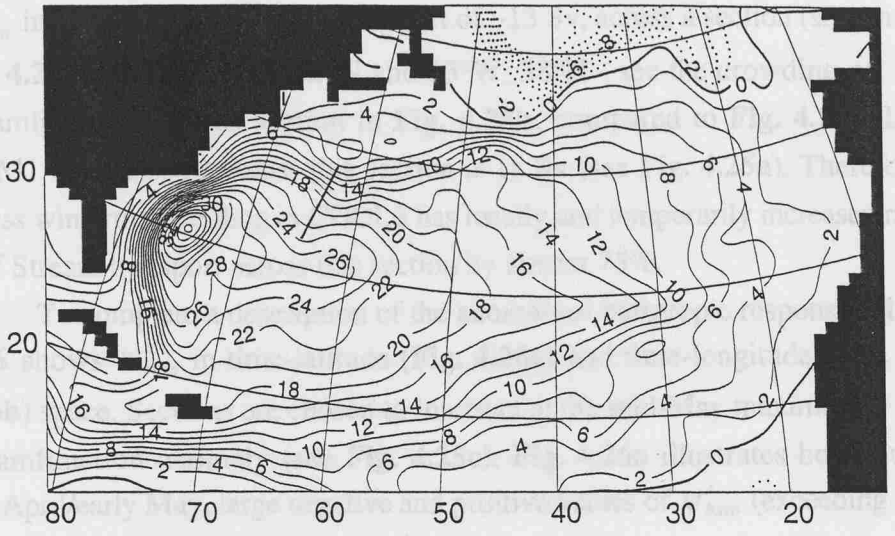

(b) COOL3

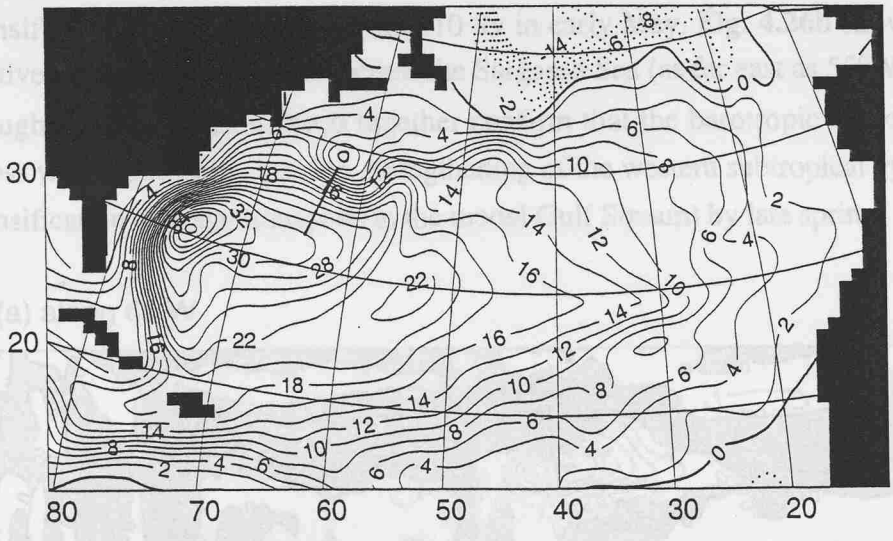

(c) COOL3 minus CLIM1

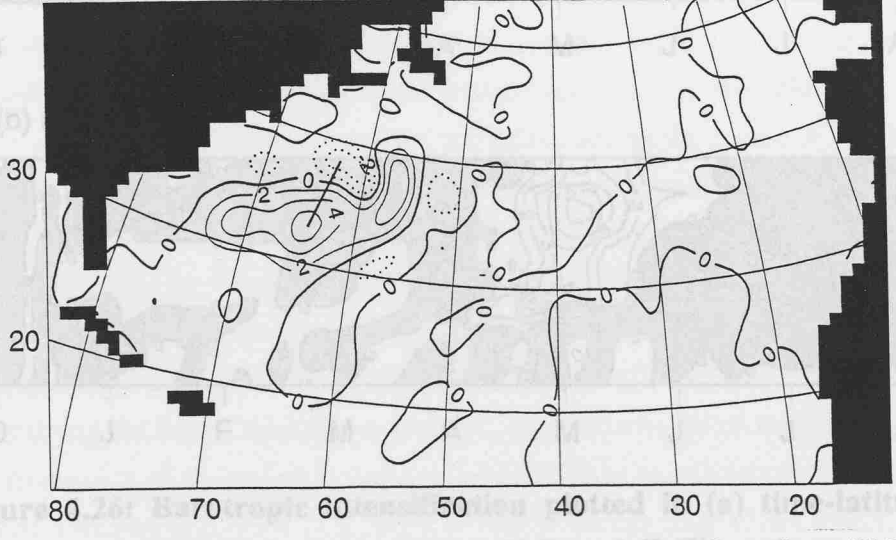

Figure 4.25: Mid-May fields of barotropic streamfunction (C.I. = 2 Sv) in (a) CLIM1, (b) COOL3 and (c) COOL3 minus CLIM1.

there is, in fact, a local *weakening* of ψ_{baro}, by almost 6 Sv. These differences in ψ_{baro} imply a local increase in transport of ~13 Sv, across a section (shown in **Fig. 4.25**) between 64°W, 33°N and 63°W, 38°N - see the crowding of streamlines across this section in **Fig. 4.25b**, compared to **Fig. 4.25a**. In CLIM1 the transport across this section is 18 Sv (see **Fig. 4.25a**). Therefore, the excess wintertime cooling in COOL3 has locally and temporarily increased model Gulf Stream transport across this section by almost 75%.

To complete a description of the anomalous barotropic response, **Fig. 4.26** shows ψ'_{baro} in time-latitude (**Fig. 4.26a**) and time-longitude (**Fig. 4.26b**) space. Sections are chosen to intersect at the mid-May maximum streamfunction anomaly (see **Fig. 4.25c**). **Fig. 4.26a** illustrates how, during late April/early May, large negative and positive values of ψ'_{baro} (exceeding ±5 Sv) develop in close proximity, north and south (respectively) of 35-40°N, locally intensifying zonal flow by more than 10 Sv in early May. **Fig. 4.26b** shows that positive values of ψ'_{baro} extend across the Sargasso Sea (as far east as 55°W) throughout May. **Figs. 4.26a,b** together confirm that the barotropic response to excess winter buoyancy loss is a strengthening of the western subtropical gyre and intensification of zonal transport (in the model Gulf Stream) by late spring.

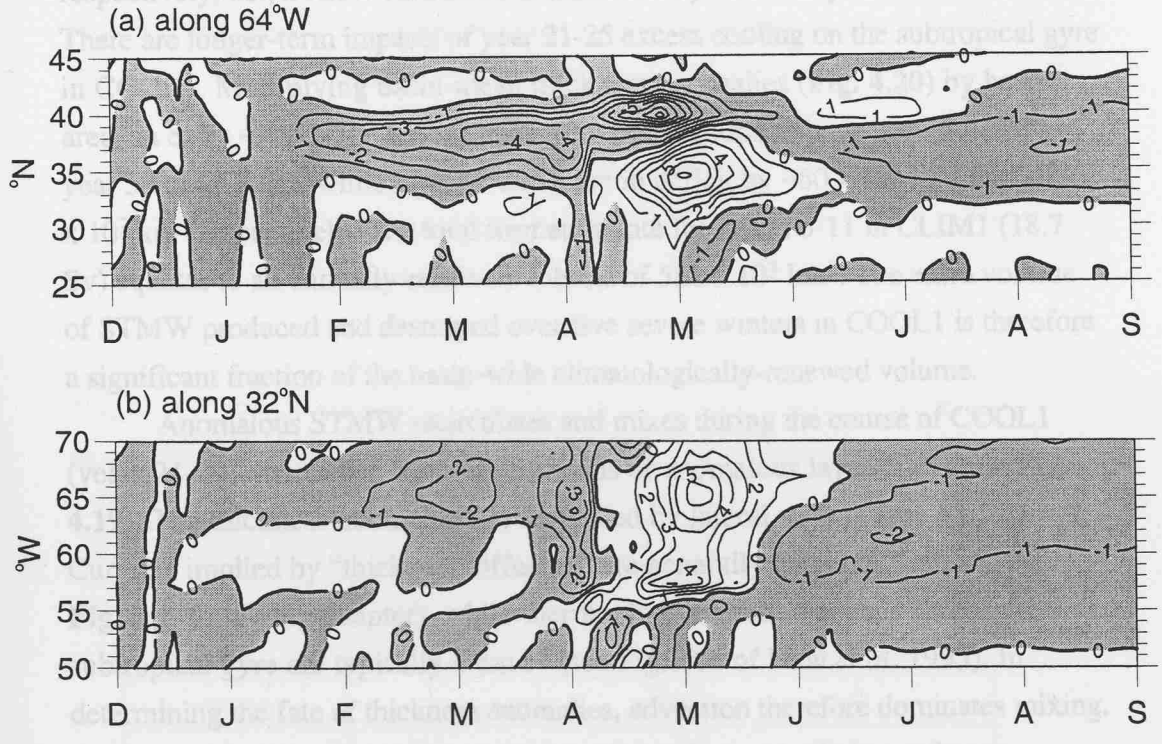

Figure 4.26: Barotropic intensification plotted in (a) time-latitude and (b) time-longitude space (along N-S and E-W sections across the Sargasso Sea recirculation gyre, labelling the monthly mid-points).

4.4 Modelling 18° Water variability and Gulf Stream intensification under excess buoyancy loss: a summary

The variability of model 18° Water in COOL1 (**Fig. 4.18**) is strikingly similar, qualitatively, to the evolution of low PV in 18° Water observed at *Panulirus* over 1964-71 (Talley and Raymer 1982). Year 21-25 evolution of anomalous 18° Water may also involve the storage mechanism proposed by Jenkins (1982). During the second and successive cold winters in COOL1, anomalous water residing in the *seasonal* thermocline is entrained back into the mixed layer, which is thus preconditioned for deeper mixing in subsequent winters at some locations. Indeed, comparing **Fig. 4.17b** to **Fig. 4.16b**, it is clear that by the fifth cold winter two lobes of deeper mixing extend eastwards and southeastwards from the main site of anomalous deep mixing.

Area-integrated STMW formation rates (ΔV_k) quantify the net impact of excess cooling on the mode waters of the subtropical gyre. Further integrating layer 5 (σ_θ = 26.10) to layer 11 (σ_θ = 27.00) ΔV_k data (**Fig. 4.21**) for CLIM1 and COOL1, yields total STMW formation estimates of 18.7 Sv and 22.3 Sv respectively, i.e., STMW formation is enhanced by ~20% in year 21 of COOL1. There are longer-term impacts of year 21-25 excess cooling on the subtropical gyre in COOL1. Multiplying basin-mean thickness anomalies (**Fig. 4.20**) by basin area, an extra ~200 x 10^3 km^3 of layer 10 water is found to have accumulated by year 30 of COOL1, while layers 7 and 8 are in deficit by ~60 x 10^3 km^3 and ~130 x 10^3 km^3 respectively. The total formation rate for layers 5-11 in CLIM1 (18.7 Sv) equates to an annually-renewed volume of 582 x 10^3 km^3. The extra volume of STMW produced and destroyed over five severe winters in COOL1 is therefore a significant fraction of the basin-wide climatologically-renewed volume.

Anomalous STMW recirculates and mixes during the course of COOL1 (years 21-30), evidenced by evolving fields of anomalous layer thickness (**Fig. 4.19**). The thickness anomalies are dispersed by lateral mixing (see §3.1.2). Currents implied by "thickness diffusion" are generally less than 1 cm s^{-1} (see **Fig. 5.1**, following chapter), while thermocline advection speeds across the subtropical gyre are typically 4 cm s^{-1} (see Fig. 16b of New *et al.* 1995). In determining the fate of thickness anomalies, advection therefore dominates mixing. The timescales of recirculation vary according to layer ventilation pathways. Lighter varieties of STMW (e.g., layer 8) follow shorter trajectories around the gyre (see **Fig. 4.8b**) and therefore recirculate faster than denser varieties (e.g., layer 10 - see **Fig. 4.8d**). By the end of COOL1, little evidence remains of

positive layer 8 thickness anomalies (**Fig. 4.19b**), which have fully recirculated and re-entrained into the Gulf Stream. In contrast, anomalous layer 10 thickness has only spread halfway around the gyre by year 30 (**Fig. 4.19d**). Comparison of COOL1, COOL2 and COOL3 (**Fig. 4.21**) indicates that 18° Water formation rates, roughly proportional to *total* excess buoyancy loss over the Gulf Stream, are independent of the *spatial pattern* of excess cooling.

The sensitivity experiments also display dynamical response to anomalous buoyancy forcing. Upon early spring restratification of anomalously deep winter mixed layers there is a steepening of isopycnals across the Gulf Stream (relative to CLIM1). The associated increase in horizontal pressure gradients (oriented across the Stream) drives enhanced geostrophic circulation in upper layers (**Fig. 4.22**). By late spring, barotropic responses are apparent. Barotropic streamfunction anomalies indicate that increased transports are associated with an intensified model Gulf Stream. The pattern of streamfunction anomaly obtained here (positive and negative, north and south of the excess-cooled Gulf Stream) is consistent with the lateral displacement of upper and lower layer transport in an idealized two-layer model subjected to sudden cooling (Stommel and Veronis 1980) - see §2.3.2. Strongest intensification in COOL3 (**Fig. 4.23**) is seemingly associated with strongest ocean-to-atmosphere buoyancy flux in that experiment. The initial (end-of-winter) dynamical response to excess cooling is spin-up of anomalously thick 18° Water layers in the Sargasso Sea (**Fig. 4.22**), followed in late spring by the barotropic intensification (**Fig. 4.25**). **Table 4.2** summarizes the relation of peak Gulf Stream intensification (the difference between maximum and minimum differences in the barotropic streamfunction) in May (when strongest barotropic responses are obtained) to peak cooling rates (see, for example, **Fig. 4.24a**).

Table 4.2. Peak cooling rates and peak Gulf Stream barotropic intensification in May, for each of the four sensitivity experiments.

Experiment	Peak excess cooling rates (Wm^{-2}, compared to ~350 Wm^{-2} in CLIM1)	Peak intensification (Sv)
COOL1	~110	8.2
COOL2	~110	8.9
COOL3	~310	14.6

There is little difference between the peak intensifications obtained in COOL1 and COOL2, although more extensive heat loss was imposed in COOL2, i.e., the intensification is locally-forced (by peak cooling in the close vicinity of the Gulf Stream). Compared to COOL1 and COOL2, peak excess cooling in COOL3 is stronger by ~200%, while COOL3 peak intensification is correspondingly stronger (than that in COOL1 and COOL2) by only ~75%. So, while the strength of intensification increases with excess cooling, this relationship is not simply linear.

The persistence of layer thickness anomalies, and the evolving dynamical response, must depend to some extent on the parameterization of lateral thickness mixing. To examine this dependancy, further sensitivity experiments are carried out with three different levels of parameterized "thickness diffusion" (applying the excess buoyancy loss of COOL3). These experiments are described in the next chapter, which also outlines a likely mechanism for the barotropic intensification.

CHAPTER 5. THE ROLE OF LAYER THICKNESS DIFFUSION: A MECHANISM FOR BAROTROPIC INTENSIFICATION IN THE CASE OF LOW DIFFUSION

Having established the sensitivity of model 18° Water and Gulf Stream transports to excess buoyancy loss, it remains to determine the extent to which simulated 18° Water variability and Gulf Stream intensification are dependent on model details. Full consideration of this issue would require an extensive range of model experiments, ideally varying horizontal and vertical resolution, as well as exploring a wide range of parameters (viscosity, isopycnal mixing, diapycnal mixing, etc.). However, for logistical reasons (see §3.2.2) only a limited number of further sensitivity experiments are possible. The prime motive here is to determine how the lateral mixing of potential vorticity (PV) by eddies (parameterized in MICOM by "layer thickness diffusion") smooths thickness anomalies and thereby damps the end-of-winter Gulf Stream intensification (as proposed by Marshall and Nurser 1988). In the following sections, the conservation of anomalous PV (following column trajectories) and the role of thickness diffusion (violating this conservation) are briefly considered (§5.1). The results of further sensitivity experiment pairs (climatologically-forced and excess-cooled) are presented, for cases of low and high thickness diffusion (§5.2). Taking the extreme case of low thickness diffusion, Gulf Stream intensification is then considered in terms of a barotropic vorticity balance (§5.3). The role of layer thickness diffusion and the mechanism for barotropic intensification (best evidenced in the case of low diffusion) are summarized in §5.4.

5.1 Potential Vorticity considerations

Potential vorticity (q) changes in balance with source/sink terms ($\mathcal{F}$ and $\mathcal{D}$ repectively):

$$\frac{Dq}{Dt} = \mathcal{F} - \mathcal{D} \tag{5.1}$$

and is otherwise conserved along flow trajectories. In the model, $\mathcal{F}$ acts at the surface to increase q through buoyancy input and to decrease q through surface buoyancy loss (the effects of wind mixing will also contribute somewhat to this term), while $\mathcal{D}$ diffuses q primarily through lateral mixing of layer thickness, a

model process which parameterizes the effects of eddies in homogenizing the field of q (see Rhines and Young 1982a).

Given the Sverdrupian approximation of q [Eqn. (3.15)], conservation of PV along a fluid trajectory involves adjustments of both stratification (inversely proportional to layer thickness in the model) and the Coriolis parameter (equivalently latitude). *If conserved following their motion*, layer thickness anomalies must therefore be accommodated in the model thermocline by corresponding changes in the trajectories of fluid columns. Changes in the Coriolis parameter f and h_k (the thickness of model layer k) must satisfy the balance

$$\frac{f(\Theta)\Delta\sigma_\theta}{\rho_o h_k(\Theta)} = \frac{f(\Theta-\Delta\Theta)\Delta\sigma_\theta}{\rho_o h_k(\Theta-\Delta\Theta)} \tag{5.2}$$

where $\Delta\sigma_\theta$ is the density range represented by layer k, Θ is latitude, and, moving to a lower latitude $\Theta-\Delta\Theta$, planetary vorticity and layer thickness must decrease in equal proportion.

Consider now the decadal-timescale recirculation of layer 10 in COOL1 and CLIM1. Once subducted, layer 10 thickness anomalies in COOL1 continue to evolve in the model permanent thermocline on decadal timescales (evident from comparison of **Figs. 4.19c-d**). Contours of Montgomery potential in **Fig. 4.8d** suggest that layer 10 thickness advects southwards and westwards in the recirculation. If the model thermocline was adiabatic, thickened layers in COOL1 might be expected to recirculate along trajectories which lie to the north of those followed by the thickest fluid columns in CLIM1. While the maximum positive thickness anomaly in COOL1 does appear to follow a somewhat northerly recirculation trajectory (compare **Fig. 4.8d** and **Fig. 4.19d**), the source latitude (subduction site) for anomalous thickness may also lie north of that (associated with strongest subduction) in CLIM1. The dynamics and fate of thickness anomalies are not, however, determined by advection alone. In the model thermocline, "thickness diffusion" (see Bleck *et al.* 1992 and §3.1.2) parameterizes subgrid-scale turbulence in the along-isopycnal flow, acting to disperse horizontal thickness gradients. Consider the effective velocity (analogous to, but not exactly the same as, the bolus velocity) due to thickness diffusion in layer k, $\mathbf{u}_k^*$:

$$\mathbf{u}_k^* = \left(\frac{U_k^*}{h_k^u \Delta y}, \frac{V_k^*}{h_k^v \Delta x} \right) \tag{5.3}$$

where U_k^* and V_k^* are zonal and meridional diffusive volume fluxes of layer k, h_k^u and h_k^v are the thicknesses of layer k at u and v-points, and Δx and Δy are the zonal and meridional dimensions of a gridbox. In the model thermocline (i.e., away from layer outcrops into the mixed layer), $\mathbf{u}_k^*$ is typically O(0.1-1.0 cm s^{-1}), an order of magnitude smaller than the advection velocity. Thickness diffusion is, however, generally perpendicular to the advection, accounting largely for the lateral spreading of thickness anomalies. The field of $\mathbf{u}_k^*$ for layer 10 in September year 30 of CLIM1 is obtained by Eqn. (5.3) and shown in **Fig. 5.1**.

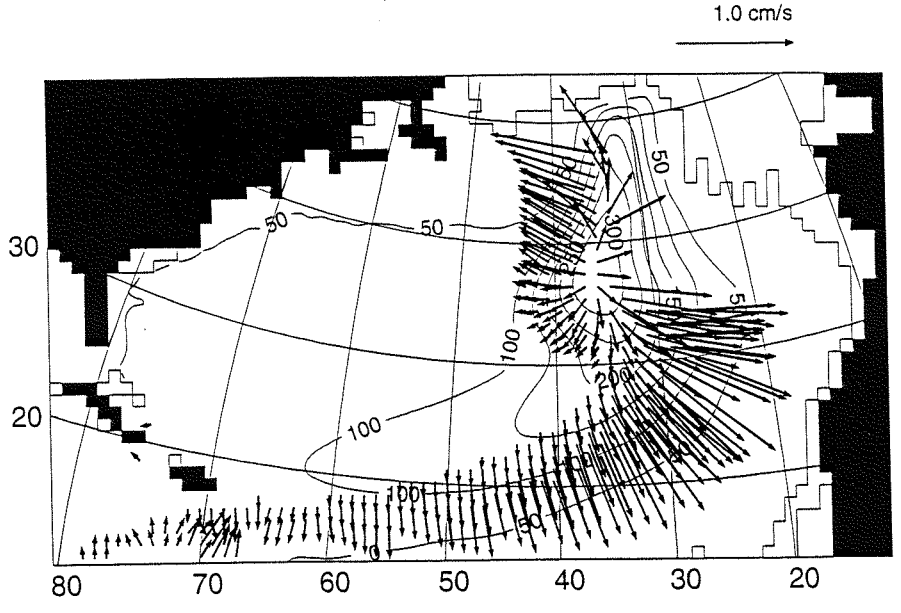

Figure 5.1: Layer 10 thickness field (m) and currents implied by thickness diffusion along maximum thickness gradient, in September year 30 of CLIM1.

Note that layer 10 thickness diffuses predominantly to the south and east, as lateral thickness gradients are strongest along the southern and eastern flanks of the layer. Layer thickness diffusion thus acts to disperse thermocline PV anomalies.

5.2 Thickness diffusion sensitivity experiments

The sensitivity to thickness diffusion of 18° Water variability and Gulf Stream intensification is now assessed by a comparison of the following experiment pairs (see **Table 3.2**): CLIM1 and COOL3 (with "best-estimated" thickness diffusion velocity, u_d = 1.0 cm s^{-1}); LOMIX and LOMIXCOOL (weak thickness diffusion, parameterized by u_d = 0.1 cm s^{-1}); HIMIX and HIMIXCOOL (strong thickness diffusion, parameterized by u_d = 10.0 cm s^{-1}). The philosophy of varying the thickness diffusion parameter by two orders of magnitude is to approach both the ventilated limit (in LOMIX and LOMIXCOOL), of Luyten, Pedlosky and Stommel (1983) and the diffusive limit (in HIMIX and HIMIXCOOL) of Rhines and Young (1982a).

The thickness diffusion velocity was changed after 20 years spin-up of a new control experiment CLIM2, in which u_d = 1.0 cm s^{-1}. The CLIM2 fields and sections are very similar to those for CLIM1 (as shown in §4.1). The major difference between CLIM1 and CLIM2 is the inclusion of diapycnal mixing in the latter experiment. Diapycnal mixing does not impact significantly on the thermocline, where conditions are near-adiabatic and mixing is oriented strongly along isopycnals. However, by changing the thickness diffusion velocity after 20 years of spin-up with u_d = 1.0 cm s^{-1}, the "background" stratification and circulation are forced to re-adjust during year 21 of cooling experiments LOMIXCOOL and HIMIXCOOL. If the model was spun up with u_d = 0.1 cm s^{-1} and u_d = 10.0 cm s^{-1}, the year 20 steady state would certainly be quite different (from the control CLIM2) in both cases. The decision to change u_d at year 20 is governed by logistics: to spin up two further (20-year) control experiments required too much computer time. In the first sub-section below, the spun-up control experiments LOMIX and HIMIX are first compared to CLIM2.

5.2.1 Changes in "background" stratification and circulation under low/high thickness diffusion

The effect of changing the thickness diffusion velocity (u_d) has a significant impact on the stratification and circulation of the subtropical gyre. In this respect the control experiments LOMIX and HIMIX differ markedly from CLIM2 (itself only slightly different from CLIM1), and differences (in stratification and circulation) develop rapidly, in the first few months of year 21. **Fig. 5.2** shows the monthly peak strengths of the subtropical gyre barotropic transport (equivalent

to the Gulf Stream transport), for the three control experiments, and the differences LOMIX-CLIM2 and HIMIX-CLIM2.

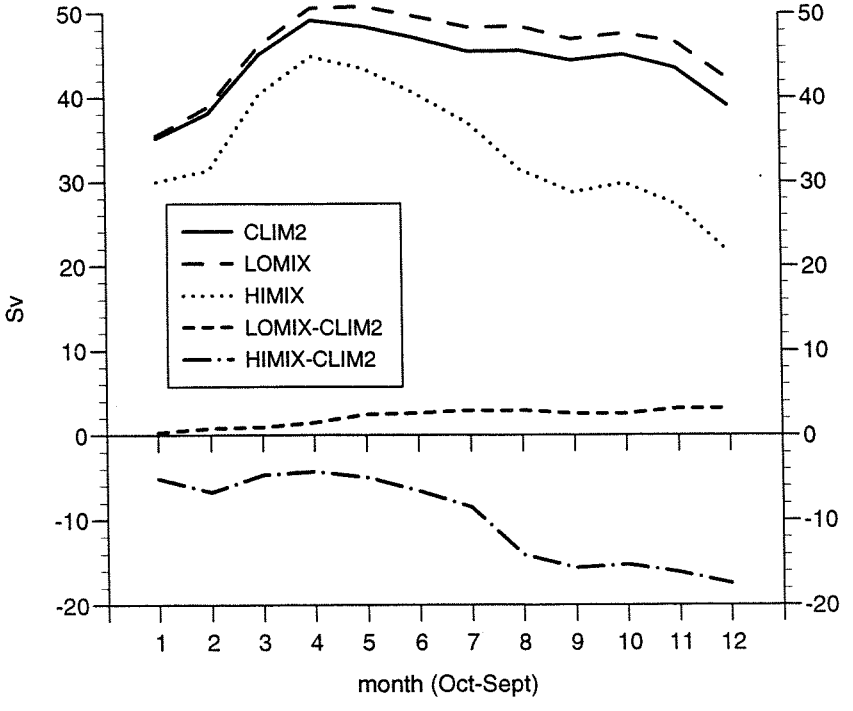

Figure 5.2: Year 21 monthly subtropical gyre strength for the three control experiments, varying the thickness diffusion parameter.

There is relatively little difference between the subtropical gyres of CLIM2 and LOMIX, although peak transport in LOMIX increases by about 3 Sv over year 21. However, the subtropical gyre in HIMIX is markedly weaker than in CLIM2, by nearly 18 Sv at the end of the year. Most notable in **Fig. 5.2** is the strong decrease in HIMIX transport after the end of winter, and the overall impression of a seasonal cycle which more closely resembles the Sverdrup response to seasonal variation in wind forcing (see **Fig. 4.4**). The implication - further tested in the excess buoyancy loss experiments - is that strong thickness diffusion weakens the end-of-winter barotropic response to cooling, leaving a clearer wind-forced seasonal cycle in transport. This is consistent with the stronger horizontal smoothing of layer thickness in HIMIX - weak horizontal density gradients in that experiment will lessen the impact of JEBAR and BPT (which acts to enhance spring barotropic transports and counter the wind-forced seasonal cycle in gyre strength - see §4.1.1)

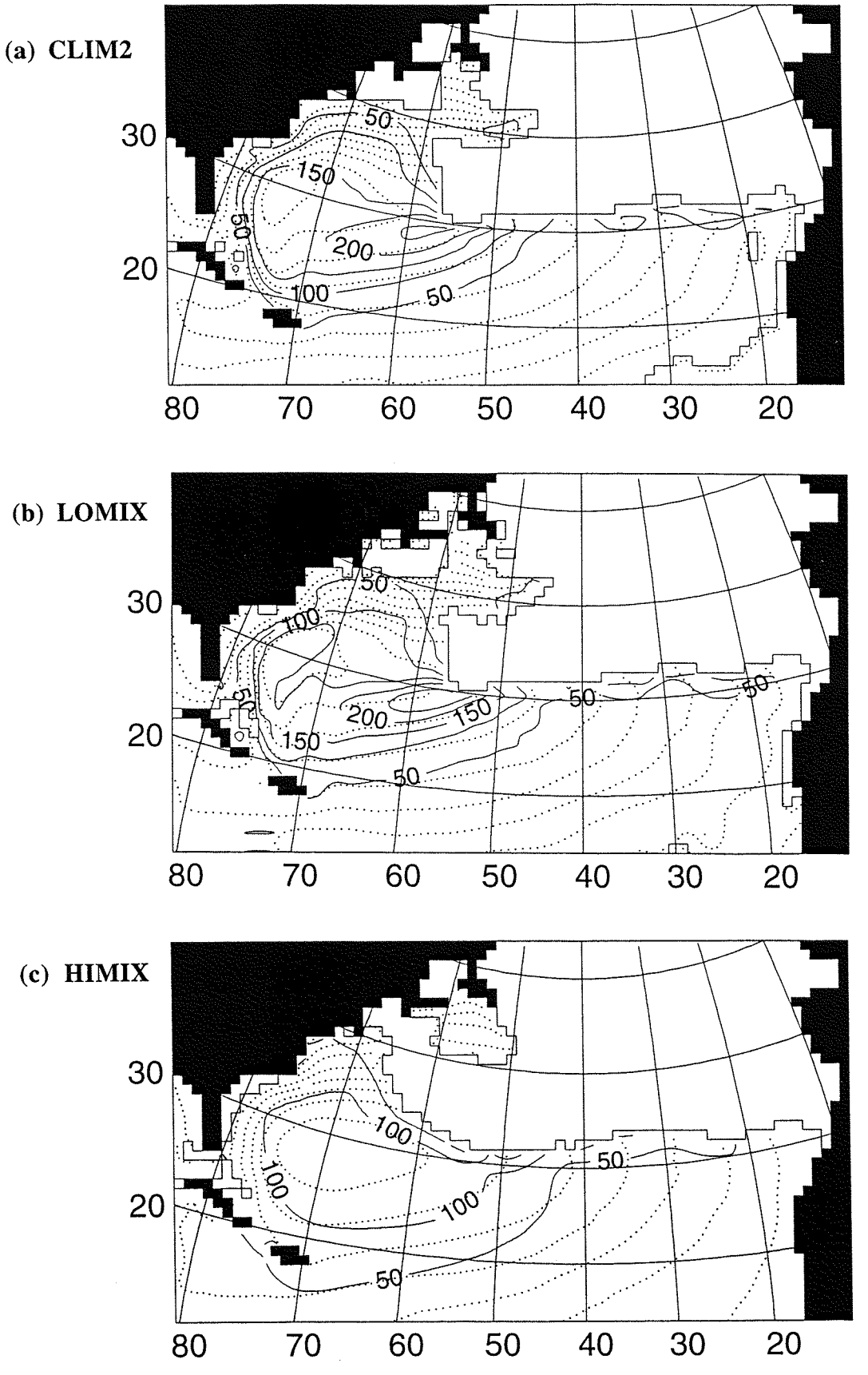

Figure 5.3: March year 21 layer 8 thickness fields (solid contours, C.I. = 50 m) and Montgomery potential (dotted contours, C.I. = 0.5 m^2s^{-2}) for three control experiments (CLIM2, LOMIX and HIMIX).

(a) CLIM2

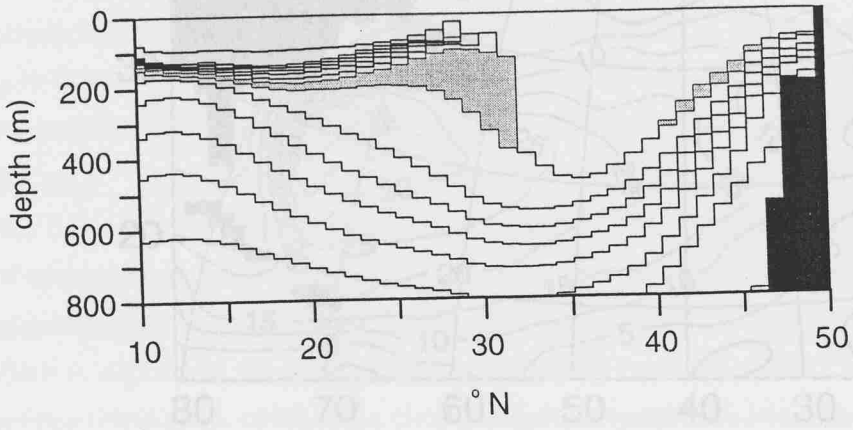

(b) LOMIX

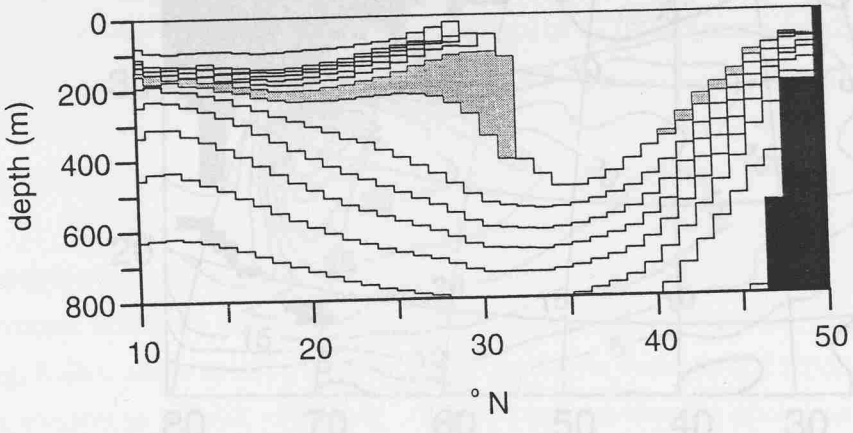

(c) HIMIX

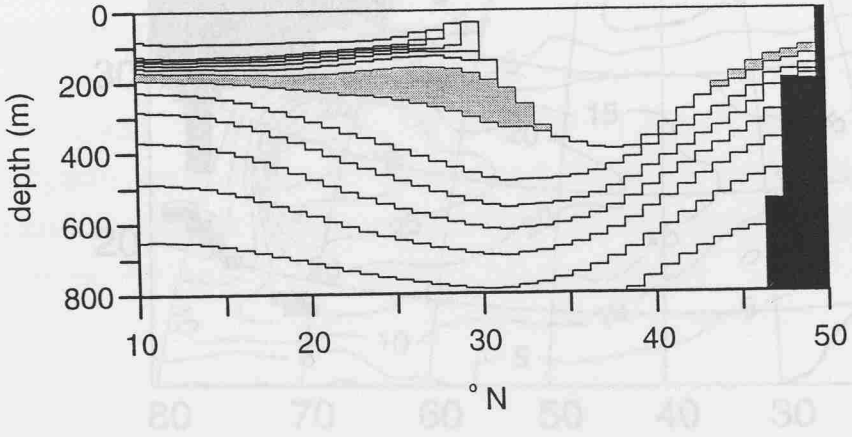

Figure 5.4: March year 21 meridional sections across the Sargasso Sea and Gulf Stream (along 55°W) for the three control experiments.

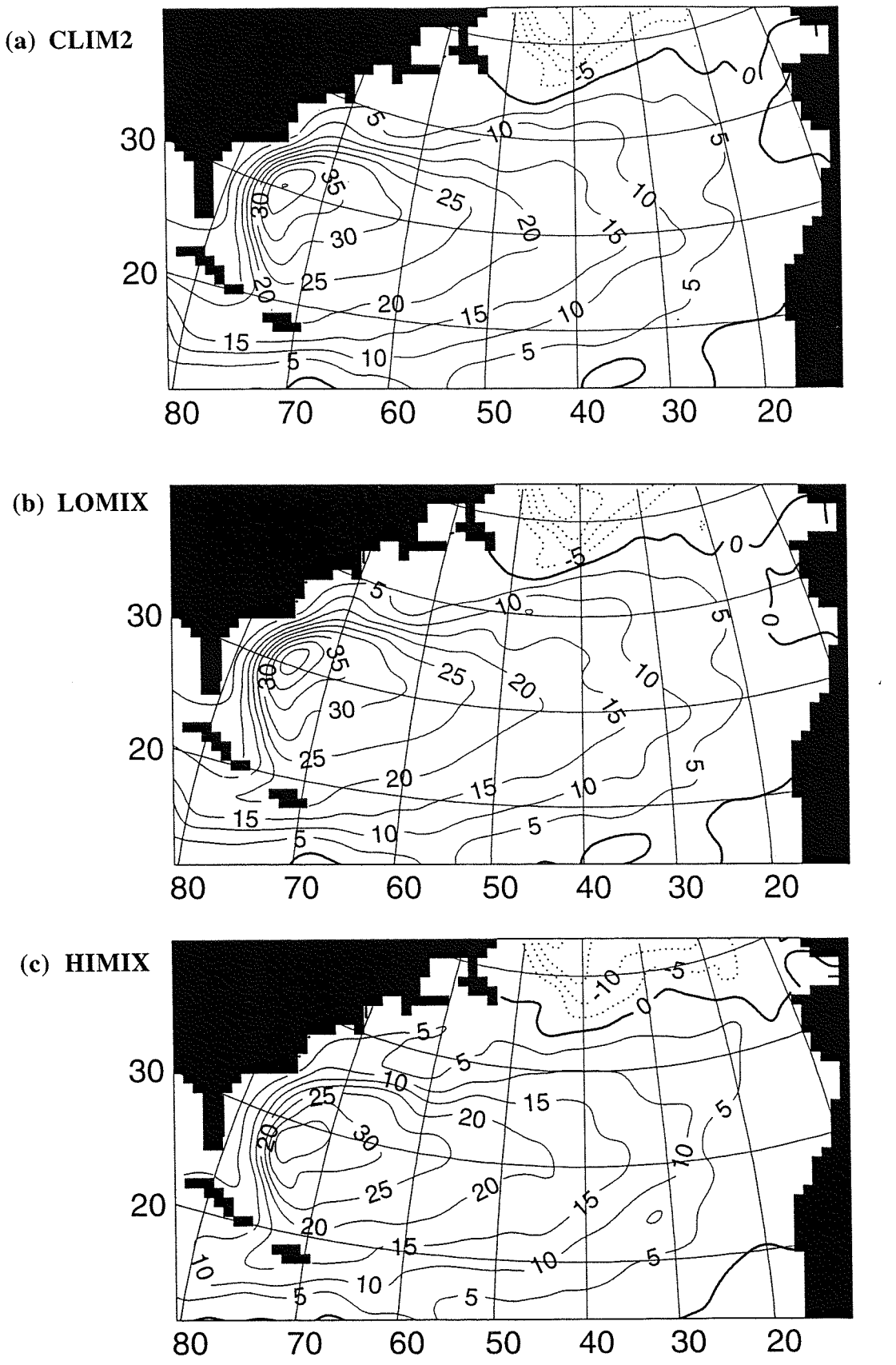

Figure 5.5: March year 21 barotropic streamfunction (Sv) for the three control experiments.

Fig. 5.3 shows March year 21 layer 8 thickness fields and Montgomery potential (M) streamlines for CLIM2, LOMIX and HIMIX. The effect of reducing u_d to 0.1 cm s^{-1} results (**Fig. 5.3b**) in only slightly stronger lateral thickness gradients compared to CLIM2 (**Fig. 5.3a**), while the effect of increasing u_d to 10.0 cm s^{-1} is to dramatically smooth the layer 8 thickness field by March year 21, after only 6 months (**Fig. 5.3c**). Also evident in **Fig. 5.3** are varying degrees of PV conservation following motion (i.e., along M contours). Thickness diffusion decreases high PV (by increasing thickness where layers are thin), the extent of which is implied by the angle/location at which M contours intersect thickness isolines (New *et al.* 1995). As a clear example, consider the 50m thickness isoline which lies south and east of the Sargasso Sea. In **Fig. 5.3a** this isoline is intersected by a M contour at 60°W, while in **Fig. 5.3b** the intersection of the same two contours is shifted to the vicinity of Hispaniola, indicating that layer 8 thickness (and hence PV) is better conserved in LOMIX (than CLIM2). In **Fig. 5.3c** the 50m thickness isoline lies further to the south (layer 8 having spread out more in HIMIX) and now intersects two M contours between 40°W and 70°W, illustrating the strongest thickness diffusion along layer trajectories in HIMIX.

Fig. 5.4 shows meridional sections (again for March year 21 of the three experiments) across the Sargasso Sea and Gulf Stream (along 55°W). Slightly stronger thickness gradients are apparent in LOMIX (comparing **Fig. 5.4a** and **Fig. 5.4b**), while notably weaker lateral thickness and implied pressure gradients are evident in HIMIX (**Fig. 5.4c**). Again it is clear that the thickness of layer 8 (grey-shaded) has been strongly smoothed (**Fig. 5.4c**). One would expect that weaker horizontal pressure gradients lead to a weaker subtropical gyre in HIMIX.

Fig. 5.5 shows the March year 21 barotropic streamfunction, again for the three experiments. The barotropic streamfunctions of CLIM2 and LOMIX are very similar, with subtropical gyre maxima of 45 Sv and 48 Sv respectively (comparing **Fig. 5.5a** and **Fig. 5.5b**), while the circulation in HIMIX (**Fig. 5.5c**) is significantly weakened (the subtropical gyre maximum transport is only 39 Sv). The relative weakness of the streamfunction in HIMIX is associated with a slackening of internal pressure gradients in that experiment.

5.2.2 The sensitivity of anomalous 18° Water formation and Gulf Stream intensification to thickness diffusion

Fig. 5.6 shows fields of thickness anomaly (COOL3 minus CLIM1; LOMIXCOOL minus LOMIX; HIMIXCOOL minus HIMIX) for layer 8 - the principal 18° Water layer - in May of year 21 (coincident with Gulf Stream intensification). In COOL3 (**Fig. 5.6a**) layer 8 thickens in the central and western Sargasso Sea while thinning (see grey-shading in **Fig. 5.6**) further to the east (as described at length in §4.3.1), with thickness anomalies reaching maximum and minimum values of 243 m and -373 m respectively. By comparison, the anomalies in LOMIXCOOL (**Fig. 5.6b**) range more widely, between 306 m and -411 m, while in HIMIXCOOL the extremes are limited to 124 m and -200 m (**Fig. 5.6c**). Having established that the Gulf Stream intensifies in the vicinity of anomalous 18° Water (see §4.3.3), differences in the *horizontal gradients* of anomalous thickness can be expected to drive intensifications of varying strength. The low level of thickness diffusion in LOMIXCOOL permits the strongest anomalous thickness gradients to persist in that experiment, while strong thickness diffusion acts to rapidly mix away anomalous thickness gradients in HIMIXCOOL. LOMIXCOOL and HIMIXCOOL may be expected to display Gulf Stream intensifications which are, respectively, stronger and weaker than in COOL3.

The evolving barotropic responses to cooling in LOMIXCOOL and HIMIXCOOL are obtained as for COOL3. **Fig. 5.7** shows the month-by-month maximum/minimum differences (COOL3 minus CLIM1; LOMIXCOOL minus LOMIX; HIMIXCOOL minus HIMIX) in barotropic streamfunction, reflecting the end-of-winter evolution of Gulf Stream intensification. There are appreciable differences between the three experiment pairs. The intensifying effects of excess cooling are strongest in the case of LOMIXCOOL, and weakest in HIMIXCOOL, suggesting that thickness diffusion plays an important role in the modelled Gulf Stream intensification. Strong thickness diffusion in HIMIX limits cooling-driven increases in horizontal pressure gradient, and hence the degree of intensification.

The extreme-case mid-May streamfunction difference field under low thickness diffusion (LOMIXCOOL minus LOMIX) is shown in **Fig. 5.8**. Changes in the barotropic streamfunction, in the vicinity of excess winter cooling, suggest some enhancement of the intensification seen previously in COOL3 (see **Fig. 4.25c**).

(a) COOL3

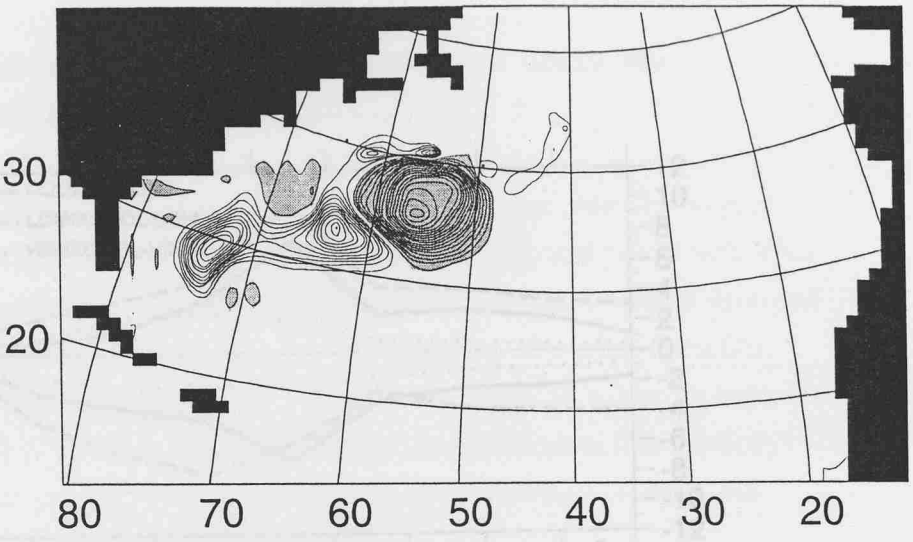

(b) LOMIXCOOL

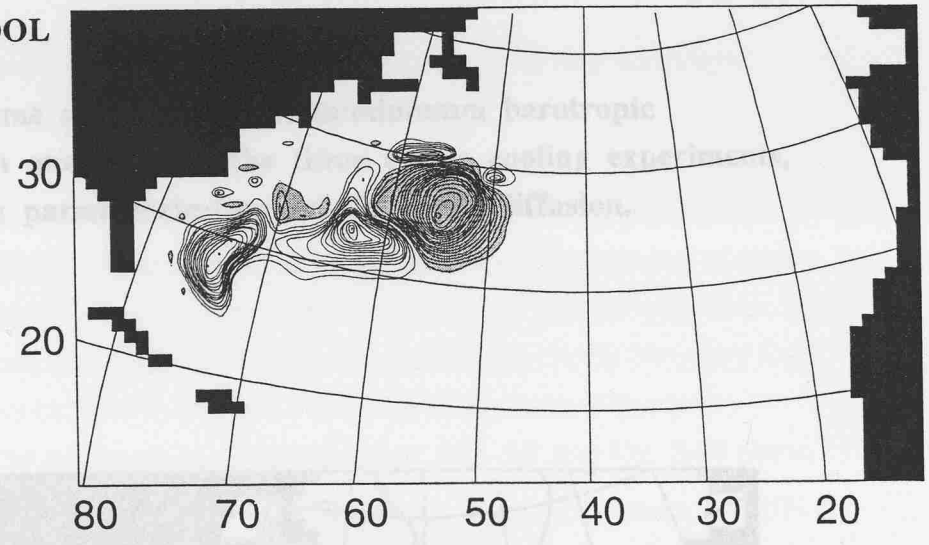

(c) HIMIXCOOL

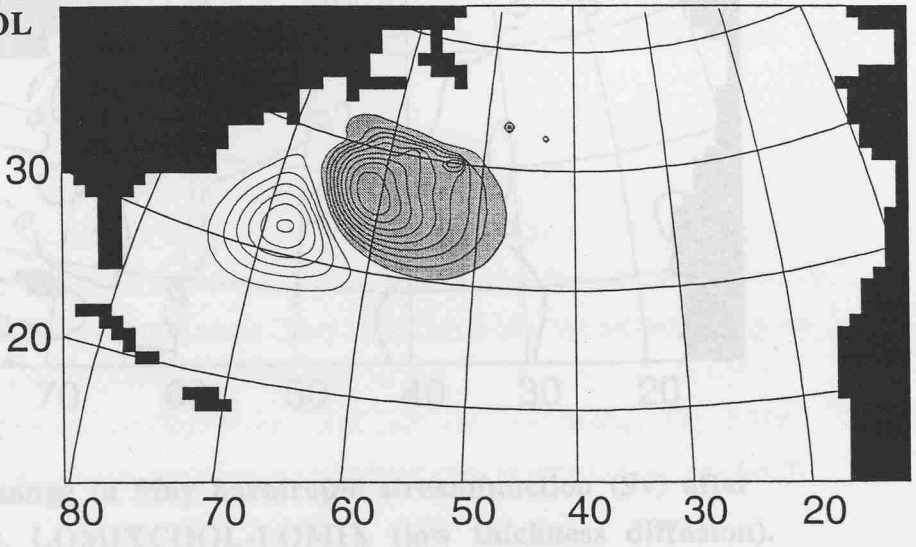

Figure 5.6: May year 21 anomalous layer 8 thickness fields (C.I. = 20 m), using the three thickness diffusion parameters.

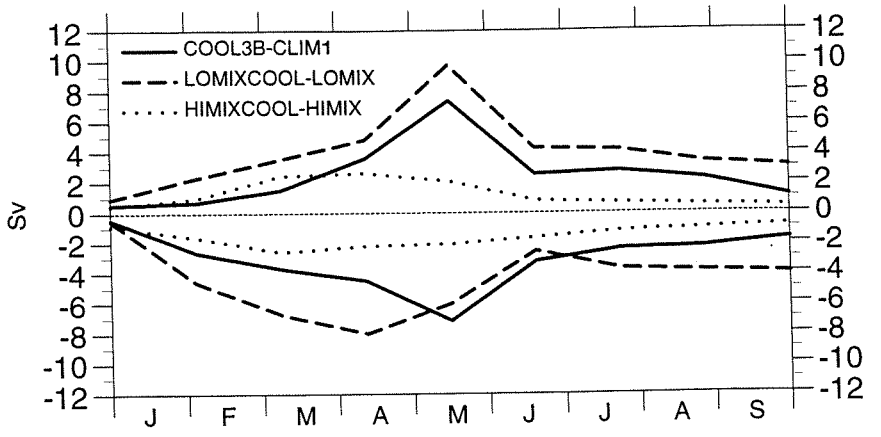

Figure 5.7: Time series of maximum/minimum barotropic streamfunction anomalies in the three excess cooling experiments, under varying parameterizations of thickness diffusion.

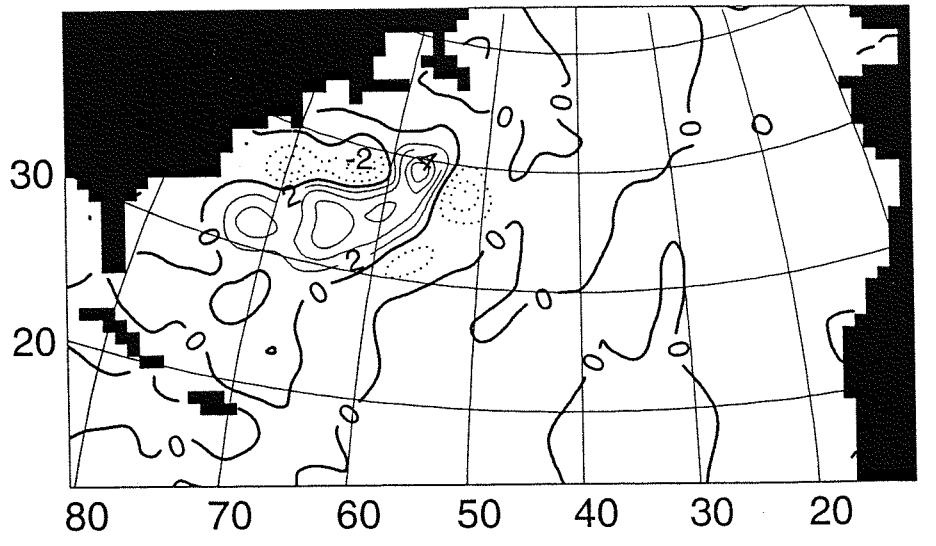

Figure 5.8: Change in May barotropic streamfunction (Sv) after excess cooling, LOMIXCOOL-LOMIX (low thickness diffusion).

5.3 The mechanism for barotropic intensification under low thickness diffusion

The mechanism for barotropic intensification is now examined, namely the process by which end of winter cooling forces a peak barotropic response two months after the end of excess cooling. Consider the case of LOMIXCOOL, for which strongest barotropic intensification is obtained under excess cooling. The initial baroclinic adjustment in the upper ocean (see §5.3.1 below) is followed by a deep dynamical response (see §5.3.2) which suggests that changes in stratification (baroclinicity) enhance barotropic transports through anomalous bottom pressure torques and JEBAR (see §2.2.2).

5.3.1 The vertical structure of transport preceding and during barotropic intensification

The dynamical response to excess buoyancy loss has been shown to be significantly barotropic. Buoyancy forcing might, however, be expected to drive a purely baroclinic circulation, averaging zero in a full-depth vertical integration. The distinction between baroclinic and barotropic responses (to excess buoyancy loss) is now clarified by examining changes in the vertical structure of transport preceding and during barotropic intensification. **Fig. 5.9** and **Fig. 5.10** show, respectively, March and May *layer-partitioned* zonal transports across 32-38°N at 65°W, a meridional section in the vicinity of strongest Gulf Stream transport and intensification (see **Fig. 5.5b** and **Fig. 5.8**), for LOMIX, LOMIXCOOL and the difference "LOMIXCOOL minus LOMIX".

Fig. 5.9c indicates an extra 9 Sv eastward transport in the March mixed layer, essentially at the expense of layers 7-9: a deeper end-of-winter mixed layer in LOMIXCOOL has entrained part of the layer 7-9 flow. The vertically-integrated anomalous transport is close to zero - i.e., the end-of-winter dynamical response to excess cooling is highly baroclinic. In May (see **Fig. 5.10**), the situation is quite different, with a vertically averaged transport anomaly of 6.1 Sv - i.e., delayed intensification of the model Gulf Stream is significantly barotropic. **Fig. 5.10c** indicates that this barotropic response is strongly related to transport anomalies in dense, deep layers 16-18. This deep response to surface cooling is now examined in further detail.

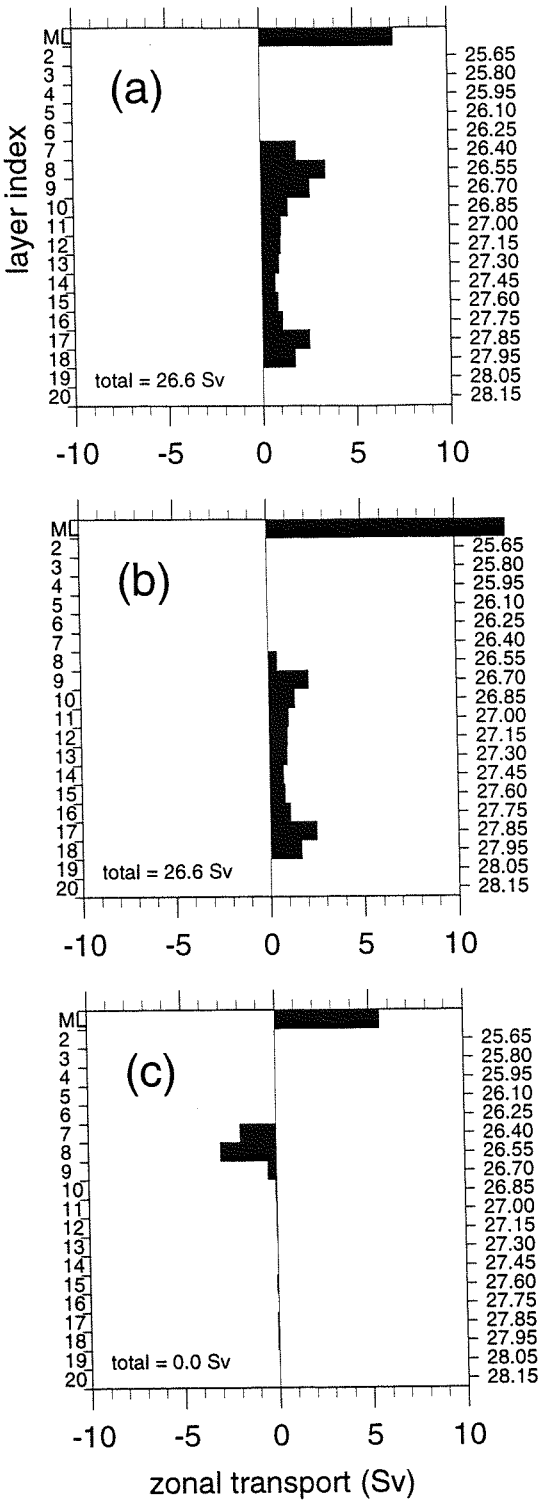

Figure 5.9: Layer-partitioned zonal transport (across 32-38°N at 65°W) in March: (a) LOMIX, (b) LOMIXCOOL (c) LOMIXCOOL minus LOMIX.

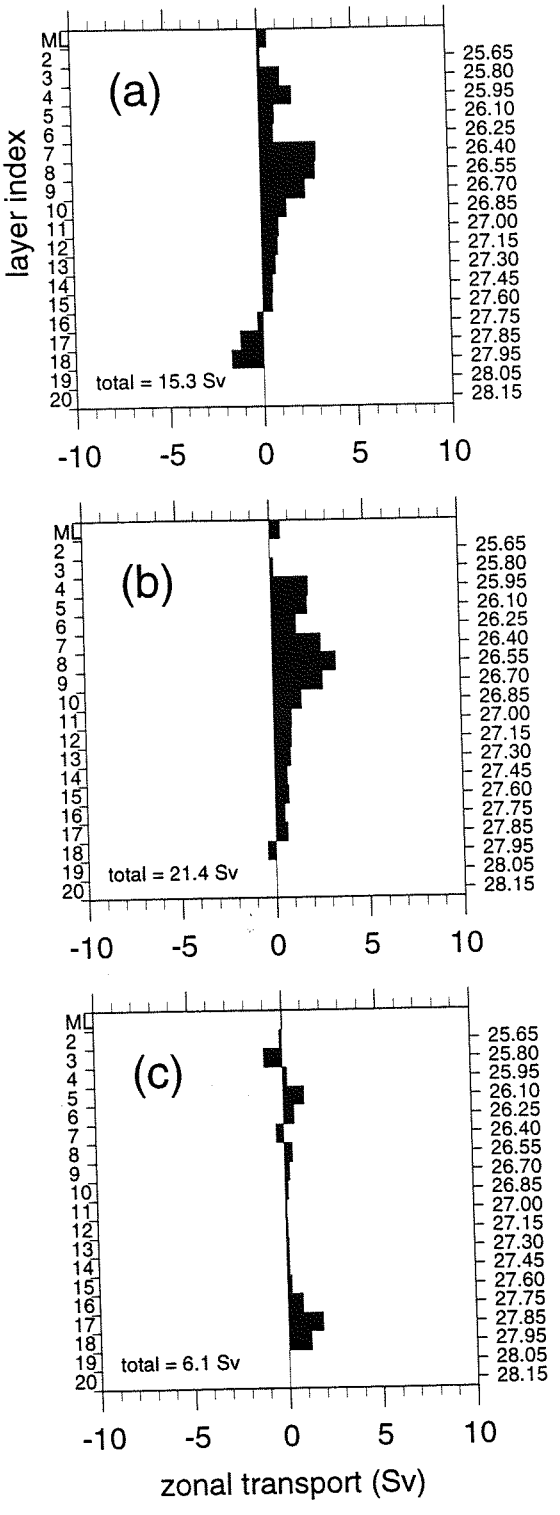

Figure 5.10: As Fig. 5.9, for May.

5.3.2 Anomalous bottom currents: do bottom pressure torques drive the barotropic intensification?

The barotropic intensification in May of LOMIXCOOL (**Fig. 5.8**) and the extra deep transports at 65°W (**Fig. 5.10c**), suggest a deep dynamical response to excess cooling. This is confirmed by May "LOMIXCOOL minus LOMIX" anomalous currents of around 1 cm s^{-1} in deep layers of the model (**Fig. 5.11**): layers 16, 17 and 18, which lie below about 1500 m and incorporate the model bottom currents, where these layers occupy the abyss (layer 16 is the abyssal layer along the continental slope, while layers 17 and 18 are abyssal layers in the western basin).

How might this full-depth response be forced by excess cooling? Consider the barotropic vorticity balance (Eqn. 2.10). Away from the immediate boundary, the compensating effects of lateral friction can be neglected (as in Holland 1973). Neglecting also changes in non-linear advection, and given that wind forcing remains climatological in both LOMIX and LOMIXCOOL, the balance of *anomalous* vorticity simplifies to:

$$\frac{\partial}{\partial t}\nabla^2(\rho_0\psi') = -\beta\frac{\partial(\rho_0\psi')}{\partial x} - J[p_b', H(x,y)] \tag{5.4}$$

where p_b' is anomalous bottom pressure, $H(x,y)$ is variable bottom depth, and, given a streamfunction anomaly ψ', $\rho_0\psi'$ is the anomalous barotropic mass transport. The left hand term in Eqn. (5.4) is the rate of change of relative vorticity, forced by sources/sinks (on the right hand side) of vorticity through changes in the planetary vorticity tendency and Bottom Pressure Torque (BPT). Holland (1973) showed that, in a steady state, vorticity generated by the wind stress curl is balanced by the planetary vorticity tendency and BPT in the region of recirculation, so the balance of anomalous vorticity may further simplify to:

$$\beta\frac{\partial(\rho_0\psi')}{\partial x} = -J[p_b', H(x,y)] = \frac{\partial p_b'}{\partial y}\frac{\partial H}{\partial x} - \frac{\partial p_b'}{\partial x}\frac{\partial H}{\partial y} \tag{5.5}$$

and from the geostrophic approximation implicit in Eqn. (5.5),

$$\beta\frac{\partial(\rho_0\psi')}{\partial x} = -f\rho_0\left(u_b'\frac{\partial H}{\partial x} + v_b'\frac{\partial H}{\partial y}\right) = -f\rho_0\mathbf{u}_b'.\nabla H = -f\rho_0 w_b' \tag{5.6}$$

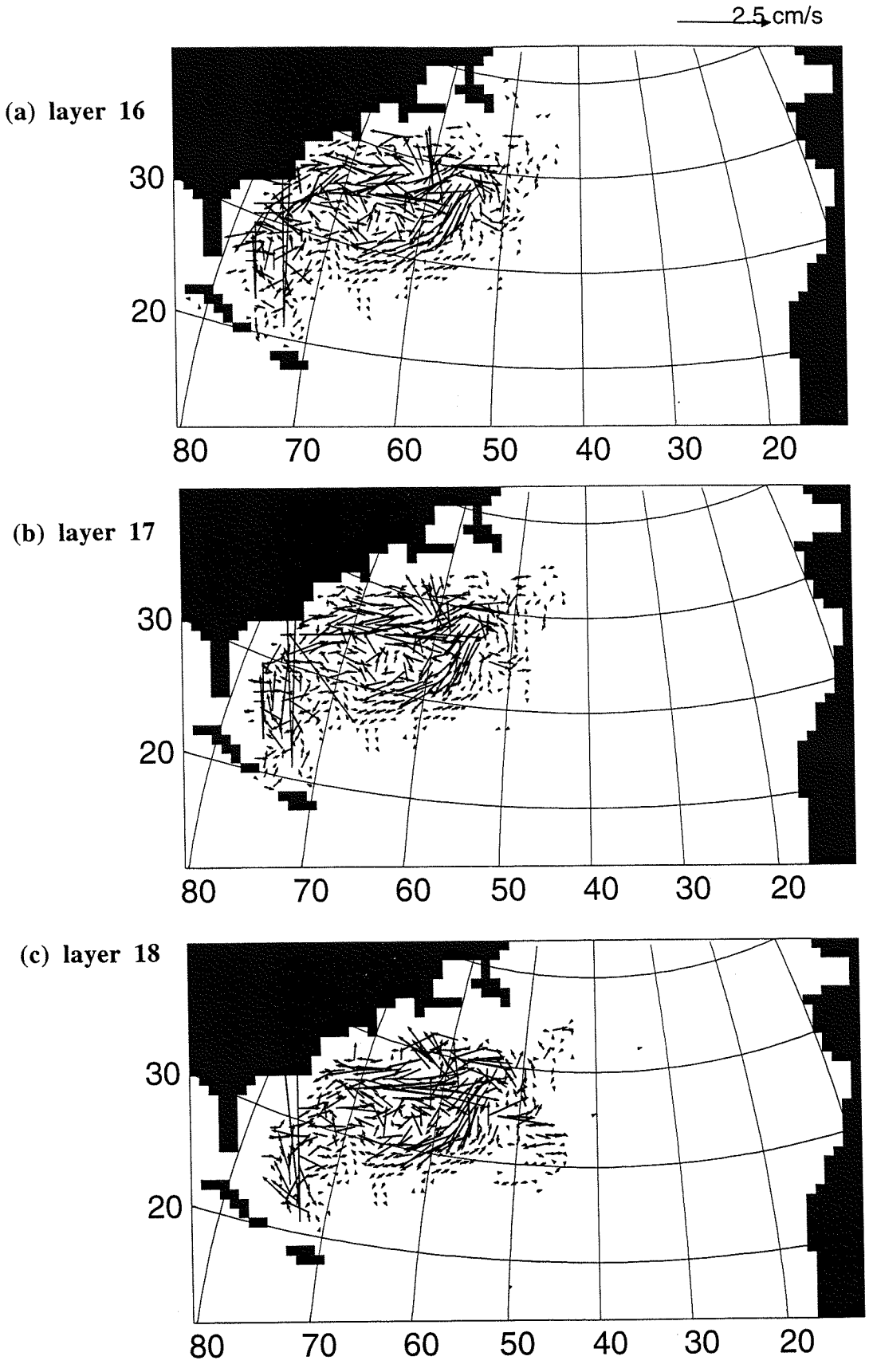

Figure 5.11: Anomalous abyssal layer currents (LOMIXCOOL minus LOMIX) in May year 21: (a) layer 16, (b) layer 17, (c) layer 18.

where $\mathbf{u}'_b = (u'_b, v'_b)$ is the anomalous velocity along the bottom and w'_b is the anomalous implied vertical velocity at the bottom (more strictly speaking, at the top of a thin bottom boundary layer).

Here it is hypothesized that the rate of change of vorticity is small, and the intensified barotropic recirculation in May reflects a balance between BPT and the planetary vorticity tendency:

$$\beta \frac{\partial \psi'}{\partial x} = -f w'_b \tag{5.7}$$

The intensified abyssal (layer 18) circulation is characterized by strong anomalous currents (**Fig. 5.11c**) in the mid-Atlantic Bight. **Fig. 5.12a** shows the model topography, in this region (60-65°W, 30-35°N) characterized by a plateau feature (incorporating the Bermuda Rise). Where the anomalous currents traverse isobaths, vorticity generation through the BPT term will be evidenced by non-zero anomalous bottom velocities. On the model C-grid, mass-point centred values for w'_b are obtained as $\overline{w'_{i,j,k}} = \mathbf{u}'_{i,j,k}.\nabla H_{i,j}$ where the abyssal layer is of index k.

Fig. 5.12b shows w'_b for layer 18 in May. While the field is rather noisy, note that a band of positive (upward) w'_b, with values up to ~20 m month^{-1}, predominates in the region of intensification, consistent with strengthened southward barotropic flow (an intensified recirculation). Large upward and downward motions along the continental shelf (exceeding ± 50 m month^{-1} in places) are associated with very steep slopes there (see **Fig. 5.12a**), and are probably balanced by lateral friction and non-linear terms (see Eqn. 2.10).

To determine whether vorticity generation through anomalous bottom pressure torques is locally balanced by an anomalous barotropic circulation tendency, these two terms [see Eqn. (5.7)] are computed, again for May year 21 of LOMIXCOOL, and plotted as fields in **Fig. 5.13a,b**. Note that bottom velocity is now computed *everywhere* (taking $\mathbf{u}'_b$ for the abyssal model layer). For an intensified *anticyclogenic* circulation, extra *negative* vorticity must be generated. This is indeed suggested by the predominant negative anomaly of planetary vorticity tendency in **Fig. 5.13b**. However, the field of $-f w'_b$ in **Fig. 5.13a** is very noisy, and can be compared only tentatively with $\beta \partial \psi'/\partial x$ in the region of intensification, where there is some correspondance between negative lobes oriented southwest-northeast from (60°W, 30°N) to (65°W, 35°N). **Fig. 5.13b** also shows patches of alternately positive and negative planetary vorticity

tendency, perhaps indicating the southwestward propagation of topographic shelf-edge waves away from the region of strong barotropic intensification. The wavelength is suggested by positive-negative-positive patterns spanning 10° of longitude, or ~1000 km. Such a wavelength is consistent with that for a first mode barotropic shelf wave (Slørdal and Weber 1996).

(a) bathymetry

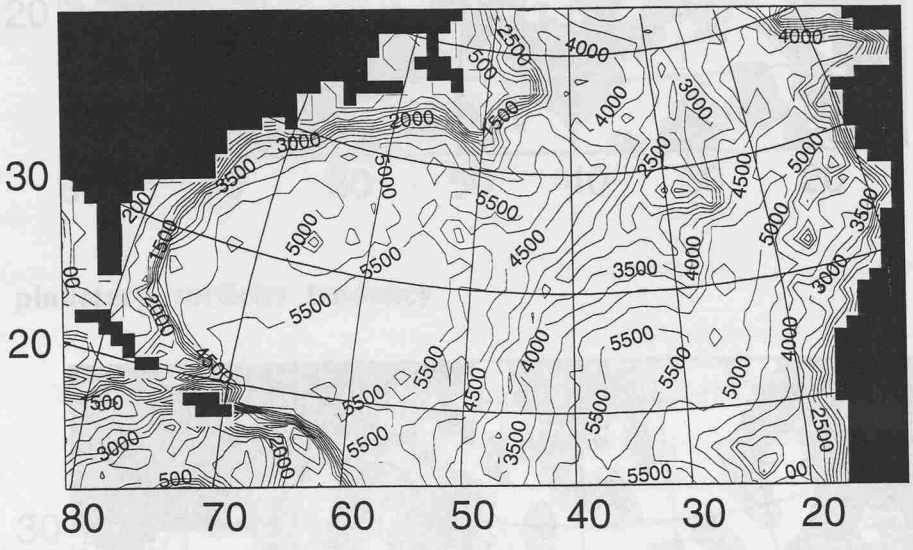

(b) vertical velocity

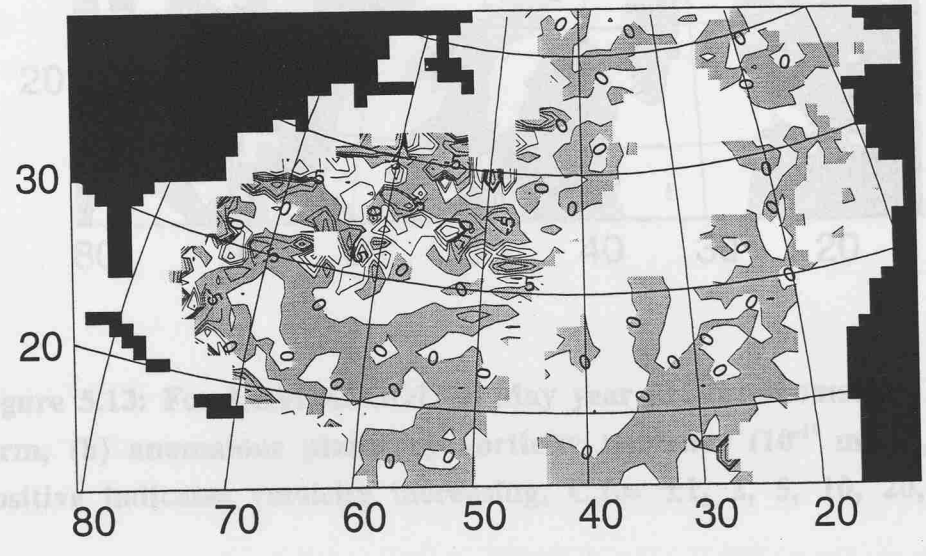

Figure 5.12: (a) model bathymetry (C.I. = 500 m), (b) implied anomalous bottom (layer 18) vertical velocities (m month^{-1}, positive upwards, C.I. = ±5, 10, 20, 50) in May year 21 of LOMIXCOOL.

(a) BPT term

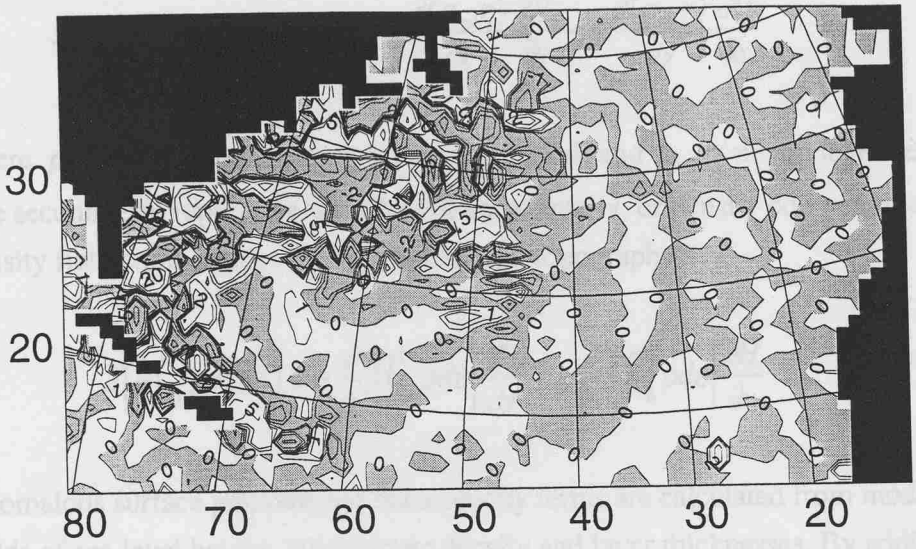

(b) planetary vorticity tendency

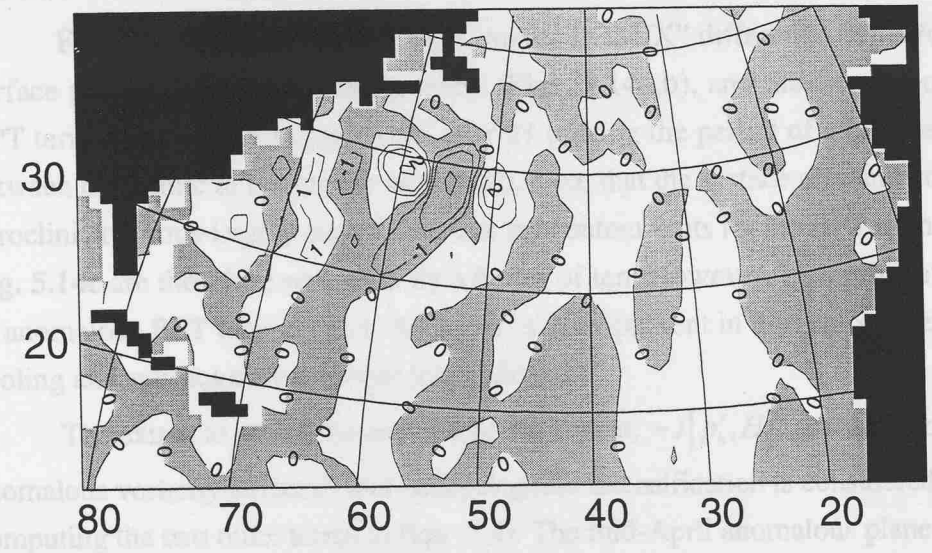

Figure 5.13: For LOMIXCOOL in May year 21: (a) anomalous BPT term, (b) anomalous planetary vorticity tendency (10^{-10} m^{-2} s^{-2}, positive indicates vorticity increasing, C.I.= ±1, 2, 5, 10, 20, 50).

BPT provides the connection between changes in the stratification (principally through anomalous STMW formation) and barotropic vorticity generation. The BPT term can be split into two terms [Eqn. (2.12)]. The first term represents the effect of sea surface topography, or surface pressure:

$$J[p_s,H]=J[(g\rho_{ml}\eta),H]=g\frac{\partial(\rho_{ml}\eta)}{\partial x}\frac{\partial H}{\partial y}-g\frac{\partial(\rho_{ml}\eta)}{\partial y}\frac{\partial H}{\partial x} \tag{5.8}$$

where p_s is surface pressure, η is mean sea level, and ρ_{ml} is mixed layer density. The second term represents the effect of baroclinicity, or density compensation (the density field compensates for variable bottom topography):

$$J\left[g\int_{-h}^{0}\rho dz,H\right]=g\frac{\partial}{\partial x}\left[\int_{-h}^{0}\rho dz\right]\frac{\partial H}{\partial y}-g\frac{\partial}{\partial y}\left[\int_{-h}^{0}\rho dz\right]\frac{\partial H}{\partial x} \tag{5.9}$$

Anomalous surface pressure and baroclinicity terms are calculated from model fields of sea level height, mixed layer density and layer thicknesses. By adding surface pressure and baroclinicity terms, the residual term, $J[p_b',H]$, is recovered. The BPT term in a balance of anomalous barotropic vorticity is then $-J[p_b',H]$.

Fig. 5.14 shows "LOMIXCOOL minus LOMIX" difference fields for the surface pressure and baroclinicity terms (**Figs. 5.14a,b**), and the anomalous BPT term (**Fig. 5.14c**), in mid-April year 21 (during the period of adjustment between baroclinic to barotropic responses). Note that the surface pressure and baroclinicity terms largely cancel, and that the contour units for the BPT term in **Fig. 5.14c** are therefore scaled up by a factor of ten. However, a significant level of anomalous BPT (around -2 x 10^{-7} kg m^{-2} s^{-2}) is apparent in the region of excess cooling and subsequent barotropic intensification.

The extent to which the anomalous BPT term, $-J[p_b',H]$, accounts for a net anomalous vorticity tendency and anticyclogenic intensification is considered by computing the two other terms in Eqn (5.4). The mid-April anomalous planetary vorticity tendency term, $\beta\partial/\partial x(\rho_0\psi')$, is shown in **Fig. 5.15a**. The anomalous transient term, $\partial/\partial t(\nabla^2\rho_0\psi')$, is computed by taking April-centred "May minus March" differences in $\nabla^2\psi'$, and is shown in **Fig. 5.15b**. Values of $\partial/\partial t(\nabla^2\rho_0\psi')$, although rather small, do reach -1 x 10^{-7} kg m^{-2} s^{-2} in the Sargasso Sea. The net rate of change in vorticity, $\partial/\partial t(\nabla^2\rho_0\psi')+\beta\partial/\partial x(\rho_0\psi')$, is shown in **Fig. 5.15c**. Consistent with the March to May intensification of anticyclogenic circulation, the net change in vorticity is predominantly negative in the Sargasso Sea. A reasonable degree of similarity between **Fig. 5.14c** and **Fig. 5.15c** (e.g., coincidence of similar-magnitude positive and negative values) suggests that the anticyclogenic intensification is primarily driven by anomalous BPT.

(a) surface pressure term

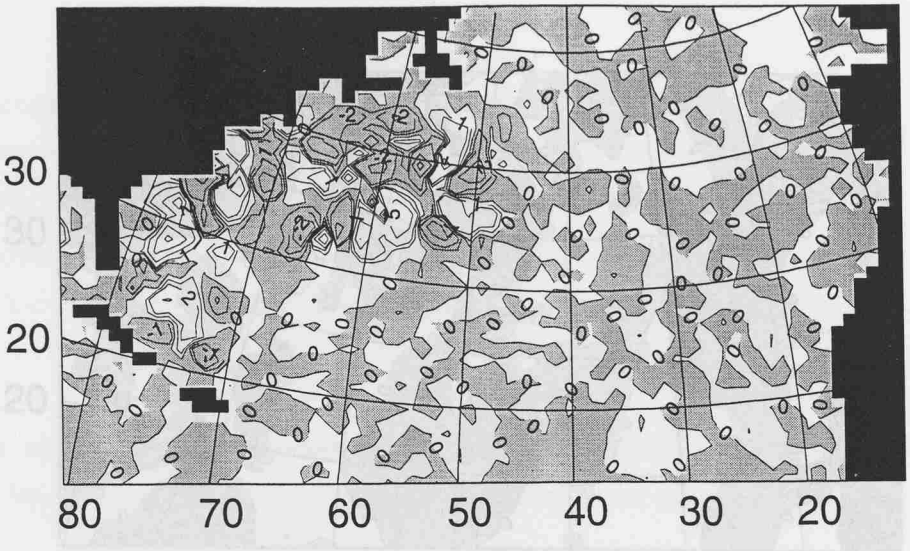

(b) baroclinicity term

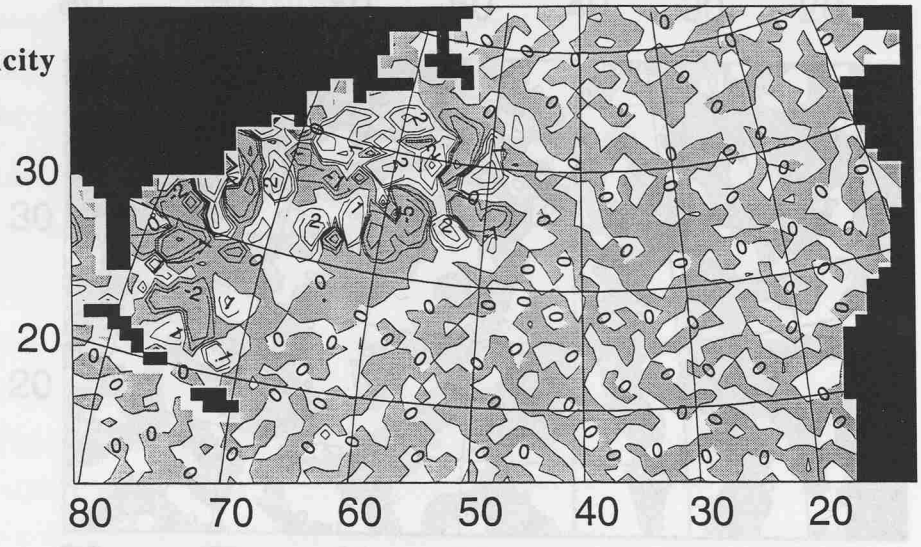

(c) BPT

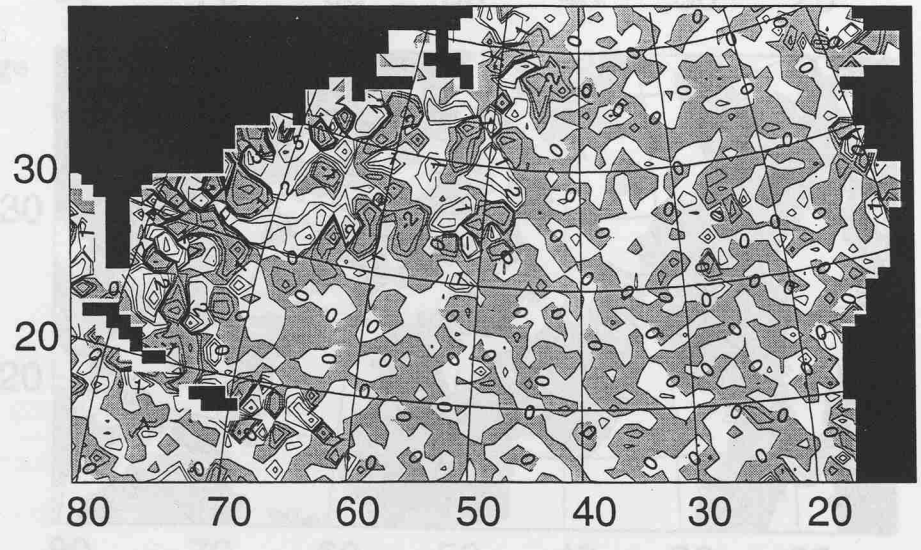

Figure 5.14: April year 21 LOMIXCOOL minus LOMIX differences in barotropic vorticity generation through changes in (a) surface pressure, (b) baroclinicity (units 10^{-6} kg m^{-2} s^{-2}), and (c) the residual anomalous BPT term (units 10^{-7} kg m^{-2} s^{-2}).

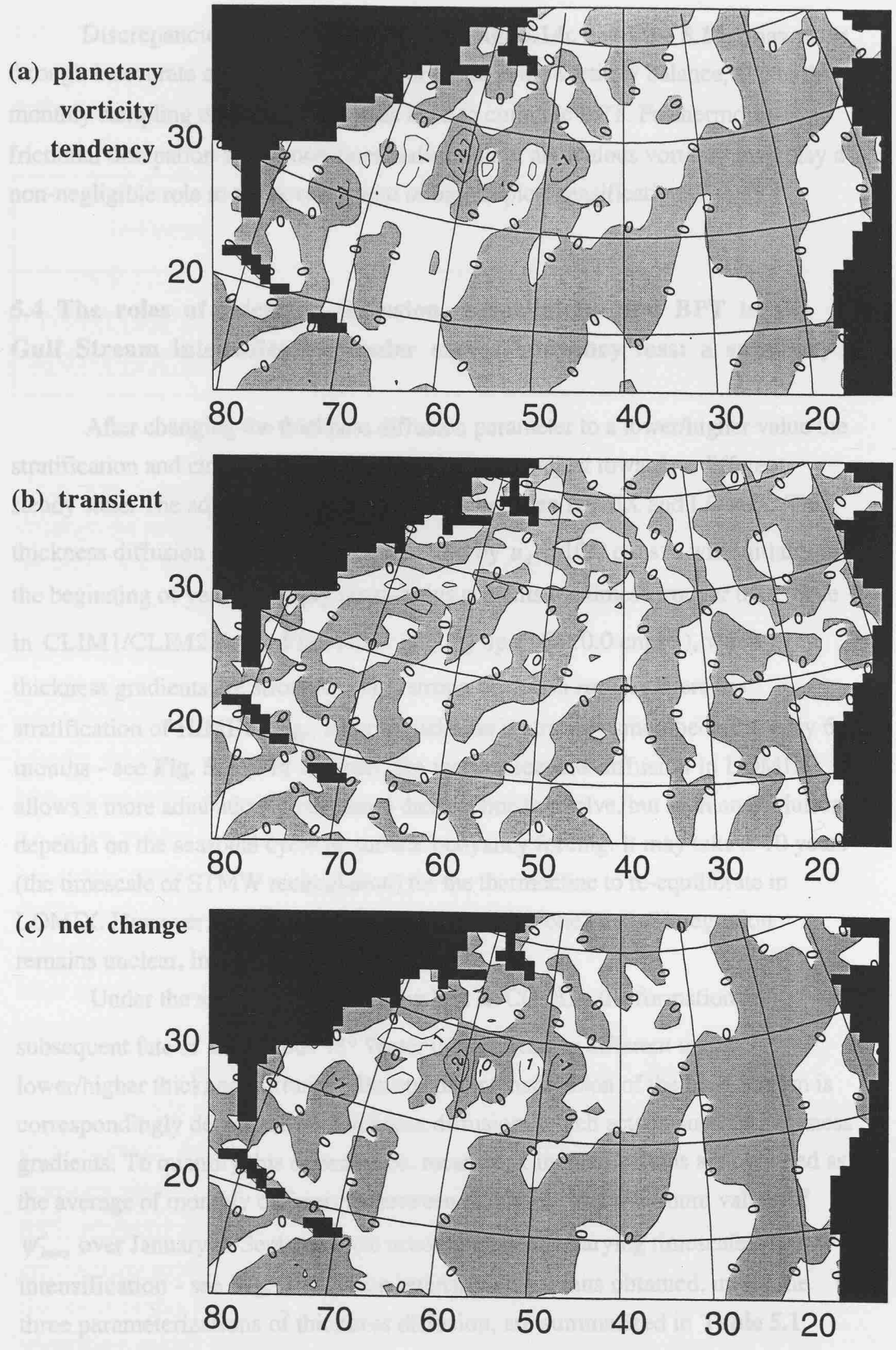

Figure 5.15: LOMIXCOOL minus LOMIX differences in (a) April planetary vorticity tendency, (b) March-to-May barotropic vorticity transient, and (c) net vorticity change (units 10^{-7} kg m^{-2} s^{-2}).

Discrepancies between the fields in **Fig. 5.14c** and **Fig. 5.15c** may arise through inaccurate offline computation of terms in the vorticity balance, due to the monthly sampling of ψ' and the fields used to compute BPT. Furthermore, frictional dissipation and/or non-linear advection of anomalous vorticity may play a non-negligible role in the development of barotropic intensification.

5.4 The roles of thickness diffusion, baroclinicity and BPT in the Gulf Stream intensification under excess buoyancy loss: a summary

After changing the thickness diffusion parameter to a lower/higher value the stratification and circulation of the subtropical gyre adjust towards a different steady state. The adjustment timescale differs between HIMIX and LOMIX. The thickness diffusion in HIMIX, parameterized by u_d = 10.0 cm s^{-1}, will initially (at the beginning of year 21) imply quasi-bolus currents ten times stronger than those in CLIM1/CLIM2 (e.g., **Fig. 5.1**) - i.e., $\mathbf{u}_k^*$ up to O(10.0 cm s^{-1}), where thickness gradients are strongest. This strong diffusion *rapidly* alters the stratification of HIMIX (e.g., layer 8 thickness is strongly smoothed after only 6 months - see **Fig. 5.3c**). In contrast, the weak thickness diffusion in LOMIX allows a more adiabatically ventilated thermocline to evolve, but such an evolution depends on the seasonal cycle of surface buoyancy forcing. It may take 5-10 years (the timescale of STMW recirculation) for the thermocline to re-equilibrate in LOMIX. However, the extent of re-adjustment after one year of integration remains unclear, in both HIMIX and LOMIX.

Under the same excess buoyancy loss as COOL3, the formation and subsequent fate of anomalous 18° Water is significantly different under lower/higher thickness diffusion. Barotropic intensification of the Gulf Stream is correspondingly dependent on thickness diffusion, which acts to smooth thickness gradients. To quantify this dependence, mean peak intensifications are obtained as the average of monthly differences between maximum and minimum values of ψ'_{baro} over January to September (to accommodate the varying timescales of intensification - see **Fig. 5.7**). Mean intensifications thus obtained, under the three parameterizations of thickness diffusion, are summarized in **Table 5.1**.

Table 5.1 Peak barotropic intensification of the Gulf Stream, averaged over January to September, for each of the three thickness diffusion sensitivity experiments.

Experiment pairs (differenced)	thickness diffusion velocity, u_d (cm s^{-1})	Mean peak intensification (Sv)
COOL3 minus CLIM1	1.0	5.6
LOMIXCOOL minus LOMIX	0.1	8.5
HIMIXCOOL minus HIMIX	10.0	2.8

Mean peak intensification is clearly stronger under lower thicknes diffusion, although the relationship appears to be rather non-linear (as was the relationship between peak intensification and excess cooling rate).

The mechanism for barotropic intensification has been further examined in the case of LOMIXCOOL. Considering "LOMIXCOOL minus LOMIX" layer transport anomalies in a section across the model Gulf Stream, it is shown that in mid-March, shortly before the cessation of excess buoyancy loss (at the end of March), the dynamical response of the model is primarily baroclinic, while by mid-May an anomalous barotropic structure has emerged. Anomalous barotropic transports in May are confined to deep and abyssal layers. An approximate barotropic vorticity balance is used to demonstrate how the bottom pressure torque (BPT) and baroclinicity (i.e., JEBAR) are implicated in the generation of anticyclogenic intensification. Associated with anomalous currents in the abyssal layer are anomalous vertical velocities. Assuming a steady state, and neglecting the non-linear advection and frictional dissipation of vorticity, the BPT must be balanced by a planetary vorticity tendency. This is not clearly the case during intensification in mid-May. However, in mid-April (while barotropic intensification is developing), the *net* generation of anomalous barotropic vorticity (transient plus planetary vorticity tendency terms) is roughly explained in terms of anomalous BPT, explicitly obtained as the residual of surface pressure plus compensating baroclinicity terms. While a full and accurate barotropic vorticity balance is beyond the scope of this study, the evidence presented here strongly suggests that wintertime excess buoyancy loss drives a springtime barotropic response of the subtropical gyre via JEBAR and BPT.

CHAPTER 6. INFERRING THERMOHALINE CIRCULATION FROM SURFACE BUOYANCY FLUXES

The model experiments have established that anomalous surface buoyancy forcing over the Sargasso Sea drives 18° Water variability and, to a degree, intensification of the Gulf Stream. The modelling of these effects was motivated by observational evidence (Worthington 1977, Talley and Raymer 1982). The challenge now is to further examine buoyancy flux data, to shed more light on these phenomena.

This chapter is arranged as follows. A theoretical relationship between the thermohaline circulation (THC), water mass unsteadiness, and zonally-averaged water mass transformation is outlined (§6.1). For the case of CLIM2, the model THC is thus diagnosed and partitioned (§6.2). Observed heat and freshwater fluxes (§3.4.2) are then used to diagnose the surface buoyancy-forced part of the meridional overturning (§6.3). Different averaging strategies are assessed, and the fluxes are globally-adjusted, to ascertain the sensitivity of the diagnosed THC to systematic bias in the net heat flux. Having validated the methodology, the results of diagnosing the surface-forced overturning in individual years, over 1980-97, are presented (§6.4). Variability in the transformation and circulation of different water masses is evident, and this is addressed. Finally, the methodology and results are summarized and discussed (§6.5).

6.1 The overturning streamfunction in density space, water mass transformation and unsteadiness: a theoretical framework

6.1.1 The problem of defining a meridional streamfunction zonally integrated along density surfaces

In the Boussinesq approximation the flow of water is non-divergent,

$$\nabla_z.\mathbf{u} + \partial w/\partial z = 0 \qquad (6.1)$$

writing ∇_z as the horizontal gradient operator at constant z and $\mathbf{u}$ as the horizontal velocity. Hence it is always possible to define a meridional overturning streamfunction integrated zonally on level surfaces,

$$\psi_{lev}(\Theta,z)=\int_{\{\mathbf{x}:\theta(\mathbf{x})=\Theta\}}\int_{z=z_b(\mathbf{x})}^{z} v\,dz\,dl \tag{6.2a}$$

where $z_b(\mathbf{x})$ is a zonally-dependent bottom depth, and Eqn. (6.2a) satisfies

$$\int_{\mathscr{C}(z,\theta)} v\cdot dl=\frac{\partial\psi_{lev}}{\partial z};\qquad \int_{\mathscr{C}(z,\theta)} w\cdot dl=-\frac{\partial\psi_{lev}}{\partial y} \tag{6.2b,c}$$

where $\mathscr{C}(z,\theta)$ is a closed loop with latitude θ and depth z constant.

However, problems arise in the definition of an overturning streamfunction zonally-integrated on surfaces of constant density, resulting from the form of the continuity equation in density space:

$$\nabla_\rho\cdot(h\mathbf{u})+\frac{\partial g}{\partial\rho}=-\frac{\partial h}{\partial t}\neq 0 \tag{6.3}$$

writing ∇_ρ as the horizontal gradient operator at constant ρ, and defining $h=-\partial z/\partial\rho$ [so $h\delta\rho$ is the thickness of the layer sandwiched between the $\rho+\delta\rho$ and ρ isopycnals] and g as a diapycnal flux (from light to dense) per unit area. The crucial point is that there is a possibility of layer inflation, $\partial h/\partial t\neq 0$. Hence, in density space, the flow is *not* nondivergent. Integrating Eqn. (6.3) around a closed zonal loop $\mathscr{C}(\rho,\theta)$, holding latitude θ and density ρ constant, one obtains:

$$\int_{\mathscr{C}(\rho,\theta)}\left[\left.\frac{\partial}{\partial y}\right|_\rho(hv)+\frac{\partial g}{\partial\rho}\right]\cdot dl=-\int_{\mathscr{C}(\rho,\theta)}\frac{\partial h}{\partial t}\cdot dl \tag{6.4}$$

(A) (B) (C)

Here term (A) represents isopycnal flow, term (B) represents diapycnal flow and term (C) water mass unsteadiness. The unsteady term (C) on the right hand side need not vanish. Hence one *cannot* in general define a streamfunction ψ which relates to the meridional transport on the isopycnal, and the diapycnal transport across the isopycnal, according to

$$\int_{\mathscr{C}(\rho,\theta)} hv\cdot dl=-\frac{\partial\psi}{\partial\rho} \tag{6.5a}$$

$$\int_{\mathscr{C}(\rho,\theta)} g \cdot dl = \frac{\partial \psi}{\partial y} \tag{6.5b}$$

for differentiating Eqn. (6.5a) by y and Eqn. (6.5b) by ρ, and summing, gives zero on the right hand side, but the left hand side is the unsteady term (C) in Eqn. (6.4) *which is in general not zero.* As shown below, one can introduce a ψ to satisfy either Eqn. (6.5a) or Eqn. (6.5b), but *not both simultaneously.*

Note that the sign convention here is such that ψ increases with decreasing density (that is, up through the water column) for northward flow, in agreement with the convention chosen for ψ_{lev} above. There are various approaches that could be taken to separate out the time-dependent inflation term (C); consider here (below) a simple, physically meaningful decomposition.

6.1.2 Partitioning the meridional streamfunction into "transformation" and "unsteady" components

The meridional streamfunction zonally integrated on density surfaces is now related to the diapycnal flux across density surfaces, making plain the intimate link between the two. The meridional streamfunction,

$$\psi(\Theta,\rho) = \int_{\{\mathbf{x}:\theta(\mathbf{x})=\Theta\}} \int_{z=z_b(\mathbf{x})}^{z(\rho)} v \, dz \, dl = \int_{\{\mathbf{x}:\theta(\mathbf{x})=\Theta\}} \int_{\rho}^{\rho_{max}} h v \cdot d\rho \, dl \tag{6.6}$$

is defined to be the total northward transport of waters denser than ρ across the line of latitude $\theta = \Theta$ (by both resolved $\bar{v}$ and bolus v^* velocities), where ρ_{max} is the maximum (bottom) density at that latitude. The total volume of fluid with density greater than ρ lying north of $\theta = \Theta$ can be expressed as

$$V(\Theta,\rho) = \int_{\{\mathbf{x}:\theta(\mathbf{x})<\Theta\}} \int_{z=z_b(\mathbf{x})}^{z(\rho)} dz \, dA = \int_{\{\mathbf{x}:\theta(\mathbf{x})<\Theta\}} \int_{\rho}^{\rho_{max}} h \, d\rho \, dA \tag{6.7}$$

Note that $\psi(\Theta,\rho)$, $V(\Theta,\rho)$ and the other fields defined below *do* depend on time, despite not being written with explicit time dependence.

Assuming incompressibility (as in MICOM), it follows that the total diapycnal flow "down across" the ρ isopycnal (from light to dense) north of $\theta = \Theta$,

$$G(\Theta,\rho) = \int_{\{\mathbf{x}:\theta(\mathbf{x})<\Theta\}} g\, dA \tag{6.8}$$

must appear partly as volume inflation and partly as export (see **Fig. 6.1a**), according to

$$G(\Theta,\rho) = \psi(\Theta,\rho) + \partial V(\Theta,\rho)/\partial t \tag{6.9}$$

In the steady state, all of the flow across ρ must be exported, such that $G(\Theta,\rho) = \psi(\Theta,\rho)$, as noted by Speer (1997). However, the point is that, when the inflation rate $\partial V(\Theta,\rho)/\partial t \neq 0$, part of the diapycnal flow may be used to inflate the volume beneath ρ, and the streamfunction does *not* correspond exactly to the diapycnal flow, $G(\Theta,\rho) \neq \psi(\Theta,\rho)$. In particular,

$$\frac{\partial G}{\partial \Theta} = \frac{\partial \psi}{\partial \Theta} + \frac{\partial^2 V}{\partial t \partial \Theta} \tag{6.10}$$

Hence (see **Fig. 6.1b**), a divergence of fluid denser than ρ ($\partial\psi/\partial\Theta > 0$) need not imply a light-to-dense transformation at Θ ($\partial G/\partial\Theta > 0$). Instead, it could imply a decrease in the volume of water with density greater than ρ at Θ ($\partial^2 V/\partial\Theta\,\partial t < 0$). On the other hand, the streamfunction $\psi(\Theta,\rho)$ as defined above does have the useful property that it satisfies Eqn. (6.5a), viz:

$$-(\partial\psi/\partial\rho) = U \tag{6.11}$$

where

$$U(\Theta,\rho)\delta\rho = \int_{\{\mathbf{x}:\theta(\mathbf{x})=\Theta\}} h\,\delta\rho \cdot v\, dl \tag{6.12}$$

is the northward transport of waters with density between ρ and $\rho + \delta\rho$. Moreover, $\psi = 0$ at boundaries (seafloor, coasts) and is only non-zero at the ocean surface if there is depth-integrated flow— i.e., it looks like a streamfunction!

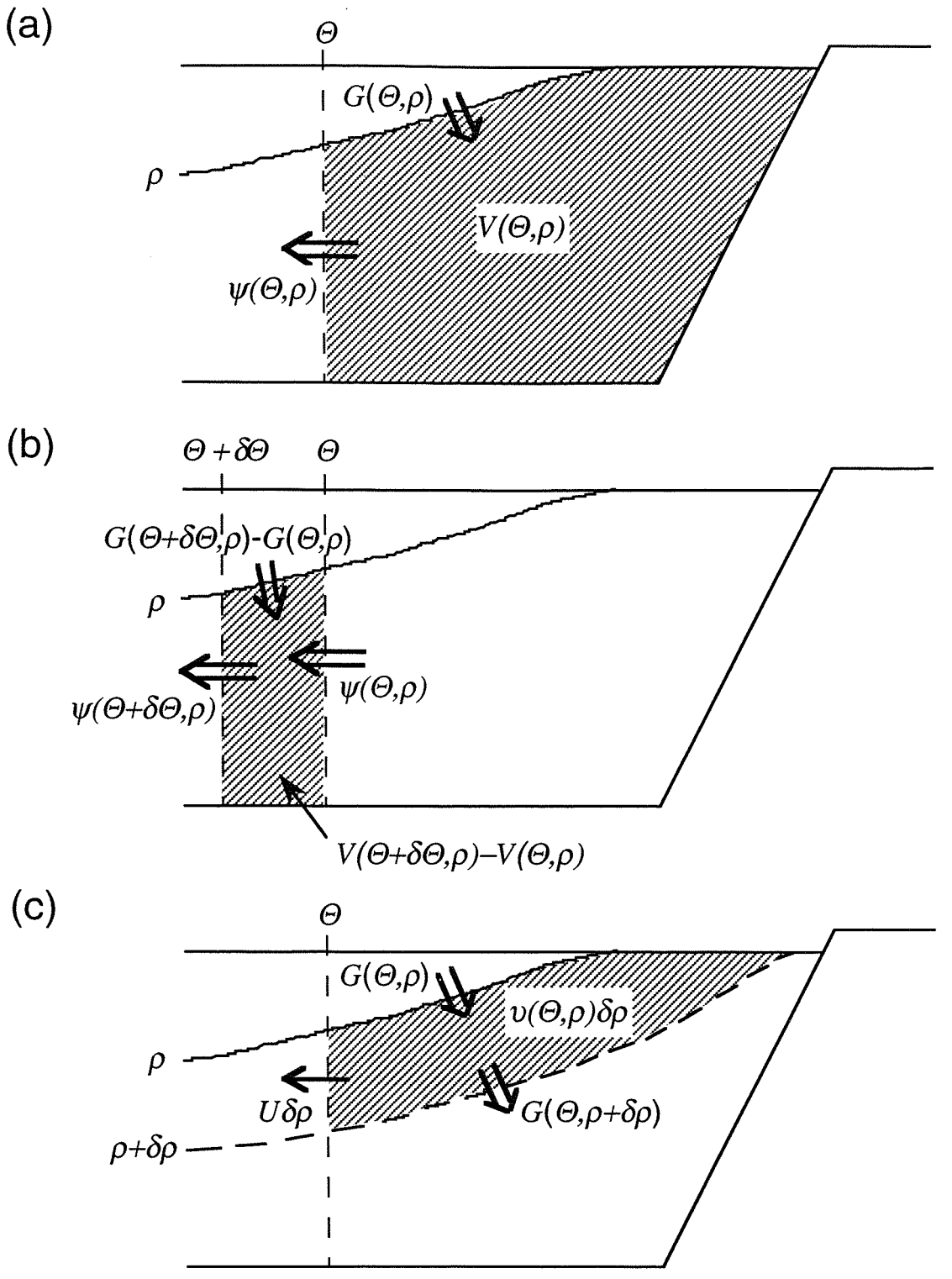

Figure 6.1: Schematic meridional sections across the North Atlantic (adapted from Marsh *et al.* 2000) showing: (a) north of Θ, the diapycnal flux across ρ [$G(\Theta,\rho)$], volume "below" ρ [$V(\Theta,\rho)$], and the southwards flow across Θ of waters denser than ρ [$\psi(\Theta,\rho)$]; (b) the relationship between meridional convergences of $\psi(\Theta,\rho)$ and $G(\Theta,\rho)$, and (c) the relationship between diapycnal flux convergence and water mass formation.

The "transformation streamfunction", $G(\Theta,\rho)$, of course gives the correct diapycnal flux, $\partial G/\partial\Theta$, of waters at latitude Θ. However, we now have (**Fig. 6.1c**):

$$-\frac{\partial G}{\partial \rho} = U - \frac{\partial^2 V}{\partial t \partial \rho} = U + \frac{\partial \upsilon}{\partial t} \tag{6.13}$$

[writing $\upsilon = -\partial V/\partial\rho$, so that $\upsilon(\Theta,\rho)\cdot\delta\rho$ is the volume of water with density between ρ and $\rho+\delta\rho$ north of Θ]. Thus $-\partial G/\partial\rho$ now includes the rate of inflation of the layer with density between ρ and $\rho+\delta\rho$ north of Θ, together with the northward export across the latitude Θ. Walin (1982) termed this sum the water mass *formation* rate M. Furthermore, of course, $G(\Theta,\rho)$ will not in general be zero at the northern boundary of a closed basin, if the volume below the ρ isopycnal is inflating or deflating—i.e., $G(\Theta,\rho)$ does *not* look like a streamfunction.

So there are two candidate streamfunctions, $\psi(\Theta,\rho)$ and $G(\Theta,\rho)$ in terms of which one might consider zonally-integrated flow along surfaces of constant density. Both have deficiencies when the density structure is evolving: $\psi(\Theta,\rho)$ gives the incorrect diapycnal flow (but correct isopycnal flow) and $G(\Theta,\rho)$ the wrong isopycnal flow (but correct diapycnal flow). However, the important thing is that $G(\Theta,\rho)$ has a clear physical interpretation, being the total flux of waters down across ρ, north of Θ, and the deviation of $G(\Theta,\rho)$ from $\psi(\Theta,\rho)$ gives a simple and direct measure of the importance of water mass unsteadiness.

6.1.3 Diapycnal fluxes and density forcing

There must be some source of density to allow diapycnal flow across ρ, i.e., $G(\Theta,\rho)\neq 0$. This source is associated with either the surface outcrop of ρ, or a convergence of the interior diapycnal density flux. Hence (Walin 1982; Speer and Tziperman 1992; Nurser *et al.* 1999):

$$G(\Theta,\rho) = F(\Theta,\rho) - \frac{\partial D_{diff}(\Theta,\rho)}{\partial \rho} + C(\rho,\Theta) \tag{6.14}$$

where $F(\Theta,\rho)$, $\partial D_{diff}(\Theta,\rho)/\partial\rho$ and $C(\Theta,\rho)$ are diapycnal volume fluxes associated with surface buoyancy forcing, interior diapycnal mixing and cabbeling [density gain through mixing on ρ - see McDougall 1987]. Furthermore,

$$F(\Theta,\rho) = -\frac{\partial}{\partial\rho} D_{in}(\Theta,\rho) \tag{6.15}$$

and, following Speer and Tziperman (1992):

$$D_{in}(\Theta,\rho) = \int_{\theta>\Theta;\rho<\rho_m(\mathrm{x})} \mathscr{D}_{in}(\mathrm{x})dA \tag{6.16}$$

where $\mathscr{D}_{in}(\mathbf{x})$ is the surface density flux at a point $\mathbf{x}$, expressed in terms of heat and freshwater fluxes, as a function of temperature and salinity [see Eqn. (6.21) below]. The second right hand side term in Eqn. (6.14) represents the water mass transformation due to diapycnal divergence of the diffusive density flux, $D_{diff}(\Theta,\rho)$, where

$$D_{diff}(\Theta,\rho) = \int_{\rho(\mathbf{x})=\rho;\theta(\mathbf{x})>\Theta} \mathbf{D}.\mathbf{n}\ dA \tag{6.17}$$

and $\mathbf{D}$ is the non-advective density flux field, $\mathbf{n} = \nabla\rho/|\nabla\rho|$ is a unit vector normal to the isopycnal surface defined by ρ.

6.1.4 A surface-forced meridional streamfunction

A striking consequence of the relationship between $\psi(\Theta,\rho)$ and $G(\Theta,\rho)$ is that, for the particular case in which (i) the surface fluxes dominate mixing and (ii) the ocean is in steady state, it follows that $\psi(\Theta,\rho) \approx F(\Theta,\rho)$, and the meridional overturning streamfunction in density coordinates can be inferred from surface density forcing alone. Indeed, Walin (1982) established a formal relation between thermally-forced circulation (a meridional overturning) and net heat and volume fluxes across isothermal surfaces, a formalism which can be trivially extended to the buoyancy-forced circulation and density/volume fluxes across isopycnals. The validity of $\psi(\Theta,\rho) \approx F(\Theta,\rho)$ will be tested in the model Atlantic (see following section).

Consider first the likely balance of surface forcing and mixing in an idealized North Atlantic basin. Averaged over a region of ocean north of latitude Θ, a non-zero volume flux across an isopycnal ρ, $G(\Theta,\rho) \neq 0$, must, *given a steady balance of water masses*, be supported by sources or sinks of density. The schematic in **Fig. 6.2** shows how $G(\Theta,\rho)$ is related to convergences and divergences of $D_{in}(\Theta,\rho)$ and $D_{diff}(\Theta,\rho)$. There is a diapycnally-*convergent* surface density gain everywhere that isopycnals $\rho-\Delta\rho$ and $\rho+\Delta\rho$ are outcropped at the surface: $D_{in} > 0$ and $D_{in}(\Theta,\rho-\Delta\rho) > D_{in}(\Theta,\rho+\Delta\rho)$. In the ocean interior, there is down-gradient mixing of density, $D_{diff} < 0$, which is a diapycnally-*divergent*, $D_{diff}(\Theta,\rho-\Delta\rho) < D_{diff}(\Theta,\rho+\Delta\rho)$.

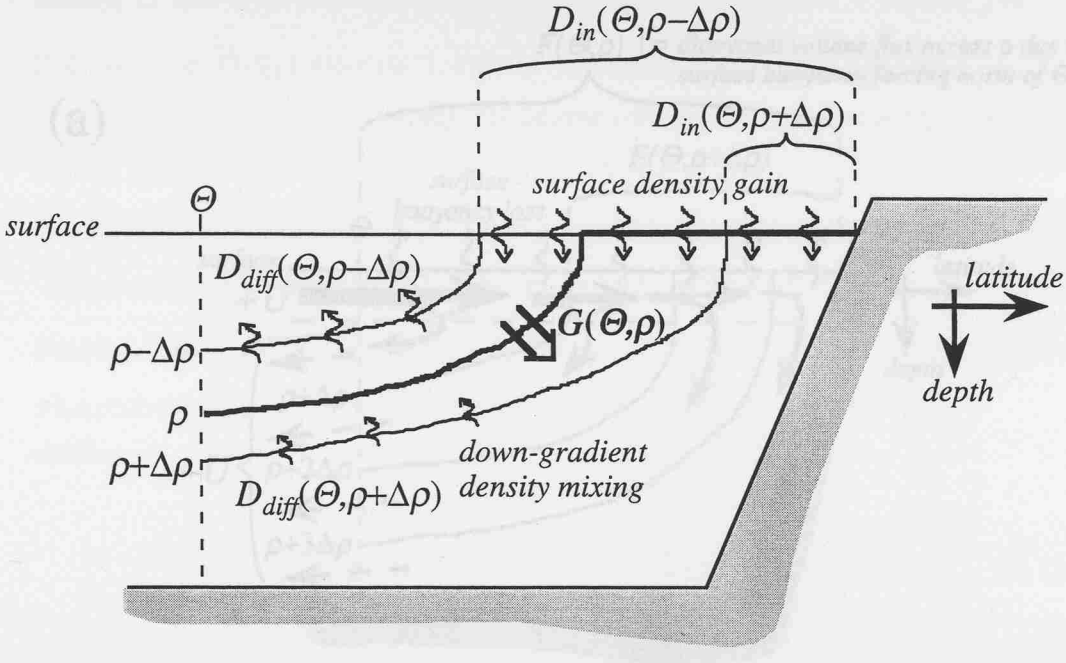

Figure 6.2: Schematic showing the surface and interior diapycnal density and volume fluxes in an idealized North Atlantic basin.

In **Fig. 6.2**, the convergence of D_{in} dominates the divergence of D_{diff}, such that there is a net *positive* diapycnal volume flux, $G(\Theta,\rho) > 0$, implying that, north of Θ, water is, *on average*, being transformed to higher density across ρ. Assuming incompressibility, and given a steady state of water masses, all of the water north of Θ which is transformed across ρ must be exported southward across Θ.

Fig. 6.3 shows schematically how the surface-forced transformation (and implied formation) of water masses is related to the meridional circulation in an idealized North Atlantic *in which there is no mixing*, in both latitude-depth space (**Fig. 6.3a**) and latitude-density space (**Fig. 6.3b**). In **Fig. 6.3**, U is the northward surface transport across latitude Θ of water with density greater than ρ. Poleward of Θ, the surface flow loses buoyancy everywhere [$F(\Theta,\rho)$, $F(\Theta,\rho+\Delta\rho)>0$, etc.] and the density of northward-flowing water increases. Furthermore, $F(\Theta,\rho)>F(\Theta,\rho+\Delta\rho)$, such that fractions of the flow are progressively diverted downward and southward (**Fig. 6.3a**) in regular intervals of density, $\Delta\rho$ (**Fig. 6.3b**). In the absence of interior mixing, the cumulative southward flows of water in density classes ρ to $\rho+\Delta\rho$ (etc.) reach Θ unaltered, balancing the northward surface flow.

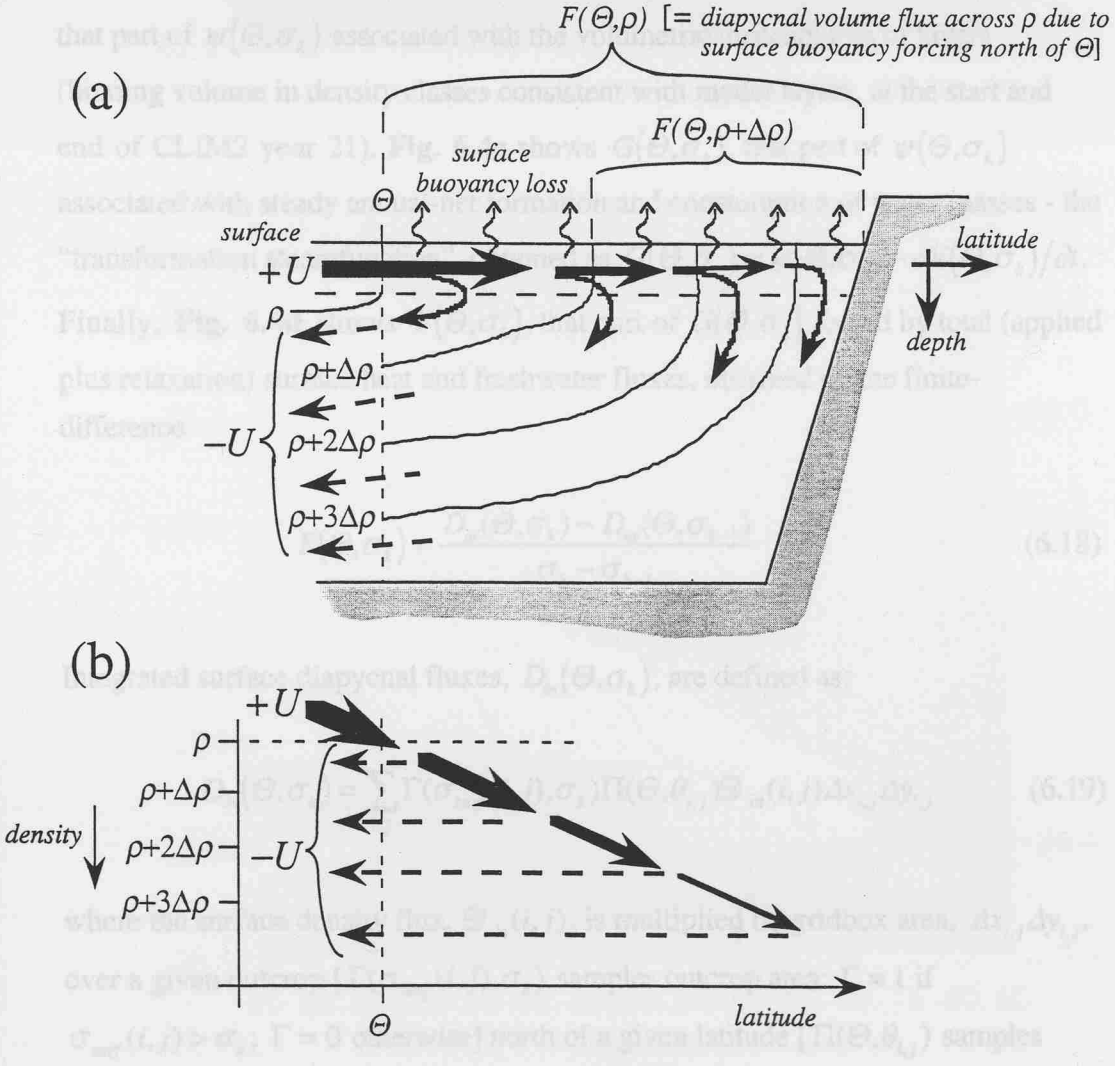

Figure 6.3: The surface-forced circulation across a series of isopycnals, shown (a) in section through an idealized North Atlantic, and (b) in latitude-density space.

6.2 Application to the model

For the present model, and using the diagnostics introduced in §6.1, the relative roles of water mass unsteadiness, water mass transformation and surface buoyancy forcing are examined. Consider the case of CLIM2 year 21. In **Fig. 6.4**, diapycnal volume fluxes are contoured as a function of latitude and density. Positive cells in **Fig. 6.4** correspond to "clockwise" overturning (either real or equivalent), and a black mask is applied at densities lower than (non-existent) minima, and higher than (abyssal layer) maxima, at each latitude. Dashed lines indicate year-round maximum surface (mixed layer) density at a given latitude.

Fig. 6.4a shows $\psi(\Theta,\sigma_k)$, the meridional streamfunction as a function of latitude Θ and layer density σ_k (see §3.3.6). **Fig. 6.4b** shows $\partial V(\Theta,\sigma_k)/\partial t$ that part of $\psi(\Theta,\sigma_k)$ associated with the volumetric unsteadiness of layers (binning volume in density classes consistent with model layers, at the start and end of CLIM2 year 21). **Fig. 6.4c** shows $G(\Theta,\sigma_k)$, that part of $\psi(\Theta,\sigma_k)$ associated with steady annual-net formation and consumption of water masses - the "transformation steamfunction", obtained as $G(\Theta,\sigma_k)=\psi(\Theta,\sigma_k)-\partial V(\Theta,\sigma_k)/\partial t$. Finally, **Fig. 6.4d** shows $F(\Theta,\sigma_k)$, that part of $G(\Theta,\sigma_k)$ forced by total (applied plus relaxation) surface heat and freshwater fluxes, obtained by the finite-difference

$$F(\Theta,\sigma_k)=\frac{D_{in}(\Theta,\sigma_k)-D_{in}(\Theta,\sigma_{k-1})}{\sigma_k-\sigma_{k-1}} \tag{6.18}$$

Integrated surface diapycnal fluxes, $D_{in}(\Theta,\sigma_k)$, are defined as:

$$D_{in}(\Theta,\sigma_k)=\sum_{i,j}\Gamma(\sigma_{surf}(i,j),\sigma_k)\Pi(\Theta,\theta_{i,j})\mathcal{D}_{in}(i,j)\Delta x_{i,j}\Delta y_{i,j} \tag{6.19}$$

where the surface density flux, $\mathcal{D}_{in}(i,j)$, is multiplied by gridbox area, $\Delta x_{i,j}\Delta y_{i,j}$, over a given outcrop [$\Gamma(\sigma_{surf}(i,j),\sigma_k)$ samples outcrop area: $\Gamma=1$ if $\sigma_{surf}(i,j)>\sigma_k$; $\Gamma=0$ otherwise] north of a given latitude [$\Pi(\Theta,\theta_{i,j})$ samples gridpoints by latitude: $\Pi=1$ if $\theta_{i,j}>\Theta$; $\Pi=0$ otherwise]. Differences between $G(\Theta,\sigma_k)$ and $F(\Theta,\sigma_k)$ are accounted for by diapycnal mixing.

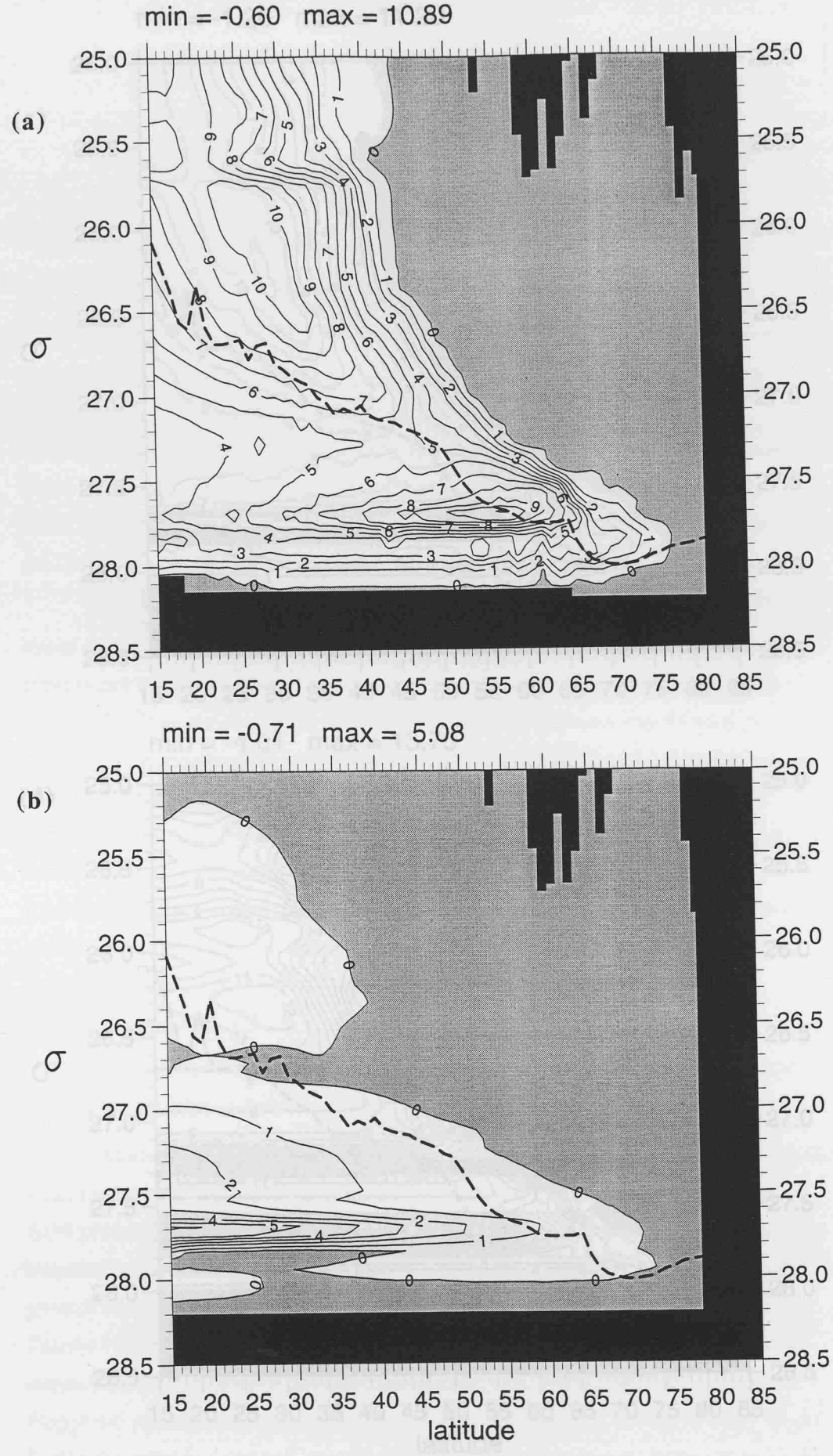

Figure 6.4: For year 21 of CLIM2: (a) $\psi(\Theta,\sigma_k)$, (b) $\partial V(\Theta,\sigma_k)/\partial t$, (c) $G(\Theta,\sigma_k)$, and (d) $F(\Theta,\sigma_k)$ [units Sv, contour interval 1 Sv].

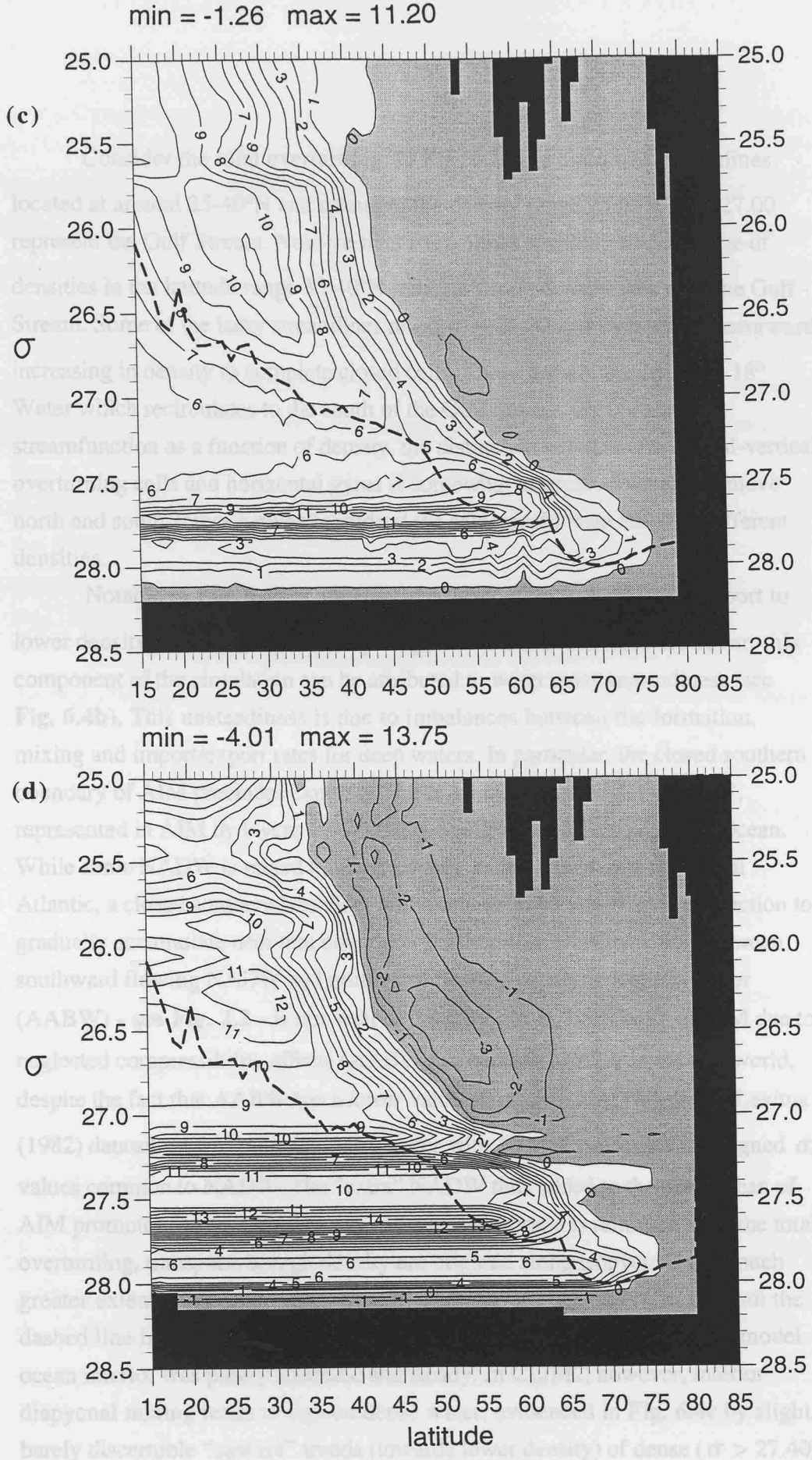

Figure 6.4 (ctd)

Consider the total overturning. In **Fig. 6.4a** the cluster of streamlines located at around 25-40°N and spanning the density range $25.65 < \sigma < 27.00$ represent the Gulf Stream. Near-vertical streamlines spanning a wide range of densities in the latitude range 35-40°N indicate strong density gain over the Gulf Stream. Some of the latter streamlines reach $\sigma \sim 26.50$ and then turn equatorward, increasing in density to complete closed cells. These streamlines trace the 18° Water which recirculates to the south of the Gulf Stream. By plotting the streamfunction as a function of density, the distinction between meridional-vertical overturning cells and horizontal gyres is somewhat blurred, as water can move north and south across a given latitude at the same depth level but with different densities.

Notable in **Fig. 6.4a** is apparently considerable upwelling (transport to lower density) in the latitude-density range 15-50°N, $\sigma > 27.00$. However, this component of the circulation can be attributed to water mass unsteadiness (see **Fig. 6.4b**). This unsteadiness is due to imbalances between the formation, mixing and import/export rates for deep waters. In particular, the closed southern boundary of AIM precludes export of North Atlantic Deep Water (NADW, represented in AIM by layers 16-19) to the South Atlantic and Southern Ocean. While some NADW is mixed to lower density in subtropical and equatorial Atlantic, a closed southern boundary will allow the otherwise-exported fraction to gradually accumulate near that boundary. Furthermore, the distinction between southward flowing NADW and northward flowing Antarctic Bottom Water (AABW) - see **Fig. 2.2** - is not well defined by the σ_0 coordinate of AIM due to neglected compressibility effects (AABW lies beneath NADW in the real world, despite the fact that AABW has a *lower* value of σ_0 than NADW). In the Levitus (1982) dataset used to initialize AIM, water with AABW properties is assigned σ_0-values common to NADW. The "extra" NADW thus added to the deep ocean of AIM promotes further unsteadiness. When unsteadiness is removed from the total overturning, transports at high density are oriented along isopycnals to a much greater extent (**Fig. 6.4c**). Above the highest surface densities (i.e. beneath the dashed line in **Fig. 6.4c**), the streamlines would appear horizontal if the model ocean interior was purely adiabatic and steady. In CLIM2, however, interior diapycnal mixing tends to lighten dense water, evidenced in **Fig. 6.4c** by slight, barely discernible "upward" trends (towards lower density) of dense ($\sigma > 27.40$) equatorward flows.

The transformation streamfunction in **Fig. 6.4c** is characterized by northward flow at progressively higher densities, weakening as fractions of the flow return in equatorward branches. The overall circulation in **Fig. 6.4c**, traced by streamlines which cross all latitudes south of ~65°N, is essentially driven by the formation of ~3 Sv of Greenland Sea Deep Water (GSDW, with density $\sigma \approx 27.85$) in the Nordic Seas (north of ~65°N). Superimposed on this circulation are regional features, confined to limited latitude ranges: specifically the subtropical gyre (south of ~40°N) and the subpolar gyre (the zone 40-65°N), the formation sites for ~4 Sv of Subtropical Mode Water, (STMW, including 18° Water, in the density range $26.00 < \sigma < 27.00$, centred on $\sigma \approx 26.50$) and ~7 Sv of Labrador Sea Water (LSW, with $\sigma \approx 27.75$) respectively. Note the general correspondance between these circulations in **Fig. 6.4c** and the idealized transport scheme in **Fig. 6.3b**.

Consider finally the overturning circulation implied by model surface thermohaline forcing (observed plus relaxation surface heat and freshwater fluxes), shown in **Fig. 6.3d**. There is a degree of similarity between **Fig. 6.3c** and **Fig. 6.3d**, with differences attributable to total diapycnal mixing. Note that STMW, LSW and GSDW formation and recirculation can be identified to in **Fig. 6.3d**, at rates similar to those in **Fig. 6.3c**, suggesting that these water masses are indeed surface-formed. A striking difference between **Fig. 6.3c** and **Fig. 6.3d** is in the density range $27.00 < \sigma < 27.50$, where mixed layer entrainment and detrainment largely balances the implied strong surface forcing. Having established that surface heat and freshwater fluxes drive the model North Atlantic thermohaline circulation (THC) to a substantial degree, consider next the THC implied by *observed* surface fluxes.

6.3 The surface-forced THC diagnosed from observed fluxes

Computation of the surface-forced THC streamfunction is a two-step procedure. Firstly, fields of surface density and surface density flux are prepared. The fields are then zonally integrated, to infer a meridional circulation. These two steps are outlined below (in §6.3.1 and §6.3.2). Time series of surface-forced THC over 1980-97 are then obtained and examined for trends and variability (§6.3.3).

6.3.1 Computing surface density and surface density flux

Sea surface temperature and salinity, T and S, net heat flux, Q, and evaporation minus precipitation, E-P, are used to compute the state variable [$\sigma_{surf} = \rho_{surf} - 1000$, where ρ_{surf} is surface density in kg m^{-3}] and a surface density flux, $\mathcal{D}_{in}$. Density is computed from a third degree polynomial approximation of the equation of state for seawater (Friedrich and Levitus 1972):

$$\sigma_{surf}(T,S) = -0.072169 + 0.8056S + T(0.049762 - 0.0030063S + T(-0.0075911 + 0.000037S + 0.000035T)) \quad (6.20)$$

where T is in °C and S is in practical salinity units (psu). The surface density flux (actually a mass flux, in units of kg m^{-2} s^{-1}) is computed as a function of net heat and freshwater forcing (Schmitt *et al.* 1989):

$$\mathcal{D}_{in} = -\frac{\alpha(T,S)}{C_p}Q + \rho_o\beta(T,S)\frac{S}{1-S}(E-P) \quad (6.21)$$

where C_p is the specific heat of seawater (4000 J kg^{-1} K^{-1}), ρ_o is an reference density for seawater (1025 kg m^{-3}), and α and β, the thermal expansion and haline contraction coefficients,

$$\alpha(T,S) = -\frac{1}{\rho_o}\frac{\partial\sigma}{\partial T}\bigg|_{T,S} \quad (6.22a)$$

$$\beta(T,S) = \frac{1}{\rho_o}\frac{\partial\sigma}{\partial S}\bigg|_{T,S} \quad (6.22b)$$

are derived from the equation of state (Eqn. 6.20).

For this diagnosis, monthly fields of T, Q, and E-P are obtained from the database of the SOC surface flux climatology (Josey *et al.* 1999 - see §3.4.2), while monthly climatological values of S are obtained from the climatology of Levitus (1982). For the extra-tropical North Atlantic, **Fig. 6.5** shows the annual-mean (over 1980-97) thermal and haline components of $\mathcal{D}_{in}$, in units of 10^{-6} kg m^{-2} s^{-1}. For typical values of sea surface temperature and salinity in the subtropics (20°C, 35‰), a density flux of 10^{-6} kg m^{-2} s^{-1} is equivalent to a heat flux of 14.3

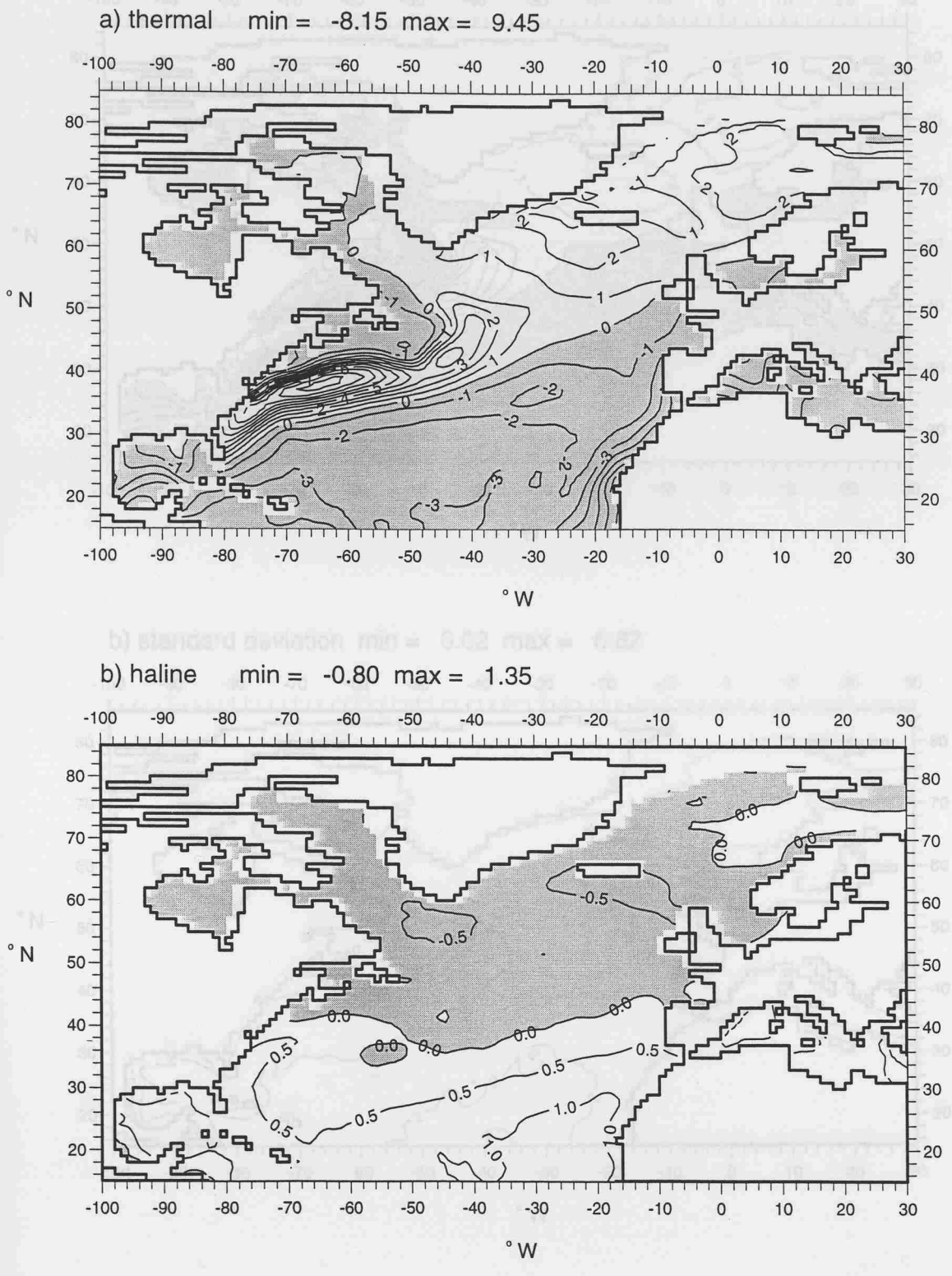

Figure 6.5: Fields of 1980-97 mean (annual-average) thermal and haline surface density flux (10^{-6} kg m^{-2} s^{-1}) over the North Atlantic.

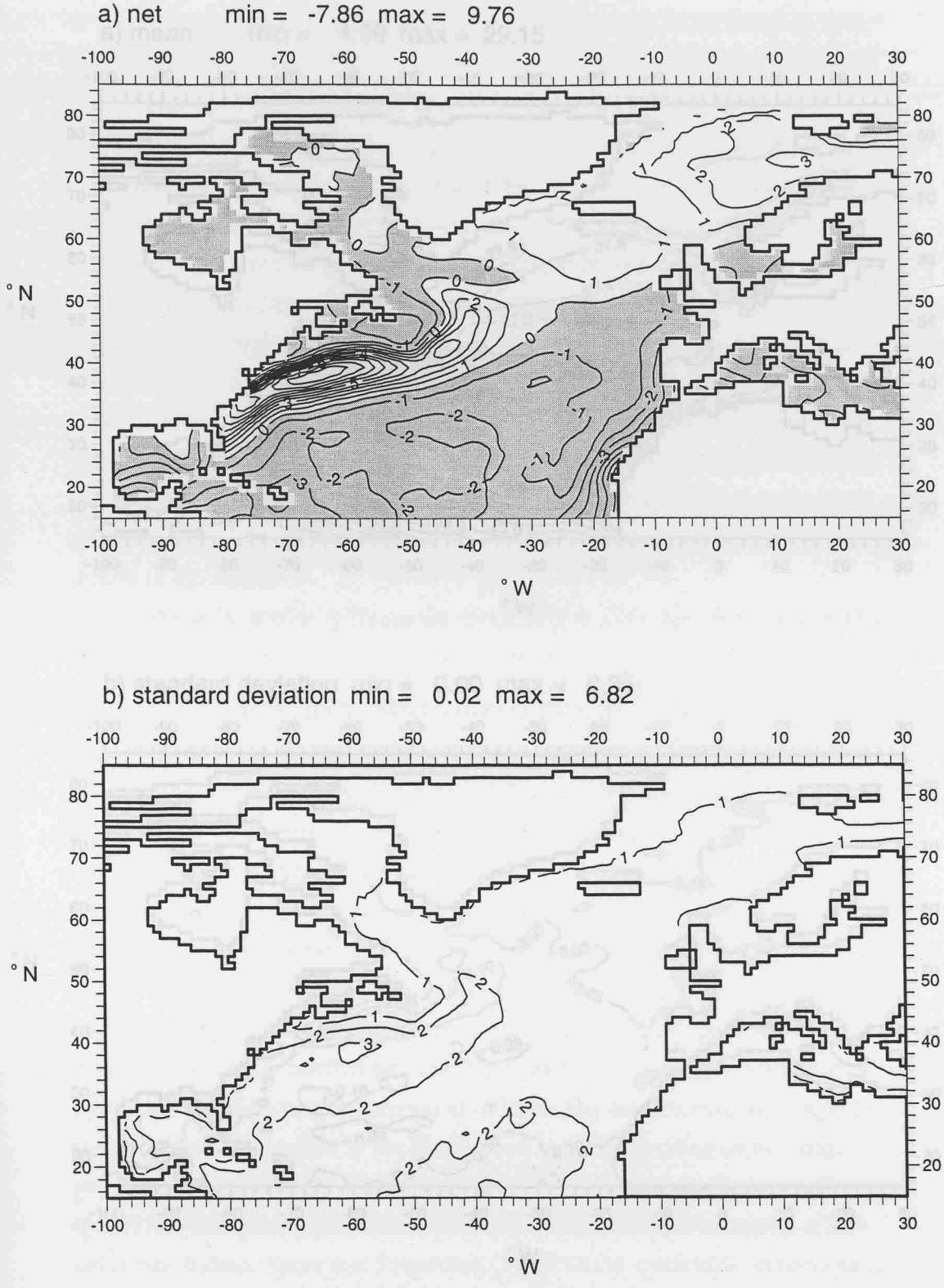

Figure 6.6: Fields of the mean and standard deviation of annual-average net surface density flux (10^{-6} kg m^{-2} s^{-1}) over the North Atlantic.

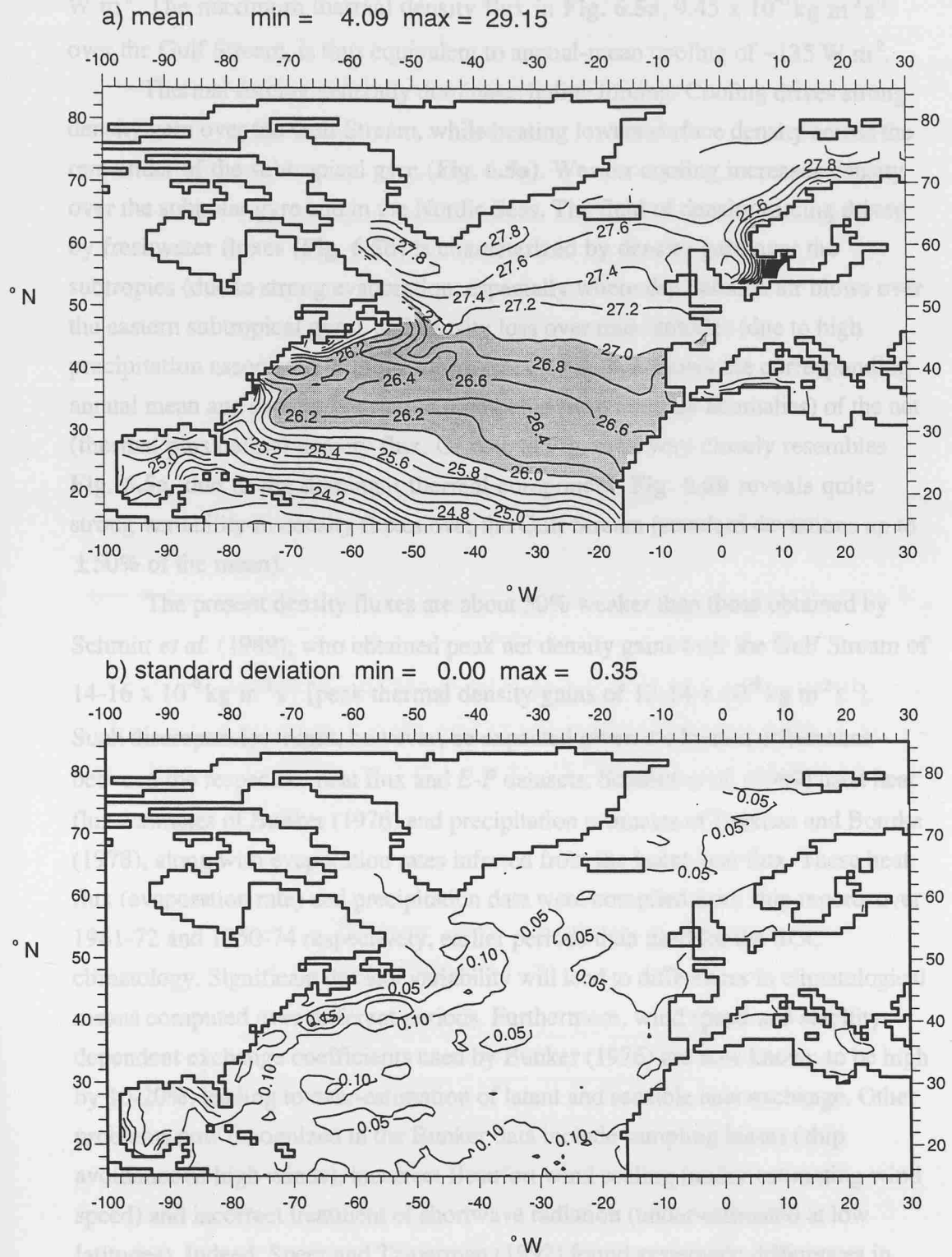

Figure 6.7: Fields of the mean and standard deviation of year-round maximum in σ_{surf} (kg m^{-3}, shaded in the STMW σ_{surf}-range 26.0-27.0) over the North Atlantic.

W m^{-2}. The maximum thermal density flux in **Fig. 6.5a**, 9.45 x 10^{-6} kg $m^{-2}s^{-1}$ over the Gulf Stream, is thus equivalent to annual-mean cooling of ~135 W m^{-2}.

Thermal forcing generally dominates haline forcing. Cooling drives strong density gain over the Gulf Stream, while heating lowers surface density across the remainder of the subtropical gyre (**Fig. 6.5a**). Weaker cooling increases density over the subpolar gyre and in the Nordic Seas. The field of density forcing driven by freshwater fluxes (**Fig. 6.5b**) is characterized by density gain over the subtropics (due to strong evaporation, especially where dry Saharan air blows over the eastern subtropical gyre), and density loss over mid-latitudes (due to high precipitation associated with the storm track). **Fig. 6.6** shows the corresponding annual mean and standard deviation (computed from monthly anomalies) of the net (thermal plus haline) density flux. Of course **Fig. 6.6a** very closely resembles **Fig. 6.5a**, due to the dominant thermal component. **Fig. 6.6b** reveals quite strong variability in density fluxes over the Gulf Stream (standard deviations up to ±50% of the mean).

The present density fluxes are about 50% weaker than those obtained by Schmitt *et al.* (1989), who obtained peak net density gains over the Gulf Stream of 14-16 x 10^{-6} kg $m^{-2}s^{-1}$ [peak thermal density gains of 12-14 x 10^{-6} kg $m^{-2}s^{-1}$]. Such discrepancies might, however, be expected given the known differences between the respective heat flux and *E-P* datasets. Schmitt *et al.* (1989) used heat flux estimates of Bunker (1976) and precipitation estimates of Dorman and Bourke (1978), along with evaporation rates inferred from the latent heat flux. These heat flux (evaporation rate) and precipitation data were compiled from ship reports over 1941-72 and 1950-74 respectively, earlier periods than used for the SOC climatology. Significant decadal variability will lead to differences in climatological means computed over different periods. Furthermore, wind speed and stability-dependent exchange coefficients used by Bunker (1976) are now known to be high by 10-20%, leading to over-estimation of latent and sensible heat exchange. Other problems now recognized in the Bunker data include sampling biases (ship avoidance of high winds), incorrect Beaufort wind scaling (under-estimating wind speed) and incorrect treatment of shortwave radiation (under-estimated at low latitudes). Indeed, Speer and Tziperman (1992) found systematic differences in North Atlantic water mass transformation rates (derived from surface density fluxes) computed with the Bunker (1976) data and the revised Bunker data of Isemer and Hasse (1987).

In general (and particularly across the subtropical gyre) water masses are formed at the surface, and subduct as end-of-winter mixed layer water characterized by the year-round maximum surface density (Marshall *et al.* 1993).

Fig. 6.7 shows the annual mean and standard deviation of the end-of-winter maximum in σ_{surf}, computed from the SOC monthly SST data and Levitus *climatological* surface salinity (i.e., all the interannual variability in σ_{surf} is through SST). The subtropical North Atlantic is characterized by maximum surface density in the rather narrow range $26.0 < \sigma < 27.0$ (**Fig. 6.7a**, shaded area), with highest variability again found over the Gulf Stream (**Fig. 6.7b**), reaching a peak value of 0.34 sigma units downstream of separation (coincident with peak interannual variability of surface density forcing).

6.3.2 Computing annual-mean zonally-integrated transformation rates and the inferred climatological THC

For a given density σ, fields of $\mathcal{D}_{in}$ are integrated wherever $\sigma_{surf} > \sigma$ over the area north of 1° lines of latitude, to determine $D_{in}(\Theta,\sigma)$ - the total surface density flux across σ north of a latitude Θ [assuming $D_{in}(\Theta_{nb},\sigma)= 0$ where Θ_{nb} is the latitude of a northern boundary, 85°N in the present case]. After testing the method with varying density "bin-width" ($\Delta\sigma$), a set of 29 densities were chosen, to best resolve the range of water masses which are transformed north of 15°N in the Atlantic. Bin-widths thus vary over the density range $25.00 \leq \sigma \leq 28.50$, as summarized in **Table 6.1**.

Table 6.1 Density bin-widths over the range of densities chosen to represent North Atlantic water masses.

density range	density bin-width
$25.00 \leq \sigma \leq 27.00$	0.20
$27.00 \leq \sigma \leq 27.70$	0.10
$27.70 \leq \sigma \leq 28.00$	0.05
$28.00 \leq \sigma \leq 28.50$	0.10

Divergences of $D_{in}(\Theta,\sigma)$ with respect to σ give $F(\Theta,\sigma)$, the total diapycnal volume flux (or water mass transformation rate) across σ, north of Θ. Annual averages, $\langle F(\Theta,\sigma)\rangle$, can then be reinterpreted and contoured as $\psi_{surf}(\Theta,\sigma)$, the surface-forced part of the THC. Such streamfunctions are

computed using fields of $\mathcal{D}_{in}$ and σ_{surf} obtained from different sources: the climatological forcing fields used in CLIM1 and CLIM2; the new SOC climatology. The implication of using *climatological mean* SOC data is exposed by recomputing $\psi_{surf}(\Theta,\sigma)$ as the mean over 1980-97. Furthermore, the SOC fluxes are globally adjusted, to determine the effect of systematic flux bias on $\psi_{surf}(\Theta,\sigma)$. **Table 6.2** summarizes the various different calculations of $\psi_{surf}(\Theta,\sigma)$. The surface-forced streamfunctions are shown in **Fig. 6.8** and **Fig. 6.10**. Black masks in **Fig. 6.8** and **Fig 6.10** apply at densities higher/lower than maximum/minimum mixed layer density, at a given latitude.

Table 6.2 The data and averaging strategy used to calculate annual-mean transformation streamfunctions.

Fields used	averaged over	$\psi_{surf}(\Theta,\sigma)$ figure
monthly climatologies of Esbensen and Kushnir (1981) surface heat flux and evaporation, Jaeger (1976) precipitation, Levitus (1982) SST and surface salinity	12 months	**Fig. 6.8a**
monthly climatologies of SOC (Josey *et al.* 1999) heat and freshwater fluxes, sea surface temperature, Levitus (1982) sea surface salinity	12 months	**Fig. 6.8b**
individual monthly (1980-97) unadjusted SOC heat and freshwater fluxes, sea surface temperature, Levitus (1982) sea surface salinity (assumed climatological)	216 months	**Fig. 6.8c**
as above, but with globally-adjusted heat and freshwater fluxes (see text)	216 months	**Fig. 6.10a**

Using the SOC 1980-97 database, a "climatological" annual-mean streamfunction can be computed either from monthly mean fields of surface density and density flux, averaged over the 18 year period (**Fig. 6.8b**), or using individual months (**Fig. 6.8c**) - see **Table 6.1**. The latter calculation is the

formally "correct" averaging strategy, due to covariability of $\mathcal{D}_{in}$ and σ_{surf}, and there are indeed small differences between **Fig. 6.8b,c** (a somewhat smoother streamfunction is obtained in the latter case).

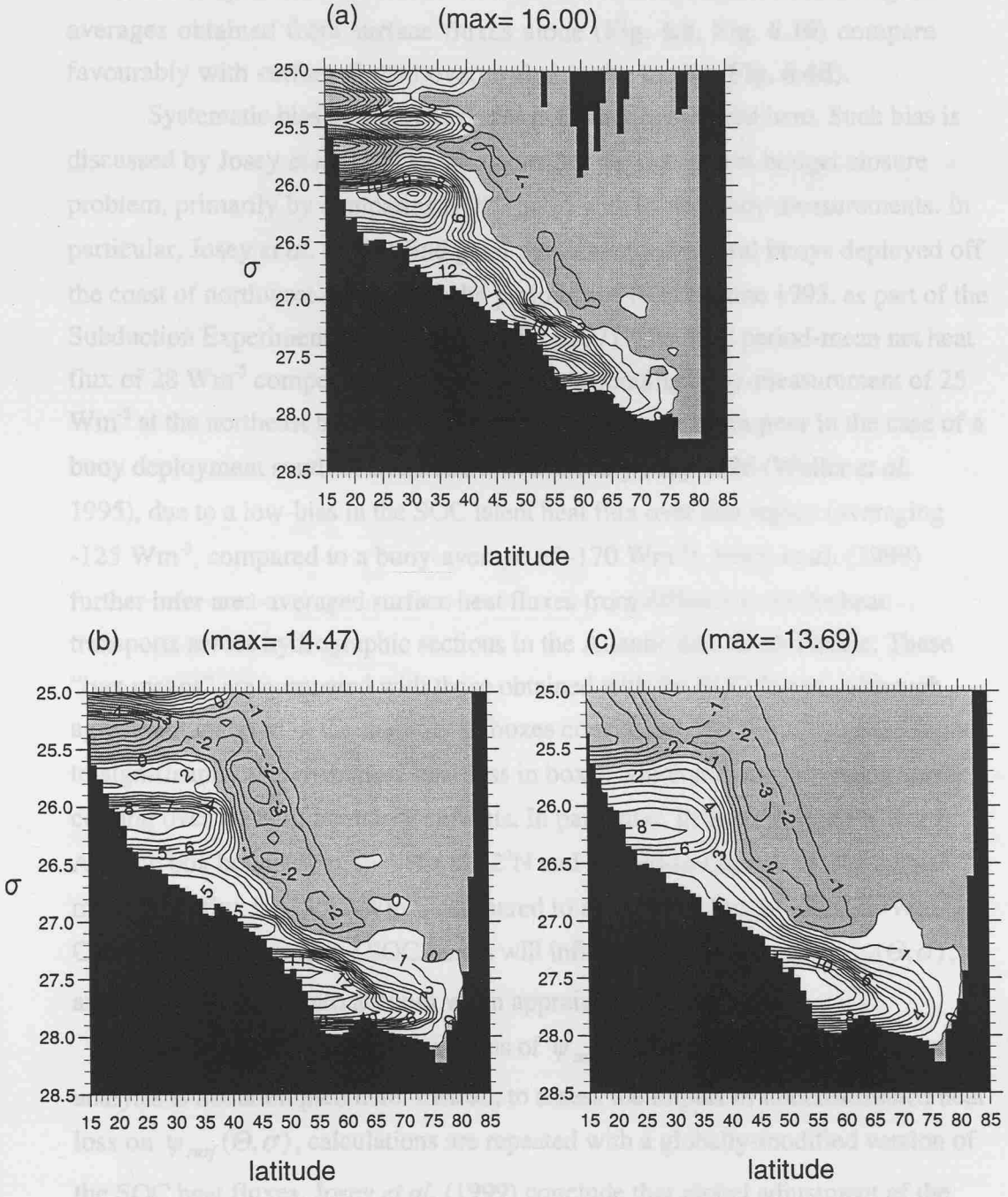

Figure 6.8: Annual-mean surface-forced streamfunctions (Sv, with C.I. = 1 Sv) based on (a) the climatologies used to force the model, and (b), (c) the SOC climatology [using monthly means (b) and averaging over 1980-97 (c)].

Furthermore, the climatologies used to force the model (Esbensen and Kushnir 1981; Jaeger 1976; Levitus 1982) are diagnosed for $\psi_{surf}(\Theta,\sigma)$ (**Fig. 6.8a**). Note that the overturning in **Fig. 6.8a** is much stronger at low density, and weaker at high density, compared to the SOC climatology equivalent (**Fig. 6.8b**), due to systematic differences between the climatologies. Climatological averages obtained from surface fluxes alone (**Fig. 6.8, Fig. 6.10**) compare favourably with surface-forced overturning in the model (**Fig. 6.4d**).

Systematic bias in the SOC fluxes is further considered here. Such bias is discussed by Josey *et al.* (1999), who consider the ocean heat budget closure problem, primarily by comparing SOC fluxes with in situ buoy measurements. In particular, Josey *et al.* (1999) find good agreement for several buoys deployed off the coast of northwest Africa over the period July 1991 to June 1993, as part of the Subduction Experiment (Moyer and Weller 1997). The SOC period-mean net heat flux of 28 Wm^{-2} compared closely to the corresponding buoy-measurement of 25 Wm^{-2} at the northeast buoy site. However, the agreement was poor in the case of a buoy deployment south of Bermuda over February-May 1986 (Weller *et al.* 1995), due to a low-bias in the SOC latent heat flux over that region (averaging -125 Wm^{-2}, compared to a buoy-average of -170 Wm^{-2}). Josey *et al.* (1999) further infer area-averaged surface heat fluxes from differences in the heat transports across hydrographic sections in the Atlantic and North Pacific. These "box means" are compared with those obtained with the SOC fluxes. Although agreement is found in the majority of boxes considered, the SOC fluxes are found to significantly *underestimate* heat loss in boxes which include the strong surface cooling over western boundary currents. In particular, in the mid-latitude North Atlantic box bounded by sections at 32°N and Ireland-to-Greenland, the annual-mean SOC flux is -13 ± 7 Wm^{-2}, compared to an inferred flux of -84 ± 16 Wm^{-2}. Clearly, such errors in the SOC fluxes will influence calculation of $\psi_{surf}(\Theta,\sigma)$, and should be taken into account when appraising this diagnostic.

Owing to the complex diagnosis of $\psi_{surf}(\Theta,\sigma)$, a comprehensive error analysis is not attempted here. Instead, to assess the impact of underestimated heat loss on $\psi_{surf}(\Theta,\sigma)$, calculations are repeated with a globally-modified version of the SOC heat fluxes. Josey *et al.* (1999) conclude that global adjustment of the heat fluxes, in order to balance the heat budget, can lead to significant regional biases, and therefore advocate *regional* corrections instead. However, for present purposes (the assessment of ψ_{surf}) SOC fluxes are adjusted following Da Silva *et al.* (1994): the shortwave radiation is reduced by 8% and the latent heat flux (and

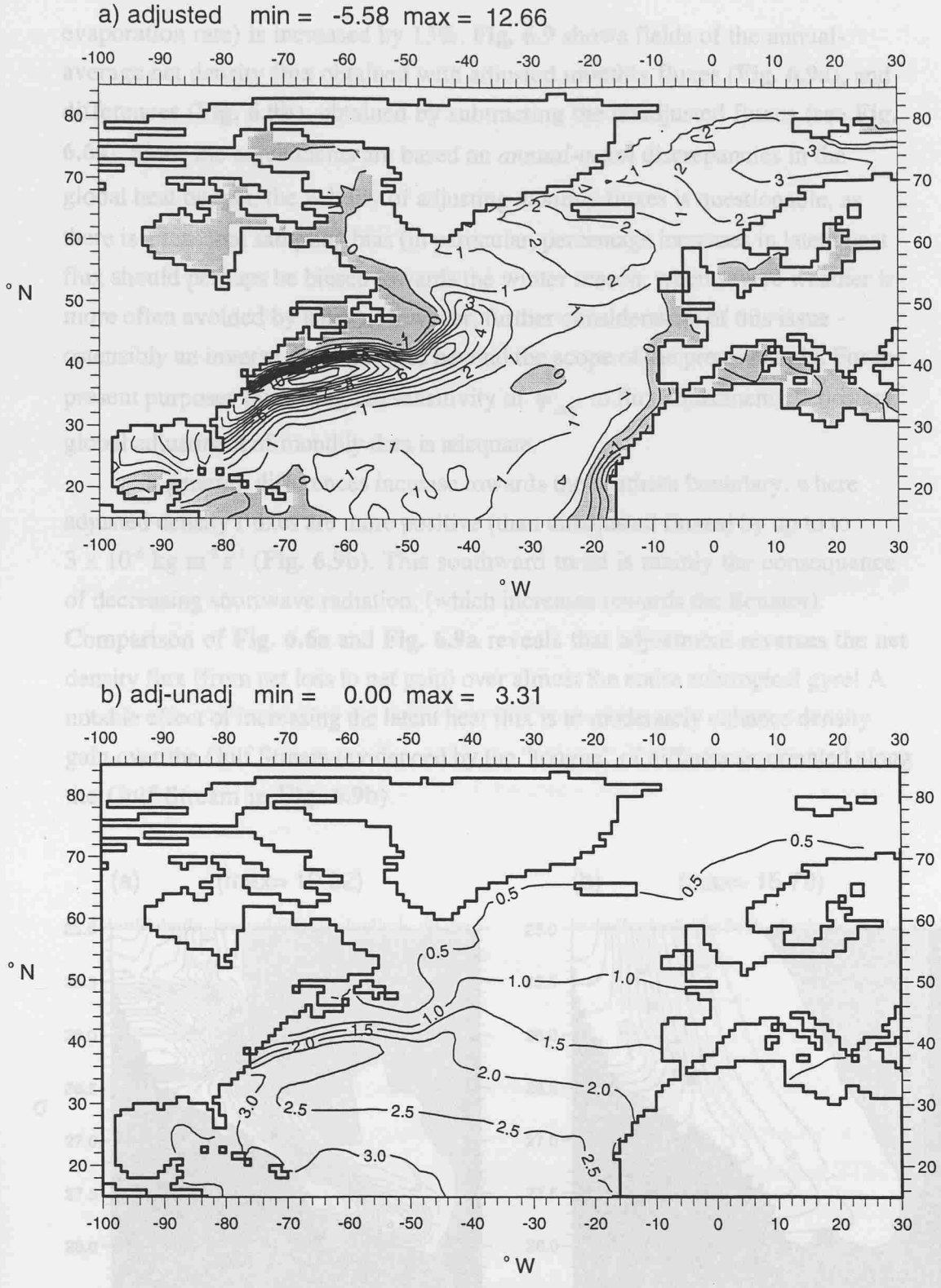

Figure 6.9: Fields of 1980-97 mean (annual-average) net surface density flux (10^{-6} kg m^{-2} s^{-1}) over the North Atlantic, (a) using globally-adjusted fluxes, (b) the "adjusted minus unadjusted" difference.

evaporation rate) is increased by 13%. **Fig. 6.9** shows fields of the annual-average net density flux obtained with adjusted monthly fluxes (**Fig. 6.9a**), and differences (**Fig. 6.9b**), obtained by subtracting the unadjusted fluxes (see **Fig. 6.6a**). Since the adjustments are based on *annual-mean* discrepancies in the global heat budget, the validity of adjusting *monthly* fluxes is questionable, as there is a seasonal sampling bias (in particular, percentage increases in latent heat flux should perhaps be biased towards the winter season, when severe weather is more often avoided by ships). However, further consideration of this issue - ostensibly an inverse problem - lies beyond the scope of the present study. For the present purposes (assessing the sensitivity of ψ_{surf} to flux adjustment), "constant" global adjustment of monthly data is adequate.

In general, differences increase towards the southern boundary, where adjusted density fluxes are more positive (than unadjusted fluxes) by up to to 3×10^{-6} kg m^{-2} s^{-1} (**Fig. 6.9b**). This southward trend is mainly the consequence of decreasing shortwave radiation, (which increases towards the Equator). Comparison of **Fig. 6.6a** and **Fig. 6.9a** reveals that adjustment reverses the net density flux (from net loss to net gain) over almost the entire subtropical gyre! A notable effect of increasing the latent heat flux is to moderately enhance density gain over the Gulf Stream (evidenced by the "tongue" of differences oriented along the Gulf Stream in **Fig. 6.9b**).

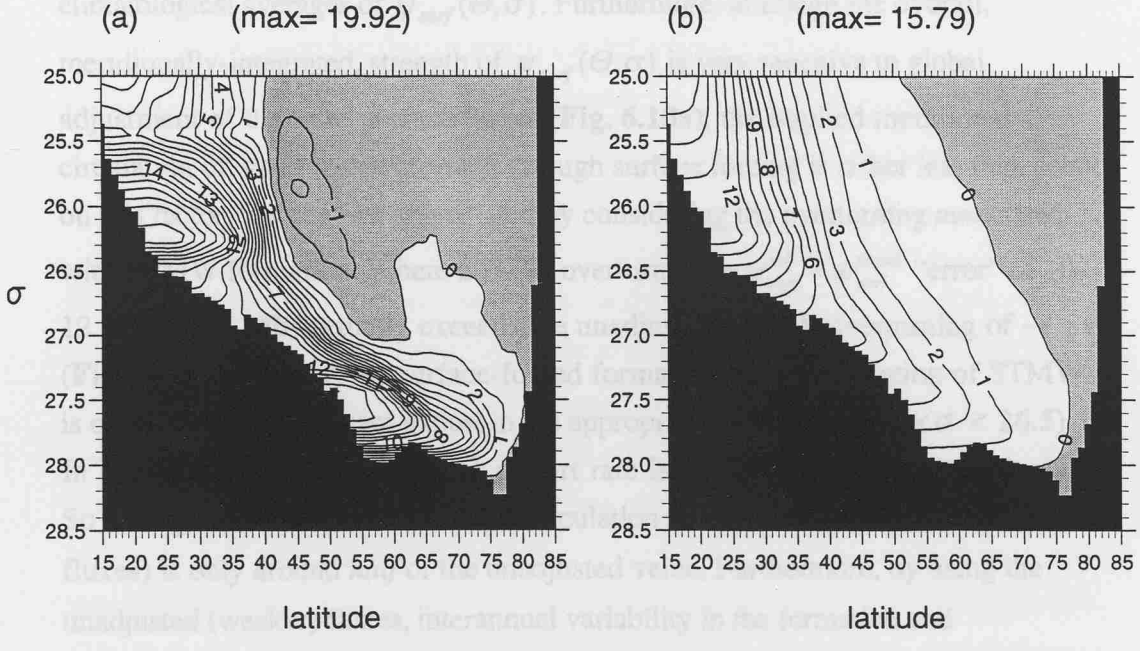

Figure 6.10: (a) as Fig. 6.8d, but based on globally-adjusted fluxes, (b) the difference ("adjusted minus unadjusted") between streamfunctions computed with adjusted and unadjusted fluxes.

Fig. 6.10 shows $\psi_{surf}^{adj}(\Theta,\sigma)$, the streamfunction computed with adjusted fluxes for each month over 1980-97 (**Fig. 6.10a**) and $\psi_{surf}^{adj}(\Theta,\sigma) - \psi_{surf}^{unadj}(\Theta,\sigma)$ (**Fig. 6.10b**), where $\psi_{surf}^{unadj}(\Theta,\sigma)$ is as computed with unadjusted fluxes (**Fig. 6.8c**). The result of using adjusted fluxes in the computation of ψ_{surf} is generally to strengthen implied overturning rates. This is consistent with the adjustment, which is designed to balance a global-mean *heating* of 30 W m^{-2} under the unadjusted fluxes (da Silva *et al.* 1994). Stronger cooling and evaporation rates over the North Atlantic result in stronger thermohaline overturning. As a consequence of southward increase in flux adjustment, $\psi_{surf}^{adj}(\Theta,\sigma) - \psi_{surf}^{unadj}(\Theta,\sigma)$ increases likewise, reaching just over 15 Sv at the southern boundary (15°N). The adjustment of surface fluxes thus has a considerable impact on $\psi_{surf}(\Theta,\sigma)$, and the difference field in **Fig. 6.10b** is, to a degree, representative of uncertainty in $\psi_{surf}(\Theta,\sigma)$.

In summary, the differences between **Figs. 6.8a**, **6.8b** and **6.8c** are significant, reflecting both the differences between air-sea flux climatologies (comparing **Figs 6.8a** and **6.8b**) and the correlation between surface density flux and surface density (comparing **Figs 6.8b** and **6.8c**). However, good general agreement is obtained between surface-forced overturning in the model and climatological averages of $\psi_{surf}(\Theta,\sigma)$. Furthermore, although the overall, meridionally-integrated, strength of $\psi_{surf}(\Theta,\sigma)$ is very sensitive to global adjustment of the SOC surface fluxes (**Fig. 6.10a**), the implied meridional circulation of water masses formed through surface forcing is rather less dependent on this factor. This can be appreciated by considering the overturning associated with STMW formation. Where STMW overturns, the $\psi_{surf}^{adj} - \psi_{surf}^{unadj}$ "error" of 10-12 Sv (**Fig. 6.10b**) actually exceeds the unadjusted STMW overturning of ~8 Sv (**Fig. 6.8c**). However, the surface-forced formation and recirculation of STMW is obtained as equatorward export in the appropriate σ-range ($26.3 < \sigma < 26.5$). In **Fig. 6.8c** and **Fig. 6.10a**, this export rate is ~4 Sv and ~6 Sv respectively. So the adjusted increase in STMW recirculation (due to uncertainties in surface fluxes) is only around *half* of the unadjusted value. Furthermore, by using the unadjusted (weaker) fluxes, interannual variability in the formation and recirculation of water masses (see below) is conservatively estimated.

6.3.3 Results: the surface-forced North Atlantic THC, 1980-97

Having established that *climatological* overturning streamfunctions can be obtained with observed fields of $\mathcal{D}_{in}$ and σ_{surf}, the SOC climatology database is now used to diagnose streamfunctions for individual years. **Fig. 6.11** shows $\psi_{surf}(\Theta,\sigma)$ in the latitude range 15-85°N, for each year of the database, 1980-97. For this diagnosis, unadjusted fluxes are used (in preference to adjusted fluxes), on the basis that global adjustment is by no means a correct methodology [indeed, Josey *et al.* (1999) find that such adjustment actually worsens the agreement between SOC fluxes and buoy-measured fluxes in the eastern subtropical gyre]. Furthermore, relative to the streamfunction overall, the overturning of individual water masses, especially at higher latitudes, is much less sensitive to flux adjustment.

In **Fig. 6.11**, a variable number of streamlines appear in given density ranges, in each year, reflecting differences in the overturning of a range of surface-formed North Atlantic water masses: in particular, subtropical (18° Water), intermediate (LSW) and dense (GSDW) varieties. Associated with these three water masses are "lower branch" flows, the strengths of which can be defined as the maximum equatorward transports, in density ranges $26.30 \leq \sigma \leq 26.50$, $27.65 \leq \sigma \leq 27.775$ and $\sigma > 27.775$ respectively, and extracted from **Fig. 6.11**. Of course, strictly speaking (by geographical definition), LSW cannot form north of 65°N and GSDW cannot form south of 65°N. However, the definition of these water masses is generalized in terms of density alone, in order to highlight changes in the North Atlantic overturning.

Figs. 6.12a-d show the 1980-97 time series of total, subtropical, intermediate and dense overturning rates (as defined above) extracted from yearly plots of ψ_{surf}. The time series of subtropical overturning rate is fitted with a least-squares linear-regressed trend. Given recent speculation about a relationship between Atlantic sector climate and water mass variability (Dickson *et al.* 1996), also plotted (**Fig. 6.12e**) are three versions of the NAO index, plus the AO-index. NAO-1 and NAO-2 are December-March averages of normalized sea level pressure (SLP) differences between Lisbon and Iceland, (after Hurrell 1995), and Gibraltar and Reykjavik (Jones *et al.* 1997). NAO-3 is a December-March average of the standardized amplitude in a NAO teleconnection pattern constructed from rotated Principal Component Analysis (NCEP Climate Prediction Center 1999).

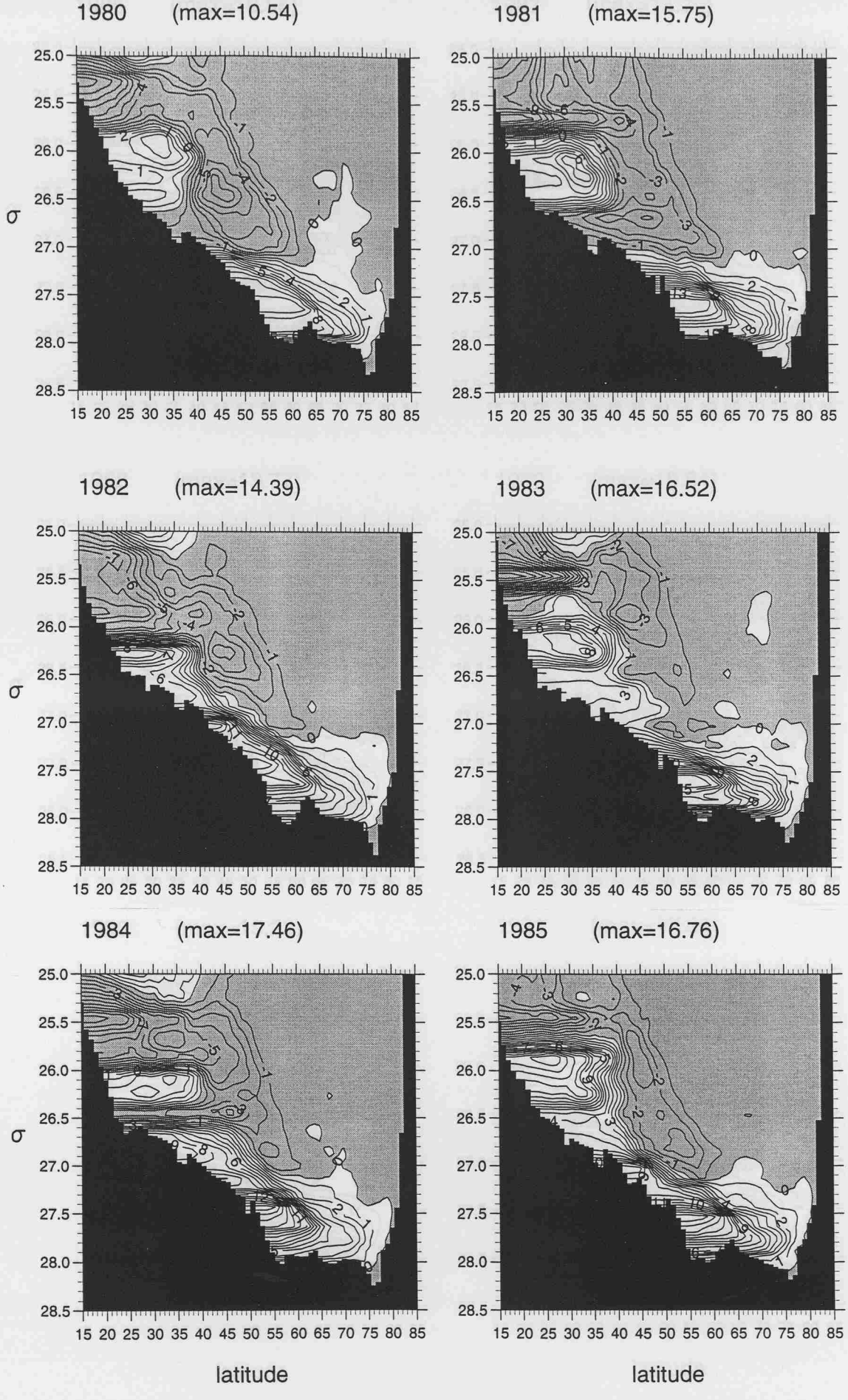

Figure 6.11: Annual-mean surface-forced streamfunctions obtained from unadjusted surface buoyancy fluxes, 1980-97.

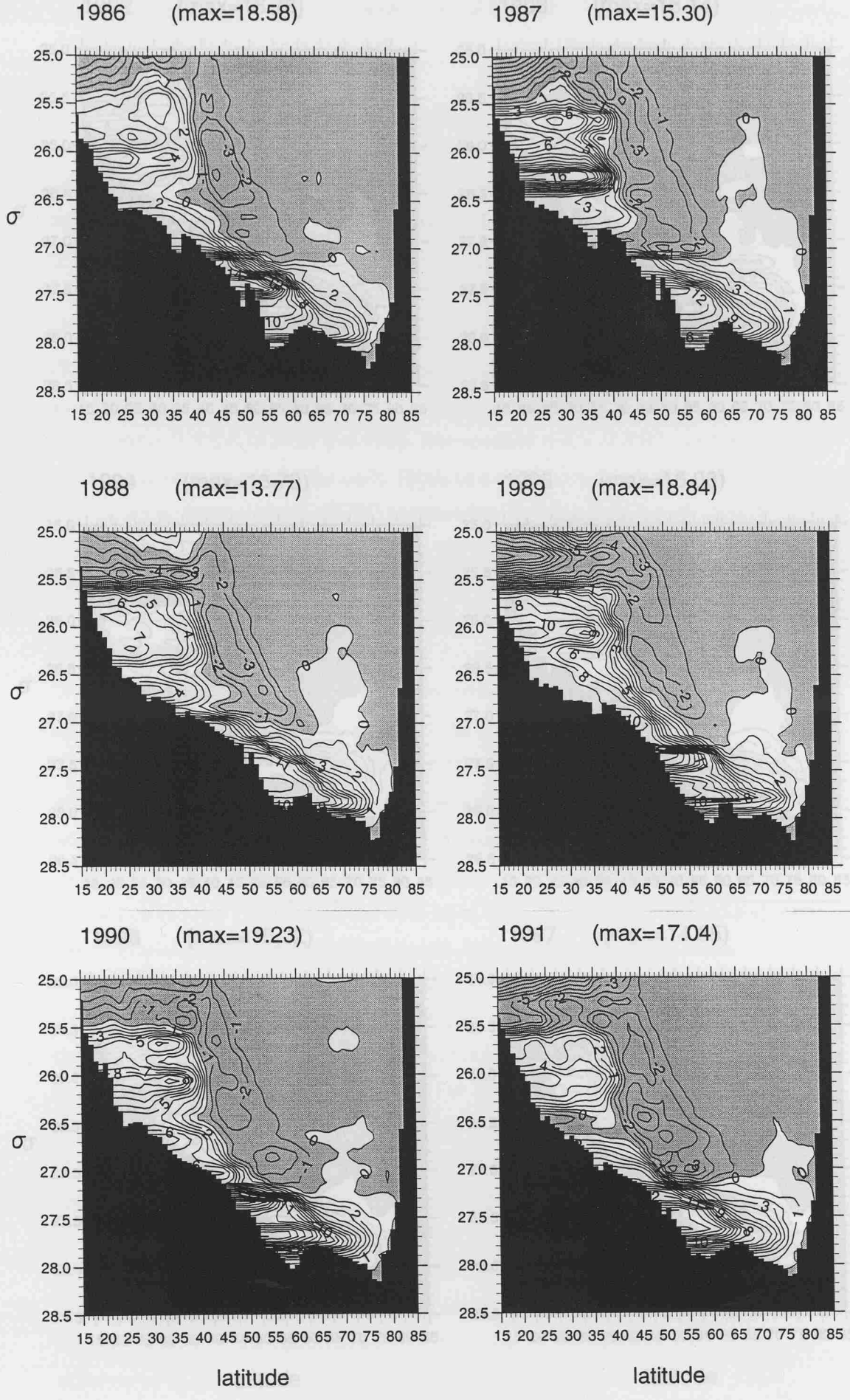

Figure 6.11 (ctd)

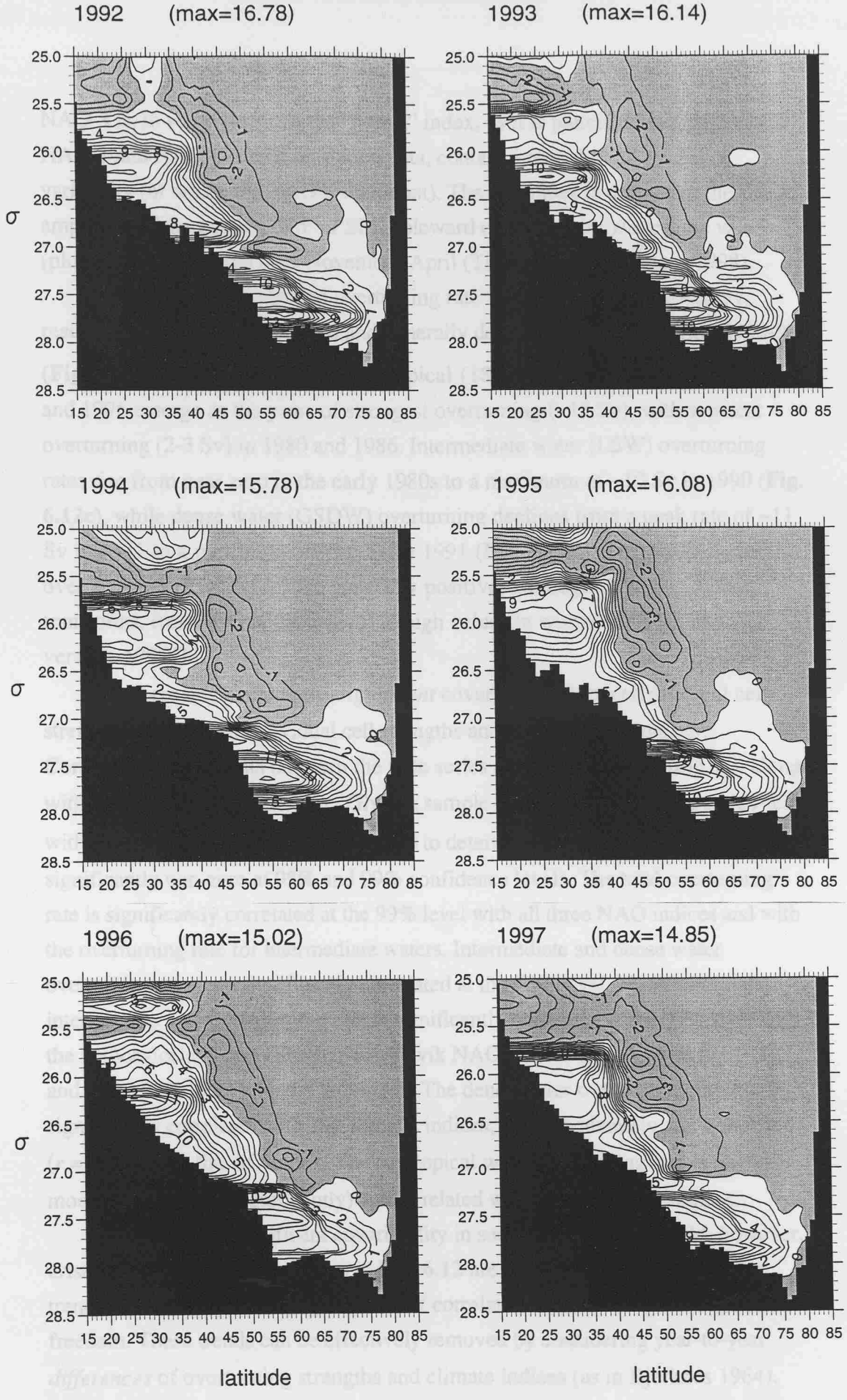

Figure 6.11 (ctd)

NAO-3 is, in some respects, the "purest" index, as it is pattern-based, whereas NAO-1 and NAO-2, based on station data, contain a record of all modes of variability (of which the NAO is dominant). The AO-index is defined as the amplitude of the leading EOF of SLP poleward of 20°N, with wintertime values (plotted here) averaged over November-April (Thompson and Wallace 1998).

The total surface-forced overturning rate varies in the range 10-20 Sv, reaching peak values in 1989-90 and generally decreasing over the period 1990-97 (**Fig. 6.12a**). In the case of the subtropical (18° Water) cell (**Fig. 6.12b**), 1987 and 1996 emerge as the years of strongest overturning (~15 Sv), with weakest overturning (2-3 Sv) in 1980 and 1986. Intermediate water (LSW) overturning rates rise from near zero in the early 1980s to a maximum of ~10 Sv in 1990 (**Fig. 6.12c**), while dense water (GSDW) overturning declines from a peak rate of ~11 Sv in 1981 to a minimum of ~3.5 Sv in 1991 (**Fig. 6.12d**). The NAO-indices over 1980-97 (**Fig. 6.12e**) are generally positive, although there are sudden transitions, from normal (near-zero) to high values in winter 1988/89, and vice versa in 1995/96.

Is there any *statistically significant* covariability between different cell strengths, or between individual cell strengths and the NAO/AO indices? Correlation coefficients between the time series are presented in **Table 6.3**, along with indications of significance. Given a sample size of only 18, a Student's *t*-test with *n*-2 (16) degrees of freedom is used to determine whether correlations are significantly non-zero at 95% and 99% confidence levels. The total overturning rate is significantly correlated at the 99% level with all three NAO indices and with the overturning rate for intermediate waters. Intermediate and dense water overturning rates are significantly correlated at the 95% level. Furthermore, the intermediate water overturning rate is significantly correlated at the 95% level with the Lisbon-Iceland and Gibraltar-Reykjavik NAO indices (NAO-1 and NAO-2), and at the 99% level with the AO-index. The dense water overturning rate is not significantly correlated with any climatic indices, but is moderately anti-correlated (r = -0.33) with the AO-index. The subtropical water overturning rate is likewise moderately (but not significantly) anticorrelated with all three NAO indices.

Statistically-significant covariability in such a short record could, however, arise by chance. The time series in **Fig. 6.12** are characterized by multi-year trends which diminish the significance of correlations by reducing the degrees of freedom. These trends can be effectively removed by considering year-to-year *differences* of overturning strengths and climate indices (as in Bjerknes 1964).

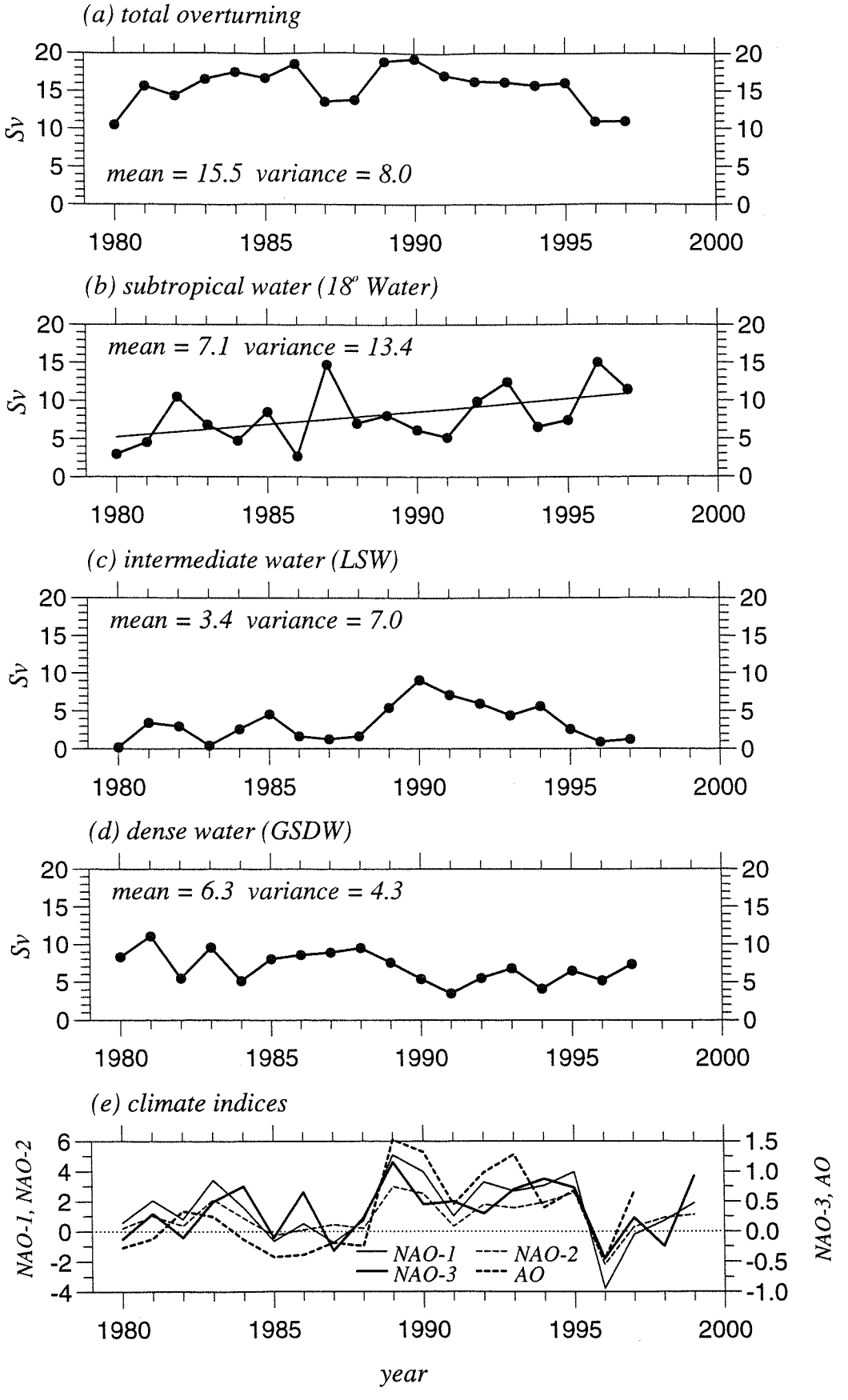

Figure 6.12: Time series over 1980-97 of: annual-mean overturning rates, (a) total, and for (b) subtropical, (c) intermediate, (d) dense water masses; and (e) three versions of wintertime NAO-index and the AO-index.

Correlations between the differenced variables are presented in **Table 6.4**. Wherever correlation coefficients in **Table 6.4** are smaller than respective values in **Table 6.3** (and, in many cases, no longer significant), the implied covariability is trend-dominated. The covariability of year-to-year "noise" can thus be tentatively distinguished from covariability which is dominanted by biennial-to-decadal trends. Note that significant anti-correlation between intermediate and dense water overturning rates is only obtained if trends are included in the time series. Likewise, intermediate water overturning rates are only significantly correlated with total overturning and NAO/AO indices on longer timescales. In other cases, the removal of presumably *uncorrelated* trends leaves significantly correlated interannual noise. In particular, there is highly significant anti-correlation of subtropical water overturning rates with the NAO-3 index (but not with NAO-1 and NAO-2 indices, which are weighted towards variability in the eastern Atlantic), and with total overturning rates.

Table 6.3: Correlations between overturning rates and climate indices, indicating correlations which are significantly different from zero at 95% and 99% confidence levels, based on a Student's *t*-test.

	subtropical	intermediate	dense	NAO-1	NAO-2	NAO-3	AO
total	-0.41	0.64**	-0.13	0.66**	0.61**	0.70**	0.41
subtropical		-0.13	-0.13	-0.39	-0.27	-0.45	0.14
intermediate			-0.53*	0.51*	0.47*	0.41	0.63**
dense				-0.04	-0.02	-0.17	-0.33
NAO-1					0.98**	0.80**	0.74**
NAO-2						0.75**	0.76**
NAO-3							0.58*

** significantly non-zero at 99% confidence level

* significantly non-zero at 95% confidence level

Table 6.4: As Table 6.3, but correlating year-to-year differences in overturning rates and climate indices.

	subtropical	intermediate	dense	NAO-1	NAO-2	NAO-3	AO
total	-0.52*	0.42	0.20	0.71**	0.62**	0.76**	0.49*
subtropical		-0.05	-0.04	-0.44	-0.27	-0.70**	0.07
intermediate			-0.28	0.16	0.17	0.03	0.23
dense				0.37	0.38	0.16	0.17
NAO-1					0.97**	0.75**	0.76**
NAO-2						0.63**	0.79**
NAO-3							0.46

Fig. 6.11 also reveals interannual variability in the σ-value about which the subtropical cell overturns: in particular, STMW overturns at low/high σ-values in 1986/1987, coincident with weak/strong cell strength respectively. It is this variability in σ-range (of the equatorward STMW branch) which leads to a climatological subtropical cell (**Fig. 6.8c**) which is weaker (~4 Sv) than the mean overturning obtained by the STMW cell definition adopted for **Fig. 6.12** (7.1 Sv). However, the necessarily coarse σ-resolution used here (see **Table 6.1**) permits detection of no more than gross variability in these modal σ-values.

6.4 Surface buoyancy forcing of the THC: a summary

The overturning streamfunction in density space, $\psi(\Theta,\rho)$, can be related to the combined zonally-averaged transformation and unsteadiness of water masses, $G(\Theta,\rho)$ and $\partial V(\Theta,\rho)/\partial t$ respectively, introducing novel diagnostics of the THC in GCMs. Furthermore, $G(\Theta,\rho)$ can be partitioned between $F(\Theta,\rho)$ and $\partial D_{diff}(\Theta,\rho)/\partial\rho$, terms which represent the effects of surface buoyancy forcing and diapycnal mixing respectively.

To demonstrate the applicability of these new diagnostics, annual means of $\psi(\Theta,\sigma_k)$, $\partial V(\Theta,\sigma_k)/\partial t$, $G(\Theta,\sigma_k)$ and $F(\Theta,\sigma_k)$ are obtained from the spun-up

model (CLIM2, year 21). In the model North Atlantic, significant unsteadiness of dense layers leads to spurious upwelling. Removing this unsteadiness from $\psi(\Theta,\sigma_k)$, the remaining "transformation streamfunction", $G(\Theta,\sigma_k)$, truly reflects the overturning of water masses which are formed at the surface - i.e., the steady THC. Computed from model fields of surface heat and freshwater fluxes, and mixed layer density, $F(\Theta,\sigma_k)$ bears close resemblence to $G(\Theta,\sigma_k)$ - i.e., the majority of the THC is explained by surface forcing and $F(\Theta,\sigma_k)$ can be interpreted as a "surface-forced streamfunction", $\psi_{surf}(\Theta,\sigma_k)$. Remaining discrepancies between $F(\Theta,\sigma_k)$ and $G(\Theta,\sigma_k)$ are accounted for by diapycnal mixing.

Given that the North Atlantic THC is indeed predominantly surface-forced, $\psi_{surf}(\Theta,\sigma)$ is computed from *observed* surface fields of heat flux, freshwater flux and density. An annual-mean climatological estimate of ψ_{surf} must carefully account for the fact that monthly surface density and surface density flux are correlated. The climatological surface-forced streamfunction obtained with the SOC dataset is broadly similar to the surface-forced THC in AIM. The problem of systematic bias in the SOC fluxes (net heat losses over western boundary currents are probably too weak) is addressed by globally adjusting shortwave radiation, latent heat flux and evaporation rate, and recomputing ψ_{surf} from the adjusted fluxes. The sensitivity of $\psi_{surf}(\Theta,\sigma)$ to flux data is thus examined. By using adjusted fluxes, ψ_{surf} is enhanced by up to 15 Sv, although the majority of this enhancement is due to stronger flux adjustment in subtropical and equatorial regions - the implied meridional circulation of surface-formed water masses at mid and high latitudes is relatively less sensitive to flux adjustment.

In the real world (as in the model) the THC is unsteady to a significant degree. While the THC might take several years to adjust to a change in surface density forcing, interannual variability in ψ_{surf} can nevertheless be expected to drive THC variability. Computed from unadjusted SOC fluxes for individual years over 1980-97, ψ_{surf} reveals considerable interannual-to-decadal variability.

Selecting equatorward branches of ψ_{surf} in density ranges characteristic of 18° Water, LSW and GSDW, time series of separate THC components ("cell strengths") are shown to vary likewise. In particular, the high latitude, high density overturning, associated with LSW and GSDW, varies markedly on a quasi-decadal timescale. While ψ_{surf} is dominated by transformation of dense water (GSDW)

throughout the 1980s, intermediate water (LSW) transformation assumed dominance in the early 1990s.

Correlations of intermediate water cell strength with two (out of three) versions of the NAO-index are statistically significant at a 95% confidence level, according with the observations of increased convection in the Labrador Sea (and the annually-renewed volume of LSW) during the late 1980s, peaking in the early 1990s with the NAO-index (Dickson *et al.* 1996). Interannual variability of the subtropical (18° Water) renewal cell is also evident. Taking year-to-year differences in subtropical cell strength and NAO-indices, covariability (of 18° Water formation and the NAO) is statistically significant at a 99% confidence level in the case of the NAO-3 index (the standardized amplitude in a NAO teleconnection pattern constructed from rotated Principal Component Analysis) which perhaps best represents variability in wind patterns over the mid-latitude North Atlantic. The impact on 18° Water of NAO-related anomalous wind forcing is addressed in the following chapter.

CHAPTER 7. NAO-MINIMUM WIND FORCING OF THE NORTH ATLANTIC SUBTROPICAL GYRE

Guided by a historical record of monthly-mean sea level pressure (SLP), an anomalous wind-forcing experiment (NAOWIND) is designed, with the purpose of simulating the time-evolving response of the North Atlantic circulation to idealized NAO-minimum basin-scale wind forcing. This chapter is organized as follows. NAO-minimum fields of SLP and wind anomalies are presented (§7.1). Idealized NAO-minimum wind stress fields (to force the model in NAOWIND) are constructed (§7.2). The results of NAOWIND are presented (§7.3) and summarized (§7.4), emphasizing the changes in the large-scale circulation and water masses due to NAO-minimum wind forcing.

7.1 NAO-minimum SLP anomalies and associated wind forcing.

To generate smoothly contoured fields of SLP, the 10^o x 5^o gridded data (see §3.4.3) are interpolated to a 1^o x 1^o grid by fitting quasi-Hermite polynomials (to the coarsely-gridded data). Variability in wintertime (December-April) SLP patterns reveal the spatial character of NAO-minimum wind forcing. Consider the four consecutive NAO-index minimum winters 1962/63-1965/66. **Fig. 7.1** shows the field of mean wintertime SLP anomaly for this period. Negative SLP anomalies over the subtropical gyre indicate a southward-shift of the Icelandic Low characteristic of NAO-minimum periods (Kushnir 1994).

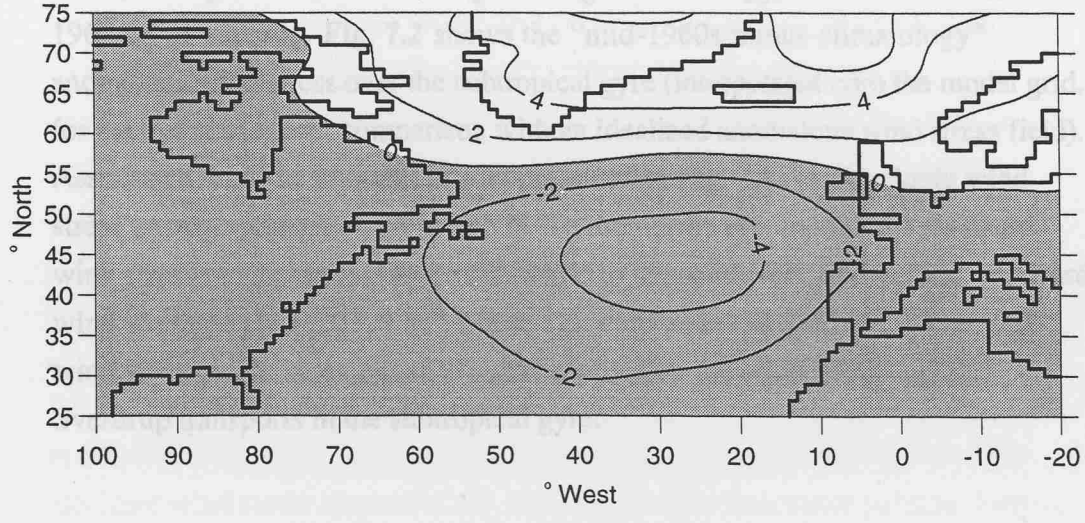

Figure 7.1: Wintertime SLP anomaly (mb) over the North Atlantic during the low NAO-index mid-1960s.

Associated with the anomalous SLP field in **Fig. 7.1** are wind stress anomalies, which can be estimated as follows. Assuming that the atmospheric circulation is in approximate geostrophic balance, zonal and meridional components of surface wind (u_g and v_g) are computed from the 1° x 1° SLP fields. Zonal and meridional components of surface wind stress (τ_x and τ_y) are then calculated from u_g and v_g:

$$\tau_x = \rho_{air} C_D u_g \left({u_g}^2 + {v_g}^2 \right)^{1/2} \tag{7.1a}$$

$$\tau_y = \rho_{air} C_D v_g \left({u_g}^2 + {v_g}^2 \right)^{1/2} \tag{7.1b}$$

where ρ_{air} is air density (1.225 x 10^{-3} g cm^{-3}) and C_D is the drag coefficient. Based on shipboard anemometer measurements, Yelland *et al.* (1998) established an empirical relationship between C_D and the wind speed at a height 10 m above the sea surface (U_{10}, in m s^{-1}):

$$C_D = 0.0005 + 0.000071 U_{10} \tag{7.2}$$

which is valid in the wind speed range $6 \leq U_{10} \leq 26$ m s^{-1}. For the present purposes, U_{10} is estimated to be $({u_g}^2 + {v_g}^2)^{1/2}$.

December-April mean wind stress fields are thus obtained from the SLP fields, averaged over 1873-1991 (providing a climatology) and over the winters 1962/63 to 1965/66. **Fig. 7.2** shows the "mid-1960s minus climatology" anomalous wind stress over the subtropical gyre (interpolated onto the model grid, for ease of subsequent comparison with an idealized anomalous wind stress field). Associated with the anomalous low pressure (in **Fig. 7.1**) is a cyclonic wind stress pattern, centred on 25°W, 45°N. To the northwest, anomalous eastward wind stress ranges up to 0.04 N m^{-2}, while to the southwest, anomalous westward wind stress reaches 0.03 N m^{-2}. These eastward and westward components of wind stress might be expected to significantly alter the wind stress curl and Sverdrup transports in the subtropical gyre.

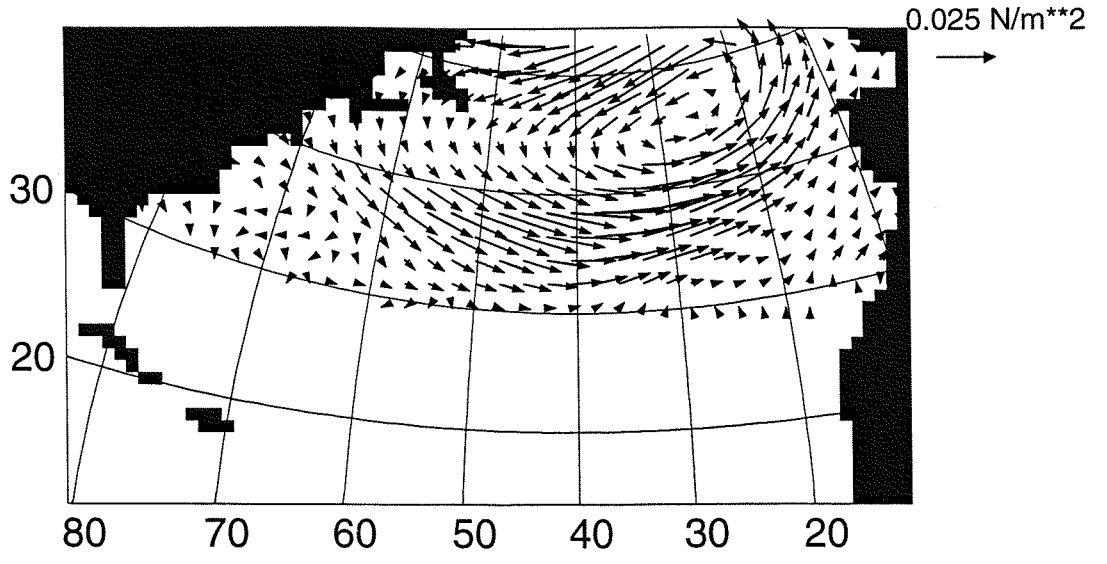

Figure 7.2: Anomalous wintertime (Dec-April mean) wind stress over the North Atlantic during the mid-1960s.

7.2 Constructing idealized NAO-minimum wind forcing

Based on anomalous pattern of wind stress in the mid-1960s, idealized NAO-minimum wind forcing is constructed. Climatological wind stress vectors (Hellerman and Rosenstein 1983) are "southwards-shifted" in mid-latitudes. This shift is applied to wind stress fields (already interpolated to the rotated grid of the model) over the approximate latitude range 30-60°N, southward shift increasing linearly from zero at ~30°N to a maximum of ~10° at ~45°N and decreasing linearly back to zero at ~60°N. Anomalous forcing is thus constructed for every month of the year - while the NAO-minimum wind forcing is essentially confined to the winter (December-April), climatological and idealized anomalous wind stress is weak during the rest of the year. The intention is to apply an extreme wind stress anomaly such is observed during persistent NAO-minimum phases (e.g. **Fig. 7.2**). Selecting the same subtropical gyre region shown in previous plots, **Fig. 7.3** shows wintertime (December-April averaged) wind stress fields: from the climatology used in CLIM1 (**Fig. 7.3a**) and from the idealized NAO-minimum forcing to be used in NAOWIND (**Fig. 7.3b**). The difference ("NAOWIND - CLIM1") reveals a southward displacement of cyclonic circulation in NAOWIND (**Fig. 7.3c**), similar to that in the mid-1960s (**Fig. 7.2**). The idealized wind stress anomalies are, however, around four times stronger than the SLP-derived estimates. In the real world, interannual variability during a "NAO-minimum" phase will to some extent smooth out the characteristic pattern, weakening the strength of inferred wind stress anomalies.

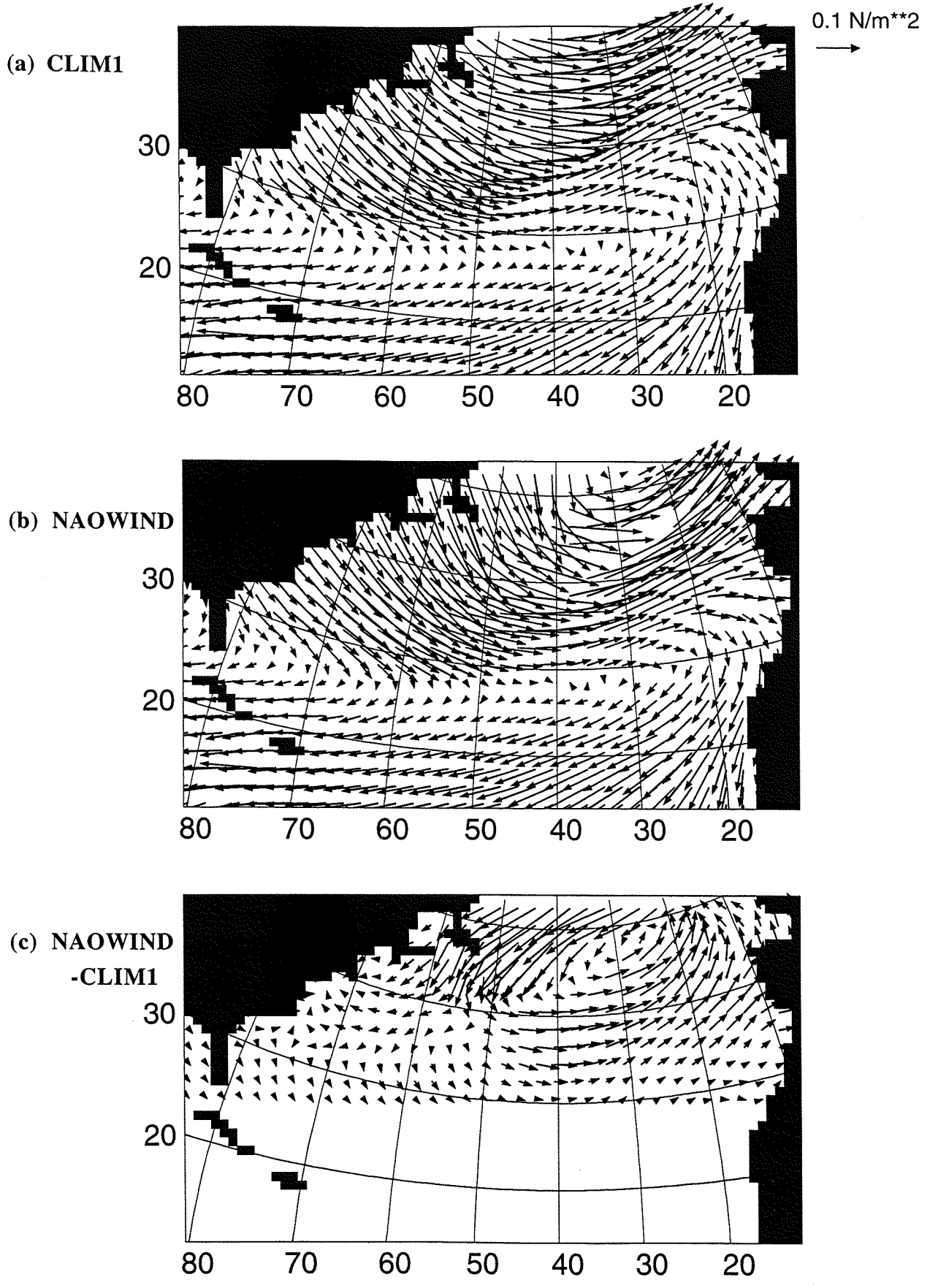

Figure 7.3: Dec-April mean wind stress fields used to force the model in (a) CLIM1 and (b) NAOWIND, and (c) NAOWIND-CLIM1

The Sverdrup balances implied by the wind forcing of CLIM1 and NAOWIND are used to predict the annual-mean WBC transports shown in **Fig. 7.4**. By shifting the mid-latitude westerlies southwards, a secondary minimum appears at 45-50°N (predicting a southward expansion of the subpolar gyre), while WBC maxima in the subtropics strengthen slightly, from ~40 Sv to ~50 Sv.

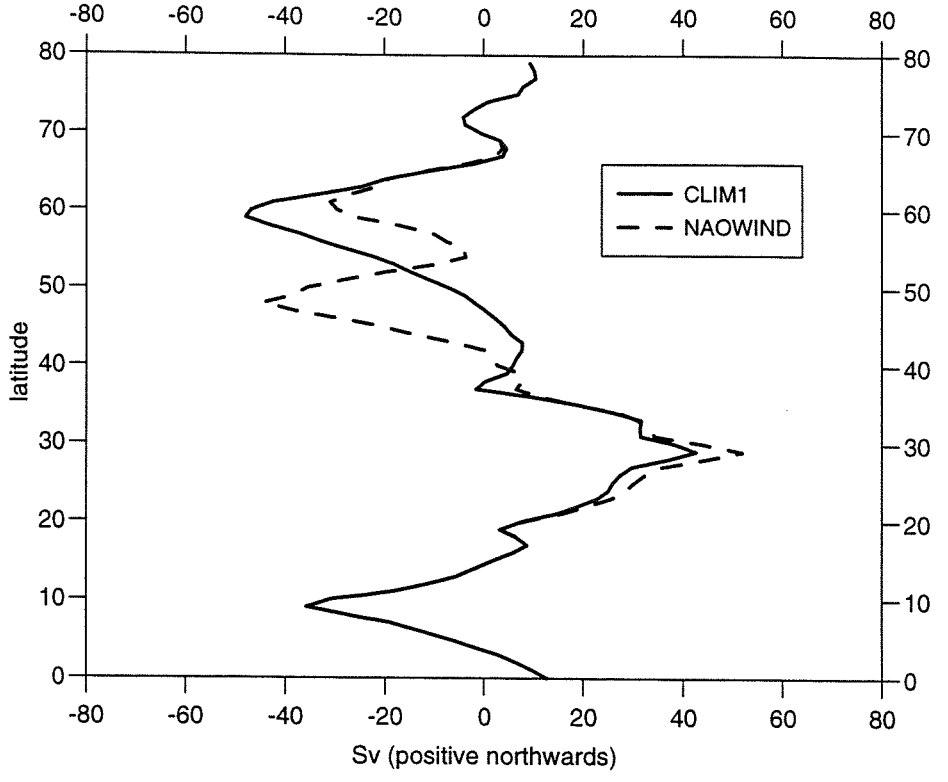

Figure 7.4: Annual-mean WBC transports predicted from Sverdrup balances implied by the wind forcing of CLIM1 and NAOWIND.

7.3 Model response to the NAO-minimum wind forcing

The 10-year sensitivity experiment (NAOWIND) is started after 20 years spin-up of CLIM1. The idealized NAO-minimum wind forcing is imposed at the beginning of year 21. Climatological wind forcing resumes (linearly interpolating the change in forcing over a one month period) at the end of year 25. Apart from a time-interpolated transition during the month between imposition of changes in wind forcing (all forcing data are linearly interpolated to each model time step), these changes are instantaneous. In this respect the year 21-30 wind forcing in NAOWIND represents a 5-year duration shift in the regime of atmospheric circulation. For model years 21-30, NAOWIND is compared with CLIM1. Changes in large-scale circulation and water masses are described in turn.

7.3.1 Changes in circulation

Fig. 7.5 shows the monthly basin-wide maximum and minimum of differences (NAOWIND minus CLIM1) in barotropic streamfunction (ψ'_{baro}), over years 21-30. It is shown below (see **Fig. 7.6c**) that positive values of ψ'_{baro} are generally associated with a strengthening of the subtropical gyre, while negative values are due to a southward expansion and strengthening of the subpolar gyre.

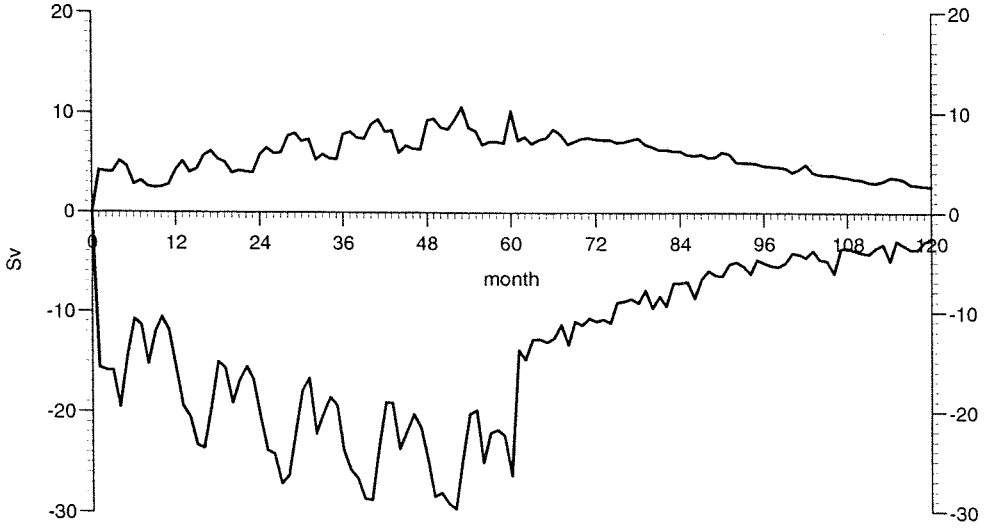

Figure 7.5: Time series of monthly maximum/minimum differences in the barotropic streamfunction, over years 21-30.

The barotropic circulation responds rapidly to a change in wind forcing, with extreme postive and negative values of ψ'_{baro} each January in years 21-25 (coincident with the largest wind stress anomalies). There are also interannual trends, the differences increasing over years 21-25, as the circulation adjusts towards a new equilibrium. An NAO-minimum equilibrium state is approached, but not reached, by year 25. After year 25, year-round climatological wind forcing resumes, and the largest circulation anomalies quickly decrease towards zero over years 26-30.

Fig. 7.6 shows fields of streamfunction (NAOWIND and CLIM1) and the difference (NAOWIND minus CLIM1), in January of year 25, when differences are largest (see **Fig. 7.5**). The anomalous wind forcing impacts most strongly in mid-latitudes (coincident with the largest wind stress anomalies), increasing circulation of the southern subpolar gyre. Further south, the subtropical gyre is strengthened by nearly 10 Sv. The largest positive differences are thus associated

(a) CLIM1 max=48.7 min=-24.3

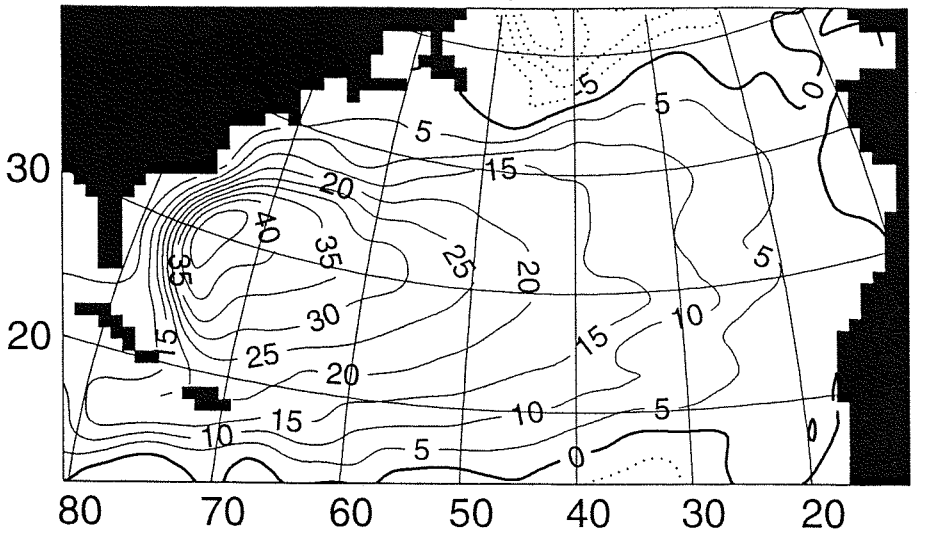

(b) NAOWIND max=54.8 min=-39.8

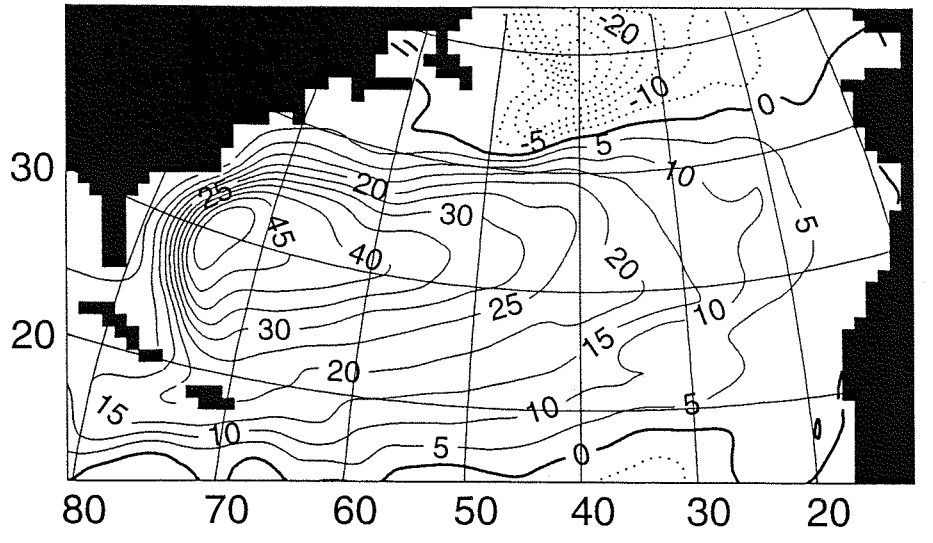

(c) NAOWIND minus CLIM1 max=9.8 min=-29.5

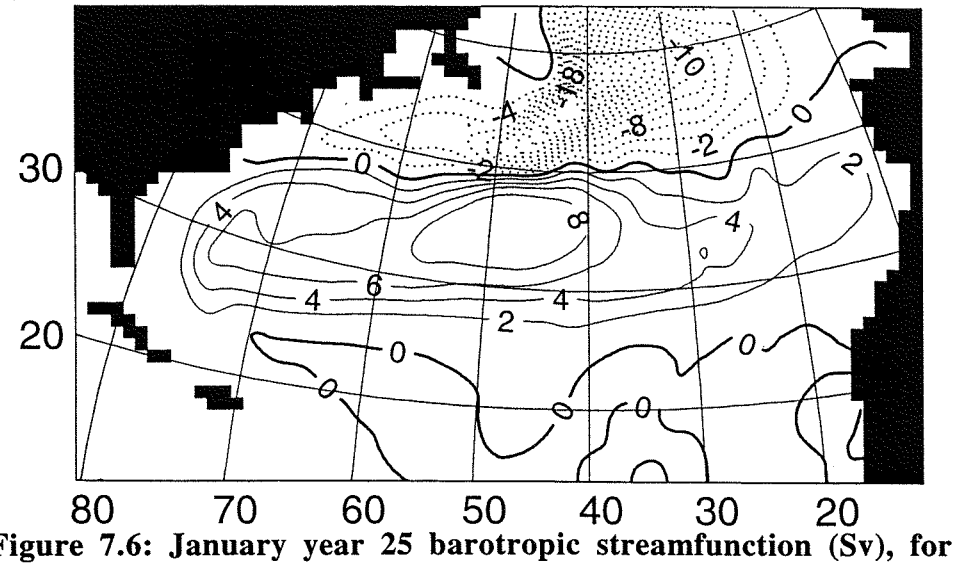

Figure 7.6: January year 25 barotropic streamfunction (Sv), for (a) CLIM1, (b) NAOWIND, and (c) NAOWIND minus CLIM1.

with a strengthening of the northern subtropical gyre, while largest negative differences reflect a southward expansion (and similar strengthening) of the subpolar gyre.

7.3.2 Changes in water masses

Computed as in §4.3.1, **Fig. 7.7** shows the year 21-30 trend of layer thickness anomalies. Layers 8 and 9 (light Subtropical Mode Water, including 18° Water) increase in basin-integrated thickness, at the expense of layers 11-13 (denser varieties of STMW). At higher density, layer 15 (a light Subpolar Mode Water) rapidly inflates over years 21-25, decreasing back to the year 20 (climatological) thickness over years 26-30. These changes can be understood by

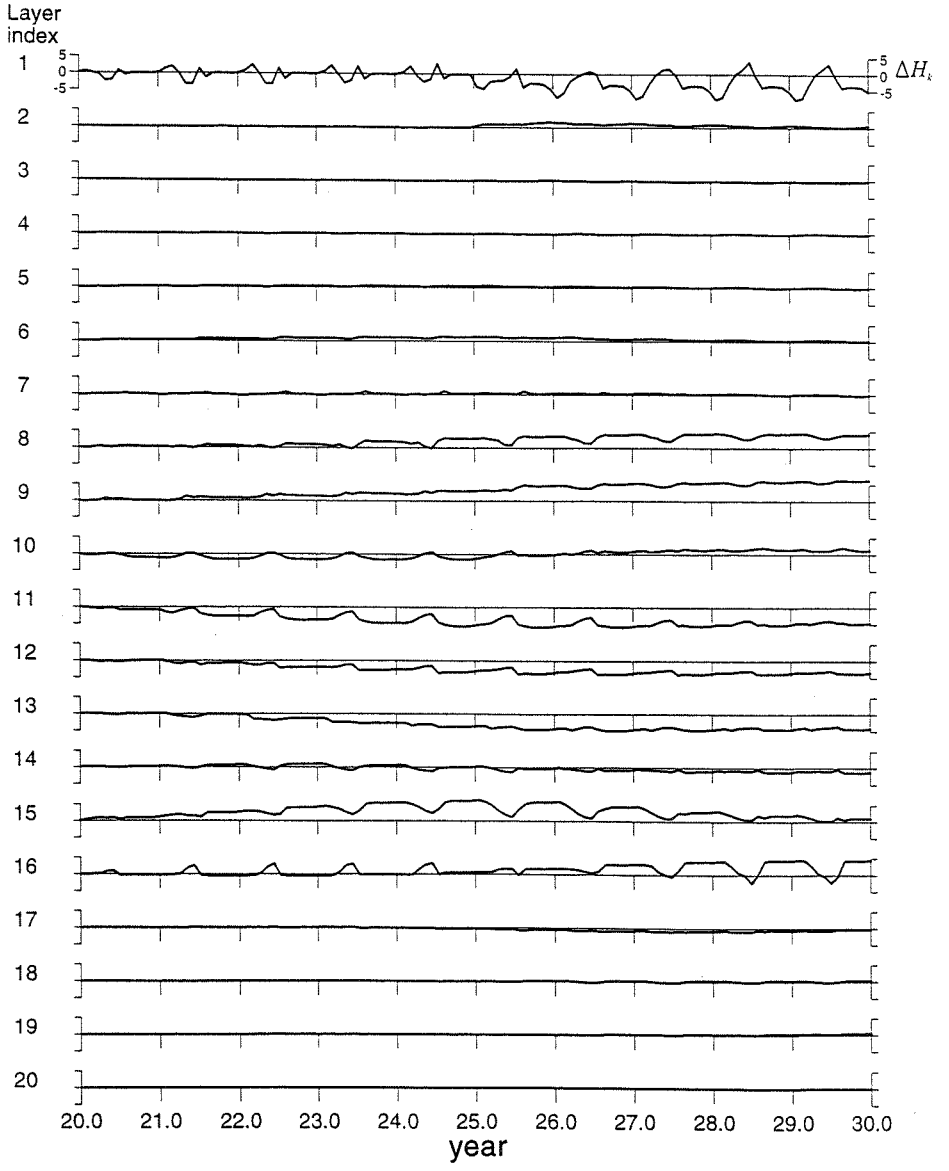

Figure 7.7: Basin-integrated layer thickness anomaly (m) trends during NAOWIND.

examining the spatial distributions of anomalous layer thickness. **Fig. 7.8** (as **Fig. 4.19**) shows thickness anomaly fields for STMW layers 8 and 10 in March of year 25, (**Figs. 7.8a,b**) and year 30 (**Figs. 7.8c,d**). Patches of anomalous layer thickness, formed under year 21-25 NAO-minimum wind forcing, spread across the subtropical gyre over years 26-30. The formation of extra STMW (see the positive anomalies in **Fig. 7.8c**) is attributed to enhanced ventilation in the central Atlantic by year 25, which can be in turn attributed to intensified near-surface circulation in that region (see **Fig. 7.6c**).

(a) layer 8, March year 25 max=140.2 min=-48.7

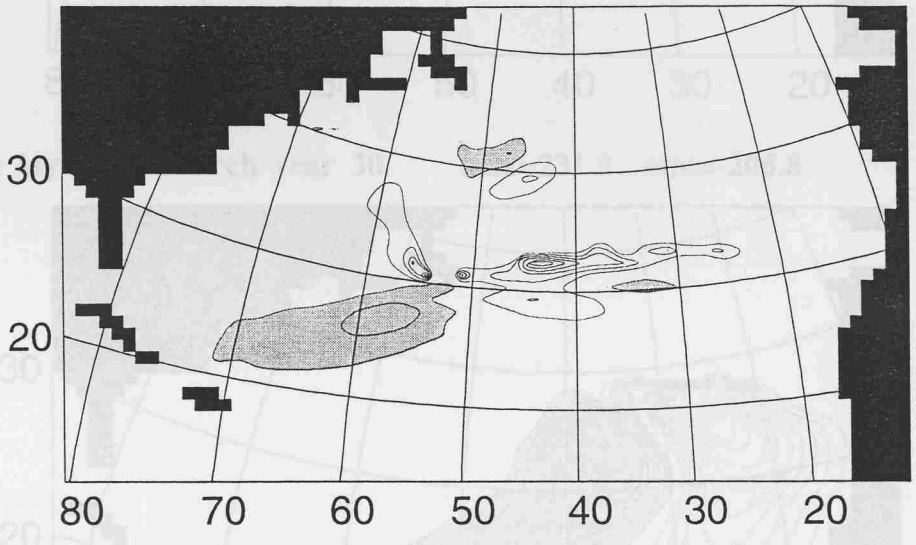

(b) layer 10, March year 25 max=265.2 min=-251.0

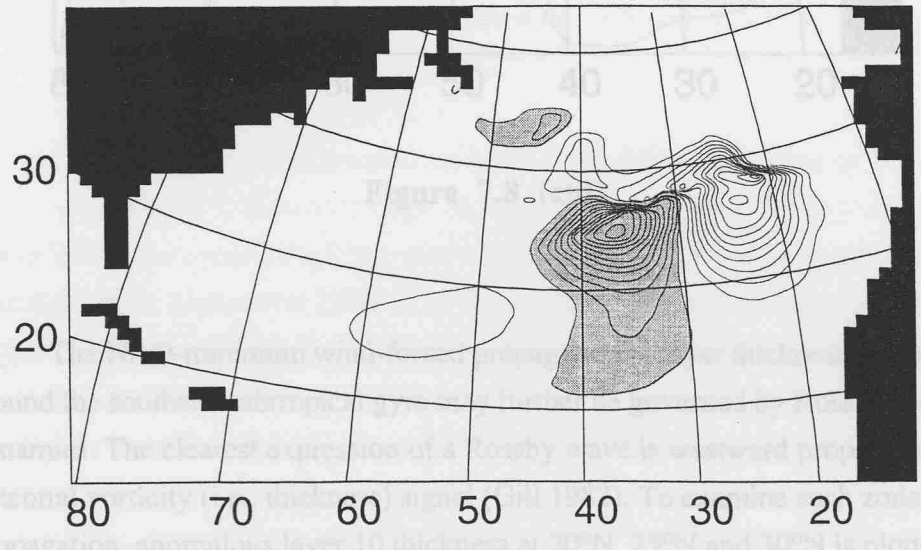

Figure 7.8: Thickness anomaly fields (C.I. = 20 m) for two mode water layers after five years of NAO-wind forcing, and after a further five climatological years.

(c) layer 8, March year 30 max=120.0 min=-28.1

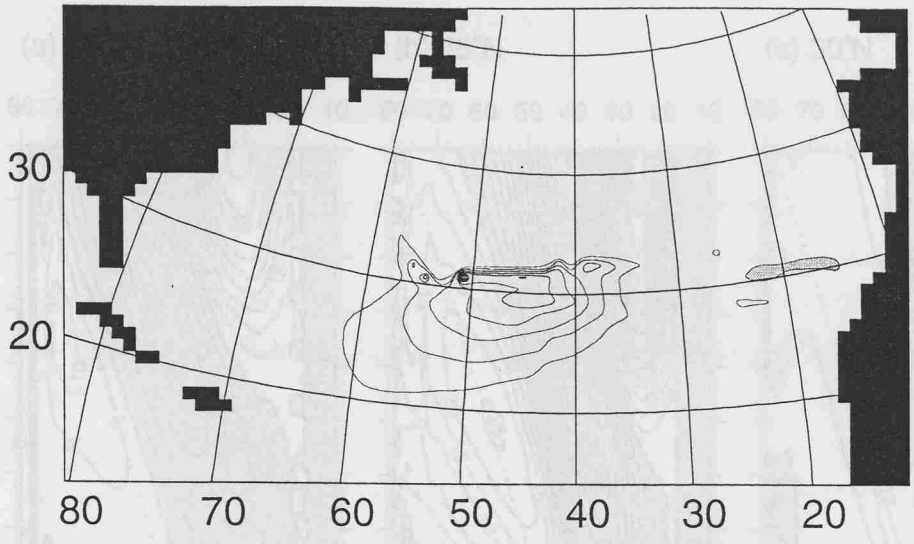

(d) layer 10, March year 30 max=231.9 min=-206.8

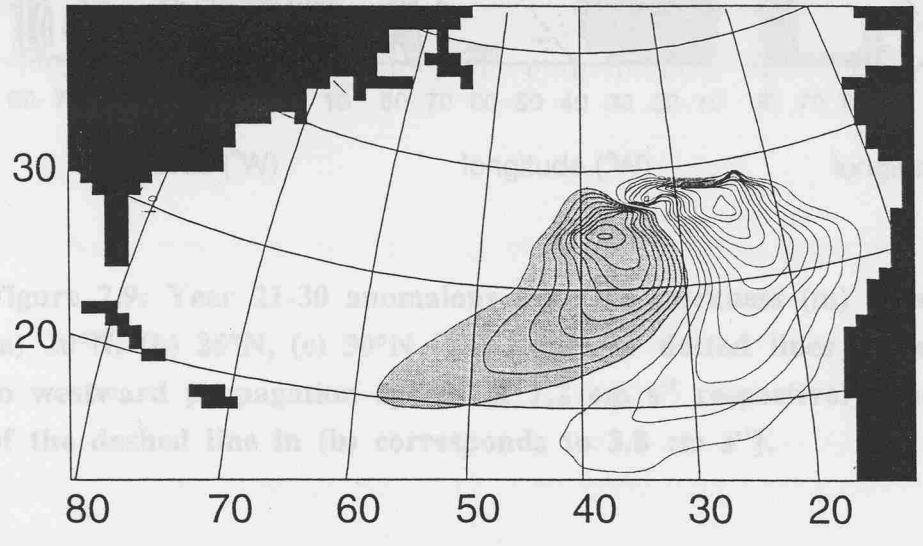

Figure 7.8 (ctd)

The NAO-minimum wind-forced propagation of layer thickness anomalies around the southern subtropical gyre may further be governed by Rossby wave dynamics. The clearest expression of a Rossby wave is westward propagation of a potential vorticity (i.e., thickness) signal (Gill 1982). To examine such zonal propagation, anomalous layer 10 thickness at 20°N, 25°N and 30°N is plotted in time-longitude space (**Fig. 7.9**).

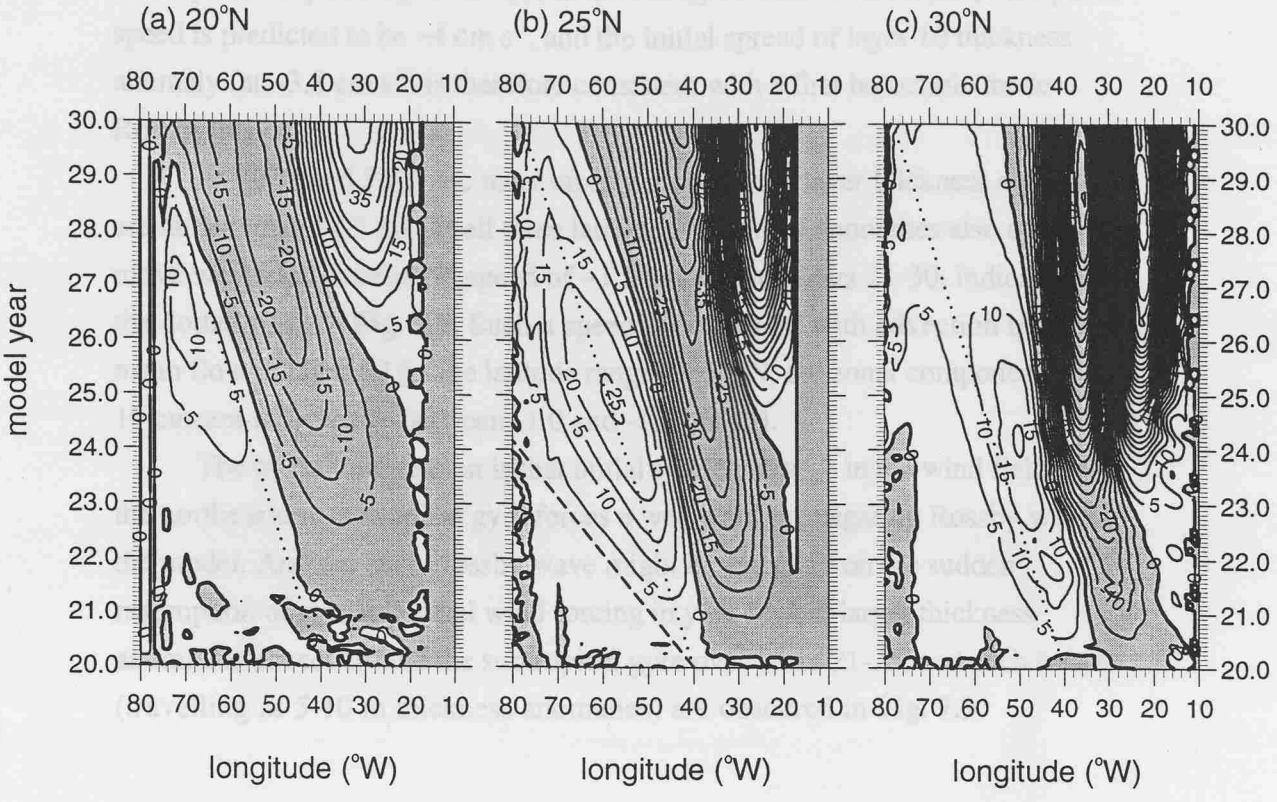

Figure 7.9: Year 21-30 anomalous layer 10 thickness (m) along: (a) 20°N, (b) 25°N, (c) 30°N [the slopes of dotted lines correspond to westward propagation speeds of 1.2 cm s^{-1} respectively, the slope of the dashed line in (b) corresponds to 3.8 cm s^{-1}].

Zonal propagation of anomalous layer 10 thickness is implied by "sloping" contours in **Fig. 7.9**. Contours slope almost exclusively from the lower right to upper left of the panels, implying westward propagation. Clearest westward propagation is apparent at 25°N (**Fig. 7.9b**), for which a fastest propagation speed of ~3.8 cm s^{-1} is indicated during years 22-24 by the 5 m contour (and the dashed line). Killworth *et al.* (1997) have prepared a map of the phase speed for first mode baroclinic Rossby waves in the presence of background westward flow. Rossby waves, the transient response to latitudinal perturbations of fluid on a β-plane, are governed by the conservation of potential vorticity. Apart from the variation of f with latitude, the potential vorticity gradient induced by a baroclinic zonal flow (i.e., vertical shear) modifies the effective local value of β. As a consequence, mean flows have the effect of increasing phase speeds of the fastest

long (first baroclinic mode) Rossby waves by a latitude-dependent factor. In the subtropics, the phase speed is thus increased by around 50%. At 25°N the phase speed is predicted to be ~4 cm s^{-1}, and the initial spread of layer 10 thickness anomaly (at ~3.8 cm s^{-1}) is therefore consistent with a first baroclinic mode Rossby wave.

At 20°N and 30°N the most rapidly propagating layer thickness anomalies are rather small (< 5 m). At all three latitudes, thickness anomalies also appear to move westward at a slower speed of ~1.2 cm s^{-1} over years 21-30, indicated by the dotted lines in **Fig. 7.9**. Such a speed is consistent with advection by the mean flow in layer 10 (in the latitude range 20-30°N, the zonal component of layer 10 current is typically between -1.0 and -1.4 cm s^{-1}).

The overall impression is that initial sudden change in the wind field over the northeastern subtropical gyre forces a westward-propagating Rossby wave in the model. Another such Rossby wave might be expected on the sudden resumption of climatological wind forcing in year 26, but larger thickness anomalies advect around the subtropical gyre over years 21-25, and such waves (travelling as 5-10 m thickness anomalies) are obscured in **Fig. 7.9**.

7.4 NAO-minimum wind forcing of the subtropical gyre: a summary

The principal characteristic of the NAO is a north-south shift of the mid-latitude westerlies on decadal timescales. A mid-latitude southward shift is applied to the wind stress fields which force the model ocean. Under this NAO-minimum wind forcing, the barotropic circulation of the model ocean significantly changes (as might be expected, given the Sverdrupian character of large-scale circulation - see §4.1.1). Largest changes occur in mid-latitudes. The subpolar gyre expands southwestward and approximately doubles in strength. The subtropical gyre strengthens by up to 5-10 Sv in the mid-gyre region, enhancing thermocline ventilation in the central gyre. The 18° Water of the western Sargasso Sea and the Gulf Stream are relatively unaffected, as NAO-minimum wind forcing is applied here as a remote anomaly (although locally, anomalous northwesterlies are associated with more frequent cold outbreaks during a NAO-minimum winter). Further east in the subtropical gyre, the model response to suddenly-imposed NAO-minimum wind forcing is a small-amplitude (5-10 m thickness anomaly) westward-propagating baroclinic Rossby wave.

To compare the impacts on the Gulf Stream of anomalous wind-forcing and excess winter cooling, **Fig. 7.10** shows the January (strongest anomalous wind

forcing) and May (peak cooling-related intensification) year 21 differences (NAOWIND minus CLIM1) in barotropic streamfunction (to compare with COOL3). Although the subtropical gyre is somewhat enhanced (by up to 5.2 Sv) in January, this increase has diminished by May (when the maximum increase is only 2.6 Sv). Compared to **Fig. 4.25c** (which indicated a maximum increase of over 6 Sv, in response to excess cooling), this relatively small change suggests that an end-of-winter Gulf Stream intensification (Worthington 1977) is more likely the result of excess winter cooling, rather than basin-scale NAO-minimum wind forcing.

(a) January year 21 max=5.2 min=-19.4

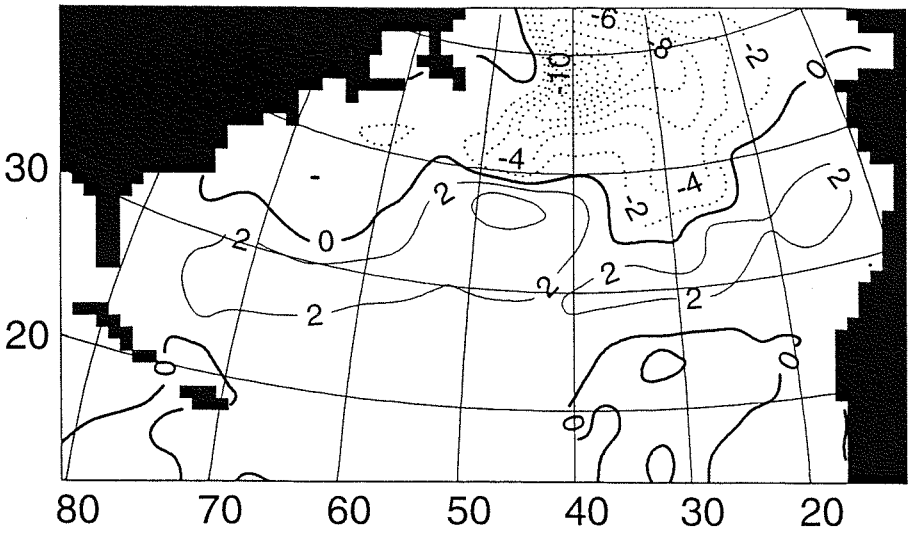

(b) May year 21 max=2.6 min=-15.1

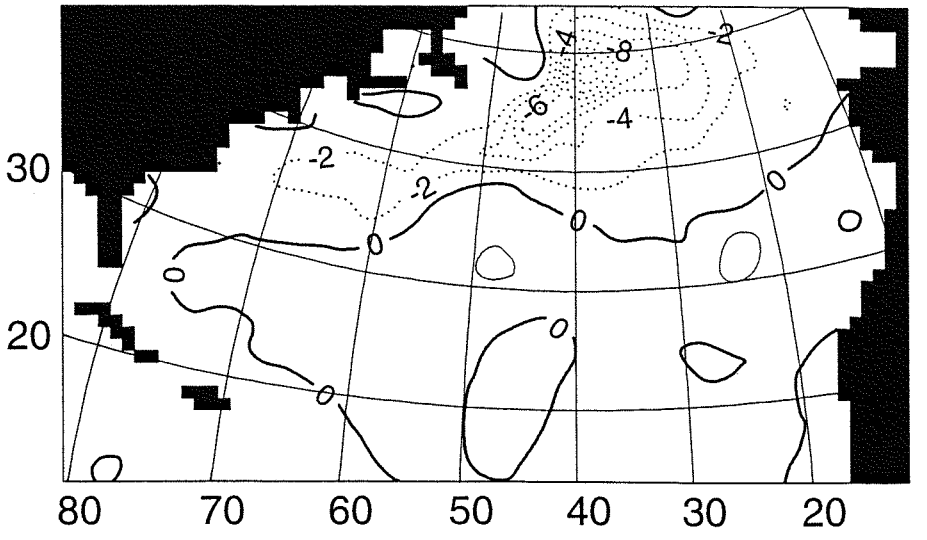

Figure 7.10: Fields of NAO-minimum wind forced changes in barotropic streamfunction, for January and May in year 21.

CHAPTER 8. DISCUSSION

In this final chapter, the findings of chapters 4-7 are summarized in §8.1. Variability of model 18° Water and intensification of the model Gulf Stream (both due to excess cooling) is discussed in §8.2 and §8.3 respectively, with reference to observations. With the benefit of hindsight, §8.4 reviews the suitability of the present model for sensitivity experiments such as those undertaken here. Possible further work is outlined in §8.5, and final remarks are made in §8.6.

8.1 Overall summary of results

Observations of interannual variability in 18° Water (Talley and Raymer 1982) and Gulf Stream transport (Worthington 1977) have motivated a modelling sensitivity study. The North Atlantic circulation is simulated with a three-dimensional isopycnic-coordinate GCM. Idealized anomalous buoyancy-forcing fields (associated with outbreaks of cold, dry continental air over the Gulf Stream/Sargasso Sea region) are constructed. In a series of sensitivity experiments, wintertime buoyancy loss over the Gulf Stream and Sargasso Sea is thus increased to varying degrees, with anomalous ocean-to-atmosphere buoyancy fluxes of up to double climatological values.

Under excess buoyancy loss, winter mixed layer depths increase, and a greater volume of model 18° Water is formed. End-of-winter mixed layer density also increases, leading to the formation of a denser variety of 18° Water. The anomalous 18° Water recirculates around the Sargasso Sea as a signal of low potential vorticity, which spreads out and weakens on a decadal timescale. Strengthened horizontal pressure gradients in the vicinity of the anomalous 18° Water drive intensified baroclinic transports at the "immediate" end of winter (in March), after which a full-depth barotropic intensification of the Gulf Stream develops. Strongest intensification occurs in May, when the Gulf Stream barotropic transport is increased locally by up to 10 Sv.

The anomalous transports which account for barotropic intensification are confined to deep and abyssal layers of the model. Where the associated anomalous bottom currents traverse isobaths, "extra" bottom pressure torque (BPT) is invoked. An anomalous BPT term in the barotropic vorticity balance may therefore account for the intensification. Computed from the model fields of density and sea surface height, such a term does appear to produce the extra negative vorticity associated with anticyclogenic intensification. It is concluded that wintertime

excess buoyancy loss drives a springtime barotropic response of the subtropical gyre, through BPT, due to "JEBAR" (the Joint Effect of Baroclinicity And Relief).

The Gulf Stream intensification decreases after May as lateral eddy mixing weakens anomalous cross-stream pressure gradients. This eddy mixing is parameterized in the model by a layer thickness diffusion velocity, u_d, nominally chosen to be 1.0 cm s^{-1}. Further experiments establish the sensitivity of intensification strength to the choice of u_d. With $u_d = 0.1$ cm s^{-1} (weak thickness diffusion), the intensification is increased by ~50%, while, for $u_d = 10$ cm s^{-1} (strong thickness diffusion), the intensification is roughly halved. These further sensitivity experiments also reveal the varying degrees to which the model subtropical gyre can be dominated by diffusive eddy mixing (Rhines and Young 1982a, 1982b) or adiabatic (non-diffusive) ventilation of the thermocline (Luyten, Pedlosky and Stommel 1983).

In light of the model results, recent (1980-97) interannual variability in the formation and recirculation of 18° Water, and other water masses, is deduced from observed surface heat and freshwater fluxes. Interannual variations in the strength of 18° Water renewal (thus deduced) and a wintertime index of the North Atlantic Oscillation (NAO) are found to be strongly anti-correlated (with a correlation coefficient of -0.70, statistically significant at a 99% confidence level). Distinct formation episodes (when the inferred equatorward transport of 18° Water reaches 15 Sv) are highlighted, in 1987 and 1996.

A separate sensitivity experiment shows that changes in wind forcing alone (characteristic of successive severe winters during persistent minima of the NAO index) do not lead to the 18° Water variability and Gulf Stream intensification driven by excess buoyancy loss. The NAO-minimum wind forcing does, however, increase barotropic transport in the southern subpolar gyre and enhance thermocline ventilation in the central subtropical gyre.

The idealized excess cooling and anomalous wind forcing fields applied in the model experiments are typically associated with a low index of the NAO. It is concluded that 18° Water is strongly renewed, and the Gulf Stream intensifies, under NAO-minimum *buoyancy* forcing.

8.2 18° Water variability

Despite rather coarse density (vertical) resolution ($\Delta\sigma_\theta = 0.15$), it has been possible to simulate model 18° Water variability which is strikingly similar to that reported by Talley and Raymer (1982): in particular, evolution of the anomalously

low PV and higher modal density at *Panulirus* during the mid/late 1960s. The sensitivity experiment COOL1 suggests a direct relationship between this low PV and excess winter cooling of the Gulf Stream.

To what extent does such a relationship apply to the real world? Over the period 1954-80, Jenkins (1982) only found significant *lagged* correlation coefficients between local annual-mean heat flux (averaged over 30-40°N, 60-70°W) and isopycnal salinities (for σ_θ = 26.1, 26.3 and 26.5) at *Panulirus*. Talley and Raymer (1982) computed monthly heat loss over a smaller region (34-36°N, 65-70°W), and were unable to deduce a strong direct correlation between properties of the *Panulirus* 18° Water and local heat flux.

The poor correlations between heat flux and 18° Water properties lead Talley and Raymer (1982) to conclude that a long-period storage process may offset the impact of individual cold winters. Jenkins (1982) proposes more specifically that, in the subtropical gyre, the upper ocean stores buoyancy interannually and that the response of 18° Water production to anomalous heat loss may consequently be non-linear. The five-year evolution of lower PV and higher modal density (**Fig. 4.18b**) suggest that such a storage process is indeed important. Furthermore, the variability of model 18° Water is forced by anomalous buoyancy loss *over winter* (rather than over the entire year). It is this wintertime forcing which crucially determines the end-of-winter mixed layer depth and density fields, and in turn sets the charcteristics of the subducting mode waters. Once subducted, patches of anomalous layer thickness appear to advect with the background circulation rather than propagate as wave-like PV disturbances. Only westward-propagating thickness anomalies forced by sudden changes of wind-forcing (in NAOWIND) travel at speeds consistent with first baroclinic mode Rossby waves.

Worthington (1972) proposed a shallow meridional circulation cell: 18° Water sinks along the southern flank of the Gulf Stream and spreads equatorward, compensated by gradual upwelling across the Sargasso Sea and a poleward surface drift converging on the Stream (**Fig. 2.15**). A meridional streamfunction in density space (**Fig. 6.4a**) includes an analagous "overturning" cell associated with 18° Water formation, recirculation and dissipation, which can be related to surface buoyancy forcing (**Fig. 6.4d**). Furthermore, surface-forced "transformation streamfunctions" are diagnosed from observed surface heat and freshwater fluxes over 1980-97 (**Fig. 6.11**). These streamfunctions reveal interannual variability in the overturning of 18° Water, as well as Labrador Sea Water (LSW) and Greenland Sea Deep Water (GSDW). The period 1980-97 is characterized by generally positive indices of the NAO (**Fig. 6.12e**). Along with LSW and GSDW, 18° Water is reported to co-vary with the NAO: 18° Water and

GSDW are believed to convect in a coordinated fashion, reflected in sustained renewal of these water masses at minima of the NAO index, while LSW is convectively renewed at NAO-index maxima (Dickson *et al.* 1996). Indeed, 18° Water was strongly renewed in the mid/late 1960s and the late 1970s (**Fig. 2.22c**), periods when NAO indices were low (**Fig. 2.21**). Over the period 1980-97, based on the diagnosis of surface fluxes, the 18° Water renewal rate is only weakly anti-correlated with different versions of the NAO-index. However, considering interannual differences in the 18° Water renewal rate and NAO indices, much stronger (and statistically significant) anti-correlations are obtained, with up to 49% of renewal rate variability explained by interannual variations of the NAO-index.

Detailed investigation of a possible link between these water mass formation rates and the NAO has only recently been undertaken. Estimating annual water mass formation rates in the North Atlantic over the period 1945-89 (from COADS data), Speer (1998) confirms the assertion of Dickson *et al.* (1996), namely that subpolar and subtropical mode water formation is respectively correlated and anticorrelated with the NAO-index. Speer (1998) notes a marked increase of subtropical mode water formation in the "last few years" (of the 1945-89 time series), as is evident in the present study (**Fig. 6.12b**). This recent strong 18° Water renewal is, however, coincident with *high* values of the NAO-index. This is contrary to the anti-correlation generally obtained between renewal rates and NAO-index over 1945-89. It seems likely, then, that 18° Water renewal is *variably dependent* on the NAO. That is, 18° Water variability might sometimes (as in the late 1980s) be better explained by modes (of variability) other than the NAO.

8.3 Gulf Stream intensification

The modestly enhanced Gulf Streams (in all three buoyancy flux sensitivity experiments), driven by anomalously deep late winter mixed layers, provide some evidence in support of Worthington's (1972) anticyclogenesis hypothesis. However, modelled Gulf Stream intensifications (barotropic transport increases of up to 20%) are somewhat weaker than observed changes in end-of-winter Gulf Stream transport. Worthington (1977) presents evidence that Gulf Stream transport after the severe winter of 1976-77 (~95 Sv) was around 50% stronger than after the mild winter of 1974-75 (~62 Sv). The modelled intensification, characterized by positive and negative extremes in barotropic transport anomaly, evolves most notably during May (see **Fig. 4.24b**). There are no suitable observations with which to compare this ~1 month timescale of intensification.

Worthington (1977) considers Gulf Stream transport relative to 2000 m, finding that gross variability in the upper half of the Gulf Stream (thus defined) is nearly double the total mean theoretical wind-driven transport. This alludes to cooling-related variability in the *baroclinic* component of Gulf Stream transport. However, theoretical studies suggest a *barotropic* response to cooling. Stommel and Veronis (1980) show that a geostrophic adjustment to time-dependent cooling might appear as a significant increase in barotropic transport. Considering the Gulf Stream recirculation as confined to a low PV bowl (associated with the region of 18° Water formation), Marshall and Nurser (1988) show that the depth of this bowl descends hyperbolically towards the Gulf Stream (see **Fig. 2.17**), striking the ocean floor a few hundred kilometres south of the Stream axis. They argue that the barotropic recirculation intensifies as cooling forces the bowl to deepen and strike the ocean floor further south of the Gulf Stream.

In the present study, excess winter buoyancy loss over the Gulf Stream is followed in spring by increases of up to 10 Sv in barotropic transport. Considering the barotropic vorticity balance, the most obvious mechanism for anticyclogenic intensification is negative vorticity production through anomalous BPT. Holland (1973) showed that BPT plays an important role in enhancing the wind-driven subtropical gyre of an idealized model (see **Fig. 2.12**). A degree of similarity between fields of net vorticity change (**Fig. 5.15c**) and the diagnosed production of vorticity through anomalous BPT (**Fig. 5.14c**) suggest that this is indeed the mechanism for barotropic intensification in the model. BPT effects are implicit in the barotropic recirculation mechanism proposed by Marshall and Nurser (1988). The more subtle responses to cooling predicted by the idealized models of Nof (1983) and Adamec and Elsberry (1985a, 1985b), involving the dynamical response of an upper ocean frontal jet, are not clearly substantiated in this study.

Intensification of the Gulf Stream, such as observed in spring 1977 (Worthington 1977), may be due to a combination of anomalies in both thermohaline and wind forcing. SLP patterns during the winter of 1976/77 (**Fig. 3.6**) resemble the mid-1960s minimum state of the NAO (**Fig. 7.1**), implying anomalous wind forcing (in 1976/77) similar to that considered in chapter 7. However, when idealized NAO-minimum wind forcing is applied to the model, the largest changes in subtropical gyre transport occur in winter rather than spring, and are located in the central part of the gyre (**Fig. 7.6c**), remote from the Gulf Stream. It seems unlikely, therefore, that the Gulf Stream intensification of spring 1977 was forced by NAO-minimum winds. However, associated with anomalous low pressure centred over the northeastern United States in that winter (**Fig. 3.6**) was a cyclonic air flow which brought cold continental air across the southeastern

US throughout January and February of 1977. The consequent "pool" of cold air over that region (**Fig. 3.5**) led to the unusually severe cold outbreaks, and excess cooling of the Gulf Stream, in early 1977. In this respect the record-strength April 1977 Gulf Stream is most likely to be an extreme case of anticyclogenic intensification indirectly associated with a NAO-minimum pressure pattern.

In conclusion then, excess winter cooling, associated with a minimum state of the NAO, is followed by an increase in Gulf Stream transport. Relating the results of these sensitivity studies to the climatological mean circulation, Worthington's (1977) argument endures: namely that annual-mean Gulf Stream transport *is* significantly enhanced by the barotropic recirculation due to winter cooling.

8.4 Strengths and weaknesses of the model

The control and sensitivity experiments are here critically appraised, raising the issue of model limitations. In this respect, model responses to both excess surface buoyancy loss and idealized NAO-minimum wind forcing further highlight such limitations.

8.4.1 A recirculating 18° Water layer

The characteristics of 18° Water are most closely represented by model layer 8 (σ_θ = 26.55), the thickest subtropical mode water layer across the majority of the model Sargasso Sea. Ventilation of layer 8 is clearly indicated by fields of end-of-winter layer thickness and Montgomery potential (**Fig. 4.8b**). Anomalous layer 8 thickness is, to some extent, a tracer of recirculating model 18° Water. This anomalous 18° Water spreads around the subtropical gyre (to rejoin the Gulf Stream) on timescales of around 5 years (**Fig. 4.19a**). This recirculation timescale, associated with gyre interior advection speeds of 2-3 cm s^{-1} (New *et al.* 1995), is somewhat longer than in the real world, due to the artificially high viscosity used in such a low resolution model. Based on measurements from a mooring current meter array centred on 55°W, 40°N, Klein and Hogg (1996) obtain a mean westward advection speed at 550 m (a nominal depth for recirculating 18° Water) of 5 cm s^{-1}. Overall though, the model is successful, qualitatively, in simulating the properties and circulation of 18° Water.

8.4.2 Thermocline ventilation versus PV homogenization

In the three thickness diffusion control experiments (chapter 5), fields of layer thickness and Montgomery potential are shown to depend on the choice of a thickness diffusion velocity. With a small value for this parameter (weak thickness diffusion), the layer 8 thickness field (**Fig. 5.3b**) conforms most closely (of the three experiments) to the ventilated thermocline of Luyten, Pedlosky and Stommel (1983), while for a high value (strong thickness diffusion), a uniformly thick (100-150m) patch of layer 8 forming in the Sargasso Sea (**Fig. 5.3c**) resembles the unventilated, PV-homogenized "pool region" of Rhines and Young (1982a). The ventilated thermocline and PV homogenization theories represent opposing views of 18° Water renewal and maintenance. Surface buoyancy forcing is implicit in ventilated thermocline theory (in which eddy mixing is neglected), while eddy mixing is central to homogenization theory (in which surface buoyancy forcing is excluded). In recognition of both buoyancy forcing and eddy dynamics, a unifying reconciliation of these theories has been sought (e.g., Dewar 1986, Cushman-Roisin 1987). To represent both the buoyancy-forced ventilation and lateral eddy mixing of model 18° Water layers, an intermediate value for the thickness diffusion parameter (used in the original control and sensitivity experiments of chapter 4) therefore seems to be a reasonable choice in the present 1° model.

8.4.3 The formation, dissipation and maintenance of 18° Water

In the model subtropical gyre, mode waters are climatologically renewed at an annual rate of 18.7 Sv (summing formation rates for layers 5-11 - see **Fig. 4.21**). Using observed surface density flux data to diagnose water mass formation rates, Speer and Tziperman (1992) calculated a mass source for Subtropical Mode Water (STMW) of 14 Sv (over the density range $26 < \sigma_\theta < 27$). By integrating a one-dimensional mixed layer model along 4-year trajectories of water columns advecting across the Sargasso Sea, Woods and Barkmann (1986) simulate 18° Water formation (by integrating instantaneous subduction rates along ten trajectories west of the Azores, in an approximate longitude range 30-70°W), and infer an almost identical renewal rate. The model is therefore forming STMW (including 18° Water) at an annual rate which is consistent with other independent estimates.

Apparent near-steady maintenance of seasonally-renewed model 18° Water layers (**Fig. 4.6**) requires a dissipation process in balance with the buoyancy-forced formation rates. In MICOM, this dissipation is most obviously represented

by mixed layer re-entrainment of "old" 18° Water in the Gulf Stream (see large entrainment rates north of the subduction zone in **Fig. 4.10**). Interior diffusive diapycnal mixing, while absent from the early version of MICOM used here (CLIM1), was included in the later version (CLIM2). Near-identical fields of 18° Water layer thickness in CLIM1 and CLIM2 after 20 years of spin-up (**Fig. 4.8b** and **Fig. 5.3a**) suggest that diffusive diapycnal mixing is too weak to play an important role in the dissipation of 18° Water.

Whether the re-entrainment of model 18° Water is a realistic physical process remains unclear. Garrett and Tandon (1997) have developed a thermodynamic algorithm to determine a re-entrainment rate, dependent on the buoyancy "jump" at the mixed layer base and the surface buoyancy field. Using results from a one-dimensional mixed layer model (to obtain buoyancy jump data) and climatological surface buoyancy data (Da Silva *et al.* 1994), Garrett and Tandon (1997) estimate that re-entrainment "consumes" only about 2 Sv of STMW. This dissipation rate is much less than the estimated STMW formation rates. Using CLIM2, Nurser *et al.* (1999) find that, north of ~24°N (on the rotated grid), the seasonal entrainment cycle results in a similar re-entrainment volume flux (towards lower density across σ = 26.5) of ~2 Sv, while diapycnal mixing drives a flux of ~1 Sv. Over the same extratropical region, net surface buoyancy loss drives a surface-forced transformation rate (towards *higher* density across σ = 26.5) of ~10 Sv. So, for the σ = 26.5 isopycnal in the extratropics of CLIM2, total dissipation of around -3 Sv clearly does not balance surface-forced water mass transformation.

The imbalance between these formation and dissipation rates imply that the model is *locally* (in the extra-tropics) failing to maintain a steady volume of 18° Water. However, the thickness of layers representing 18° Water appear to be interannually steady in the Sargasso Sea by year 20 of CLIM1 (**Fig. 4.6**). In other words, the majority of model 18° Water must be dissipated *away from the extratropical formation region.* An annual-mean streamfunction in density space (**Fig. 6.4a**) indicates that streamlines returning equatorward in the 18° Water density range do not form a closed cell in the subtropics, but rather continue towards equatorial latitudes. A significant fraction of 18° Water thus reaches the equatorial region of the model. In this region, strong thermocline stratification leads to large interior diapycnal mixing rates (in CLIM2), while upwelling along the Equator and off west Africa leads to large entrainment fluxes across the mixed layer base (in CLIM1 and CLIM2). In this way, 18° Water (in CLIM2) can be strongly dissipated by diapycnal mixing and (once transformed to lower density) then upwell diapycnally at the mixed layer base (Nurser *et al.* 1999). In CLIM1,

in the absence of interior diapycnal mixing, 18° Water is directly upwelled into the mixed layer. In summary then, the present model forms, maintains and dissipates 18° Water in a plausible manner.

8.4.4 Structure and strength of the Gulf Stream

Compared to the observed Gulf Stream, the model western boundary current (WBC) is rather broad and weak, and separates from the coast further north than the latitude of Cape Hatteras. Such shortcomings in the structure and strength of the model WBC are mainly the consequence of using too-coarse horizontal resolution (New *et al.* 1995). In recent simulations with much higher resolution models of the Atlantic Ocean [e.g., at $\frac{1}{6}°$ resolution with the Parallel Ocean Program (POP) model (Chao *et al.* 1996) and at $\frac{1}{12}°$ with MICOM (Bleck *et al.* 1995)], the Gulf Stream is a realistic narrow current which separates from the US seaboard at Cape Hatteras and develops into downstream meanders.

Furthermore, annual-mean WBC transport in the model subtropical gyre is largely explained in terms of a topographic Sverdrup balance (**Fig. 4.3**). The southern recirculation gyre, which may be inertial and anticyclogenic, is poorly resolved so that rather than exhibiting downstream development (increasing in barotropic transport), the model Gulf Stream *weakens* beyond Cape Hatteras (**Fig. 4.1a**).

A seasonal cycle of Gulf Stream transport is evident in both the Gulf Stream geostrophic transports computed from hydrographic data (Worthington 1977) and the transport variability estimated by satellite altimeter (Fu *et al.* 1987, Wang and Koblinsky 1996) - see **Fig. 2.14** and **Fig. 2.16**. The seasonal cycle is a topographically-modified Sverdrup response to the seasonal variation of wind stress curl over the subtropical gyre (Anderson and Corry 1985). Through JEBAR and BPT, the effects of winter cooling may therefore play an important role in intensifying the Gulf Stream after each winter. Seasonal cycles of subtropical gyre strength are reasonably well predicted by the topographically-modified Sverdrup balance (**Fig. 4.4**), and approach the wind-driven prediction as the thickness diffusion velocity is increased (**Fig. 5.2**). Stronger thickness diffusion will limit cooling-related end-of-winter intensification, since horizontal density gradients, baroclinicity and BPT are all weakened. As well as displaying clearer wind-driven seasonal cycles, the high thickness diffusion experiment is characterized by a weaker annual-mean subtropical gyre. This supports Worthington's general hypothesis (1972, 1977), namely that *climatological* winter cooling is integral to

the maintenance of annual-mean Gulf Stream transport at strengths well in excess of theoretical wind-driven values.

Gulf Stream intensification in the excess cooling experiments was rather weak, even under the most intense cooling and minimal thickness diffusion (**Fig. 5.8**). As the Gulf Stream is poorly resolved in the coarse resolution model used here, one would expect that a stronger Gulf Stream intensification would result from cooling in a high resolution model. However, 18° Water is poorly represented in the POP model (Chao *et al.* 1996). Only with a high resolution model which can realistically simulate 18° Water will the dependence of the Gulf Stream on winter cooling be properly established. In this respect the present study serves to guide further, higher resolution, model studies of the relationship between Gulf Stream transport and winter cooling.

8.5 Further work

A full and accurate barotropic vorticity balance was beyond the scope of this study. Ideally, an on-line vorticity balance (integrated as the model runs) should be sought, to confirm that excess winter cooling of the Gulf Stream leads to barotropic intensification through anomalous BPT effects.

Having considered separately the effects on the subtropical gyre of NAO-minimum buoyancy and wind forcing, a natural progression would be to force the model with anomalous fields of both buoyancy and wind forcing which are self-consistent (e.g., strong excess cooling beneath anomalous northwesterly winds over the Sargasso Sea). Such a study would more categorically establish whether the spring 1977 Gulf Stream intensification reported by Worthington (1977) was the result of both excess cooling *and* NAO-minimum wind forcing.

The ocean-atmosphere coupling in the present model experiments was limited to a weak negative thermohaline feedback via the Haney-style relaxation of mixed layer temperature and salinity. During cold outbreaks over the Gulf Stream, large amounts of heat and moisture are transferred from ocean to atmosphere. A truly comprehensive model study should therefore include more realistic ocean-atmospheric coupling, incorporating cloud processes and atmospheric transports of heat and moisture.

The thickness diffusion sensitivity experiments (Chapter 5) are compromised somewhat by the short length of the integrations (one model year). It would be worthwhile to spin up the model (from rest) with low and high thickness

diffusion, to establish longer-term control experiments, for which the water masses and circulation are in a steadier state.

The diagnosis of surface-forced overturning in Chapter 6 revealed recent (1980-97) variability in the annual-mean recirculation of 18° Water. Kelly and Watts (1994) show that Gulf Stream transport can be reliably monitored by a satellite-mounted radar altimeter, using "exact repeat" Geosat subtracks every 17 days, and obtain November 1986-May 1989 time series of cross-stream differences in sea surface height. Gulf Stream transport (altimetrically measured) could be compared to the strength of buoyancy-forced recirculation, on an approximate monthly basis, as a further test of the Worthington (1972) hypothesis.

In-situ evidence is now emerging for recent NAO-related variability in Labrador Sea Water (LSW). Curry *et al.* (1998) show that varying properties of LSW can be tracked to mid-depths in the subtropics, about 6 years later, and that this remote variability is seemingly lag-correlated with an index of the NAO (Hurrell 1995). The wind and buoyancy forcing of 1980-97 (available from the SOC climatology database) could be applied to the model in the knowledge that anomalous LSW should form. Decadal-timescale spreading of anomalous LSW (formed at the early 1990s NAO-maximum) could be thus investigated.

The analysis of Chapter 6 can also be easily applied elsewhere in the World Ocean, wherever observational coverage is sufficiently dense. Perhaps the most obvious place to repeat the diagnosis is over the North Pacific, where formation of Subtropical Mode Water is reported to have varied in recent years (Suga *et al.* 1989, Qiu and Joyce 1992).

8.6 Final remarks

The results of this study have revealed strengths and weaknesses in the approaches adopted. The 18° Water variability simulated in the decade-long NAO-minimum excess winter cooling experiment provides a close analog to the 1960s variability reported by Talley and Raymer (1982). On the other hand, relatively weak end-of-winter Gulf Stream intensifications were obtained in the excess cooling experiments, even under the most intense cooling and minimal thickness diffusion.

While the horizontal resolution used here (equivalent to ~100 km) is too coarse to properly resolve the relatively narrow (~50 km wide) Gulf Stream, similar resolutions are typically used in present climate models (e.g., the HADCM coupled models currently used by the U.K. Hadley Centre for Climate Prediction

and Research have an ocean grid resolution of 1.25°). So the present experiments indicate how changes in ocean currents, and associated transports, might be forced by the variable surface forcing in coupled ocean-atmosphere models.

In this study, an attempt has been made to synthesize observations and modelling. Numerical model experiments were motivated by observations of related phenomena: 18° Water variability and Gulf Stream intensification. The results of these experiments then led back to a re-examination of sea surface data, yielding further insights. Only in this way can we progress in our understanding of large-scale variability of the ocean, the details of which will otherwise continue to defy isolated observational or modelling efforts alone.

REFERENCES

Adamec, D., and R. L. Elsberry, 1985a: Response of an intense oceanic current system to cross-stream cooling events. *J. Phys. Oceanogr.* **15**, 273-287.

Adamec, D., and R. L. Elsberry, 1985b: The response of intense oceanic current systems entering regions of strong cooling. *J. Phys. Oceanogr.* **15**, 1284-1295.

Anderson, D. L. T., and R. A. Corry, 1985: Seasonal transport variations in the Florida Straits: A model study. *J. Phys. Oceanogr.* **15**, 773-786.

Andersson, L., Rudels, B., and G. Walin, 1982: Computations of heat flux through the ocean surface as a function of temperature. *Tellus*, **34**, 196-198.

Arakawa, A., and V. R. Lamb, 1977: Computational design of the basic processes of the UCLA General Circulation Model. *Methods Comput. Phys.*, **17**, 174-265.

Bane, J. M., and K. E. Osgood, 1989: Wintertime air-sea interaction processes across the Gulf Stream. *J. Geophys. Res.*, **94**, 10755-10772.

Barnier, B., 1988: A numerical study on the influence of the Mid-Atlantic Ridge on nonlinear first-mode baroclinic Rossby waves generated by seasonal winds. *J. Phys. Oceanogr.* **18**, 417-433.

Barnier, B., Siefridt, L., and P. Marchesiello, 1995: Thermal forcing for a global ocean circulation model from a three-year climatology of ECMWF analyses. *J. Marine Systems*, **6**, 363-380.

Barnston, A. G., and R. E. Livezey, 1987: Classification, seasonality and persistence of low-frequency atmospheric circulation patterns. *Mon. Wea. Rev.*, **115**, 1083-1126.

Bjerknes, J., 1964: Atlantic air-sea interaction. *Adv. Geophys.*, **10**, 1-82.

Bleck, R., Hanson, H. P., Hu, D., and E. B. Krauss, 1989: Mixed-layer thermocline interaction in a three-dimensional isopycnic coordinate model. *J. Phys. Oceanogr.*, **19**, 1417-1439.

Bleck, R., and L. T. Smith, 1990: A wind-driven isopycnic coordinate model of the North Atlantic and Equatorial Atlantic Ocean. 1. Model development and supporting experiments. *J. Geophys. Res.* **95**, 3273-3286.

Bleck, R., Rooth, C., Hu, D., and L. T. Smith, 1992: Salinity-driven thermocline transients in a wind- and thermohaline-forced isopycnic coordinate model of the North Atlantic. *J. Phys. Oceanogr.*, **22**, 1486-1505.

Bleck, R., Dean, S., O'Keefe, M., and A. Sawdey, 1995: A Comparison of data-parallel and message-passing versions of the Miami Isopycnic Coordinate Ocean Model. *Parallel Computing*, **21**, 1695-1720.

Blumberg, A. F., and G. L. Mellor, 1987: A description of a three-dimensional coastal ocean circulation model, *Three-Dimensional Coastal Ocean Models*, Vol 4., N. Heaps, Ed., Amer. Geophys. Union, 208 pp.

Böhnecke Günther, 1936: Atlas zu : Temperatur, Salzgehalt und Dichte an der Oberfläche des Atlantischen Ozeans. Deutsche Atlantische Expedition METEOR 1925-1927. *Wiss. Erg., Bd.* V, Berlin.

Böning, C. W., Doscher, R., and R. G. Budich, 1991: Seasonal transport variation in the western subtropical North Atlantic: Experiments with an eddy-resolving model. *J. Phys. Oceanogr.*, **21**, 1271-1289.

Bosart, L. F., Chung-Chieng, L., and E. Rogers, 1995: Incipient explosive marine cyclogenesis: coastal development. *Tellus*, **47A**, 1-29.

Bryan, F. O., and W. R. Holland, 1989: A high resolution simulation of the wind- and thermohaline driven circulation in the North Atlantic Ocean. *Parameterization of Small-Scale Process Proc. 'Aha Huliko'a, Hawaiian Winter Workshop*, P. Muller, and D. Henderson, Eds., University of Hawaii at Manoa, 99-115.

Bryan, K., 1963: A numerical investigation of a nonlinear model of a wind-driven ocean. *J. Atmos. Sci.*, **20**, 594-606.

Bryan, K., and J. L. Sarmiento, 1984: Modeling ocean circulation, in *Issues in Atmospheric and Oceanic Modeling*, pp. 433-459, Academic, Orlando, Fla.

Bunker, A. F., 1976: Computations of surface energy flux and annual air-sea interaction cycles of the North Atlantic Ocean. *Mon.Weath. Rev.*, **104**, 1122-1140.

Cayan, D. R., 1992a: Latent and sensible heat flux anomalies over the northern oceans: the connection to monthly atmospheric circulation. *J. Climate* **5**, 354-369.

Cayan, D. R., 1992b: Variability of latent and sensible heat fluxes estimated using bulk formulae. *Atmos.-Ocean* **30**, 1-42.

Cayan, D. R., 1992c: Latent and sensible heat flux anomalies over the northern oceans: Driving the sea surface temperature. *J. Phys. Oceanogr.* **22**, 859-881.

Chao, S-Y., 1992: An air-sea interaction model for cold-air outbreaks. *J. Phys. Oceanogr.*, **22**, 821-842.

Chao, Y., Gangopadhyay, A., Bryan, F. O., and W. R. Holland, 1996: Modeling the Gulf Stream system: how far from reality? *Geophys. Res. Letts.*, **23**, 3155-3158.

Charney, J. G., 1955: The Gulf Stream as an inertial boundary layer. *Proc. Nat. Acad. Sci. Wash.*, **41**, 731-740.

Chassignet, E. P and R. Bleck, 1993: The influence of layer outcropping on the seperation of boundary currents. Part I: The wind-driven experiments. *J. Phys. Oceanogr.*, **23**, 1485-1507.

Cook, E. R., D'Arrigo, R. D., and K. R. Briffa, 1998: The North Atlantic Oscillation and its expression in circum-Atlantic tree-ring chronologies from North America and Europe. *The Holocene*, **8**, 9-17.

Cornillon, P., 1986: The effect of the New England Seamounts on Gulf Stream meanderingas observed from satellite IR imagery. *J. Phys. Oceanogr.*, **16**, 386-389.

Csanady, G. T., 1982: The thermohaline driving mechanism of oceanic jet streams. *J. Mar. Res.*, **40**(Suppl.), 113-142.

Curry, R. G., M. S. McCartney, and T. M. Joyce, 1998: Oceanic transport of subpolar climate signals to mid-depth subtropical waters. *Nature*, **391**, 575-577.

Cushman-Roisin, B., 1987: On the role of heat flux in the Gulf Stream-Sargasso Sea subtropical gyre system. *J. Phys. Oceanogr.*, **17**, 2189-2202.

Da Silva, A. M., 1991: Estimates of monthly mean wind stress from monthly mean pseudo-stress, winds, and wind standard deviations. Dept. of Geophys., Univ. of Wis., Milwaukee.

Da Silva, A. M., Young, C. C., and S. Levitus, 1994: Atlas of Surface Marine Data. Vol. 1: Algorithms and Procedures. NOAA Atlas Series, 74 pp.

Dewar, W., 1986: On the potential vorticity structure of weakly ventilated isopycnals: A theory of subtropical mode water maintenance. *J. Phys. Oceanogr.*, **16**, 1204-1216.

Diaz, H. F., and R. G. Quayle, 1978: The 1976-77 winter in the contiguous United States in comparison with past records. *Mon. Wea. Rev.* **106**, 1393-1421.

Dickson, R. R., and J. Namias, 1976: North American influences on the circulation and climate of the North American sector. *Monthly Weather R.*, **104(10)**, 1255-1265.

Dickson, R. R., and J. Brown, 1994: The production of North Atlantic Deep Water: Sources, rates and pathways. *J. Geophys. Res.* **99**, 12319-12341.

Dickson, R. R., Lazier, J., Meincke, J., Rhines, P., and J. Swift, 1996: Long-term coordinated changes in the convective activity of the North Atlantic. *Prog. Oceanogr.*, **38**, 241-295.

Dorman, C. E., and R. H. Bourke, 1978: A temperature correction for Tucker's ocean rainfall estimates. *Quart. J. Roy. Meteor. Soc.*, **104**, 765-773.

Ertel, H., 1942: Ein neuer hydrodynamischer Wirbelsatz. *Met. Z.*, **59**, 271-281.

Esbensen, S. K., and Y. Kushnir, 1981: The heat budget of the global ocean: An atlas based on estimates from surface marine observations. Oregon State Univ. Clim. Res. Inst. Rep., **29**, 27pp.

Ezer, T., and G. L. Mellor, 1994: Diagnostic and prognostic calculations of the North Atlantic circulation and sea level using a sigma coordinate ocean model. *J. Geophys. Res.* **99**, 14159-14171.

Ezer, T., Mellor, G. L., and R. J. Greatbatch, 1995: On the interpentadal variability of the North Atlantic Ocean: Model simulated changes in transport, meridional heat flux and coastal sea level between 1955-59 and 1970-74. *J. Geophys. Res.* **100**, 10559-10566.

Fanning, A. F., Greatbatch, R. J., Da Silva, A. M., and S. Levitus, 1994: Model-calculated seasonal transport variations through the Florida Straits: A comparison using different wind-stress climatologies. *J. Phys. Oceanogr.*, **24**, 30-45.

Fofonoff, N. P., 1954: Steady flow in a frictionless homogeneous ocean. *J. Mar. Res.*, **13**, 254-262.

Friedrich, H., and S. Levitus, 1972: An approximation to the equation of state for sea water, suitable for numerical ocean models. *J. Phys. Oceanogr.*, **2**, 514-517.

Fu, L-L., Vazquez, J., and M. E. Parke, 1987: Seasonal variability of the Gulf Stream from satellite altimetry. *J. Geophys. Res.* **92**, 749-754.

Fuglister, F. C., 1963: Gulf Stream '60. *Prog. Oceanogr.*, **1**, 267-373.

Gadd, A. J., 1978: A split-explicit integration scheme for numerical weather prediction. *Q. J. R. Meteorol. Soc.*, **104**, 569-582.

Garrett, C., and A. Tandon, 1997: The effects on water mass formation of surface mixed layer time-dependence and entrainment fluxes. *Deep Sea Res.*, **44**, 1991-2006.

Gent, P. R., and J. C. McWilliams, 1990: Isopycnal mixing in ocean circulation models. *J. Phys. Oceanogr.*, **20**, 150-155.

Gerdes, R., and C. Wübber, 1991: Seasonal variability of the North Atlantic Ocean - A model intercomparison. *J. Phys. Oceanogr.* **21**, 1300-1322.

Gill, A E., 1982: *Atmosphere-Ocean Dynamics*. Academic Press, 662 pp.

Greatbatch, R. J., Fanning, A. F., Goulding, A. D., and S. Levitus, 1991: A diagnosis of interpentadal circulation changes in the North Atlantic. *J. Geophys. Res.* **96**, 22009-22023.

Greatbatch, R. J., and J. Xu, 1993: On the transport of volume and heat through sections across the North Atlantic: Climatology and the pentads 1955-59, 1970-74. *J. Geophys. Res.* **98**, 10125-10143.

Hall, M. M., and N. P. Fofonoff, 1993: Downstream development of the Gulf Stream from 68° to 55°W. *J. Phys. Oceanogr.*, **23**, 225-249.

Haney, R. L., 1971: Surface thermal boundary conditions for ocean circulation models. *J. Phys. Oceanogr.*, **4**, 241-248.

Hayden, B. P., 1981: Secular variation in the Atlantic coast extratropical cyclones. *Mon. Wea. Rev.* **109**, 159-167.

Hazeleger, W., and S. S. Drijfhout, 1998: Mode water variability in a model of the subtropical gyre: Response to anomalous forcing. *J. Phys. Oceanogr.* **28**, 266-288.

Hazeleger, W., and S. S. Drijfhout, 1999: Stochastically forced mode water variability. *J. Phys. Oceanogr.* **29**, 1772-1786.

Hellerman, S., and M. Rosenstein, 1983: Normal monthly wind stress over the world ocean with error estimates. *J. Phys. Oceanogr.* **15**, 773-786.

Herrmann, P., and W. Krauss, 1989: Generation and propagation of annual Rossby waves in the North Atlantic. *J. Phys. Oceanogr.* **19**, 727-744.

Holland, W. R., 1973: Baroclinic and topographic influences on the transport in western boundary currents. *Geophys. Fluid Dyn.*, **4**, 187-210.

Holland, W. R., Keffer, T., and P. B. Rhines, 1984: Dynamics of the oceanic general circulation: the potential vorticity field. *Nature*, **308**, 698-705.

Hoskins, B. J., McIntyre, M. E., and A. W. Robertson, 1985: On the use and significance of isentropic potential vorticity maps. *Quart. J. R. Met. Soc.*, **111**, 877-946.

Huang, R. X., 1986: Solutions of the ideal fluid thermocline with continuous stratification. *J. Phys. Oceanogr.*, **16**, 39-59.

Huang, R. X., 1990: Does atmospheric cooling drive the Gulf Stream recirculation? *J. Phys. Oceanogr.*, **20**, 750-757.

Hughes, C. W., and P. D. Killworth, 1995: Effects of bottom topography in the large-scale circulation of the Southern Ocean. *J. Phys. Oceanogr.*, **25**, 2485-2497.

Huthnance, J. M., 1984: Slope currents and "JEBAR". *J. Phys. Oceanogr.*, **14**, 795-810.

Hurrell, J. W., 1995, Decadal trends in the North Atlantic Oscillation: regional temperatures and precipitation. *Science*, **269**, 676-679 (updated NAO indices available at web-site *http://tao.atmos.washington.edu/data_sets/nao/*).

Intergovernmental Panel on Climate Change, 1990: Scientific assessment of climate change, Report to IPCC from Working Group 1, Chapters 4-5. World Meteorological Organization, United Nations Environmental Program, Geneva.

Iselin, C. O'D., 1936: A study of the circulation of the western North Atlantic. *Pap. Phys. Oceanogr. Meteor.* **4**, 1-101.

Iselin, C. O'D., 1940: Preliminary report on long-period variations in the transport of the Gulf Stream System. *Pap. Phys. Oceanogr. Meteor.* **8**, 1-40.

Isemer, H. J., and L. Hasse, 1987: *The Bunker Climate Atlas of the North Atlantic Ocean, Vols. 1 and 2.* Springer-Verlag, 252 pp.

Jaeger, L., 1976: Monatskarten des Niederschlags für die ganze Erde. *Ber. Dtsch. Wetterdienstes*, **18**(139), 38 pp.

Jenkins, W. J., 1982: On the climate of a subtropical ocean gyre: Decade timescale variations in water mass renewal in the Sargasso Sea. *J. Mar. Res.*, **40**(Suppl.), 427-464.

Jones, P. D., 1987: The early twentieth century Arctic high - fact or fiction? *Climate Dyn.*, **1**, 63-75.

Jones, P. D. and K. R. Briffa, 1992: Global surface air temperature variations during the twentieth century: Part 1, spatial, temporal and seasonal details, *The Holocene,* **2,2** 165-179.

Jones, P. D., T. Jonsson, and D. Wheeler, 1997: Extension to the North Atlantic Oscillation using early instrumental pressure observations from Gibraltar and South-West Iceland. *Int. J. Climatol.*, **17**, 1433-1450.

Josey, S. A., Kent, E. C., and P. K. Taylor, 1995: Seasonal variations between sampling and classical mean turbulent heat flux estimates in the eastern North Atlantic. *Annales Geophysicae*, **13**, 1054-1064.

Josey, S. A., D. Oakley, and R. W. Pascal, 1997: On estimating the atmospheric longwave flux at the ocean surface from ship meteorological reports. *J. Geophys Res.* **102**, 27961-27972.

Josey, S. A., Kent, E. C., and P. K. Taylor, 1999: New insights into the ocean heat budget closure problem from analysis of the SOC air-sea flux climatology. *J. Climate.*, **12**, 2856-2880.

Kelly, K. A., and D. R. Watts, 1994: Monitoring Gulf Stream transport by radar altimeter and inverted echo sounders. *J. Phys. Oceanogr.*, **24**, 1080-1084.

Kent, E. C., Tiddy, R. J., and P. K. Taylor, 1993: Correction of marine daytime air temperature observations for radiation effects. *J. Atmos. Oceanic Tech.*, **10**, 900-906

Kent, E. C., and P. K. Taylor, 1997: Choice of a Beaufort equivalent scale. *J. Atmos. Oceanic Tech.*, **14**, 228-242.

Killworth, P. D., Chelton, D. B., and R. A. de Szoeke, 1997: The speed of observed and theoretical long extratropical planetary waves. *J. Phys. Oceanogr.*, **27**, 1946-1966.

Klein, B. and N. Hogg., 1996: On the variability of 18 Degree water formation as observed from moored instruments at 55°W. *Deep Sea Res.*, **43**, 1777-1806.

Kraus, E. B. and J. S. Turner, 1967: A one-dimensional model of the seasonal thermocline. II. The general theory and its consequences. *Tellus*, **19**, 1, 98-105.

Kushnir, Y., 1994: Interdecadal variations in North Atlantic sea surface temperature and associated atmospheric conditions. *J. Climate*, **7**, 141-157.

Larsen, J. C., 1992: Transport and heat flux of the Florida Current at 27°N derived from cross-stream voltages and profiling data: Theory and observations. *Philos. Trans. Roy. Soc. London*, **A 338**, 169-236.

Ledwell, J. R., Watson, A. J., and C. S. Law, 1993: Evidence for slow mixing across the pycnocline from an open-ocean tracer-release experiment. *Nature*, **364**, 701-703.

Leetmaa, A., and A. F. Bunker, 1978: Updated charts of the mean annual wind stress, convergences in the Ekman Layers, and Sverdrup transports in the North Atlantic. *J. Mar. Res.*, **36**, 311-322.

Levitus, S., 1982: *Climatological Atlas of the World Ocean.* NOAA Prof. Paper, 13, U.S. Govt. Printing Office, 173 pp.

Levitus, S., 1989a: Interpentadal variability of temperature and salinity at intermediate depths of the North Atlantic Ocean, 1970-74 versus 1955-59. *J. Geophys. Res.*, **94**, 6091-6131.

Levitus, S., 1989b: Interpentadal variability of salinity in the upper 150 m of the North Atlantic Ocean, 1970-74 versus 1955-59. *J. Geophys. Res.*, **94**, 9679-9685.

Levitus, S., 1989c: Interpentadal variability of temperature and salinity in the deep North Atlantic, 1970-74 versus 1955-59. *J. Geophys. Res.*, **94**, 16125-16131.

Levitus, S., 1990: Interpentadal variability of steric sea level and geopotential thickness of the North Atlantic Ocean, 1970-74 versus 1955-59. *J. Geophys. Res.*, **95**, 5233-5238.

Liu, Z., and J. Pedlosky, 1983: Thermocline forced by annual and decadal surface temperature variation. *J. Phys. Oceanogr.*, **24**, 587-608.

Luyten, J., Pedlosky, J., and H. Stommel, 1983: The ventilated thermocline. *J. Phys. Oceanogr.*, **13**, 292-309.

Luyten, J., and H. Stommel, 1986: Gyres driven by combined wind and buoyancy flux. *J. Phys. Oceanogr.*, **16**, 1551-1560.

Marsh, R., Nurser, A. J. G., Megann, A. P., and A. L. New, 2000: Water mass transformation in the Southern Ocean of a Global Isopycnic Model. Journal of Physical Oceanography, in press.

Marsh, R., and A. L. New, 1996: Modelling 18° Water variability. *J. Phys. Oceanogr.* **26**, 1059-1080.

Marshall, J. C. and A. J. G. Nurser, 1988: On the recirculation of the subtropical gyre. *Q. J. R. Meteorol. Soc.*, **114**, 1517-1534.

Marshall, J. C. and A. J. G. Nurser, 1992: Fluid dynamics of thermocline ventilation. *J. Phys. Oceanogr.*, **22**, 583-595.

Marshall, J. C., Nurser, A. J. G., and R. G. Williams, 1993: Inferring the Subduction rate and period over the North Atlantic. *J. Phys. Oceanogr.*, **23**, 1315-1329.

Marshall, D., and J. C. Marshall, 1995: Subduction in a time-dependent thermocline model. *J. Phys. Oceanogr.*, **25**, 138-151.

Masuzawa, J., 1969: Subtropical Mode Water. *Deep Sea Res.*, **16**, 453-472.

McCartney, M. S., Worthington, L. V. and M. E. Raymer, 1980: Anomalous water mass distributions at 55W in the North Atlantic in 1977. *J. Mar. Res.*, **38**, 147-172.

McCartney, M. S., 1982: The subtropical recirculation of Mode Water. *J. Mar. Res.*, **40**(Suppl.), 427-464.

McCartney, M. S., and L. D. Talley, 1984: Warm-to-cold conversion in the northern North Atlantic Ocean. *J. Phys. Oceanogr.*, **14**, 922-935.

McCartney, M. S., Bennett, S. L., and M. E. Woodgate-Jones, 1991: Eastward flow through the Mid-Atlantic Ridge at 11°N and its influence on the abyss of the Eastern Basin. *J. Phys. Oceanogr.*, **21**, 1089-1121.

McDougall, T. J., 1984: The relative roles of diapycnal and isopycnal mixing on subsurface water mass conversion. *J. Phys. Oceanogr.*, **14**, 1577-1589.

McDougall, T. J., 1987: Thermobaricity, cabbeling and water mass conversion. *J. Geophys Res.* **92**, 5448-5464.

McDougall, T. J., and P. C. McIntosh, 1996: The temporal-residual-mean velocity. Part I: Derivation and the scalar conservation equations. *J. Phys. Oceanogr.*, **26**, 2653-2665.

McDowell, S., P. Rhines, and T. Keffer, 1982: North Atlantic potential vorticity and its relation to the general circulation. *J. Phys. Oceanogr.*, **12**, 1417-1436.

Mellor, G. L., Mechoso, C. R., and E. Keto, 1982: A diagnostic model of the general circulation of the Atlantic Ocean. *Deep Sea Res.*, **29**, 1171-1192.

Montgomery, R. B., 1937: A suggested method for representing gradient flow in isentropic surfaces. *Bull. Am. Met. Soc.*, **18**, 210-211.

Morgan, G. W., 1956: On the wind-driven ocean circulation. *Tellus*, **8**, 301-320.

Moyer, K. A., and R. A. Weller, 1997: Observations of surface forcing from the Subduction Experiment: a comparison with global model products and climatological data sets. *J. Climate.*, **10**, 2725-2742.

Munk, W. H., 1950: On the wind-driven ocean circulation. *Jour. Meteor.*, **7**, 79-93.

NCEP Climate Prediction Center, cited 1999: Current Monthly Atmospheric and SST Index Values. [Available on-line from *http://nic.fb4.noaa.gov/data/cddb/*]

New, A. L., Bleck, R., Jia, Y., Marsh, R., Huddleston, M. and S. Barnard, 1995: An isopycnic model study of the North Atlantic. Part 1: Model experiment. *J. Phys. Oceanogr.*, **25**, 2667-2699.

New, A. L., and R. Bleck, 1995: An isopycnic model study of the North Atlantic. Part 2: Interdecadal variability of the subtropical gyre. *J. Phys. Oceanogr.* **25**, 2712-2726.

Niiler, P. P., and W. S. Richardson, 1973: Seasonal variability of the Florida Current. *J. Mar. Res.*, **31**, 144-167.

Nof, D., 1983: On the response of ocean currents to atmospheric cooling. *Tellus*, **35**, 60-72.

Nurser, A. J. G., and R. G. Williams, 1990: Cooling Parsons' model of the separated Gulf Stream. *J. Phys. Oceanogr.*, **20**, 1974-1979.

Nurser, A. J. G., and J. C. Marshall, 1991: On the relationship between subduction rates and diabatic forcing of the mixed layer. *J. Phys. Oceanogr.*, **21**, 1793-1802.

Nurser, A. J. G., Marsh, R., and R. G. Williams, 1999: Diagnosing water mass formation from air-sea fluxes and surface mixing. *J. Phys. Oceanogr.*, **29**, 1468-1487.

Nurser, A. J. G., and R. Marsh, 1998: Water mass transformation theory and the meridional overturning streamfunction. International WOCE Newsletter, No. 31, 36-39.

Parsons, A. T., 1969: A two-layer model of Gulf Stream separation. *J. Fluid. Mech.*, **39**, 511-528.

Pedlosky, J., and W. R. Young, 1983: Ventilation, potential-vorticity homogenization and the structure of the ocean circulation. *J. Phys. Oceanogr.*, **13**, 2020-2037.

Pedlosky, J., 1983: On the relative importance of ventilation and mixing of potential vorticity in mid-ocean gyres. *J. Phys. Oceanogr.*, **13**, 2121-2122.

Pedlosky, J., Smith, W., and J. R. Luyten, 1984: On the dynamics of the coupled mixed layer-thermocline system and the determination of the oceanic surface density. *J. Phys. Oceanogr.*, **14**, 1159-1171.

Pedlosky, J., 1986: The buoyancy- and wind-driven ventilated thermocline. *J. Phys. Oceanogr.*, **16**, 1077-1087.

Pedlosky, J., 1990: The dynamics of the oceanic subtropical gyres. *Science*, **248**, 316-322.

Pickart, R. S., and W. M. Smethie, Jr., 1993: How does the Deep Western Boundary Current cross the Gulf Stream. *J. Phys. Oceanogr.*, **23**, 2602-2616.

Polzin, K. L., Speer, K. G., Toole, J. M., and R. W. Schmitt, 1995: Intense mixing of Antarctic Bottom Water in the equatorial Atlantic Ocean. *Nature*, **380**, 54-57.

Qiu, B., and T. M. Joyce, 1992: Interannual variability in the mid- and low-latitude western North Pacific. *J. Phys. Oceanogr.*, **22**, 1062-1079.

Qiu, B., and R. X. Huang, 1995: Ventilation of the North Atlantic and North Pacific: Subduction versus obduction. *J. Phys. Oceanogr.*, **25**, 2374-2390.

Rhines, P. B., and W. R. Young, 1982a: Homogenization of potential vorticity in planetary gyres. *J. Fluid Mech.*, **122**, 347-367.

Rhines, P. B., and W. R. Young, 1982b: A theory of wind-driven circulation. I. Mid-ocean gyres. *J. Mar. Res.*, **40**(Suppl.), 559-596.

Robinson, A. R., and H. Stommel, 1959: The ocean thermocline and the associated thermohaline circulation. *Tellus*, **11**, 295-308.

Rogers, J. C., 1984: The association between the North Atlantic Oscillation and the Southern Oscillation in the Northern Hemisphere. *Mon. Wea. Rev.*, **112**, 1999-2015.

Rossby, C.-G., 1939: Relation between variations in the intensity of the zonal circulation of the atmosphere and the displacements of the semi-permanent centers of action. *J. Mar. Res.*, **2(1)**, 38-55.

Rossby, C.-G., 1940: Planetary flow patterns in the atmosphere. *Quart. J. R. Met. Soc.*, **66**, Suppl., 68-87.

Sanders, F., and J. R. Gyakum, 1980: Synoptic-dynamic climatology of the "Bomb". *Mon. Wea. Rev.*, **119**, 967-997.

Sarkisyan, A. S., and V. F. Ivanov, 1971: Joint Effect of Baroclinicity and Bottom Relief as an important factor in the dynamics of sea currents. *Bull. Acad. Sci. USSR, Atmos. and Oceanic Phys.*, **7**, 173-188. (English Transl., p.116).

Schmitt, R. W., Bogden, P. S., and C. E. Dorman, 1989: Evaporation minus precipitation and density fluxes for the North Atlantic. *J. Phys. Oceanogr.*, **19**, 1208-1221.

Schmitz Jr., W. J. and P. L. Richardson, 1991: On the sources of the Florida Current. *Deep Sea Res.*, **38** (Suppl. 1), S389-S409.

Schmitz Jr., W. J., 1996: On the World Ocean Circulation: Volume I. Some Global Features / North Atlantic Circulation. Woods Hole Oceanog. Inst. Tech. Rept., WHOI-96-03.

Schroeder, E., Stommel, H., Menzel, D., and W. Sutcliffe, Jr., 1959: Climatic stability of eighteen degree water at Bermuda. *J. Geophys. Res.*, **64**(3), 363-366.

Schroeder, E., and H. Stommel, 1969: How representative is the series of *Panulirus* stations of monthly mean conditions off Bermuda? *Prog. Oceanogr.*, **5**, 31-40.

Slørdal, L. H., and J. E. Weber, 1996: Adjustment to JEBAR forcing in a rotating ocean. *J. Phys. Oceanogr.*, **26**, 657-670.

Smith, L. T., Bleck, R., and D. B. Boudra, 1990: A wind-driven isopycnic coordinate model of the North Atlantic and Equatorial Atlantic Ocean. 2. The Atlantic basin experiments. *J. Geophys. Res.*, **95**, 13105-13128.

Spall, M. A., 1992: Cooling spirals and recirculation in the subtropical gyre. *J. Phys. Oceanogr.*, **22**, 564-571.

Spall, M. A., 1995: Frontogenesis, subduction, and cross-front exchange at upper ocean fronts. *J. Geophys. Res.*, **100**, 2543-2557.

Speer, K., and E. Tziperman, 1992: Rates of water mass formation in the North Atlantic Ocean. *J. Phys. Oceanogr.*, **22**, 93-104.

Speer, K., 1997: A note on average cross-isopycnal mixing in the North Atlantic Ocean. *Deep Sea Res.*, **44**, 1981-1990.

Speer, K., 1998: Extratropical North Atlantic ocean/atmosphere interactions on decadal to secular time scales: Water mass formation by air-sea fluxes in the North Atlantic Ocean. in "Report of the Euroclivar/US workshop on The role of the Atlantic in Climate Variability"
(available at web site *http://www.knmi.nl/euroclivar/atlantic.html*)

Starr, V. P., and M. Neiburger, 1940: Potential vorticity as a conservative property. *J. Mar. Res.*, **3**, 202-210.

Stommel, H., 1948: The westward intensification of wind-driven currents. *Trans. Am. Geophys. Union* , **29**, 202-206.

Stommel, H., 1950: The Gulf Stream: A brief history of the ideas concerning its cause. *The Scientific Monthly*, **70**(4), 242-253.

Stommel, H., 1953: Examples of the possible role of inertia and stratification in the dynamics of the Gulf Stream System. *J. Mar. Res.*, **12**, 184-195.

Stommel, H., 1954: An oceanographic observatory. *Research Reviews*, U.S. Office of Naval Research, NAVEXOS P-510, January, pp. 11-13.

Stommel, H., (with G. E. R. Deacon, H. U. Sverdrup and D. W. Thornthwaite), 1955: Discussions on the relationships between meteorology and oceanography. *J. Mar. Res.*, **14**(4), 499-515.

Stommel, H., 1958a: *The Gulf Stream: a Physical and Dynamical Description*, University of California Press, Berkeley, and Cambridge University Press, London, 202 + xiii pp.

Stommel, H., 1958b: The abyssal circulation. *Deep Sea Res.*, **5**, 80-82.

Stommel, H., and A. B. Arons, 1960a: On the abyssal circulation of the world ocean. I. Stationary planetary flow patterns on a sphere. *Deep Sea Res.*, **6**, 140-154.

Stommel, H., and A. B. Arons, 1960b: On the abyssal circulation of the world ocean. II. An idealized model of the circulation pattern and amplitude in oceanic basins. *Deep Sea Res.*, **6**, 217-233.

Stommel, H., 1965: *The Gulf Stream, A Physical and Dynamical Description*, University of California Press, Berkeley, second edition, 248 pp.

Stommel, H., and G. Veronis, 1980: Barotropic response to cooling. *J. Geophys Res.* **85**, 6661-6666.

Suga, T., Hanawa, K., and Y. Toba, 1989: Subtropical Mode Water in the 137E section. *J. Phys. Oceanogr.*, **19**, 1605-1618.

Sun, S., Bleck, R. and E. P. Chassignet, 1993: Layer outcropping in numerical models of stratified flows. *J. Phys. Oceanogr.*, **23**, 1877-1884.

Sverdrup, H. V., 1947: Wind-driven currents in a baroclinic ocean, with application to the equatorial currents of the eastern Pacific. *Proc. Nat. Acad. Sci. U.S.A.* **33**, 318-326.

Swallow, J. C., and L. V. Worthington, 1957: Measurements of deep currents in the western North Atlantic. *Nature*, **179**, 1183-1184.

Talley, L. D., and M. E. Raymer, 1982: Eighteen degree water variability. *J. Mar. Res.*, **40**(Suppl.), 147-172.

Talley, L. D., and M. S. McCartney, 1982: Distribution and circulation of Labrador Sea Water. *J. Phys. Oceanogr.*, **12**, 1189-1205.

Thompson, D. W. L., and J. M. Wallace, 1998: The Arctic Oscillation signature in the wintertime geopotential height and temperature fields. *Geophys. Res. Lett.*, **25**, 1297-1300.

Thomson, C. Wyville, 1877: The voyage of the *Challenger*. The Atlantic. Macmillan London, Vol. 1, 1-424.

Thorpe, S. A., 1973: Turbulence in stably stratified fluids: A review of laboratory experiments. *Bound. Layer Meteor.*, **5**, 95-119.

U.S. Naval Oceanographic Office, 1965: *Oceanographic Atlas of the North Atlantic Ocean, Section I, Tides and Currents, Publ. 700*, 77 pp., Defense Mapping Agency Hydrographic Center, Washington, D.C.

Visbeck, M., Stammer, D., Toole, J., Hurrel, J., McCreary, J., McCartney, M., Marshall, J., Rhines, P., Chang, P., and C. Wunsch, 1998: Atlantic Climate Variability Experiment (ACVE): Science and Implementation Plan. (available at web site *http://puddle.mit.edu/~detlef/acve/acverep.html*).

Walin, G., 1982: On the relation between sea-surface heat flow and thermal circulation in the ocean. *Tellus*, **34**, 187-195.

Wang, L., and C. J. Koblinsky, 1996: Annual variability of the subtropical recirculations in the North Atlantic and North Pacific: A Topex/Poseiden study. *J. Phys. Oceanogr.*, **26**, 2462-2479.

Welander, P., 1959: An advective model of the ocean thermocline. *Tellus*, **11**, 309-318.

Weller, R. A., Rudnick, D. L., and N. J. Brink, 1995: Meteorological variability and air-sea fluxes at a closely spaced array of surface moorings. *J. Geophys Res.* **100**, 4867-4883.

Wertheim, G. K., 1954: Studies of the electric potential between Key West, Florida, and Havana, Cuba. *Trans. Amer. Geophys. Union*, **35**, 872-882.

Woodruff, S. D., Lubker, S. J., Wolter, K., Worley, S. J., and J. D. Elms, 1993: Comprehensive Ocean-Atmosphere Data Set (COADS) release 1a: 1980-92. *Earth Sys. Monit.*, **4**(1), 4-8.

Woods, J. D., and W. Barkmann, 1986: A lagrangian mixed layer model of Atlantic 18° Water formation. *Nature*, **319**, 574-576.

Worthington, L. V., 1954: Three detailed cross-sections of the Gulf Stream. *Tellus*, **6**, 116-123.

Worthington, L. V., 1959: The 18° water in the Sargasso Sea. *Deep Sea Res.*, **5**, 297-305.

Worthington, L. V., 1972: Anticyclogenesis in the oceans as a result of outbreaks of continental polar air. In "Studies in Physical Oceanography - a tribute to Georg Wust on his 80th birthday" (ed. Gordon, A.L.) **1**, 169-178 (Gordon and Breach, New York, 1972)

Worthington, L. V., 1976: On the North Atlantic circulation. *The John Hopkins Oceanographic Studies, 6*, The John Hopkins University Press, 110 pp.

Worthington, L. V., 1977: Intensification of the Gulf Stream after the winter of 1976-77. *Nature* , **270**, 415-417.

Xue, H., Bane, J. M., and L. M. Goodman, 1995: Modification of the Gulf Stream through strong air-sea interactions in winter: Observations and numerical simulations. *J. Phys. Oceanogr.*, **25**, 533-557.

SOUTHAMPTON UNIVERSITY LIBRARY

USER'S DECLARATION

AUTHOR: MARSH, ROBERT TITLE: VARIABILITY OF WATER MASSES AND CIRCULATION IN THE SUBTROPICAL NORTH ATLANTIC

DATE: 1999

I undertake not to reproduce this thesis, or any substantial portion of it, or to quote extensively from it without first obtaining the permission, in writing, of the Librarian of the University of Southampton.

To be signed by each user of this thesis

DATE	SIGNATURE	ADDRESS